



HAL
open science

Engineering 2D organic nanoarchitectures on Au(111) by self-assembly and on-surface reactions

David Peyrot

► **To cite this version:**

David Peyrot. Engineering 2D organic nanoarchitectures on Au(111) by self-assembly and on-surface reactions. Materials Science [cond-mat.mtrl-sci]. Université Paris Saclay (COmUE), 2017. English. NNT : 2017SACLX007 . tel-01941703

HAL Id: tel-01941703

<https://pastel.hal.science/tel-01941703v1>

Submitted on 2 Dec 2018

HAL is a multi-disciplinary open access archive for the deposit and dissemination of scientific research documents, whether they are published or not. The documents may come from teaching and research institutions in France or abroad, or from public or private research centers.

L'archive ouverte pluridisciplinaire **HAL**, est destinée au dépôt et à la diffusion de documents scientifiques de niveau recherche, publiés ou non, émanant des établissements d'enseignement et de recherche français ou étrangers, des laboratoires publics ou privés.

NNT : 2017SACLX007

THESE DE DOCTORAT
DE
L'UNIVERSITE PARIS-SACLAY
PREPAREE A
L'ÉCOLE POLYTECHNIQUE

ÉCOLE DOCTORALE N°572
Ondes et matières

Spécialité de doctorat : Nanophysique

Par

M. David PEYROT

Engineering two-dimensional organic nanoarchitectures
using self-assembly and on-surface reactions

Thèse présentée et soutenue à Saint-Aubin, le 6 janvier 2017 :

Composition du Jury :

M. Mayne Andrew
M. Lacroix Jean-Christophe
M. Bonvoisin Jacques
M. Roditchev Dimitri
M. Silly Fabien

Directeur de Recherche CNRS, ISMO
Professeur, Université Paris Diderot, ITODYS
Chargé de recherche CNRS, CEMES
Professeur, ESPCI, LPEM
Directeur de recherche, CEA Saclay

Président
Rapporteur
Rapporteur
Examineur
Directeur de thèse

Remerciements

Bien que le doctorat soit par essence un projet principalement personnel, sa réussite aussi bien sur le plan scientifique que sur le plan humain n'en demeure pas moins collective. Aussi, bien que la liste ne soit pas exhaustive, je souhaiterais remercier les personnes qui m'ont aidé, accompagné et soutenu durant ces trois ans d'aventure scientifique.

La première personne que je tiens à remercier est Fabien Silly qui en premier m'a fait confiance en acceptant de diriger ma thèse. Nous avons pu beaucoup échanger au cours de ces trois ans où ton aide et tes conseils précieux m'ont beaucoup apporté.

Je souhaiterais ensuite remercier les membres de mon jury de thèse. Tout d'abord, merci à Jean-Christophe Lacroix et Jacques Bonvoisin d'avoir accepté d'être rapporteur de ma thèse, et pour vos remarques et conseils toujours constructifs. Merci également à Andrew Mayne et Dimitri Rodichev pour les échanges scientifiques passionnants que nous avons pu avoir lors de la soutenance.

Je souhaite également remercier l'ensemble des membres du LEPO pour les nombreux échanges que nous avons pu avoir durant ces trois années. Je souhaite en particulier bonne chance à Sarah et Sylvain pour la suite de leurs thèses. Merci aussi à Mathieu pour son aide précieuse lors de runs synchrotron à Soleil et à Singapour.

Merci également aux chimistes, en particulier Guy, Bruno, Stéphane, Renaud et les autres post-docs/ thésards pour nos discussions du midi et pour les parties de foot animées de fin d'après-midi.

Merci également aux techniciens qui ont pu m'aider à résoudre les nombreux problèmes matériels qui sont apparus durant ma thèse, en particulier à Dominique et Fred. Fred qui n'a d'ailleurs jamais manqué une occasion de me chambrer sur les verts à chaque fois que je le croisais dans un couloir, ou bien lors des footings autour du centre. Je souhaite d'ailleurs une longue vie

aux SpeCitrons dont j'ai eu l'honneur de défendre les couleurs trois années consécutives au relai inter-services.

Je souhaite aussi remercier Christine pour son aide toujours bienvenue pour les démarches administratives, et Yasmina pour sa bonne humeur communicative.

Je souhaite également remercier les anciens doctorants / post-docs avec qui j'ai pu interagir durant ces trois années, notamment Jérémy et Vladimir avec qui j'ai pu travailler au quotidien.

Merci également à tous mes amis, dont je ne pourrais pas citer ici tous les noms, notamment aux Despés pour les bons moments que nous avons pu passer durant cette période.

Enfin, la thèse étant l'aboutissement d'un long parcours, je ne pourrais pas terminer ces remerciements sans évoquer ma famille, qui m'a aidé et soutenu depuis le début. En particulier, un énorme merci à Clotilde qui a partagé ces trois ans d'aventure avec moi pour son soutien et son aide précieuse.

General introduction

Over the last few years, an increasing demand for performance improvements and low energy consumption has led to a race towards miniaturization. In 1959, professor Richard Feynman gave a visionary lecture at the American Physical Society meeting in Caltech which was entitled: *“There’s plenty of room at the bottom”* [1]. He already envisioned the evolution from the milli or micrometer scale down to the nanoscale. In the electronics field for example, the size of the transistors on microprocessors has been drastically reduced to improve the transistor density on the chips and thus increasing the performance of the devices. The size of the devices has been successively reduced to few tens of nanometers and is now facing technological and physical limitations. Lots of research efforts are put into the research on nanodevices to pursue the miniaturization down to the nanoscale by two main approaches.

The first approach, called “top down”, consists in starting with bulk material and then to remove some material to engineer nanostructures. Among all the top down techniques, photolithography has been widely developed, essentially in the semiconductor and in the electronics industry. It basically consists in exposing a wafer with light through a patterning mask. Intel successfully developed commercial processors using lithography with transistors size down to 14 nm [2]. This technique shows however important physical and technological limitations.

The second approach called “bottom up” consists in assembling elementary building blocks together to create nanostructures. These building blocks can be of different size and different nature such as organic molecules, metal atoms, or ionic compounds for example. The size of the molecular building blocks usually ranges from Angströms to several nanometers. It is possible to use atomic lateral manipulation techniques to move these building blocks on a surface. However, due to their size, it is impossible to build nanostructures over large areas using these manipulation techniques. One of the solutions to overcome this problem is to take advantage of the self-assembly properties of specific molecules. These self-assembly properties are driven by the interactions between

0. GENERAL INTRODUCTION

the building blocks. Jean-Marie Lehn together with Donald Cram and Charles Pedersen were awarded the Nobel prize in chemistry in 1987 “for their development and use of molecules with structure-specific interactions of high selectivity”. They took advantage of intermolecular interactions to build 3D organic nanostructures or supramolecular assemblies.

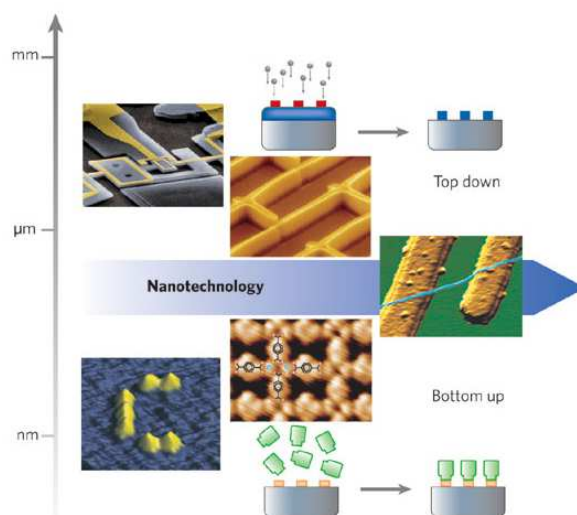


Figure 1: *Illustration of top down and bottom up approaches [3]*

The idea of two-dimensional self-assembly is to engineer supramolecular assemblies but this time on surfaces. Non covalent 2D organic self-assembly relies on reversible intermolecular interactions such as hydrogen bonds or halogen bonds. The strength, selectivity and directionality of such interactions can be used to precisely engineer 2D nanostructures. Tuning the building block geometry, molecular functions, coverage as well as the underlying surface material and temperature thus allow the formation of nanoarchitectures with different structures but also with particular electronic properties. Indeed, the electronic properties of materials strongly depend on their structure at the nanoscale. Due to the low strength of the interactions involved in the 2D self-assembly process, the corresponding structures may suffer from limited thermal stability at very high temperature for example.

Another strategy to generate more stable nanostructures is to build 2D nanoarchitectures stabilized by covalent bonds. Graphene is the archetypal 2D material composed of covalently bonded carbon atoms and has gained tremendous interest over the last few years, especially after the 2010 Nobel prize. Graphene especially exhibits very high carrier mobility [4]. However, it strongly suffers from the absence of bandgap. The ability to process a porous graphene layer with a controllable hole-superlattice would for example

lead to the realization of a 2D semiconducting carbon-layer with a significant and tunable energy band gap [5]. Controlling and tuning the formation of C-C covalently bonded 2D nanostructures is thus a promising approach to build materials with new electronic properties. One way to covalently bind the building blocks together is to take advantage of on-surface reaction of specific precursors to build surface-confined two-dimensional nanostructures. This approach has gained interest only very recently and the so-synthesized nanostructures suffer from defects due to the irreversibility of the C-C bond.

The objective of this project was to engineer novel two-dimensional organic nanostructures and investigate their properties. To that extent, novel 2D self-assembled nanostructures stabilized by hydrogen bonds, halogen bonds and hybrid ionic-organic interactions are engineered and characterized. Another approach consisting in engineering robust porous 2D covalent nanostructures by on-surface reaction is investigated for two different molecular precursors.

Scanning Tunneling microscopy (STM) is used to characterize both 2D covalently bonded nanostructures and self-assembled organic nanostructures. STM allows the characterization of the topology and the electronic properties of these organic nanostructures with capability of atomic resolution in the real space. Information on the local arrangement of the molecules and on the structure of 2D covalent nanoarchitectures is thus revealed using this powerful technique. These STM measurements are supplemented by X-ray Photoelectron Spectroscopy (XPS) measurements made at the Soleil Synchrotron. XPS allows the characterization of the chemical composition and environment of the 2D organic structures with a very high surface sensitivity.

This manuscript is divided in seven chapters and two additional appendices.

The first chapter introduces the concepts of 2D molecular self-assembly and self-organization on surfaces and gives examples and important results. A description of the molecular self-assembly process and of the intermolecular interactions involved in the self-assembly process will be given. Self-assembly engineering will be presented through various parameters which can be used to tune the resulted nanoarchitectures. Finally, on-surface covalent nanostructure engineering by Ullmann coupling reaction will be explored.

The second chapter introduces the experimental techniques and set-up used during my PhD. Scanning Tunneling Microscopy (STM) will be presented as well as the UHV experimental set-up at CEA Saclay. Au(111) reconstructed surface will also be described.

The third chapter will focus on the influence of local arrangement on the electronic properties of organic thin films. The case of two-dimensional self-assembly of perylene derivative molecules on Au(111) surface will be investigated.

0. GENERAL INTRODUCTION

In the fourth chapter, a new type of hybrid self-assembly involving molecules and ionic materials (perylene derivative and sodium chloride) will be investigated.

The fifth chapter deals with the competition between on-surface Ullmann coupling and halogen-halogen bonded self-assembly in the case of star-shaped iodinated molecules driven by the diffusion on Au(111) substrate.

In the sixth chapter, the temperature dependent hierarchical on-surface formation of 2D porous covalent nanostructures by Ullmann coupling will be investigated through the example of six-brominated star-shaped molecules on Au(111) surface.

Finally, chapter 7 gives a general conclusion, sums up all the results presented in the previous chapter and gives potential prospects.

Table of contents

General introduction	iii
1 Two-dimensional organic nanostructures based on molecular self-assembly and on-surface reactions	1
1.1 Creating molecular nanoarchitectures using self-assembly	1
1.1.1 Molecular self-assembly process	1
1.1.2 Molecular building blocks interactions	6
1.1.2.1 Van Der Waals interactions	6
1.1.2.2 Hydrogen bonds	8
1.1.2.3 Halogen-halogen interactions	10
1.1.2.4 Metal-organic interactions	11
1.1.2.5 Ionic-organic interactions	13
1.1.2.6 Covalent bonds	16
1.2 Parameters to tailor 2D self-assembled nanoarchitectures	18
1.2.1 Influence of molecular design	18
1.2.1.1 Molecular substituents	18
1.2.1.2 Molecular geometry	19
1.2.2 Influence of building block coverage	20
1.2.3 Substrate influence	21
1.2.3.1 Mobility	22
1.2.3.2 Influence of surface lattice and symmetry	24
1.2.3.3 Surface reconstruction	26
1.2.3.4 Vicinal surfaces	27
1.2.3.5 Surface catalytic activity and reactivity	28
1.2.4 Temperature influence	29
1.2.4.1 Diffusion and phase transition	29
1.2.4.2 On-surface reaction activation	30
1.3 On-surface covalent coupling reaction: Ullmann coupling	32

TABLE OF CONTENTS

1.3.1	General description	32
1.3.2	Influence of the halogen substituent	34
1.3.3	Influence of the substrate	36
1.3.4	Molecular halogen by-products	37
2	Experimental set up and techniques	41
2.1	Scanning Tunneling Microscopy	41
2.1.1	The Tunnel effect	41
2.1.2	Tunneling current models	44
2.1.2.1	Bardeen's approximation	46
2.1.2.2	Tersoff-Hamann model	48
2.1.3	Contrast and interpretation of STM images	49
2.2	Experimental set-up at CEA Saclay	51
2.2.1	STM head	51
2.2.1.1	Piezo-electric scanners	51
2.2.1.2	Current feedback loop and data acquisition	51
2.2.1.3	Vibration damping systems	52
2.2.2	Ultra high vacuum chambers	53
2.2.2.1	Pumping elements	53
2.2.2.2	Surface preparation elements	56
2.2.2.3	Evaporation sources	56
2.3	Au(111) substrate	58
3	PTCDI on Au(111): Influence of local arrangement on self-assembly electronic properties	63
3.1	Canted nanostructure	64
3.2	Side-by-side arrangement	65
3.3	Tip-induced structural reorganization	67
3.4	Localized electronic coupling	68
4	Engineering of new PTCDI-NaCl hybrid ionic-organic nanostructures	73
4.1	Sodium Chloride on Au(111)	73
4.2	Temperature dependent PTCDI-NaCl nanostructures on Au(111)	76
4.2.1	Room temperature deposition: Flower structure	76
4.2.2	Porous mesh hybrid nanostructure after 100°C annealing	79
4.2.3	Hybrid ladder and chain structures after 150°C annealing	81
4.2.4	Investigation on the PTCDI-NaCl interactions	83

5	On-surface synthesis of 2D covalent organic structures versus halogen-bonded self-assembly: competing formation of organic nanoarchitectures	87
5.1	Low coverage (<0.2ML) deposition at room temperature: porous covalent nanostructure	89
5.2	Submonolayer coverage (0.2ML<C<1ML): unexpected halogen-bonded network growth	92
5.2.1	Sine-wave X-bonded structure	94
5.2.2	Bow-tie X-bonded structure	95
5.2.3	Covalent-dimer X-bonded structure	97
5.2.4	Covalent-chain assembly	98
5.3	Supramonolayer deposition (>1ML): on-top covalent nanoarchitectures . .	98
5.4	Influence of the surface temperature	99
5.5	Investigation on the diffusion limited TIPB dehalogenation	100
6	Temperature-dependent hierarchical on-surface synthesis of porous halogen-bonded, hybrid and covalent two-dimensional nanoarchitectures	105
6.1	Halogen-bonded nanoarchitecture at room temperature	107
6.2	Formation of a 2D mixed halogen-bonded and single-covalent-bond hexagonal superstructure after annealing at 145°C	110
6.3	Disappearance of 2D halogen-bonded nanoarchitecture after annealing at 165°C	113
6.4	Single-covalent-bond chain-nanoarchitecture after annealing at 170°C . . .	114
6.5	Simultaneous formation of single and double covalently-bonded nanoarchitectures after annealing at 175°C	115
6.6	Exclusive formation of double covalently-bonded nanoarchitectures after deposition onto a 275°C Au(111) surface	118
6.7	Summary of the temperature-dependent covalent nanostructures formation	120
7	General Conclusion and Outlook	123
A	Interfacing and automating of laboratory equipments	127
A.1	Pressure monitor	128
A.1.1	AML PGC2 gauge controller	128
A.2	Power supply controller	130
A.2.1	Delta Elektronika ES230-10	130
A.2.1.1	RS232 Model	130

TABLE OF CONTENTS

A.2.1.2	Ethernet Model	132
A.2.2	Elektro automatic PS 2000	133
A.3	K-cell evaporators controller	133
A.3.1	Createc K-cell evaporators	133
A.3.2	Custom evaporators	136
B	X-ray photoemission spectroscopy and synchrotron radiation	139
B.1	X-ray photoemission spectroscopy (XPS)	139
B.1.1	General presentation and associated physical processes	139
B.1.2	Hemispherical electron analyzer	143
B.1.3	Spectroscopic measurements and peak shape	144
B.2	X-ray spectroscopy facilities and equipment	145
B.2.1	Soleil Synchrotron	145
B.2.2	TEMPO beamline	146
	References	172

Chapter 1

Two-dimensional organic nanostructures based on molecular self-assembly and on-surface reactions

The objective of this chapter is to present the fundamental concepts and results of two-dimensional organic nanostructures engineering. First, the molecular self-assembly process will be described with the main intermolecular interactions involved in this process. Then, parameters to potentially tune or tailor 2D self-assembled nanostructures will be studied. Finally, the last section will deal about 2D organic covalent self-organizations synthesized by on-surface Ullmann coupling reaction.

1.1 Creating molecular nanoarchitectures using self-assembly

1.1.1 Molecular self-assembly process

Molecular self-assembly can be defined as a process by which molecules, considered as nanosized building blocks, form organized structures. The self-assembly process is spontaneous and does not require guidance, hence the adjective “*self*”. Self-assembly is a key concept in supramolecular chemistry and can be used to engineer complex nanostructures on various surfaces [3, 6, 7, 8, 9, 10]. This process originates from the complex balance between molecule-molecule interactions and molecule-substrate interactions. Intermolecular interactions originate from both attractive and repulsive forces that can occur between

1. TWO-DIMENSIONAL ORGANIC NANOSTRUCTURES BASED ON MOLECULAR SELF-ASSEMBLY AND ON-SURFACE REACTIONS

the active sites (functional groups) of the building blocks. Many kinds of intermolecular interactions such as hydrogen bonds, halogen bonds, Van der Waals interactions, metal-organic interactions, etc... can be used to drive molecular self-assembly. Depending on the strength of these interactions (Table 1.2), a whole process of bond breaking / bond formation occurs until an equilibrium is reached. This ability, often called “self-healing”, allows the growth of molecular films with low defect amount. Molecule substrate interactions also have to be taken into account. If the molecule-substrate interactions are too strong, the molecules would be trapped and would not move on the surface, thus preventing intermolecular interactions to drive molecular self-assembly. Molecular building blocks should be able to diffuse on the surface and this diffusion is mostly governed by the temperature.

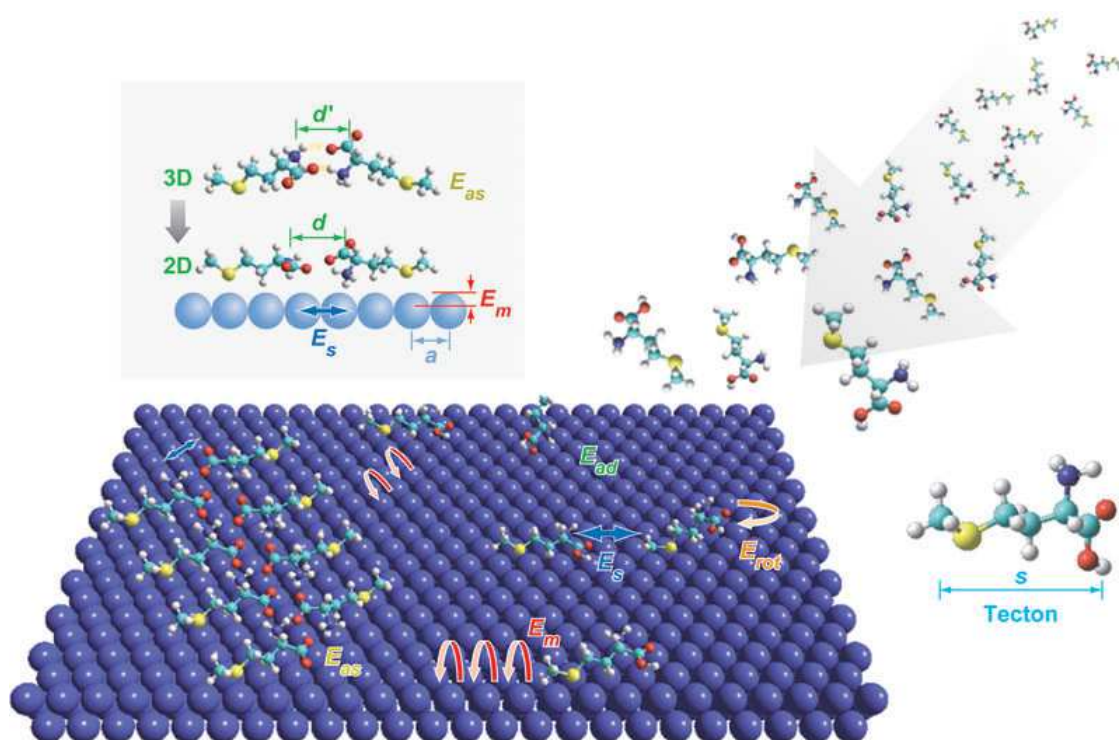


Figure 1.1: Scheme of two-dimensional organic self-assembly process on a surface (adapted from ref [11]). A molecular beam is directed toward the surface. Molecules (called here tectons) are then adsorbed on the surface (energy gain E_{ad}) and may rotate (energy barrier E_r) or diffuse (energy barrier E_m). Molecules can interact with each other through their active sites by various kinds of interactions (energy gain E_{as}) and form stable organized organic structures.

1.1 Creating molecular nanoarchitectures using self-assembly

The principle of two-dimensional molecular self-assembly was previously described by Barth [3, 11, 12]. First, a molecule arrives on a surface and is adsorbed on a specific site, associated with an energy gain E_{ad} (Figure 1.1). From this site, molecule can either move on the surface (with an energy barrier E_m) or rotate (with an energy barrier E_r). The thermal motion of the adsorbate is mediated through the coupling with thermal phonons of the substrate having a typical frequency (ν_s) of 10^{12} - 10^{13} s⁻¹ and a typical vibrational amplitude of $\approx 0.1\text{\AA}$ for surface atoms at room temperature. Two kinds of situations should be considered [13]:

- If $k_B T \ll E_m$ (k_B being the Boltzmann constant and T the temperature), the molecules are trapped in their adsorption sites and self-assembly cannot occur. This situation is typically occurring at cryogenic temperatures (below 4K) on metal surfaces or on some semiconductors at room temperature at a certain time scale. If a much larger time scale is considered, upon continuous energy exchange with the substrate, a molecule might rarely accumulate enough energy to overcome the lateral barrier and to jump to another adsorption site. These jumps are assumed to be uncorrelated and a hopping rate can be defined as:

$$\Gamma_s = \nu_s \exp\left(\frac{-E_m}{k_B T}\right) \quad (1.1)$$

Similarly, addressing the rotation motion and given that $k_B T \ll E_r$, the rotational rate can be expressed as:

$$\Gamma_r = \nu_r \exp\left(\frac{-E_r}{k_B T}\right)$$

- If $k_B T \geq E_m$, the molecules are no longer confined to their adsorption sites and can diffuse on the surface following a Brownian motion with a diffusion coefficient given by:

$$D = \frac{k_B T}{\gamma m} \quad (1.2)$$

where γ is the molecule-surface friction coefficient and m the mass of the molecule. This Brownian motion also called random walk only considers that molecule-molecule interactions are limited to elastic collisions.

1. TWO-DIMENSIONAL ORGANIC NANOSTRUCTURES BASED ON MOLECULAR SELF-ASSEMBLY AND ON-SURFACE REACTIONS

While diffusing on the surface, a molecule may come close enough to another molecule to interact with it (energy gain E_{as}). If the intermolecular interaction energy is too large with respect to the kinetic energy of the molecules ($E_{kinetic} \ll E_{as}$), the molecule-molecule bond created is irreversible. Consequently, there is no more “self-healing” and the most thermodynamically stable state (associated with the minimum free enthalpy) cannot be obtained. In contrast, if the intermolecular interactions are too weak ($E_{kinetic} \gg E_{as}$), then intermolecular bonds will be broken instantaneously and no stable structure can be achieved. If the molecules kinetic energy is much larger than their adsorption energy ($E_{kinetic} \gg E_{ad}$), then the molecules will desorb out of the surface. Indirect substrate-mediated interactions can also influence the molecular self-assembly process (energy E_s). An energy criterion for molecular self-assembly to occur can be expressed as [14]:

$$E_{ad} > E_{as} \geq E_{kinetic} > E_m$$

	Energy range	Distance	Character
Adsorption	$E_{ad} \approx 0.5-10$ eV	$\approx 1.5-3$ Å	Directional, site selective
Surface migration	$E_m \approx 0.05-3$ eV	$\approx 2.5-4$ Å	1D / 2D
Rotational motion	$E_{rot} \sim dim(E_m)$	s	2D
Indirect substrate mediated	$E_s \approx 0.001-0.1$ eV	a to nanometerrange	Oscillatory
Reconstruction mediated	$E_s \sim 1$ eV	short	Covalent

Table 1.1: *Classification of interactions involved in the self-assembly process for molecules on metal surfaces with associated energies and typical distances [11].*

1.1 Creating molecular nanoarchitectures using self-assembly

Self-assembly process is strongly influenced by the ratio between the building block diffusivity (D) and the deposition flux (F) (Figure 1.2). Small D/F ratio (deposition on substrate at low temperature for example) leads to kinetically-driven growth of metastable nanostructures. Under these small D/F ratio conditions, self-organization rather than self-assembly process *stricto sensu* is occurring since thermodynamic equilibrium is not reached. In contrast, for large D/F ratios, the adsorbed species have enough time to explore the potential energy surface so that the system reaches a minimum energy configuration.

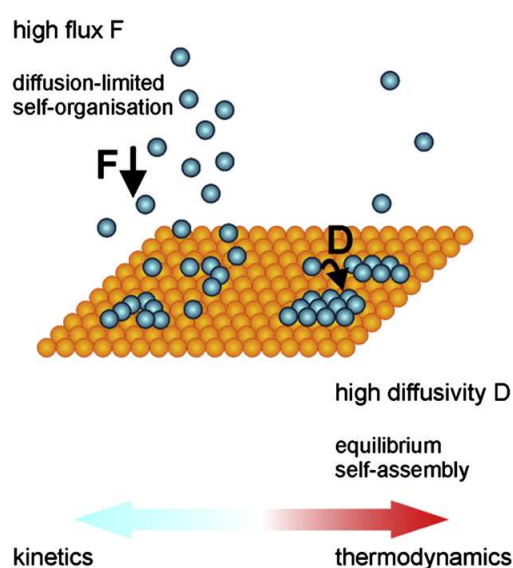


Figure 1.2: Scheme illustrating the difference between self-organisation (small D/F) and self-assembly (large D/F) processes. [14].

In conclusion, under specific conditions, molecular building blocks can diffuse on the surface. They can then interact with each other through a large range of interactions and spontaneously form stable organic structures with low defect rate. Depending on the nature of the molecules active sites (or molecular functions), different kinds of interactions (associated with different energies E_{as}) will come into play. Typical interactions involved in the molecular self-assembly process will be described in the following section.

1. TWO-DIMENSIONAL ORGANIC NANOSTRUCTURES BASED ON MOLECULAR SELF-ASSEMBLY AND ON-SURFACE REACTIONS

1.1.2 Molecular building blocks interactions

Different intermolecular interactions can occur between molecular building blocks. Each interaction has specific characteristics: the energy range (strength), the typical range (meaning the distance between the chemical groups for that interaction to occur) and also the eventual directionality and/or selectivity properties (Table 1.2). In this section, Van der Waals interactions, halogen-halogen bonds, hydrogen bonds, metal-organic interactions, ionic-organic interactions and covalent bonds will be presented. The advantages and the drawbacks of these interactions will be compared in the context of molecular self-assembly or self-organization abilities.

Interaction	Energy range (eV)	Distance	Character
Van der Waals	$\approx 0.02 - 0.1$	$< 1\text{nm}$	Non selective
Hydrogen bonds	$\approx 0.05 - 0.7$	$\approx 1.3 - 3.5\text{\AA}$	Selective, Directional
Metal-ligand interactions	$\approx 0.5 - 2$	$\approx 1.5 - 2.5\text{\AA}$	Selective, Directional
Electrostatic ionic	$\approx 0.05 - 2.5$	Long range	Non selective
Covalent bonds	$\approx 1.5 - 5.2$	$\approx 0.74 - 2.28\text{\AA}$	Directional

Table 1.2: Main intermolecular interactions characteristics and strengths [11]

1.1.2.1 Van Der Waals interactions

Van der Waals interactions, named after the Dutch scientist *Johannes Diderik Van der Waals*, are a combination of interactions between atoms or molecules that can be either attractive or repulsive. They originate from the quantum fluctuation of the electron clouds of neighboring particles. Van der Waals interactions can be decomposed in four separate components arising from different physical interactions:

- **Repulsive force** that takes into account Pauli's exclusion principle and thus prevent molecules or atoms to collapse.
- **Keesom interaction** resulting from the interaction between two permanent dipoles.
- **Debye interaction** resulting from the interaction between a polar molecule and a nonpolar molecule (that becomes polarized).
- **London interaction** (dominant interaction) that results from the interaction of a fluctuating dipole (due to the fluctuation of the electron clouds) with an induced dipole.

1.1 Creating molecular nanoarchitectures using self-assembly

These interactions are quite weak ($\approx 0.02 - 0.1$ eV) but are also non-selective and non-directional (Table 1.2). Numerous examples of two-dimensional nanostructures stabilized by Van der Waals (VdW) interactions have been reported. Schöck *et al.* [15] reported an example of two-dimensional organic self-assembly of (HtB-HBC)¹ on Cu(110) surface studied by STM under Ultra High Vacuum (UHV).

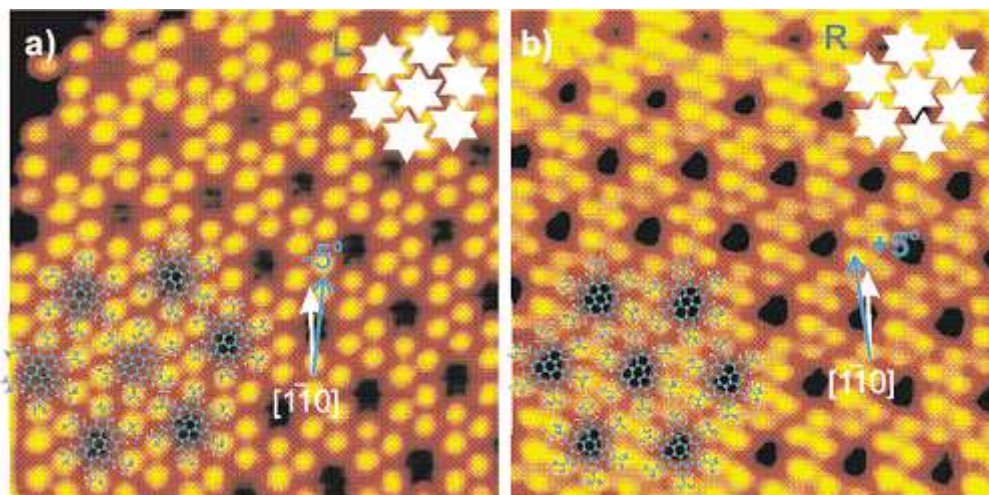


Figure 1.3: STM images (10×10 nm²) of the two mirror-symmetric domain orientations for HtB-HBC molecules on Cu(110). Models of the HtB-HBC molecules are superimposed on the experimental STM image (lower-left corners). The correspondence with a simple close-packing of star-shaped objects is shown in the upper-right corners, where the handedness of the networks is described. The blue arrows show the 5° rotation of the molecular axis with respect to the close-packed $[\bar{1}10]$ direction of the Cu(110) substrate (white arrow) [15].

These 6-star-shaped molecules possess six *tert*butyl arms and are only made of carbon and hydrogen atoms. Once evaporated on Cu(110) surface in UHV, these molecules spontaneously adopt a regular arrangement (Figure 1.3). Detailed analysis shows that HtB-HBC molecules self-assemble into two enantiomeric close-packed networks (respectively Figure 1.3a and Figure 1.3b). These nanostructures correspond to the two enantiomeric geometries of close-packed six-star-shaped molecules in two dimensions (organizational chirality). These close-packed arrangements are mirror symmetric with respect to the Cu(001) plane and the molecular axis forms an angle of $\pm 5^\circ$ with the Cu $[\bar{1}10]$ direction. In such close-packed arrangement, molecules are interdigitated, meaning that the *tert*butyl “arms” or “legs” of neighboring HtB-HBC molecules are very close to each other, maximizing the contact area. The nanoarchitectures are thus stabilized by the

¹2,5,8,11,14,17-hexa-*tert*butylhexabenzob[bc,ef,hi,kl,no,qr]coronene

1. TWO-DIMENSIONAL ORGANIC NANOSTRUCTURES BASED ON MOLECULAR SELF-ASSEMBLY AND ON-SURFACE REACTIONS

VdW interactions between these “arms”. Moreover, it should be noted that all the measurements presented here were taken at low temperature (120-170K). Chiral structures stabilized by VdW interactions were also reported by Xiao *et al.* [16] observing 1,3,5-trikis(4-carboxylphenyl)-2,4,6-trikis(4-*tert*-butylphenyl)-benzene on Au(111) surface at a temperature of 50K.

As demonstrated by these results, one can take advantage of Van der Waals interactions in order to trigger molecular self-assembly. However, VdW forces are not directive, non-selective and very weak. This is why intense research effort has been focused on stronger and directive intermolecular interactions, like hydrogen bonds.

1.1.2.2 Hydrogen bonds

According to the IUPAC¹ definition [17],

The hydrogen bond is an attractive interaction between a hydrogen atom from a molecule or a molecular fragment X-H in which X is more electronegative than H, and an atom or a group of atoms in the same or a different molecule, in which there is evidence of bond formation.

The hydrogen bond involves two elements: one hydrogen atom with a positive partial charge and another atom with a negative partial charge. The hydrogen atom is covalently bonded to a more electronegative atom. Therefore, the electronegative atom attracts the electron cloud and the hydrogen atom holds a positive partial charge (local dipole). This positively charged hydrogen can interact with another negatively charged atom from the same molecule or from another one. This interaction is much stronger than VdW interactions (Table 1.2). Contrary to VdW interactions, hydrogen bonds (or H-bonds) are highly directive. This means that a H-bond between two active sites can only be established along a specific direction or orientation, thus constraining the geometry of the arrangement. This is a very important property in order to engineer organized nanoarchitectures. This interaction or bond can only occur between a partially negatively charged group and a positively charged hydrogen atom. Consequently, this interaction is also selective. Among the examples of H-bonds, one can cite the H-bonds stabilizing water molecules or the H-bonds bridging the nucleotides together in our helix DNA structure.

Numerous two-dimensional organic self-assembly on metallic surface stabilized by H-bonds were reported so far [19, 20]. For example, Lukas *et al.* [18] reported the growth of highly ordered two-dimensional nanostructure after evaporation of adenine molecules

¹International Union of Pure and Applied Chemistry

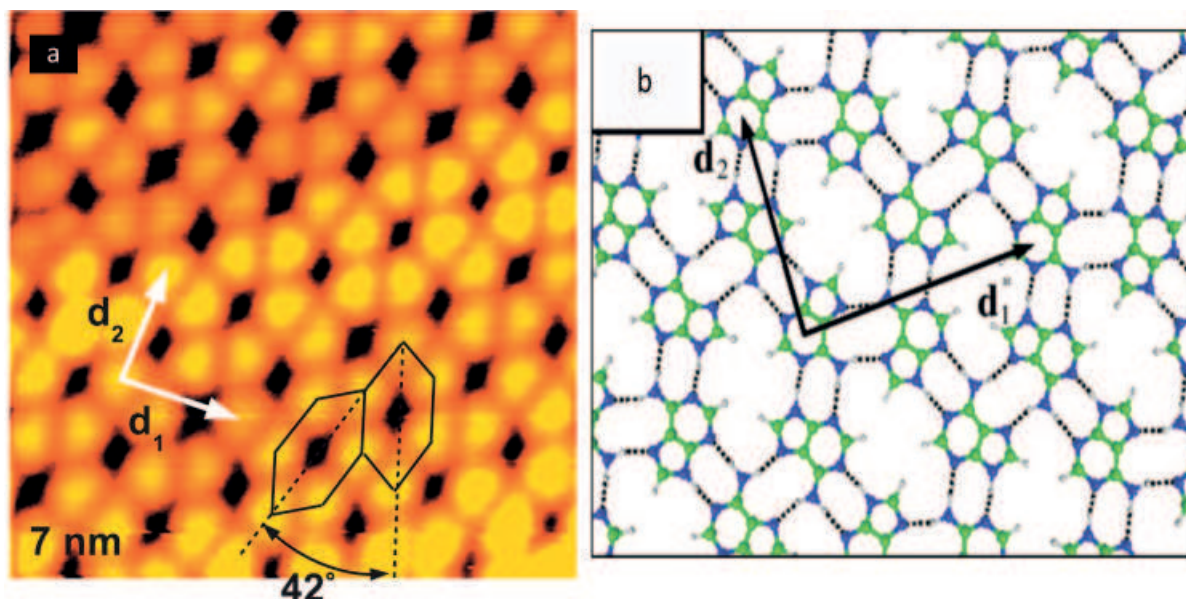


Figure 1.4: (a) STM image ($7 \times 7 \text{ nm}^2$) of two-dimensional self-assembly of adenine molecules on Au(111). Adenine molecules form a periodic structure associated with lattice parameters $d_1 = 15.6 \text{ \AA}$, $d_2 = 12.5 \text{ \AA}$ and an angle of around 42° between the two neighboring unit cells. (b) Molecular model derived from STM images showing that each adenine molecule in this structure is stabilized by double N-H \cdots O bonds (black dotted lines) with its three closest neighbors [18].

on Au(111) surface. High resolution STM observation (Figure 1.4a) reveals that adenine molecules spontaneously form a periodic structure once deposited on Au(111) surface. Figure 1.4b is the molecular model derived from the STM images proposed by the authors. This structure consists in the periodic repetition of two hexagons (each containing six adenine molecules). The molecular model clearly reveals that each adenine molecule in this structure is stabilized by double N-H \cdots O bonds (black dotted lines in Figure 1.4b) with its three closest neighbors. As shown by this example, hydrogen bonds are directive and selective interactions allowing the formation and stabilization of 2D organic self-assembly. These interactions are stronger than VdW interactions allowing a better stabilization of organized nanostructures. Intermolecular interactions between neighboring halogen atoms were also reported to stabilize 2D nanoarchitectures on surface.

1. TWO-DIMENSIONAL ORGANIC NANOSTRUCTURES BASED ON MOLECULAR SELF-ASSEMBLY AND ON-SURFACE REACTIONS

1.1.2.3 Halogen-halogen interactions

Halogen bonds are attractive highly-directional interactions between covalently-bonded halogen atoms (R-X) and a nucleophile D (like N, O, Cl, Br or I). This interaction originates from the non spherical charge distribution around the X atoms. The electrostatic potential on the surface of X atoms (Cl, Br, I) is positively charged δ^+ at the extremity of the X atom in the bond direction (σ hole). A belt around the bond axis appears to be negatively charged δ^- (Figure 1.5a) [21]. Due to this spatial inhomogeneity, halogen atoms tend to bind in a linear arrangement with nucleophiles and in a side arrangement with electrophiles.

Among the halogen bonds, halogen-halogen (C-X \cdots X-C) interactions are a particular kind of interaction. Their strength is similar to hydrogen bonds [22]. Depending on the geometry of the C-X \cdots X-C bonds, two different types of interactions were observed and studied by Bui *et al.* [23]. The so-called "Type-I" interaction corresponds to a geometry for which the C-X \cdots X-C angles, called here respectively θ_1 and θ_2 are equal (Figure 1.5b). This interaction was reported to be VdW interaction type. For the "Type-II" interaction, typical angles of $\theta_1=180^\circ$ and $\theta_2=90^\circ$ are reported (Figure 1.5c). Type-II interaction was explained taking into account the complex spatial charge distribution around the halogen atoms in this geometry (Figure 1.5a). It can be understood as an interaction between nucleophilic and electrophilic regions in adjacent halogen atoms. Oppositely polarized regions are located in front of each other in the type-II geometry. This interaction is thus electrophilic-nucleophilic in nature.

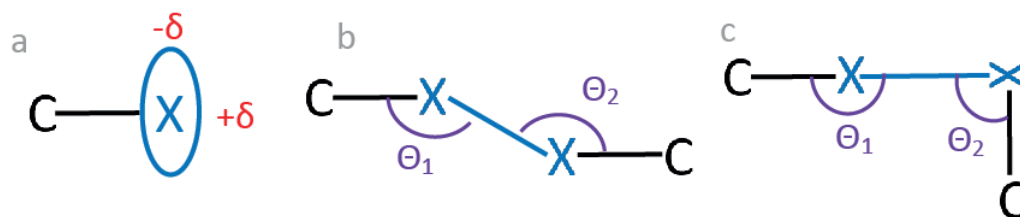


Figure 1.5: *Halogen-halogen interactions.* (a) *Polar flattening effect, showing different atomic radii (r) associated with oppositely polarized regions along perpendicular directions,* (b) *Type I interactions $\theta_1 \approx \theta_2$* (c) *Type II interactions ($\theta_1 = 180^\circ$ and $\theta_2 = 90^\circ$).*

The strength of halogen-halogen bonds depends on the nature of the X atoms. Cl, I and Br atoms have different electronegativity and polarizability thus affecting C-X \cdots X-C bond properties [24]. For example, Bosch *et al.* [25] reported that trihalomesitylenes

1.1 Creating molecular nanoarchitectures using self-assembly

molecules formed 2D arrangements for both iodine and bromine substituted molecules. They reported an interaction between three halogen atoms of neighboring molecules forming triangular halogen-halogen-halogen synthon (X_3 synthon) (Figure 1.6a). This synthon is stabilized by electrophilic-nucleophilic interactions between neighboring X atoms (Figure 1.6b) through type-II halogen bonds. Depending on the halogen substituent, the halogen-halogen separation distance varies from 0.39 nm for iodine to 0.36 nm for bromine and chlorine. Molecules with peripheral halogen atoms are promising organic building blocks to engineer different types of two-dimensional porous carbon-nanoarchitectures through the formation of intermolecular halogen-bonds [26, 27, 28, 29, 30]. Halogen-bonded self-assembled nanoarchitectures have been successfully created using molecules with bromine [31, 32, 33, 34] and iodine substituents [35]. These interactions appear to be a competitive alternative to hydrogen bonds in the context of molecular self-assembly due to their strength, directionality, selectivity and tuneability.

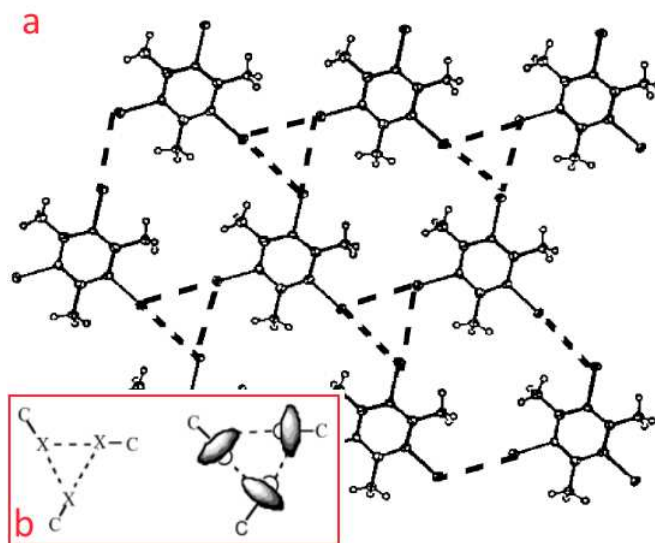


Figure 1.6: (a) Molecular model of trihalomesitylenes molecules forming 2D self-assembly stabilized by halogen-halogen interactions. (b) Molecular model showing electrophilic-nucleophilic interactions in the X_3 synthon [25].

1.1.2.4 Metal-organic interactions

Metal-organic bonds, also called metal-ligand interactions, occur between organic moieties (or ligands) and metallic centers. These interactions are usually stronger than H-bonds (Table 1.2) but also selective and directive. For these reasons, they have attracted great interest in supramolecular chemistry. Well ordered metal-organic arrangements

1. TWO-DIMENSIONAL ORGANIC NANOSTRUCTURES BASED ON MOLECULAR SELF-ASSEMBLY AND ON-SURFACE REACTIONS

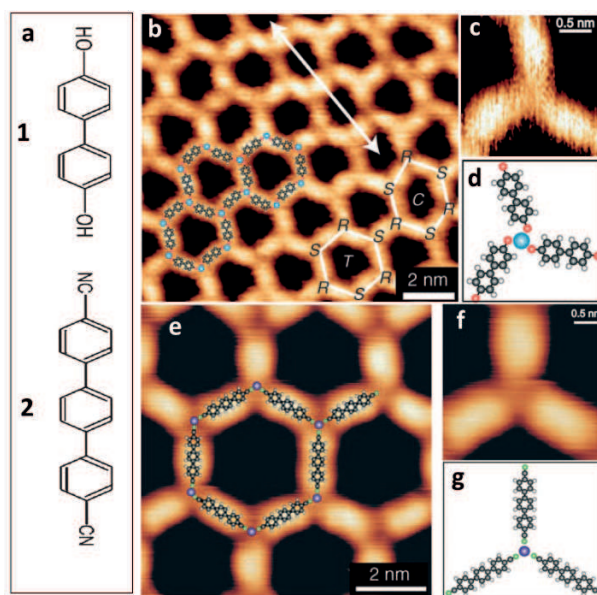


Figure 1.7: (a) Molecular skeleton of 4,4'-biphenol (ligand number 1) and 1,4;4,1'-terphenyl-4,4'-dicarbonitrile (ligand number 2). (b) STM image of porous metal-organic nanoarchitecture formed after deposition of 1 and Fe adatoms on Ag(111) surface ($I=0.1\text{nA}$, $V=0.5\text{V}$). (c) and (d) respectively high resolution image and molecular model of a chiral nodal point of the 1-Fe metal-organic nanoarchitecture showing that ligands are tilted with respect to central Fe. (e) STM image of porous metal-organic nanoarchitecture formed after deposition of 2 and Co adatoms on Ag(111) surface ($I=0.3\text{nA}$, $V=1.9\text{V}$). (f) and (g) respectively high resolution image and molecular model of a nodal point of the 2-Co metal-organic nanoarchitecture showing that ligands are pointing directly towards Co adatom in this structure.[36].

have been reported in one, two and three dimensions [37, 38, 39]. The geometry of such metal-organic arrangements is in general predetermined by both the ligand properties (geometry, chemical function, steric crowding) and the electronic properties of the metallic center involved. Recently, metal-organic interactions have been used to create organized nanoarchitectures made of organic molecules and metal centers directly on solid surfaces. Metal-ligand coordination geometry however appears to eventually deviate from the known “bulk” 3D geometry when deposited on a surface. This can be attributed to charge transfer or screening phenomena but also to the two-dimensional confinement of both ligands and metal centers related to the surface [40, 41].

For example, Stepanow *et al.* [36] managed to engineer several two-dimensional metal-organic self-assembled nanostructures using two linear ligands with different chemical groups and metallic atoms. The ligand number 1 (4,4'-biphenol) (Figure 1.7a) with two

1.1 Creating molecular nanoarchitectures using self-assembly

end phenol groups was deposited on Ag(111) surface together with Fe adatoms. Porous nanostructures were formed (Figure 1.7b). High resolution images show a three-fold symmetry around the nodes of the porous architectures (Figure 1.7c). The authors claim that the two phenol end groups of the molecule **1** are catalytically deprotonated on the surface. Deprotonated ligands are forming O-Fe metal-organic bonds and do not point directly towards Fe center but are tilted clockwise (R) or anticlockwise (S) (see molecular model on Figure 1.7d) giving rise to a chiral nanoarchitecture. They also deposited molecule number **2** (1,4;4,1-terphenyl-4,4-dicarbonitrile) (Figure 1.7a) with cyano end groups on the same Ag(111) surface with cobalt adatoms. They also observed a porous structure with hexagonal pores and three-fold symmetry at the nodes (Figure 1.7e). High resolution STM image reveals that cyano groups of molecules **2** are involved in CN-Co metal-organic bonds. Molecules **2** are this time pointing directly to the cobalt center, and no chirality is thus observed (Figure 1.7f-g). This is a good example of how metal-organic nanoarchitectures can be tuned varying the ligands and/or the nature of metal adatom. Metal-organic bonds can be an alternative to hydrogen bonds because they are also directive and selective, and most of the time stronger than H-bonds.

1.1.2.5 Ionic-organic interactions

In the review article entitled “Tailoring molecular layers at metal surfaces” [42] published in Nature Chemistry in 2010, Bartels listed the intermolecular interactions at surfaces. He considered substrate mediated interactions, VdW interactions, H-bonds, metal-organic interactions and covalent bonds. An interaction is however missing in this review: the ionic-organic interaction. Ionic salts are stabilized by the electrostatic interaction between a negatively charged anion and positively charged cation. This interaction is usually much stronger than H-bond but is also non-directive and non-selective (Table 1.2). Yet, the interaction between organic molecules and ionic salts on surfaces in UHV was the topic of only very few research articles until now and is not completely understood.

Wäckerlin *et al.* [43] reported the first modification of 2D self-assembly induced by the adjunction of ionic salt in UHV. They evaporated TCNQ¹ molecules that are strong electrophiles on Au(111) surface. TCNQ molecules form organized 2D self-assembly stabilized by H-bonds between the cyano groups (Figure 1.8a). After evaporation of sodium chloride (NaCl), the initial H-bonded self-assembly is modified and a new 2D structure appears (Figure 1.8b,c). According to the authors, the TCNQ molecules oxidized the Cl⁻ ions resulting in neutral dichlorine and negatively charged [TCNQ]⁻. They report

¹7,7,8,8-tetracyano-pquinodimethane

1. TWO-DIMENSIONAL ORGANIC NANOSTRUCTURES BASED ON MOLECULAR SELF-ASSEMBLY AND ON-SURFACE REACTIONS

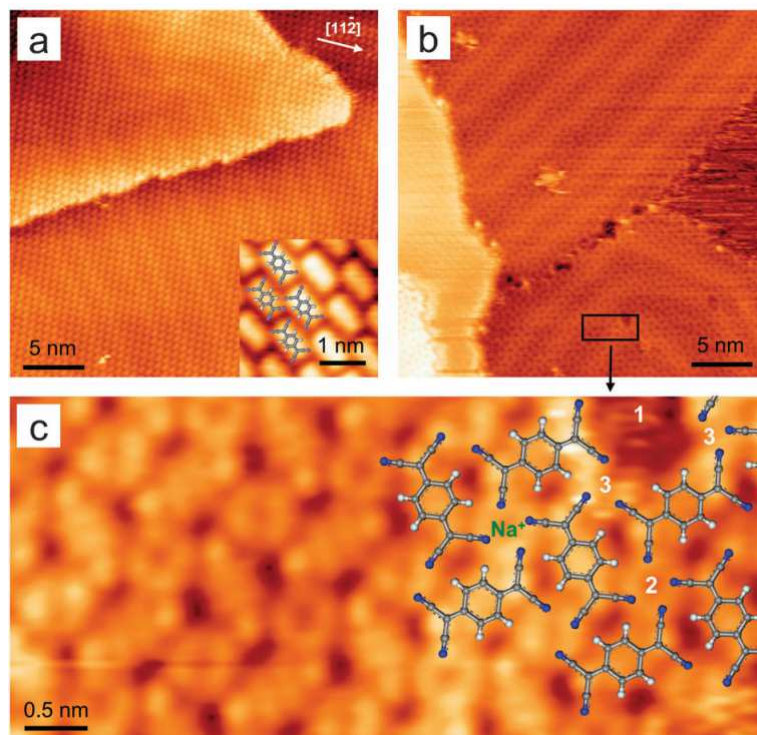


Figure 1.8: STM image of (a) TCNQ layer on Au(111) and (b,c) TCNQ layer on Au(111) after addition of NaCl [43].

[TCNQ]⁻ molecules to interact with Na⁺ ions according to XPS measurements. However, Na⁺ ions are not visible in their STM images (Figure 1.8c).

Later, Skomski *et al.* [44] reported an interaction between carboxylate groups of terephthalic acid (TPA) molecules and sodium ions based on photoemission spectroscopy measurements after deposition of TPA and NaCl on Cu(100) surface (Figure 1.9). In this case, bright spots are observed between the molecules and were attributed to Na⁺ ions by the authors (Figure 1.9c). The authors also claimed that Cl disappears from the surface and penetrates into the bulk. Shimizu *et al.* [45] reported a weak ion-dipole interaction after deposition of polar diarylethene molecules and NaCl on Cu(111).

Recently, Guo *et al.* [46] reported a modification of a H-bonded nanoarchitecture induced by the addition of an ionic salt. Figure 1.10a is an STM image of Ag(100) surface after deposition of PTCDA¹ monolayer. Molecules are self-assembling in an ordered phase stabilized by hydrogen bonds. Figure 1.10b is an STM image of the same system after deposition of 0.1% ML (monolayer) of potassium chloride (KCl). A modification in the structure is observed after KCl deposition. Figure 1.10c and d are STM images obtained after deposition increasing amount of KCl (respectively 0.3% ML and 1.5% ML).

¹3,4,9,10-perylene tetracarboxylic dianhydride

1.1 Creating molecular nanoarchitectures using self-assembly

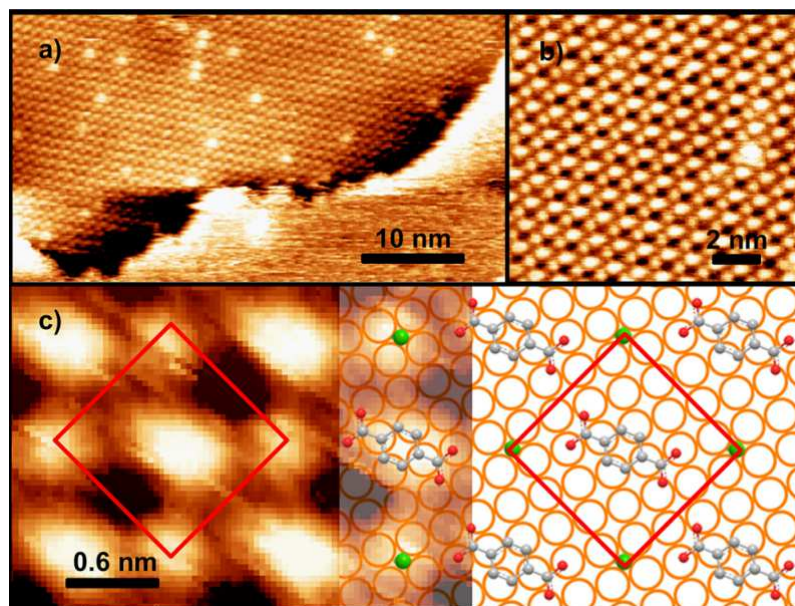


Figure 1.9: *STM images of the Cu(100) surface with TPA and NaCl, after annealing to 160 °C. (a) Large scale and (b) zoom on TPA-Na phase. (c) High resolution image with superimposed molecular model [44].*

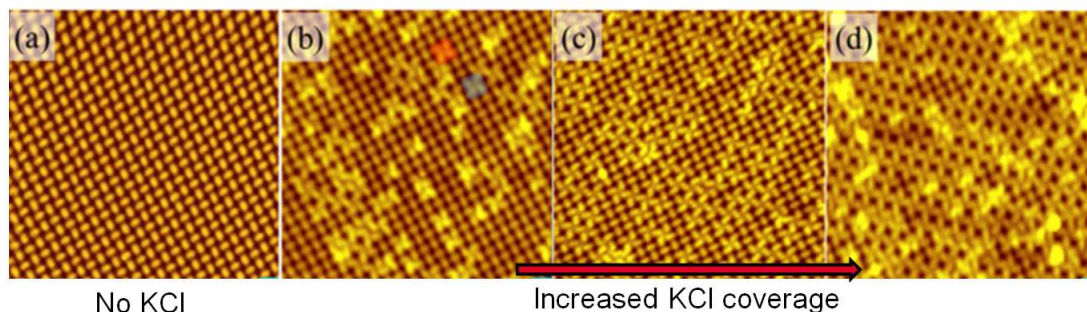


Figure 1.10: *(a) STM image of H-bonded nanoarchitecture formed after deposition of a monolayer of PTCDA molecules on Ag(100) surface. (b), (c) and (d) STM images of the same system after deposition of an increasing amount of KCl (respectively 0.1% ML, 0.3% ML and 1.5% ML). H-bonded nanoarchitecture is destroyed by KCl and another ionic-organic nanostructure is formed [46].*

Comparing the Figure 1.10a and d, one can clearly see the phase transition between pure H-bonds nanoarchitecture and ionic-organic nanoarchitecture. The position of the ions cannot be determined in their STM images however. The authors performed DFT calculations and found a structure that is stabilized by the interaction between KCl dipoles and the charge distribution of PTCDA molecules. It is difficult to verify the agreement

1. TWO-DIMENSIONAL ORGANIC NANOSTRUCTURES BASED ON MOLECULAR SELF-ASSEMBLY AND ON-SURFACE REACTIONS

between DFT calculations and their experimental results since the ion locations are not resolved in their STM images. The interactions occurring between the molecules and KCl are consequently not undoubtedly understood.

Although not completely understood and yet not much explored, ionic organic interactions are promising interactions for engineering 2D nanoarchitectures because of their strength and modularity (*e.g.* by varying the nature of the ionic salts or the organic moieties).

1.1.2.6 Covalent bonds

Covalent bonds are very strong interactions (Table 1.2) involving the sharing of electron pairs between atoms. Since the energy of such bond is very high, it requires a very high temperature activation to be broken, especially for Carbon-Carbon (C-C) bonds. The formation of C-C bonds is therefore considered as irreversible. No equilibrium can be achieved through the classical bond creation/bond breaking process that occurs for the interactions mentioned before. We cannot use the expression “self-assembly” in this case *stricto sensu*. It is very complicated to evaporate large molecules (or large covalently-bonded nanoarchitectures) because their sublimation temperature is often very high and large molecules are usually destroyed before reaching that temperature. Although it is sometimes possible to deposit large molecules in UHV by electrospray deposition [47], the formation of large covalently-bonded nanoarchitectures often requires “on-surface” formation of covalent bonds. There are many kinds of reactions leading to covalent bond formation [48] such as Ullmann coupling [49, 50] (that will be specifically addressed in section 1.3), Glaser coupling [51, 52], Bergman cyclization [53], Scholl reaction [54], alkyne cyclotrimerization [55], etc...for C-C bond formation. Different reactions are used to form covalent bonds other than C-C such as boronic acid condensation [56] for B-O bond formation.

For example, Liu *et al.* [55] deposited TEB¹ molecules on Au(111) surface in UHV. A thermally activated alkyne cyclotrimerization reaction involving three TEB molecules occurs on the noble Au(111) surface and leads to a benzene ring formation. Figure 1.11a and b show respectively general alkyne cyclotrimerization mechanism and TEB-related mechanism. After annealing at higher temperature, branched stars with terminal alkyne groups created by cyclotrimerization of TEB will, in turn, react and form bigger porous molecules with terminal alkyne (Figure 1.11c,f). After annealing at even higher temperature, the chain reaction continues and large covalent porous network is formed (Figure 1.11d,g).

¹1,3,5-tris-(4-ethynylphenyl)benzene

1.1 Creating molecular nanoarchitectures using self-assembly

Many defects are observed in the porous structure due to the irreversibility of the C-C bond created (Figure 1.11h,i). Due to their strength, covalent bonds are good candidates to engineer organized nanoarchitectures on surfaces. However, due to their irreversibility, more defects are observed with respect to molecular self-assembly interactions presented previously.

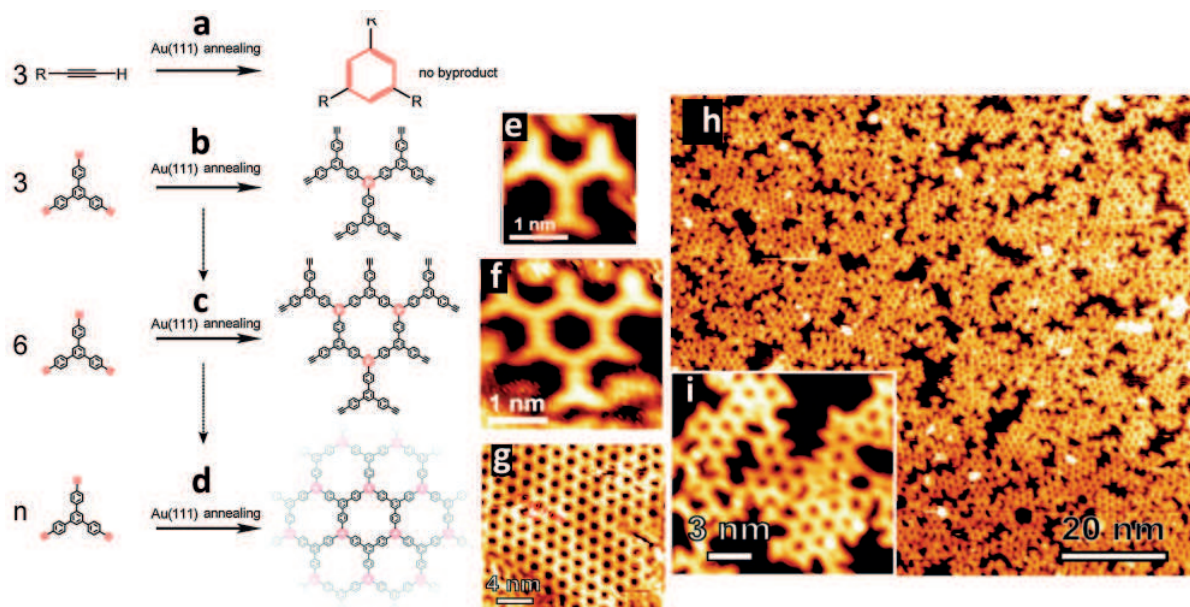


Figure 1.11: (a) General mechanism of alkyne cyclotrimerization (b) Mechanism of alkyne cyclotrimerization for TEB molecules. (c) and (d) Successive chain cyclotrimerization mechanism for TEB molecules. (e) STM image of the first product of TEB cyclotrimerization. (f) STM image of the second order product of TEB cyclotrimerization. (g), (h), (i) STM images of porous network obtained after chain cyclotrimerization of TEB [55].

1.2 Parameters to tailor 2D self-assembled nanoarchitectures

1.2.1 Influence of molecular design

1.2.1.1 Molecular substituents

It was shown in the previous section that depending on the molecular functions or substituents, different interactions can occur between the molecular building blocks. Molecular substituents choice is thus a parameter to tune molecular self-assembly at the nanometer scale. Nanostructures having different structures and properties can be engineered from a specific building block by only changing its molecular functions.

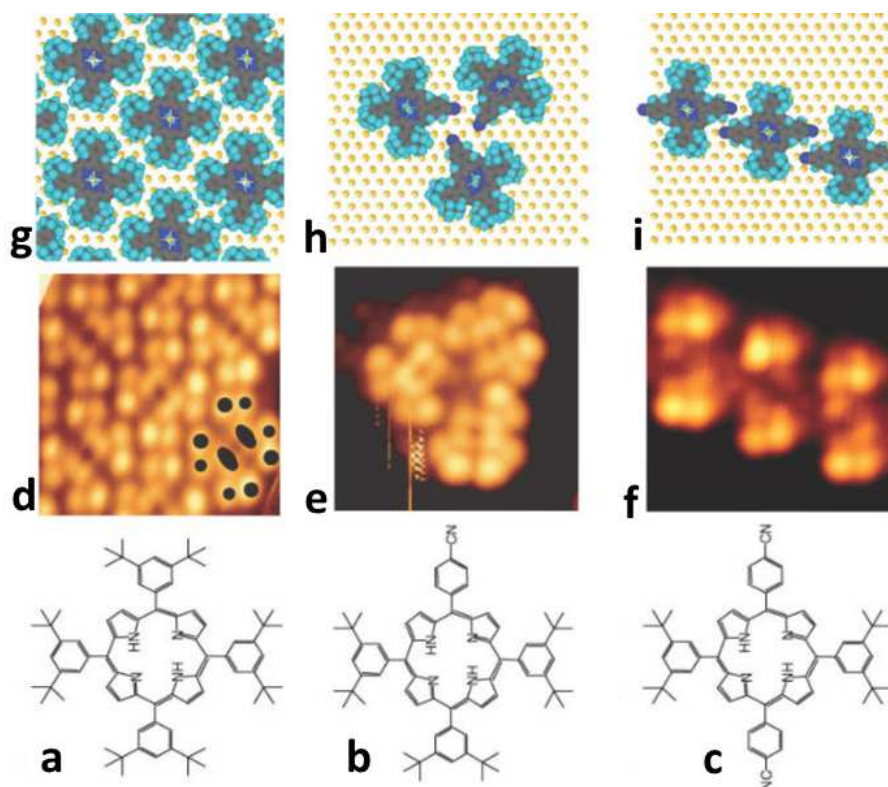


Figure 1.12: (a), (b), (c) H_2 -TBPP 1, CTBPP 2 and BCTBPP 3 (d) High resolution STM image of H_2 -TBPP VdW self-assembly (g) DFT calculations of H_2 -TBPP assembly (e) High resolution STM image of CTBPP trimers H-bonds self-assembly (h) DFT calculations of CTBPP trimers (f) High resolution STM image of trans-BCTBPP H-bonded 1D self-assembly (i) DFT calculations of trans-BCTBPP chains [57].

For example, Yokoyama *et al.* [57] evaporated three different molecules based on tertiarybutylphenyl porphyrin on Au(111) surface and observed them with STM at low

1.2 Parameters to tailor 2D self-assembled nanoarchitectures

temperature (63K). The first one is a H₂-TBPP¹ molecule, which has a porphyrin core and four di-tertiarybutylphenyl (tBP) substituents (Figure 1.12a). Once deposited on the gold surface, H₂-TBPP molecules form ordered close-packed aggregates on the surface (Figure 1.12d). These aggregates appear to be stabilized by the VdW interactions between the four di-tertiarybutylphenyl (dtB) groups of the H₂-TBPP molecules (Figure 1.12g). They also synthesized another molecule, called CTBPP² based on H₂-TBPP where one dtB group was replaced by a cyano (CN) group (Figure 1.12b). They chose CN group because it has a simple and symmetric structure as well as an asymmetric charge distribution that should induce dipole-dipole interactions. CTBPP form triangular clusters on the Au(111) surface composed of three molecules (Figure 1.12e). High resolution images as well as DFT calculation (Figure 1.12h) show that these clusters are stabilized by the hydrogen bonds between the cyano groups and hydrogens attached to carbon atoms (CH···NC H-bonds). They also synthesized a molecule with two cyano substituents at opposite position (trans) named BCTBPP³ (Figure 1.12c). BCTBPP molecules form linear 1D nanoarchitectures in which molecules are bonded through CH···NC H-bonds (Figure 1.12f,i). As seen in this example, careful choice of molecular substituents can drastically change the self-assembly structure (close-packed versus trimer and chains) as well as its stability (VdW versus H-bonds) for a same molecular skeleton.

1.2.1.2 Molecular geometry

The geometry of the molecular building block is also of prime importance for organic molecular self-assembly. First, the symmetry of the building block has to be in accordance with the geometry of the expected nanostructure. For example, star-shaped molecules with a C₃ symmetry are often used as molecular building blocks to generate hexagonal porous network [58]. Steric hindrance is also another structural parameter that can be tuned for example by varying the size of lateral chains [59]. It can affect molecular self-assembly [60]. The position of functional groups on the building block can also be tuned.

For example, we have seen in the previous section that Yokoyama *et al.* [57] evaporated BCTBPP molecules for which the two cyano substituents were positioned in trans conformation (Figure 1.13a) on Au(111) surface. This leads to 1D chains stabilized with H-bonds (Figure 1.13c,e). They also deposited another isomer of the same molecule with neighboring cyano groups in that case (cis isomer) (Figure 1.13b). Instead of 1D chains,

¹5,10,15,20-tetrakis-(3,5-di-tertiarybutylphenyl)porphyrin

²(cyanophenyl)-tris(di-tertiarybutylphenyl)porphyrin

³bis(cyanophenyl)-bis(di-tertiarybutylphenyl)porphyrin

1. TWO-DIMENSIONAL ORGANIC NANOSTRUCTURES BASED ON MOLECULAR SELF-ASSEMBLY AND ON-SURFACE REACTIONS

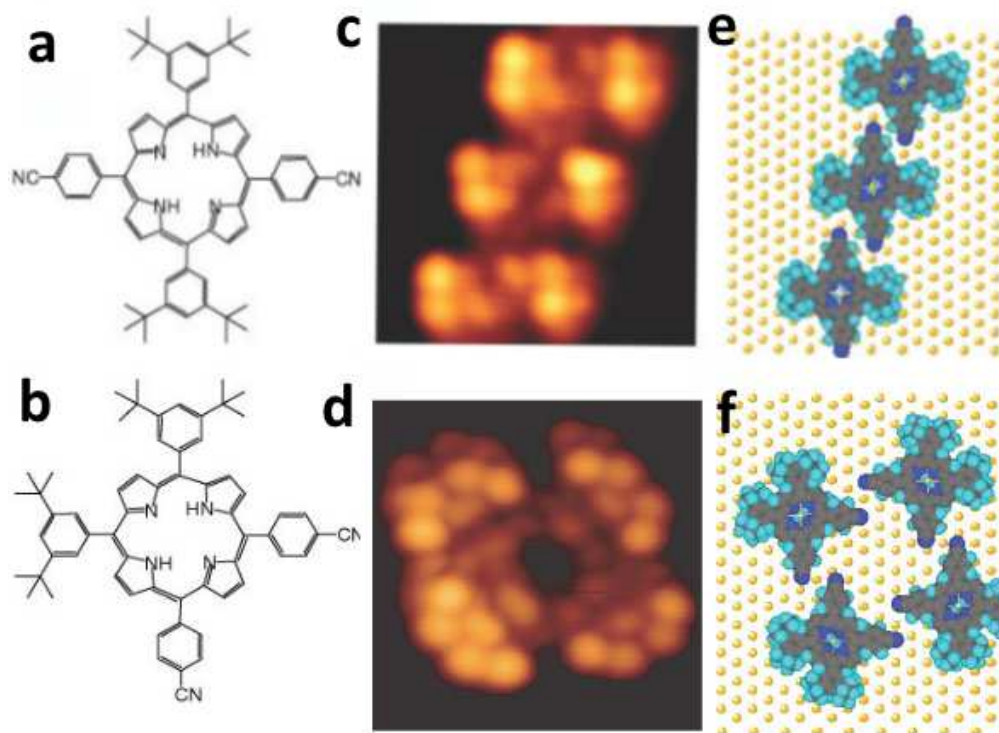


Figure 1.13: (a), (b) respectively *trans*-BCTBPP **3** and *cis*-BCTBPP **3** (c),(d) High resolution STM images of *trans*-BCTBPP self-assembly 1D and *cis*-BCTBPP 0D clusters (e),(f) DFT calculations of *trans*-BCTBPP self-assembly 1D and *cis*-BCTBPP 0D clusters. [57].

they obtained 0D clusters composed of 4 *cis*-BCTBPP molecules, also stabilized by H-bonds (Figure 1.13d,f).

In conclusion, the geometry of the building block including its symmetry, the steric hindrance and the position of the functional groups can strongly influence the corresponding formed nanoarchitectures.

1.2.2 Influence of building block coverage

Molecular self-assembly can also be influenced by the amount of building blocks that is deposited on the surface. This amount is usually expressed as molecular coverage that can be defined as the ratio between the area covered with molecules and the total area of the surface. One monolayer (ML) corresponds to a surface that is fully covered with molecules. Depending on the coverage, different phases of molecular self-assembled structures can be formed.

For example, Stöhr *et al.* [62] reported three different H-bonded nanoarchitectures

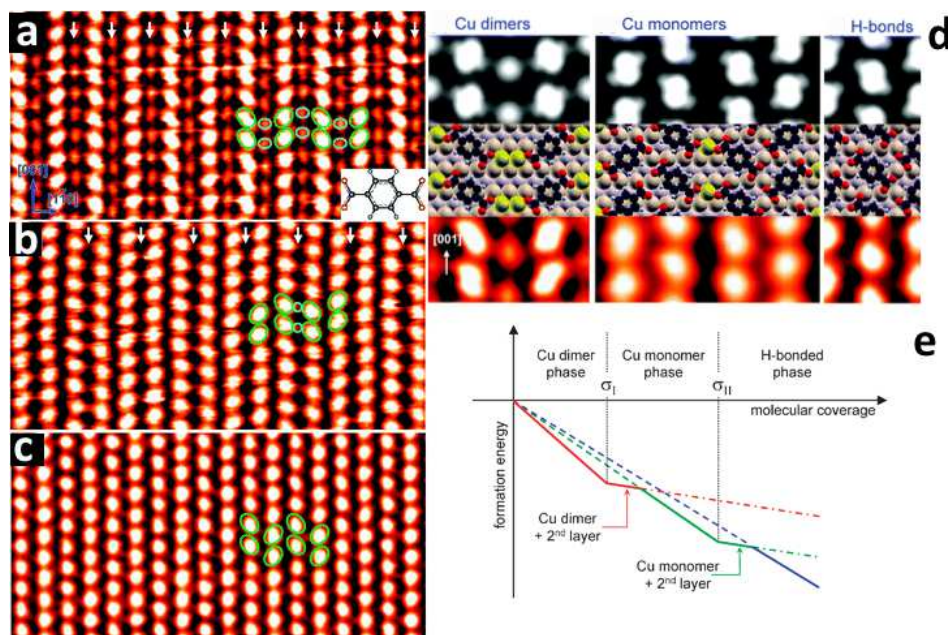


Figure 1.14: (a), (b), (c) respectively large scale STM images ($14 \times 7 \text{ nm}^2$) of Cu-dimer TPA, Cu-TPA and H-bonded TPA nanostructures corresponding to coverage $\leq 1 \text{ TPA molecule / nm}^2$, $1 \leq \text{TPA molecule / nm}^2 \leq 1.5$ and $\geq 1.5 \text{ TPA / nm}^2$ (d) High resolution STM images of the three phases and corresponding DFT models and simulated STM images (e) Phase diagram of TPA on Cu(110) [61].

depending on the DPDI¹ coverage on Cu(111) surface. Wang *et al.* [61] also reported coverage dependent metal-organic and H-bonded self-assembly of terephthalic acid (TPA) on Cu(110). For low coverage ($\leq 1 \text{ TPA molecule / nm}^2$), metal-organic nanoarchitectures are formed involving Cu dimers (Figure 1.14a,d,e). At higher coverage ($1 \leq \text{TPA molecule / nm}^2 \leq 1.5$), a new metal-organic phase is formed with another structure involving single Cu adatoms (Figure 1.14b,d,e). Finally, for coverage higher than 1.5 TPA / nm^2 , a new structure is formed (Figure 1.14c). This structure is not stabilized through metal-organic interactions like the first two phases, but through H-bonds (Figure 1.14d,e).

Molecular coverage is consequently of great importance for molecular self-assembly as it can drastically affect the interactions between the molecules.

1.2.3 Substrate influence

The substrate material and the crystallographic orientation can drastically affect molecular self-assembly. Several factors can influence the molecular self-assembly process

¹4,9-diaminoperylene-quinone-3,10-diimine

1. TWO-DIMENSIONAL ORGANIC NANOSTRUCTURES BASED ON MOLECULAR SELF-ASSEMBLY AND ON-SURFACE REACTIONS

such as the building block mobility on the surface, the surface crystallographic arrangement, its corrugation or a potential surface reconstruction. Chemical reactions can also possibly occur on the surface and consequently influence the self-assembly process.

1.2.3.1 Mobility

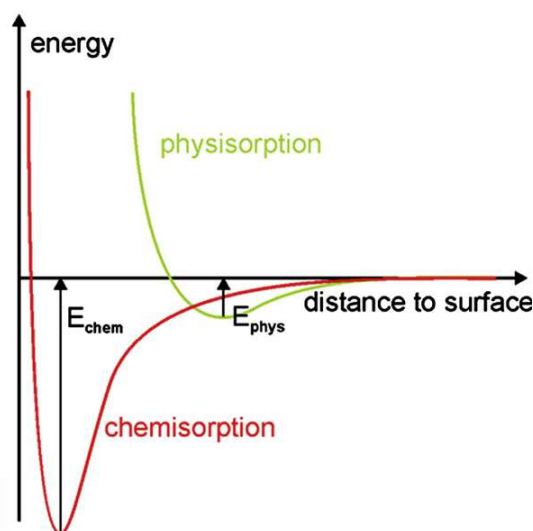


Figure 1.15: Energy diagram of *chemisorption* and *physisorption* adsorption processes. Chemisorption involves strong chemical bonds (deeper energy well) at close distance to the surface. Physisorption is driven by weak VdW interactions (shallow energy well) that occur at larger molecule-substrate distances [14].

The mobility is one of the key parameters in the self-assembly process. It is directly related to the ability of the building blocks functional groups to be in close contact and thus to interact and form self-assembled nanostructures [63]. This characteristic varies with the molecular building block. However, the mobility is usually much lower for a given molecule on a semiconductor substrate than on a metallic surface. Two main kinds of molecule-substrate adsorptions are observed: chemisorption and physisorption (Figure 1.15):

- **Chemisorption** is a strong molecule-substrate interaction involving the creation of chemical bonds between the molecules and the surface with a short bond length.
- **Physisorption** is a weaker kind of molecule-substrate interaction for which there is no chemical bonds between the molecules and the surface. Physisorption involves weak VdW interactions between the molecules and the substrate. Molecules electronic properties are usually less influenced by the substrate than for chemisorption.

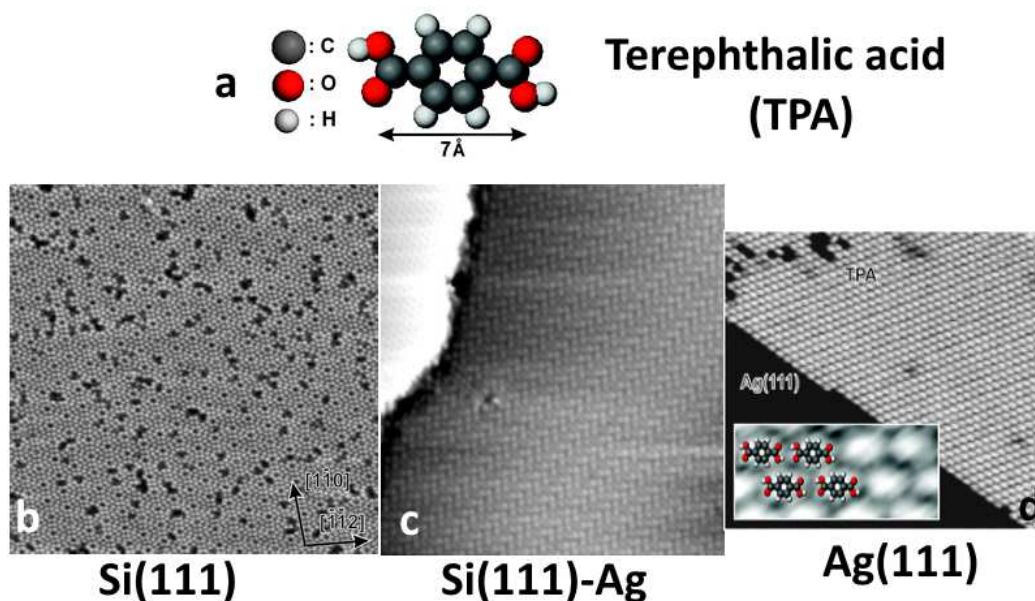


Figure 1.16: (a) Model of Terephthalic acid (TPA) molecule (b) STM image of TPA molecules on Si(111) 7×7 (c) STM image of TPA molecules on Si(111)- $\sqrt{3} \times \sqrt{3}$ -Ag forming H-bonded self-assembled structure. (d) STM image of TPA molecules H-bonded self-assembled structure on Ag(111) surface [64]

To illustrate this phenomenon, Susuki *et al.* [64] deposited terephthalic acid (TPA) molecules (Figure 1.16a) on three different substrates and observed them with STM. On Si(111)- 7×7 , TPA molecules do not form any ordered supramolecular structure (Figure 1.16b) due to strong molecule-substrate interaction (Si dangling bonds). The second substrate was also a silicon substrate but this time with a silver monolayer deposited on top of it (Si(111)- $\sqrt{3} \times \sqrt{3}$ -Ag). On this surface, TPA molecules form H-bonded self-assembled nanostructure (Figure 1.16c), meaning that their mobility increased due to the Ag overlayer deposited. Finally, TPA molecules were deposited on Ag(111) surface, and similar H-bonded self-assembled nanostructure was obtained (Figure 1.16d).

High mobility is one of the reasons why metallic substrates are often preferred, with some exceptions [65, 66], to engineer self-assembled organic nanostructures. For our experiments, we chose to use Au(111) surface because it is known to usually interact very weakly with molecules (except from the molecules with thiol groups for example).

1. TWO-DIMENSIONAL ORGANIC NANOSTRUCTURES BASED ON MOLECULAR SELF-ASSEMBLY AND ON-SURFACE REACTIONS

1.2.3.2 Influence of surface lattice and symmetry

The lattice geometry and periodicity of the surface can strongly influence the self-assembly process [67]. Growth of molecular self-assembled nanostructures along specific surface crystallographic axis or commensurable networks are often reported. For strong adsorbate-substrate interactions, the resulting self-assembled layer geometry is totally determined by the substrate templating. Same molecular building block on different substrates or molecules of different sizes but with the same interaction sites on an identical substrate lead to totally different arrangements in that case.

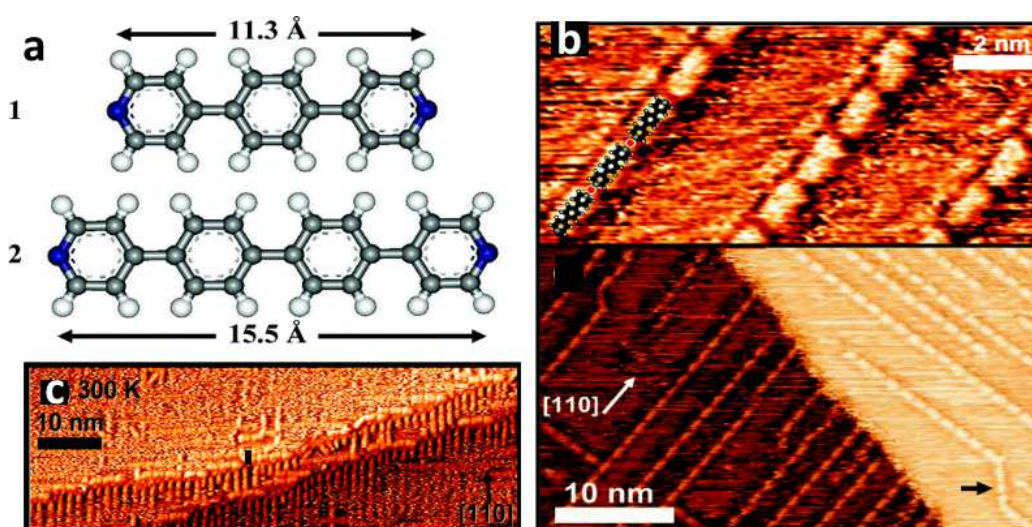


Figure 1.17: (a) Molecular structure of the ligands 1,4-bis(4-pyridyl)benzene, **1**, and 4,4-bis(4-pyridyl)biphenyl, **2**, exhibiting different distances between the nitrogen atoms. Color scheme: N = blue, C = gray, H = white. (b) STM images 1D Cu-**1** commensurate chains along $[110]$ and $[1\bar{1}0]$ directions of the Cu(100) surface at 300K. (c) STM image taken after deposition of **2** on Cu(100) surface. Unstable incommensurate metal-organic structure is destabilized by thermal excitation at room temperature [68].

For example, Tait *et al.* [68] evaporated bipyridyl molecules differing in length by only one phenyl ring (molecules **1** and **2** in Figure 1.17a) on Cu(100) surface at room temperature. Molecule **1** appears to form 1D chains with preferential growth directions. These chains are formed by molecules **1** bonded to Cu adatoms originating from substrate step edges, through N-Cu-N metal-organic interaction (Figure 1.17b). These organometallic wires appear to grow preferentially along the $[110]$ and $[1\bar{1}0]$ directions of the Cu crystal. Each chain segment in the **1**-Cu chains is measured to be six times the Cu nearest neighbor distance. This epitaxial agreement allows each Cu chain atoms in the chain to adopt the same adsorption geometry, most likely in the 4-fold hollow sites (energetically favored

1.2 Parameters to tailor 2D self-assembled nanoarchitectures

for Cu adatoms). For molecule **2**, which is longer than **1** by one phenyl ring, no stable structure is observed (Figure 1.17c). The differences between the growth of **1** and **2** were attributed to commensurability of the 1D coordination structure to the substrate. For the molecule **2**, the N-Cu-N interaction was too weak to compensate for a less-than-ideal commensurability situation. Consequently, thermal excitation at room temperature was able to destabilize the metal-organic nanoarchitecture.

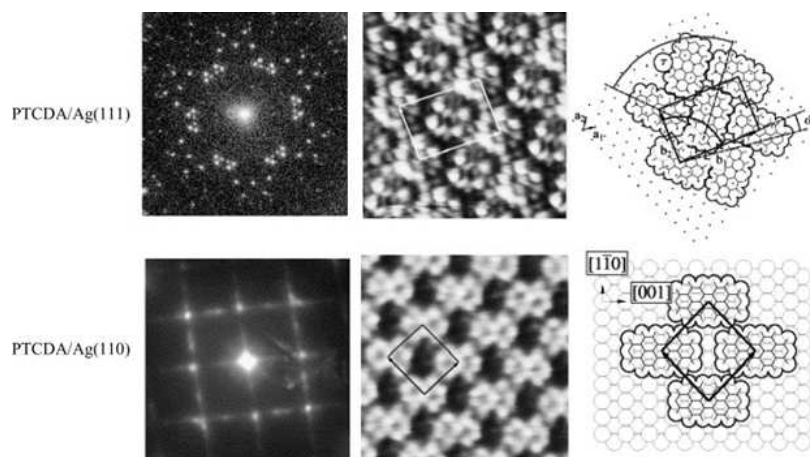


Figure 1.18: *LEED patterns, STM images, and molecular models of self-assembled PTCDA monolayers on Ag(111) (top) and Ag(110) (bottom). The layers show a different symmetry due to the different symmetry of the substrate. Scan sizes are $4.5 \times 4.5 \text{ nm}^2$ (top) and $4.4 \times 4.4 \text{ nm}^2$ [69].*

Another example highlighting the influence of lattice symmetry on molecular self-assembly is given by Zou *et al.* [69]. PTCDA¹ molecules were deposited on both Ag(110) and Ag(111) surfaces and characterized with STM and LEED² in UHV. Both LEED and STM (Figure 1.18) reveal that the interaction of PTCDA with silver surfaces is strong enough to influence the molecular self-assembly. The different crystallographic orientations of the two surfaces lead to the formation of either an herringbone pattern or a linear assembly on Ag(111) and Ag(110), respectively.

Besides, Tait *et al.* [70] successfully managed to grow 2D isostructural coordination nanoarchitectures from a specific molecule and metal adatoms on Cu(100), Ag(100) and Ag(111). In that case, the metal-organic interactions were strong enough to overcome the substrate templating effects.

¹3,4,9,10-perylene-tetracarboxylic acid dianhydride

²Low-Energy Electron Diffraction

1. TWO-DIMENSIONAL ORGANIC NANOSTRUCTURES BASED ON MOLECULAR SELF-ASSEMBLY AND ON-SURFACE REACTIONS

1.2.3.3 Surface reconstruction

Reconstructed surfaces, for which the atoms are not arranged in the same way as they are in the bulk phase, can also strongly influence the molecular self-assembly process. Surface reconstruction can also be used to template molecular nanoarchitectures with typical scale larger than the lattice of raw materials.

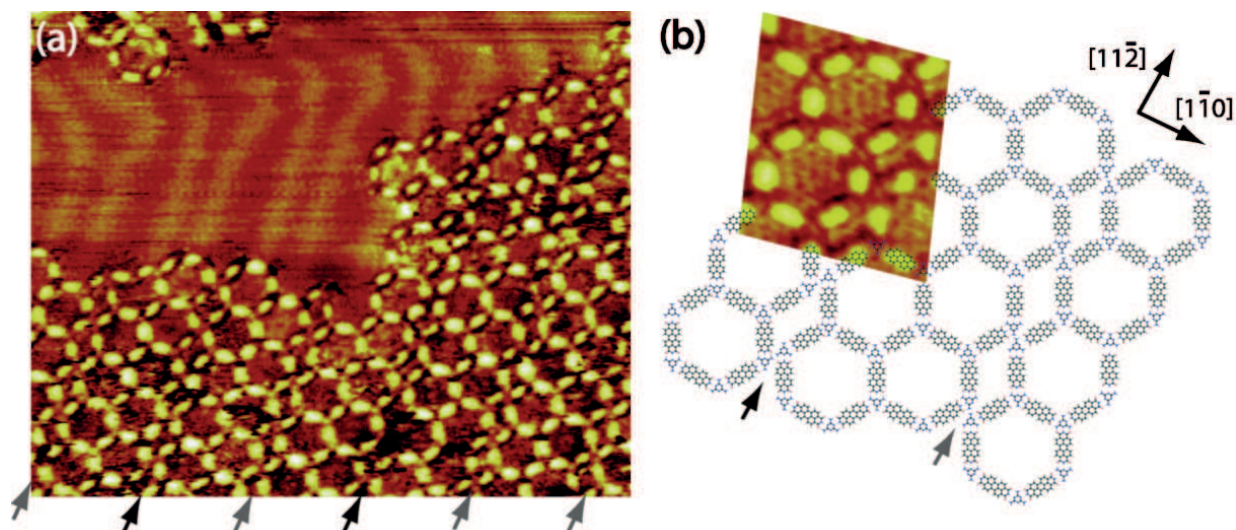


Figure 1.19: (a) Room temperature STM image of PTCDI-melamine porous nanoarchitecture (hexagons and parallelograms) with resolution on the underlying Au(111) ($22 \times \sqrt{3}$) surface reconstruction ($V=1.5V$, $I=0.15nA$). (b) Molecular model of the PTCDI-melamine nanoarchitecture with high resolution STM image superimposed. The parallelogram rows, matching the periodicity of the surface reconstruction along the $[1\bar{1}0]$ direction are indicated by black and gray arrows [71].

For example, Böhringer *et al.* [72] reported the Au(111) ($22 \times \sqrt{3}$) surface reconstruction to drive the formation of self-assembled organic nitronaphthalene nanoclusters. Another example of surface-reconstruction-mediated formation of organic self-assembly was given by Silly *et al.* [71] studying the self-assembly of PTCDI and melamine molecules on Au(111) surface. After deposition of PTCDI and melamine on Au(111) and subsequent annealing at 80°C for 15 hours, a porous organic nanoarchitecture is formed (Figure 1.19). This porous nanoarchitecture consists in the alternation of double rows of hexagons (6 PTCDI + 6 Melamine molecules for one hexagon) and single rows of parallelograms (4 PTCDI + 6 Melamine molecules each). Hexagon and parallelogram structures are both stabilized by triple hydrogen bonds ($2 \text{H} \cdots \text{O}$ and $1 \text{H} \cdots \text{N}$) between PTCDI and melamine molecules. Parallelogram rows were growing along the $[11\bar{2}]$ direction and the spacing between two adjacent parallelogram rows (6.3 nm) matches with the periodicity of

1.2 Parameters to tailor 2D self-assembled nanoarchitectures

the Au(111) ($22 \times \sqrt{3}$) surface reconstruction along the $[1\bar{1}0]$ direction (Figure 1.19a). In contrast, only hexagons were observed on Ag/Si(111) surface after deposition of PTCDI and melamine molecules [73]. The example demonstrates the influence of the Au(111) surface reconstruction to tailor the self-assembly of PTCDI and melamine molecules in order to match the surface reconstruction periodicity along the $[1\bar{1}0]$ direction.

1.2.3.4 Vicinal surfaces

Metal surfaces can also be prepared by cutting a crystal parallel to a plane slightly off a low index plane. Vicinal surfaces consist in an alternation of terraces of a particular low index plane of variable width, depending on the angle of miscut, separated by monoatomic steps. Thus, vicinal surfaces can be used as template to guide the molecule to self-assemble along a preferential direction (parallel to the step edges) and form 1D nanostructures.

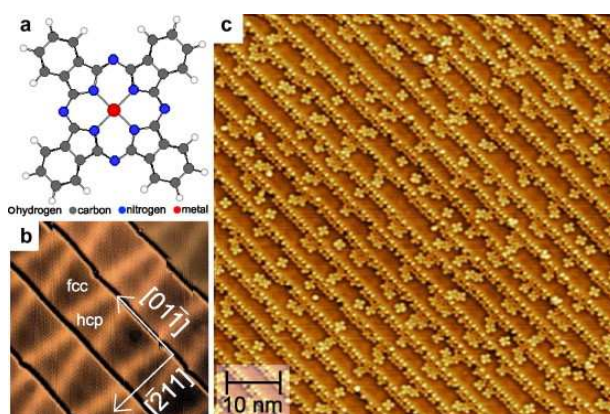


Figure 1.20: (a) Molecular structure of Co-Phtalocyanine molecule. (b) STM image of clean Au(788) showing five adjacent terraces ($14 \times 14 \text{ nm}^2$). (c) Large-scale STM image of 1D CoPc nanostructures on Au(788) surface at 8 K ($75 \times 75 \text{ nm}^2$) [74].

For example, Kröger *et al.* [74] successfully reported the formation of 1D Cobalt-Phtalocyanine (Co-Pc) (Figure 1.20a) nanostructures (Figure 1.20b) along the step edges of the Au(788) surface (Figure 1.20a).

To conclude, depending on the ratio molecule-substrate versus intermolecular interactions, the substrate can strongly influence the molecular self-assembly through templating effects. Nanoarchitectures can be influenced by the lattice geometry or by surface reconstructions or even step edges.

1. TWO-DIMENSIONAL ORGANIC NANOSTRUCTURES BASED ON MOLECULAR SELF-ASSEMBLY AND ON-SURFACE REACTIONS

1.2.3.5 Surface catalytic activity and reactivity

The word “catalyst” usually refers to a material that reacts with the initial reactors lowering the activation energy necessary for a reaction to occur compared to the situation without catalyst (Figure 1.21). Due to the high molecule-catalyst contact area compared to bulk materials, metal surfaces are promising and effective catalysts for on-surface reactions. However, the surface characteristics (material, facets, specific sites) strongly influence activation barriers for on-surface reactions. Among all the on-surface reactions, we only consider here reactions leading to the formation of organic nanoarchitectures.

To illustrate the difference of catalytic activity of surfaces, Sun *et al.* [75] compared experimentally and theoretically the activation temperature of Wurtz coupling of BMPB brominated molecule on Cu(110), Ag(110) and Au(111) surfaces. Wurtz reaction consists in dehalogenation of molecular precursor followed by recombination of radicals. The first part of the Wurtz reaction is known to be catalyzed by noble metals. Sun *et al.* [75] reported a Wurtz reaction activation temperature of 450, 420 and 350 K for Cu(110), Ag(110) and Au(111), respectively. The catalytic activity thus strongly varies between these three surfaces.

Catalytic activity can also vary locally on surfaces of the same material. Saywell *et al.* [76] evaporated α,ω -dibromoterfluorene (DBTF) molecule on a stepped Au(10,7,7) surface. They show that step edges-kinks of the surface act as preferential catalyst sites for bromine dissociation. Thus catalytic activity on surfaces may not be homogeneous but associated to specific reactive sites.

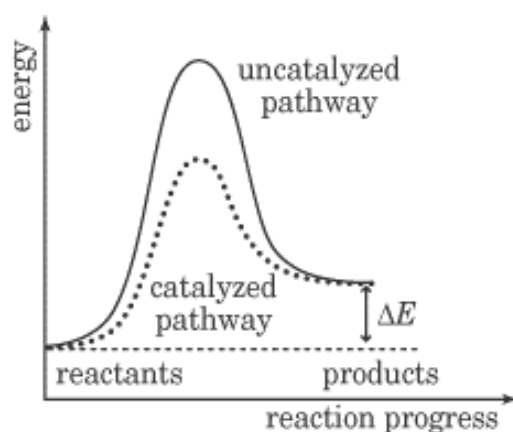


Figure 1.21: Illustration of a reaction path energy diagram showing the energy activation lowering induced by a catalyst in a chemical reaction.

1.2.4 Temperature influence

The sample temperature may affect molecular self-assembly through two main phenomena. The first one concerns the temperature dependent mobility of the molecular building-block and the corresponding phase transitions. The other one concerns the temperature activated on-surface reactions.

1.2.4.1 Diffusion and phase transition

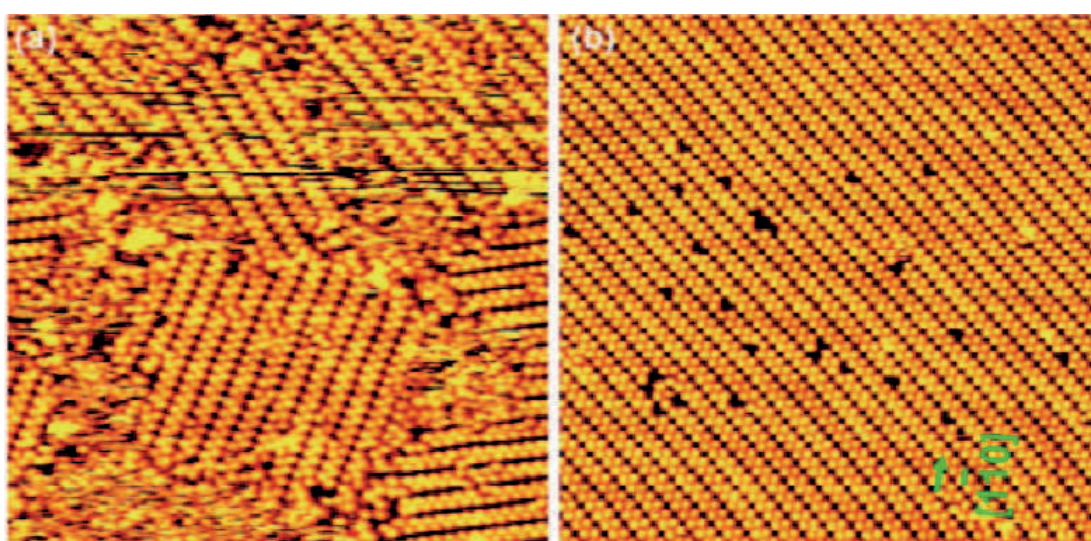


Figure 1.22: *STM images of rubrene molecules on Au(111) ($U=3V$ and $I=10pA$) (a) after post-annealing at $353K$ forming highly defective structure ($82\times 82\text{ nm}^2$) (b) after post-annealing at $363K$ forming highly ordered row structure ($57\times 57\text{ nm}^2$) [77]*

As seen on section 1.1.1, on the microscopic scale, the increase of temperature provides necessary energy to allow the molecules to migrate or rotate around their equilibrium positions. If the sample temperature during building block deposition, or during annealing, is high enough, a sufficient amount of energy will be transferred to the building blocks to reach a final state that is different from the initial state. Depending on the molecule-molecule and molecule-substrate interactions, the whole system will reorganize (self-healing) until a minimum free enthalpy state is reached, if it is possible. Depending on the temperature conditions, building blocks can be reorganized and form different arrangements. Therefore, temperature can possibly be used as a parameter to tailor two-dimensional supramolecular assembly structures. Temperature potentially permits the transition between phases that are only formed over a limited temperature range. Temperature-induced phase transition is for example observed after co-deposition

1. TWO-DIMENSIONAL ORGANIC NANOSTRUCTURES BASED ON MOLECULAR SELF-ASSEMBLY AND ON-SURFACE REACTIONS

of PTCDI and melamine molecules [71]. A pinwheel structure is formed after deposition at room temperature that turns into a porous honeycomb structure after moderate annealing at 100°C. After annealing at 120°C, another porous parallelogram phase is formed. Another example is given by Wang *et al.* [77]. They investigated rubrene molecules on Au(111) surface. Figure 1.22a shows that after annealing at 353K, rubrene molecules form highly defective structures. Figure 1.22b is an STM image taken after a post-annealing at higher temperature (363K) revealing that rubrene molecules form an ordered structure (with few remaining defects) after temperature induced phase transition. Temperature is then a key element to drive molecular diffusion and thus the formation of thermodynamically versus kinetically stable nanoarchitectures.

1.2.4.2 On-surface reaction activation

The temperature parameter can also be used to trigger non-reversible on-surface reactions, and consequently to modify the resulting supramolecular nanostructure due to the chemical transformation of the building blocks. Indeed, this property strongly depends both on the building block (functional groups) and on the surface material (catalytic activity). Many examples of nanostructure reorganization induced by temperature-driven on-surface reorganization were reported so far. For example, Dimitriev *et al.* [78] studied the evolution of trimelic acid (TMA) on Cu(100) surface. When TMA molecules were deposited and characterized at low temperature (below 200K), they appeared to form honeycomb networks that were stabilized by H-bonds between the carboxylic groups. After heating the sample to a temperature higher than 200K, a dehydrogenation of the carboxylic groups (formation of carboxylate ions) occurred, catalyzed by the Cu(100) surface. After dehydrogenation, no more H-bonded honeycomb nanostructures were observed. Instead, molecules were assembled in another arrangement forming stripes. According to the authors, molecules were no longer laying flat on the surface but were standing upright with their carboxylate groups anchored to the substrate. Similarly, Ruben *et al.* [79] reported a temperature induced deprotonation of BTA¹ molecules on Ag(111) associated with two-phase transitions.

Other temperature-activated reactions have been reported and characterized by UHV-STM such as imine coupling [80], organo-metallic coupling [81] and C-C coupling [75, 81] for example. Even if temperature is used to trigger non reversible chemical reactions, thus not leading to molecular self-assembly process *stricto sensu* since thermodynamic equilibrium is not reached, temperature activated on-surface reactions can lead to a drastic modification of the nanoarchitecture structure.

¹4,4,4-benzene-1,3,5-triyl-tribenzoic acid

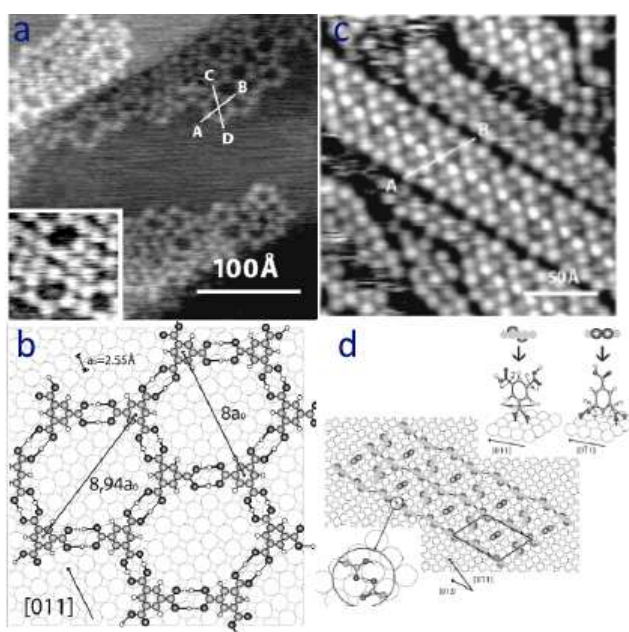


Figure 1.23: (a) STM image of TMA molecules forming H-bonded honeycomb network on Cu(100) for temperature lower than 200K. (b) Molecular model of the H-bonded network (c) STM image of TMA molecules deprotonated forming stripes for temperature higher than 200K (d) Molecular model of deprotonated TMA molecules standing upright on the Cu(100) surface [78].

1.3 On-surface covalent coupling reaction: Ullmann coupling

1.3.1 General description

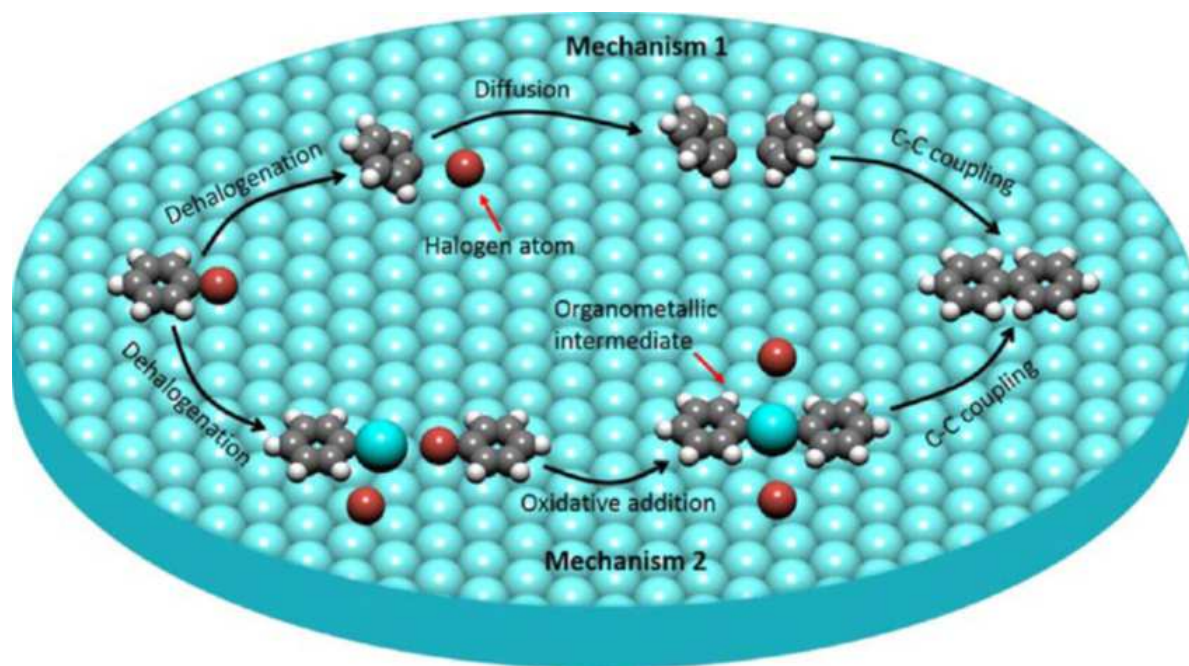


Figure 1.24: Two different mechanisms proposed by Fan et al. [82] for on-surface Ullmann reaction. Gray, white, red, and blue balls represent respectively carbon, hydrogen, halogen and metal atoms.

Many on-surface reactions were used to grow covalent structures or polymers such as Glaser-Hay coupling, dehydration reactions (boronic acid, carboxylic acid, Schiff base formation), cycloaddition reactions, etc... One of the most studied on-surface reaction so far is the so-called “Ullmann coupling” reaction. This reaction is named after the German professor Fritz Ullmann that first described a coupling reaction occurring between two aryl halides in 1904 [83]. This reaction requires three main elements: aryl-halides, metal catalyst (copper in the historical Ullmann reaction case) and temperature activation.

Depending on the catalyst material, the surface in our case, two mechanisms were proposed for the Ullmann reaction [82]. For the two mechanisms, the reaction starts with the dehalogenation of the aryl-halide, meaning the breaking of the C-X bond. This dehalogenation reaction is a very critical step and is catalyzed by transition metals such as Au [50], Ag [84], Cu [85] and Co [86]. In the first mechanism, a radical is formed and diffuses on the surface. In the second path, the product of the dehalogenation reaction interacts

1.3 On-surface covalent coupling reaction: Ullmann coupling

with a metal adatom and then forms an organometallic intermediate, that is stable and can be observed. For example, several type-2 Ullmann coupling mechanisms were reported for Cu catalyzed reactions by the observation of so-called protopolymers [87] consisting in organometallic nanostructures [88, 89, 90]. In the type-2 mechanism, the organometallic intermediate is destroyed leading to C-C covalent bond formation, if enough energy is provided to the system (for example by increasing the surface temperature). In the type-1 reaction, no organometallic intermediate is formed and radicals recombine with each other to form new C-C covalent bonds. Most of the on-surface Ullmann reactions occurring on Au substrates were reported to be of type-1 since no organometallic intermediates were observed [28, 50, 82].

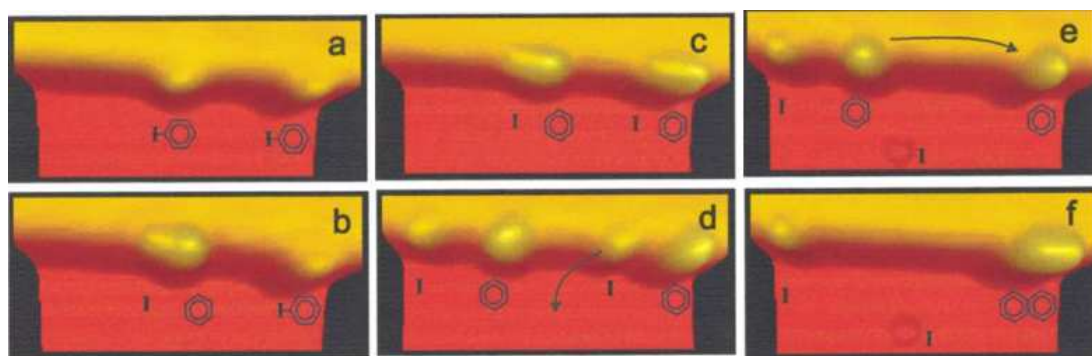


Figure 1.25: *STM images showing the initial steps of the tip-induced Ullmann-like C-C covalent coupling of two iodobenzene molecules reported by Hla et al. ($U=1.1V$, $I=530pA$, $7\times 3 nm^2$) [91].*

The Ullmann reaction was first only used in organic chemistry for C-C coupling in synthetic reactions. In 2000, almost one century after the discovery of the Ullmann coupling reaction, Hla *et al.* [91] reported a step by step on-surface Ullmann-like reaction on copper surface. They evaporated iodobenzene on Cu(111) surface held at 20K in UHV (Figure 1.25a). Then, they positioned an STM tip over a iodophenyl molecule and switched the bias value to 1.5V, inducing a dissociation of the C-I bond (Figure 1.25b). Then, they similarly dehalogenated another molecule (Figure 1.25c). They brought this molecule in the vicinity of the other radical (Figure 1.25e), still using tip lateral manipulation. In the last step, they used the tip to induce a coupling between the two radicals. They successively achieved the formation of bi-phenyl molecules using STM tip manipulation and electron-induced reactions (Figure 1.25f).

Grill *et al.* [50] were the first to report the formation of two-dimensional covalent nanostructures using on-surface Ullmann reaction on Au(111) in 2007. They used porphyrin molecules with bromine terminated arm (Br_4TPP). They selectively and specifi-

1. TWO-DIMENSIONAL ORGANIC NANOSTRUCTURES BASED ON MOLECULAR SELF-ASSEMBLY AND ON-SURFACE REACTIONS

cally functionalized one, two or four of the porphyrin arms with bromine. After heating the substrate, they achieved the formation of covalent nanostructures, respectively, dimers, chains and two-dimensional clusters of porphyrins (Figure 1.26a,b and c respectively). Thus, the position of the halogen substituents on the molecule controls the dimensionality of the covalent structure formed by the on-surface Ullmann reaction.

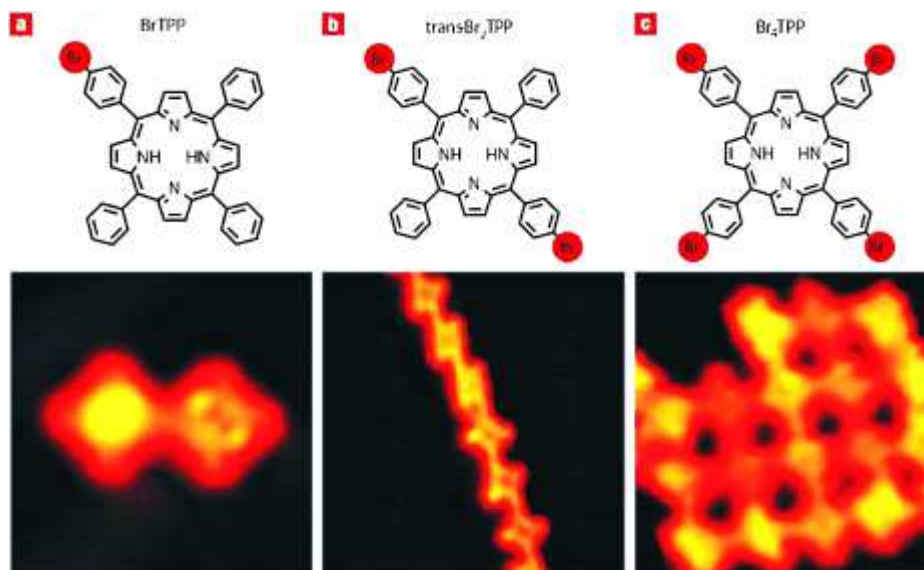


Figure 1.26: *Dimension-controlled growth of Br-substituted Tetra-phenyl porphyrins by Ullmann reaction. Different building blocks with (a) one, (b) two or (c) four Br substituents leading respectively to dimers, 1-D nanowires and 2D nanostructures after on-surface Ullmann coupling reaction [50].*

1.3.2 Influence of the halogen substituent

The first step of the Ullmann coupling reaction is the breaking of the carbon-halogen bond. Carbon-Halogen bond binding energies are lower than C-C bonds of the molecular skeleton. Consequently, selective dissociation of C-X bonds is potentially achievable without modifying or damaging the rest of the molecule, leading to the formation of organometallic intermediates or radicals. Most of the time, the halogen atoms used to functionalize the molecular building blocks for on-surface Ullmann coupling purposes are bromine, iodine and more scarcely chlorine [84, 92] or fluorine [93].

The C-X binding energy strongly varies depending on the nature of the halogen atom. C-X bond strength usually varies with X in order of $I < Br < Cl < F$. One good illustration is the variation of the dehalogenation energies of the most basic building block for

1.3 On-surface covalent coupling reaction: Ullmann coupling

Halogen substituent	Iodine	Bromine	Chlorine	Fluorine
C_6H_5-X dissociation energies	2.91 eV	3.65 eV	4.22 eV	5.52 eV

Table 1.3: Evolution of the C_6H_5-X bond dissociation energy per molecule with the X atom nature [94]

Ullmann coupling: halogeno-benzene (C_6H_5-X) [94]. The C-X bond dissociation energies are gathered in Table 1.3.

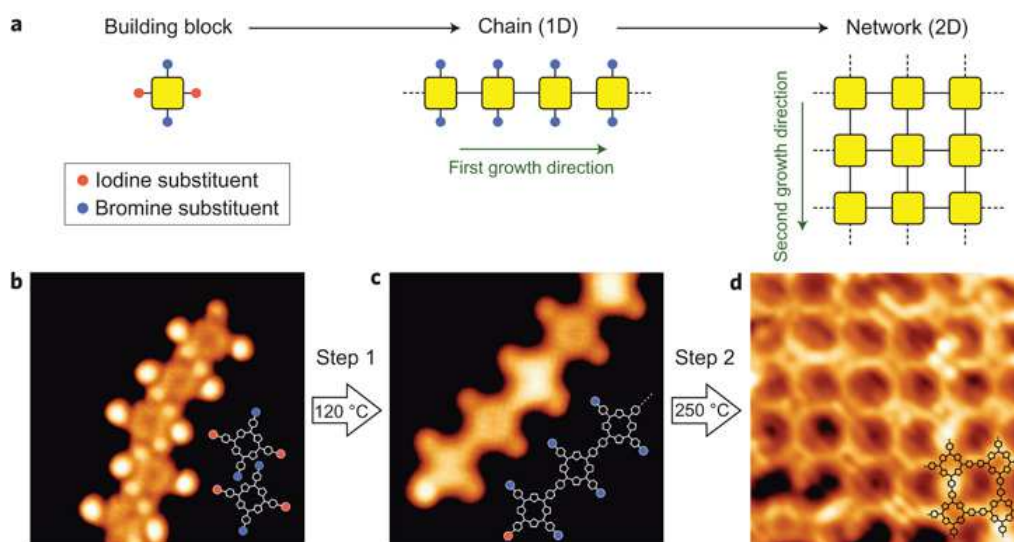


Figure 1.27: Progressive steps of the Ullmann coupling from (a) the low temperature deposition of I_2Br_2TPP molecules on $Au(111)$ surface, to (b) the 1D nanowire formation after deiodination of the molecules and partial on-surface Ullmann coupling (annealing at $120^\circ C$). Finally, (c) formation of 2D covalent network after debromination and complete Ullmann coupling of the 1D wires (annealing at $250^\circ C$) [28].

For a given molecule, the activation temperature of the dehalogenation reaction strongly depends on the halogen substituent [95]. To illustrate this property, Lafferentz *et al.* [28] evaporated halogen-functionalized porphyrins having two pairs of iodine and bromine terminated arms in trans-configuration (I_2Br_2TPP). They deposited molecules onto an $Au(111)$ surface kept at $-200^\circ C$, and confirmed by STM that molecules were intact with all their iodine and bromine atoms attached to their backbones (Figure 1.27a). After annealing at $120^\circ C$, only the C-I bonds are broken and consequently, on-surface Ullmann coupling reaction occurs only in one direction. The products of this first reaction are 1-D porphyrin nanowires with Br atoms attached to their sides arms (Figure 1.27b). They subsequently annealed the sample at a temperature of $250^\circ C$, which was high enough to break the remaining C-Br bonds, thus leading to the merging of several 1D wires into a 2D

1. TWO-DIMENSIONAL ORGANIC NANOSTRUCTURES BASED ON MOLECULAR SELF-ASSEMBLY AND ON-SURFACE REACTIONS

covalent network (Figure 1.27c). This two-step reaction was triggered by the difference in binding energy of C-Br with respect to C-I. Better results were obtained using this approach than the one-step Br₄TPP reaction presented previously. In the Chapter 5 and 6, we will investigate this difference in reactivity studying building blocks with iodine and bromine functional groups respectively.

1.3.3 Influence of the substrate

All the processes involved in the Ullmann coupling reaction critically depend on the underlying surface [84, 96]. The surface not only acts as a catalyst for the dehalogenation reaction but also significantly influences the remaining chemical reactions. Most of the results regarding on-surface Ullmann coupling reaction were obtained using metallic substrate such as Au(111), Ag(111) and Cu(111).

For example, Guzler *et al.* [97] evaporated TBPB¹ molecule on a relatively inert graphite(100) surface and on metallic Cu(111) and Ag(110) surfaces. Dehalogenation of the molecules was reported at room temperature on the metallic surfaces. In contrast, intact molecules were observed on graphite. Graphite was then annealed up to the desorption temperature of the molecules and no dehalogenation or covalent coupling were observed [97]. Covalent structures were only obtained on the metallic surfaces after annealing, illustrating the catalytic importance of the substrate in the Ullmann reaction.

A more detailed study of the substrate influence in the Ullmann reaction was given by Bieri *et al.* in 2010 [98]. They evaporated a hexaiodo substituted cyclic molecule (CHP²) on Cu(111), Ag(111) and Au(111) substrates. They used STM and XPS to characterize their samples and DFT³ calculations to model the reactions (Figure 1.28g). CHP molecules are expected to form a covalent regular porous array of polyphenylene after Ullmann coupling reaction (Figure 1.28h). XPS measurements confirmed that CHP molecules were dehalogenated after deposition on all the three substrates at room temperature. Radicals were stabilized by the interaction with the free electrons of the substrates, thus preventing the formation of covalent bonds at room temperature according to the authors. The authors subsequently annealed the sample until C-C coupling occurred.

The C-C covalent coupling occurred at different temperatures depending on the substrate. A 475K annealing was necessary to activate C-C coupling on Cu(111) whereas annealing temperatures of 525 and 575K were necessary on Au(111) and Ag(111) substrates respectively. Moreover, the shape of the covalent nanostructures formed strongly

¹1,3,5-tris(4-bromophenyl)benzene

²cyclohexa-m-phenylene

³Density Functional Theory

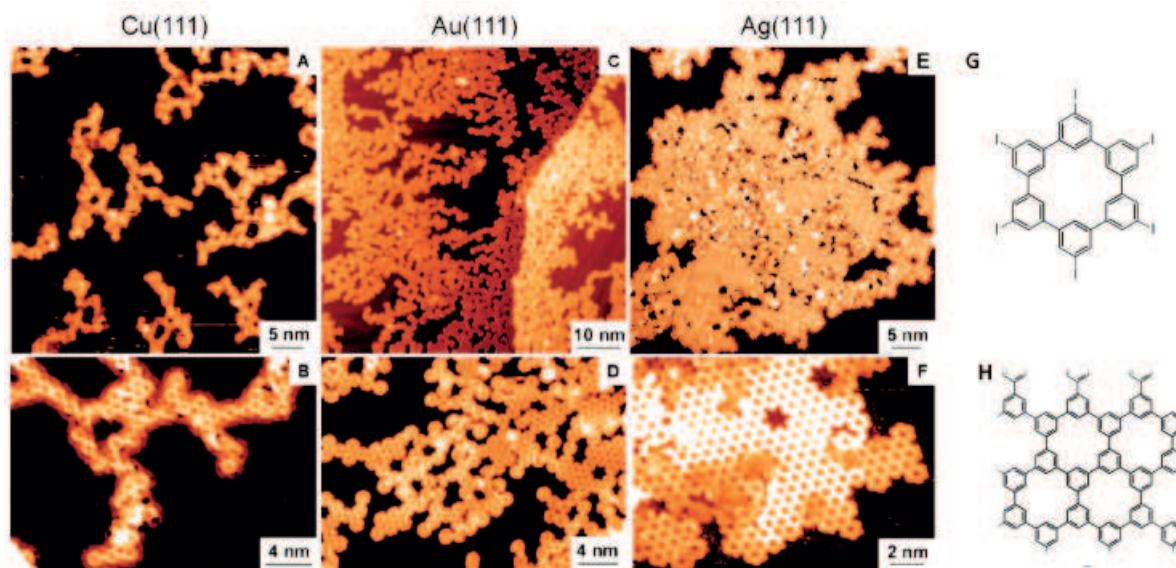


Figure 1.28: Overview (top) and high-resolution (bottom) STM images of polyphenylene networks on (a,b) Cu(111), (c,d) Au(111), and (e,f) Ag(111) (g) Chemical structure of hexaiodo-substituted CHP molecule (h) Chemical structure of a fraction of the polyphenylene network after On-surface Ullmann coupling [98].

varies between the substrates. Dendritic structures mainly composed of single-molecular-width covalent 1D structures were formed on Cu(111) substrate (Figure 1.28a,b). Small close-packed hexagonal-covalent clusters with branches are observed on the Au(111) surface (Figure 1.28c,d). On contrary, large hexagonal porous domains with low defect range are observed on the Ag(111) surface (Figure 1.28e,f). The authors simulated the C-C covalent coupling reaction path on the different substrates using DFT calculations. They found that on Cu(111) surface, radicals almost spontaneously covalently couple to each other once the initial diffusion barrier is overcome. On Ag(111), the diffusion is however favored compared to spontaneous covalent coupling leading to an increased mobility of the radicals. They confirmed their hypothesis using Monte-Carlo simulations. These simulations show that the growth of large dense covalent nanoarchitectures is favored by a high mobility (or a low coupling affinity) of the precursors (radicals in this case).

1.3.4 Molecular halogen by-products

The first step of the Ullmann coupling reaction is the dehalogenation process. During this step, molecular halogen atoms are separated from the molecular skeleton. Three main options for these halogen atoms were considered by Brønner *et al.* [99]:

1. TWO-DIMENSIONAL ORGANIC NANOSTRUCTURES BASED ON MOLECULAR SELF-ASSEMBLY AND ON-SURFACE REACTIONS

- **Independent diffusion** : The halogen atoms can diffuse independently of the organic system on the surface.
- **Poisoning** : The halogen atoms diffuse to step edges or defects.
- **Incorporation** : The halogen atoms can be incorporated into the organic structure (trapped in organic pores for example).

The halogen atoms often appear to be strongly chemisorbed on the metal surfaces after on-surface Ullmann reaction. These halogen atoms are reported to play an important role in the next steps of the Ullmann reaction. For example, split-off Bromine atoms were observed in the close vicinity of protopolymers formed after thermal dehalogenation of precursors on Cu(111). Park *et al.* [100] observed that the halogen by-products were actually bonded to the protopolymers by Br-H bonds and consequently affecting the resulting product. Pis *et al.* also reported recently that dibromotetracene forms chained-protopolymers on Ag(110) based on STM, XPS and DFT calculations. They reported that the presence of Br adatoms at the close vicinity of the organo-metallic chains was “crucial” for their stabilization.

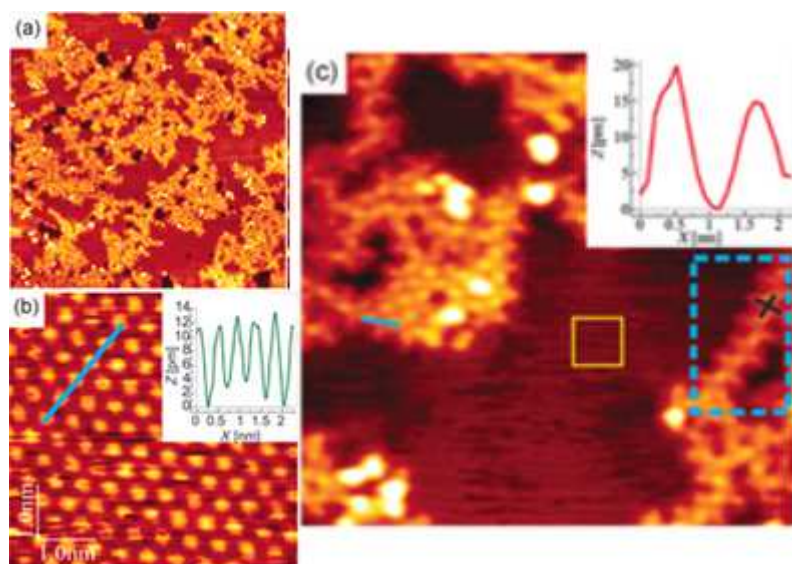


Figure 1.29: (a) Overview STM image ($60 \times 60 \text{ nm}^2$), and (c) close-up STM image ($18 \times 18 \text{ nm}^2$) of Cu(111) surface after evaporation of sub-monolayer coverage of Br_4Py molecules. Dendritic molecular network is observed with no long range order surrounded by chemisorbed Br atoms. (b) Atomic resolution of the bromine adatoms chemisorbed on the Cu surface (yellow square of image (c)) [101].

1.3 On-surface covalent coupling reaction: Ullmann coupling

Surface	Bromine	Iodine
Cu(111)	3.19 eV	2.97 eV
Ag(111)	3.23 eV	3.01 eV
Au(111)	2.80 eV	2.76 eV

Table 1.4: *Evolution of the atomic binding energies of iodine and bromine on metal surfaces [95]*

Halogen atoms can also hinder the radical recombination and subsequent formation of C-C bonds. Batra *et al.* [102] observed that the polymerization of graphene nanoribbons precursors is activated by the desorption of halogen atoms from the metal surface. Pham *et al.* [101] reported the formation of large domains of chemisorbed Br atoms (Figure 1.29b) after deposition of tetrabromopyrene (Br₄Py) molecules on Cu(111) surface. These chemisorbed Br atoms were assumed to be responsible for the precursors lack of diffusion. Consequently, no long range order was observed in the covalent nanostructures formed (Figure 1.29a,c). Fan *et al.* [81] reported similar conclusions after the evaporation of tribromophenyl benzene (TBPB) on Cu(111).

The presence of chemisorbed halogen atoms is therefore often limiting the yield and the quality of the covalent nanostructures synthesized through on-surface Ullmann coupling reaction. Consequently, these halogen atoms must be removed from the surface to improve the reaction. One solution is the thermal induced desorption. Halogen atoms are much more likely to be desorbed atomically than molecularly from metal surfaces [95]. Binding energies of atomic iodine and bromine on Cu(111), Ag(111) and Au(111) are summarized in Table 1.4. They are around typically 3 eV for both Iodine and Bromine on all the surfaces. These energies are greater than the typical dehalogenation barriers. This is consistent with the fact that X atoms are still chemisorbed on the surface after annealing at temperature higher than the dehalogenation activation temperature. One solution can be to anneal the substrate to a temperature for which halogen atoms are fully desorbed. They are however two main limitations to this strategy.

The first one is the co-desorption of physisorbed molecules. The binding energy of physisorbed molecules is supposed to be additive and ranging from 70 to 140 meV per carbon atom on Au(111) [103]. Therefore, only large molecules made of several tens of C atoms are expected to stay physisorbed at temperatures higher than halogen desorption. This is for example true in the case of some graphene nanoribbons precursors [102]. The second limitation is the integrity of the molecule. Indeed, heated at a temperature of few hundred degrees, the molecular building block can be damaged, thus resulting in poor quality nanostructures [104].

1. TWO-DIMENSIONAL ORGANIC NANOSTRUCTURES BASED ON MOLECULAR SELF-ASSEMBLY AND ON-SURFACE REACTIONS

One solution to efficiently remove the chemisorbed halogen atoms can possibly be hydrogen. Bronner *et al.* [99] reported that the introduction of molecular dihydrogen in their chamber lead to an easier desorption of the bromine atoms chemisorbed on Au(111) surface. They reported molecular hydrogen to react with the bromine atoms and form H-Br molecules. H-Br molecule desorption is reported to be kinetically favored over H₂ until all the Br atoms are desorbed from the surface.

Chapter conclusion

In conclusion, the formation of two-dimensional organized nanostructures by bottom-up approach is a fascinating and complicated process driven by a whole set of molecule-substrate and molecule-molecule interactions. A broad spectrum of intermolecular interactions with their own advantages and drawbacks is available. A large part of these interactions were investigated during my PhD including H-bonds, halogen bonds, ionic-organic interactions and finally covalent coupling. A lot of parameters can also be used to tune or modify these nanoarchitectures including molecular coverage, substrate or temperature. During my PhD, mostly molecular coverage and temperature were used to tune the nanoarchitectures structure. The electronic properties of materials strongly depend on their local structure at the atomic scale. Thus, a same building block can be used to form several different arrangements depending on the preparation conditions. The resulting nanoarchitectures potentially have different geometric structures but also different electronic properties. Scanning Tunneling Microscopy was used in an Ultra-high Vacuum environment in order to characterize these nanostructures at the atomic scale. UHV prevents pollution from the environment to degrade our sample and STM allows us to probe the electronic properties of nanoarchitectures with atomic resolution. Moreover, photoemission spectroscopy experiments were also carried out at the Soleil Synchrotron facility. X-ray Photoemission Spectroscopy (XPS) gives us complementary information on the chemical environment and composition of the building blocks. STM and XPS techniques will be briefly described in the next chapter followed by a description of the experimental set-up used during my PhD.

Chapter 2

Experimental set up and techniques

The objective of this chapter is to present the characterization techniques and the experimental set-up used during my PhD. The Scanning Tunneling Microscopy (STM) working principle will be described. The Ultra High Vacuum (UHV) experimental set-up used during my PhD at CEA Saclay will also be detailed. Au(111) substrate will also be presented. X-ray Photoemission Spectroscopy (XPS) and experimental set-up at the Soleil Synchrotron will be described in Appendix B.

2.1 Scanning Tunneling Microscopy

With the invention of the Scanning Tunneling Microscope (STM) in the early 1980s, G. Binnig and H. Rohrer [105] revolutionized the world of microscopy. They were awarded with the Nobel Prize in physics in 1986 “*for their design of the scanning tunneling microscope*”. Successively, atomic resolution on Si(111) 7×7 surface reconstruction [106], then atom manipulation and positioning [107], the most famous experiment being the formation of a quantum corral by Crommie *et al.* [108], were reported using Scanning Tunneling Microscope. They opened the door to new developments in nanotechnology permitting to explore and understand new phenomena in nanoscience. From the STM invention, a large family of microscopy techniques has been developed, known as scanning probe microscopy (SPM) [109, 110, 111]. The extreme sensitivity of SPM techniques permits to resolve individual atoms, molecules and nanocrystals.

2.1.1 The Tunnel effect

With the development of quantum mechanics, the behavior of elementary systems that could not be explained by classic mechanics equations could finally be understood. Such

2. EXPERIMENTAL SET UP AND TECHNIQUES

quantum system can be described through complex wave-function, here written $\Psi(\vec{r}, t)$. The square modulus of this wave function corresponds to the probability density of such system. Electrons wave nature was experimentally unraveled by C.J. Davisson and L.H. Germer in 1927 [112, 113]. They showed that electron beams were diffracting on crystals (periodic array of atoms). Thus, the wave function $\Psi(\vec{r}, t)$ describing the behavior of electrons of mass m in potential $V(\vec{r}, t)$, obeys the standard Shrödinger equation:

$$i\hbar \frac{\partial}{\partial t} \Psi(\vec{r}, t) = \left[-\frac{\hbar^2}{2m} \nabla^2 + V(\vec{r}, t) \right] \Psi(\vec{r}, t) \quad (2.1)$$

where ∇^2 is the Laplacian operator $\nabla^2 = \frac{\partial^2}{\partial x^2} + \frac{\partial^2}{\partial y^2} + \frac{\partial^2}{\partial z^2}$.

If the potential $V(\vec{r}, t)$ is assumed to be independent of time, *i.e.* $V(\vec{r}, t) = V(\vec{r})$, one can prove that the wave-function can be written as a product of two terms, one being independent of time.

$$\Psi(\vec{r}, t) = \psi(\vec{r}) e^{-i\omega t} \quad (2.2)$$

with ω the pulsation of the system.

In these conditions, $\psi(\vec{r})$ obeys the time-independent Shrödinger equation:

$$E\psi(\vec{r}) = \left[-\frac{\hbar^2}{2m} \nabla^2 + V(\vec{r}) \right] \psi(\vec{r}) \quad (2.3)$$

with $E = \hbar\omega$ being the energy of an electron with a pulsation ω .

If the electron is moving in free-space ($V(\vec{r}) = 0$), one can prove that its wave function can be written as a plane wave:

$$\Psi(\vec{r}, t) = A e^{i(\vec{k} \cdot \vec{r} - \omega t)} \quad (2.4)$$

with a wave vector \vec{k} following the dispersion relation $\omega = \frac{\hbar \|\vec{k}\|^2}{2m}$.

Now, if we consider that the electron is interacting with a 1D time-independent potential in the z direction, its wave function obeys the equation:

$$E\psi(z) = \left[-\frac{\hbar^2}{2m} \frac{d}{dz^2} + V(z) \right] \psi(z) \quad (2.5)$$

Let's consider this potential to be null over the whole z axis except between $z = 0$ and $z = d$ where it is equal to V_0 (Figure 2.1). In classic mechanics, if the energy of the electron coming from the $z = -\infty$ is lower than the potential barrier ($E < V_0$), the probability that such electron crosses the potential is null.

2.1 Scanning Tunneling Microscopy

Now if we solve the equation 2.5 under these conditions ($E < V_0$), we get this set of equations:

$$\begin{cases} \psi(z) = e^{ikz} - \alpha e^{-ikz} & \text{for } z < 0 \\ \psi(z) = \delta e^{\kappa z} - \gamma e^{-\kappa z} & \text{for } 0 < z \leq d \\ \psi(z) = \beta e^{ikz} & \text{for } z > d \end{cases} \quad (2.6)$$

Using the continuity of the wave functions at the interfaces, one gets:

$$\begin{cases} 1 + \alpha = \gamma + \delta \\ ik(1 - \alpha) = \kappa(\delta - \gamma) \end{cases} \quad (2.7)$$

Finally, using the continuity of the wave function first derivative at the interface, one gets:

$$\begin{cases} \delta e^{\kappa d} + \gamma e^{-\kappa d} = \beta e^{ikd} \\ \kappa(\delta e^{\kappa d} - \gamma e^{-\kappa d}) = ik\beta e^{ikd} \end{cases} \quad (2.8)$$

The interesting variable here is the amplitude β of the transmitted wave function that can be written as:

$$\beta = \frac{4ik\kappa d}{(k + i\kappa)^2 e^{\kappa d} - (k - i\kappa)^2 e^{-\kappa d}} \quad (2.9)$$

The transmission probability of an electron having an energy E through this barrier can be expressed as:

$$T(E) = |\beta|^2 = \beta\beta^* = \frac{4E(V_0 - E)}{4E(V_0 - E) + V_0^2 \sinh^2(\kappa d)} \quad (2.10)$$

Contrary to classic mechanics behavior, the electrons have a non-zero probability of crossing a potential barrier even if their energy is lower than the barrier. The transmission probability depends on the variable κ that can be understood as the inverse of the penetration depth of the electron wave function in the barrier. If the barrier width is much larger than this electron penetration depth ($d \gg 1/\kappa$), equation 2.10 can be simplified as:

$$T(E) = \frac{16E(V_0 - E)}{V_0^2} e^{-2\kappa d} \quad (2.11)$$

This result highlights the influence of the barrier width on the transmission probability.

2. EXPERIMENTAL SET UP AND TECHNIQUES

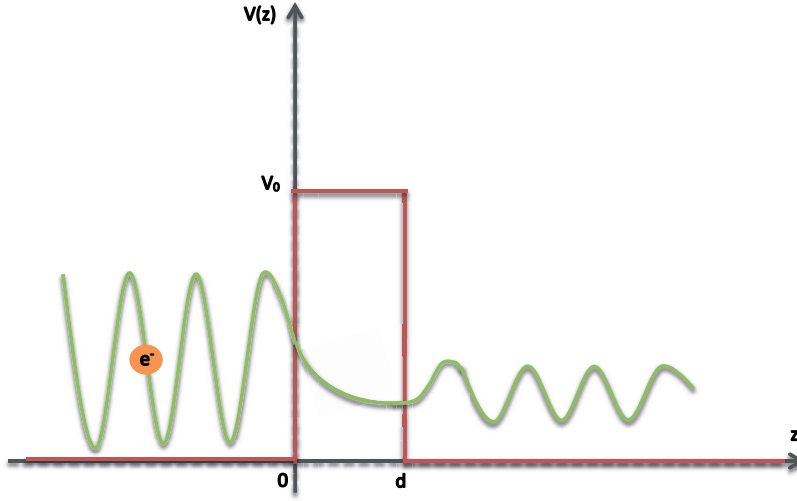


Figure 2.1: *Basic scheme illustrating the non-null probability of an electron of energy $E < V_0$ of crossing a potential barrier of height V_0 : Tunnel effect*

2.1.2 Tunneling current models

A basic model of the tunneling current would be to consider an electron traveling from a metal electrode (the sample) with a work function Φ_s to another electrode (the tip) with a work function Φ_t . One can show that the probability of an electron from the n -th state of the sample at $z = 0$ (described by its wave function $\Psi_n(z = 0)$ and its energy E_n) to tunnel through the vacuum to the tip located at a height z , can be written as:

$$P \propto T(E_n) \times |\Psi_n(z = 0)|^2 \quad (2.12)$$

Based on equation 2.10, one can show that the transmission coefficient follows the same exponential decay with a typical constant:

$$\kappa = \sqrt{\frac{2m(V_0 - E)}{\hbar^2}} \approx \sqrt{\frac{2m \langle W \rangle}{\hbar^2}} \quad (2.13)$$

where $\langle W \rangle = \frac{\Phi_s + \Phi_t}{2}$ is the average work function of the tip and the sample. The typical workfunction for metals is around 5 eV. Consequently, tunneling regime is achieved for typical distances of $Z = \frac{1}{2\kappa} = 5 \text{ \AA}$.

According to the Pauli's exclusion principle, two electrons cannot occupy the same quantum state. Consequently, electrons from an electrode cannot tunnel to occupied levels of the other electrode but must reach unoccupied states. That is why a bias is imposed between the two electrodes to shift the Fermi level of an electrode with respect to the Fermi level of the other electrode. Consequently, in case of elastic tunneling ($E_{e_{initial}}^- = E_{e_{final}}^-$),

2.1 Scanning Tunneling Microscopy

all the electrons having energy between E_F and $E_F + V_p$ can possibly tunnel from an electrode to the other [114]. Therefore, the tunneling current can be expressed as the sum of individual probabilities:

$$I \propto e \sum_{E_n=E_F}^{E_F+eV_p} |\Psi_n(z=0)|^2 \times e^{-2\kappa z} \quad (2.14)$$

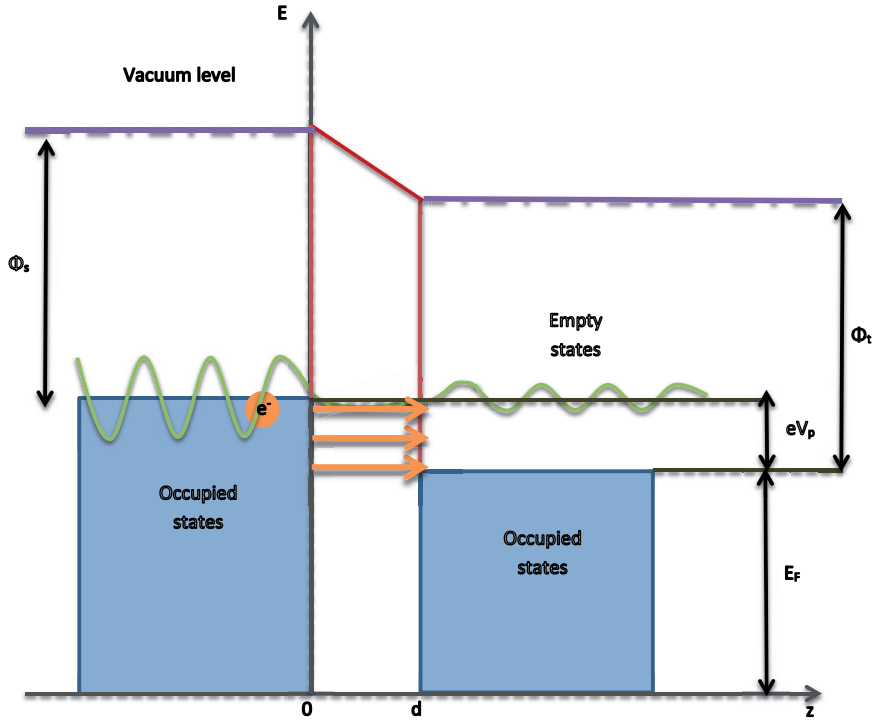


Figure 2.2: Scheme illustrating the tunnel current flowing from the occupied states of one electrode to the unoccupied states of the other electrode when a bias V_p is applied between the two electrodes.

For sufficiently small bias voltages, equation 2.14 can be conveniently written in terms of the the local density of states (LDOS, ρ_s) at the Fermi level

$$\rho_s(E_F, z) \equiv \frac{1}{eV_p} \sum_{E_n=E_F}^{E_F+eV_p} |\Psi_n(z=0)|^2 \quad (2.15)$$

The Local Density of States is a physical quantity that gives the space-resolved number of electrons per unit volume per unit energy at a given energy. Thus, injecting equation 2.15 in equation 2.14, one gets:

$$I \propto V_p \rho_s(E_F, z) \times e^{-2\kappa z} \quad (2.16)$$

2. EXPERIMENTAL SET UP AND TECHNIQUES

With this very simplified model, the tunneling current between the two electrodes appears to depend exponentially on the distance between the tip and the sample, which makes the scanning tunneling microscopy very sensitive to corrugations of the surface electron density. Typically, a variation of 1 Å in the sample-tip distance causes a change of nearly one order of magnitude in the tunneling current.

2.1.2.1 Bardeen's approximation

In 1961, two decades before the invention of the Scanning Tunneling Microscopy, Bardeen developed a model to explain tunneling in systems of planar superconducting electrodes separated by thin oxide barriers [115]. In his model, he considered both electrodes (the tip and the sample in our case) as independent systems with two different known hamiltonians. Thus, solving the Schrödinger equations of the two unperturbed systems, he used time-dependent first order perturbation theory to calculate the tunneling current between planar electrodes. The transition probability Γ of an electron for a state μ to a final state ν is determined by Fermi's golden rule and expressed as:

$$\Gamma = \frac{2\pi}{\hbar} |M_{\mu,\nu}|^2 \delta(E_\mu - E_\nu) \quad (2.17)$$

Applied to the electron tunneling from the surface to the tip, $M_{\mu,\nu}$ is the tunneling matrix element corresponding to the transition between the states Ψ_ν of the tip and Ψ_μ of the surface. E_μ and E_ν are the corresponding energies of states Ψ_μ and Ψ_ν respectively, in the absence of tunneling. Bardeen demonstrated that $M_{\mu,\nu}$ can be expressed by a surface integral on a separation surface A between the states of the probe Ψ_ν and the surface Ψ_μ :

$$M_{\mu,\nu} = -\frac{\hbar^2}{2m} \int_A \Psi_\nu^* \nabla \Psi_\mu - \Psi_\mu \nabla \Psi_\nu^* d\vec{S}. \quad (2.18)$$

The knowledge of the unperturbed states of the sample and the tip is thus required to calculate the tunneling current using Bardeen's model. Based on the Bardeen approach and using the WKB (Wentzel-Kramers-Brillouin) approximation [116], one can demonstrate that the tunneling current can be expressed as:

$$I(z, V_p, T) \propto \int_{-\infty}^{+\infty} \rho_s(E) \rho_t(E - eV_p) [f(E - eV_p) - f(E)] T(E, z, V_p) dE \quad (2.19)$$

where $f(E)$ is the Fermi-Dirac distribution, ρ_s and ρ_t the LDOS of respectively the tip and the sample.

2.1 Scanning Tunneling Microscopy

In this equation $|M(E)|^2 = T(E, z, V_p)$ is the transmission of the tunneling barrier that can be expressed as:

$$T(E, z, V_p) \propto \exp\left(-2\sqrt{\frac{2m}{\hbar} \left[\langle W \rangle + \frac{eV_p}{2} - (E - E_F)\right]} z\right) \quad (2.20)$$

where $\langle W \rangle = \frac{W_{tip} + W_{sample}}{2}$ is the mean work function of the sample and the tip. One can notice that the transmission function has not the same expression than the one for the square barrier. In this model, a trapezoidal barrier is assumed due to the bias applied between the tip and the sample.

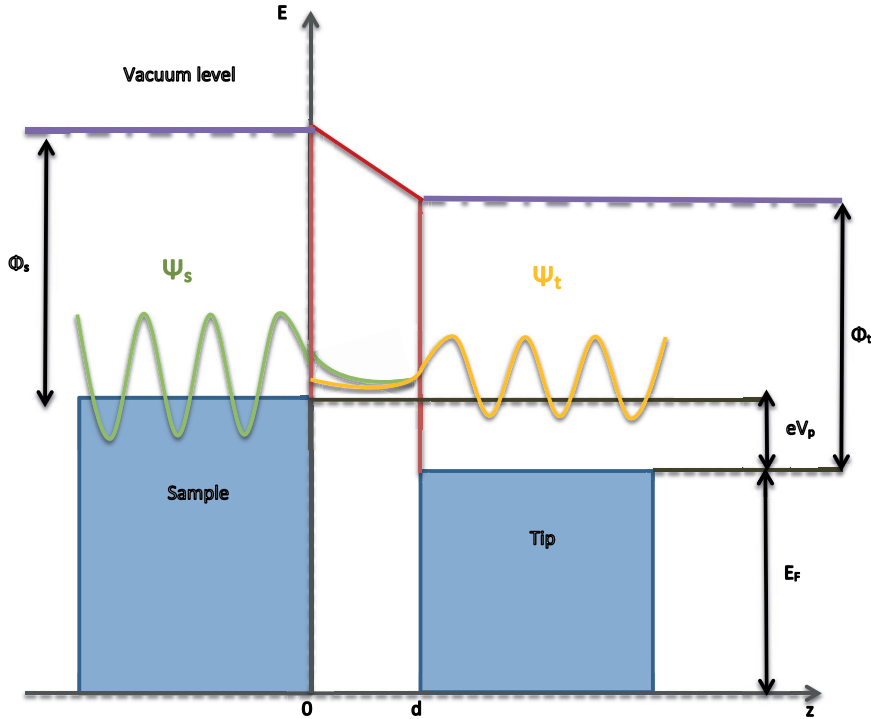


Figure 2.3: *Basic scheme illustrating the Bardeen approach for computing the tunnel current between two electrodes. Bardeen's approach consists in resolving Schrödinger equation in the two unperturbed electrodes (solutions Ψ_s and Ψ_t in this figure) and then finding the solution of the total system using 1st order perturbation by the computation of the matrix element $M_{s,t}$.*

At the limit of very low temperature, the Fermi-Dirac distribution can be approximated as a Heaviside distribution, thus leading to the limitation of the integration domain to $[E_F, E_F + V_p]$:

2. EXPERIMENTAL SET UP AND TECHNIQUES

$$I(z, V_p, T \approx 0) \propto \int_{E_F}^{E_F+V_p} \rho_s(E) \rho_t(E - eV_p) T(E, z, V_p) dE \quad (2.21)$$

Through the equation 2.21, one can see that the tunneling current depends on both sample and tip electronic properties with an exponential decay in the barrier height direction. Depending on the bias V_p sign, one can see that the current can flow either from the sample to the tip or from the tip to the sample.

2.1.2.2 Tersoff-Hamann model

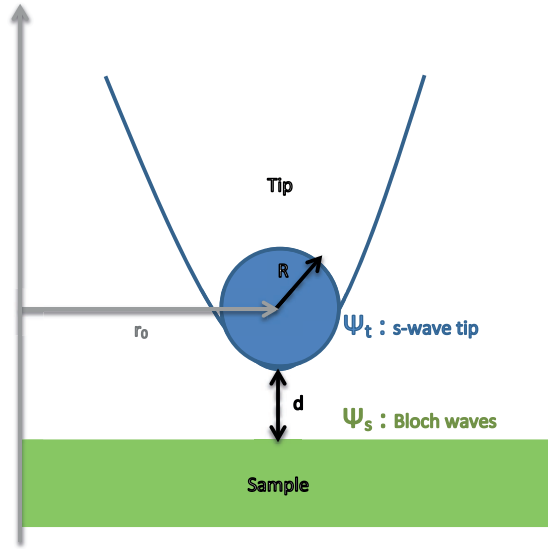


Figure 2.4: *Basic scheme illustrating the Tersoff-Hamann approach. They modeled the tip by a sphere a radius R having a s-orbital wave function. The surface is modeled by a sum of Bloch waves decaying exponentially perpendicularly to the surface.*

No clue about the spatial dependence of the tunneling current or any consideration on the tip shape is however done in the model described by the equation 2.21. To model the Scanning Tunneling Microscope, J. Tersoff and D. R. Hamann used the Bardeen approach and modeled the tip as a radially symmetric wave function (s orbital) and the sample as a sum of Bloch waves decaying exponentially perpendicularly to the surface [117, 118]. Under these conditions, the matrix element $M_{\mu,\nu}$ is found to be proportional to the sample wave function evaluated at the position of the tip center of curvature:

$$M_{\mu,\nu} \propto \Psi_\nu(\vec{r}_0) \quad (2.22)$$

Injecting this expression of the matrix element in the Bardeen's tunneling current expression (2.17) leads to:

$$I \propto \underbrace{\sum_{\nu} |\Psi_{\nu}(\vec{r}_0)|^2}_{\rho_s(\vec{r}_0, E_F)} \delta(E_{\nu} - E_F) \quad (2.23)$$

This equation shows that according to this model, in the STM imaging mode (spherical apex tip and plane surface), the tunneling current is actually proportional to the LDOS of the sample evaluated at position of the center of curvature of the tip (*i.e.* at the tip position) at the Fermi level. This basic model can thus explain why one can probe local electronic properties of the sample with the tip. However, this is not suitable to explain atomic resolution of metal surfaces as well as the imaging of adsorbed molecules, but it provides a qualitative picture of the surface.

2.1.3 Contrast and interpretation of STM images

As explained in the previous section, the current flowing between the STM tip and the sample depends on the local electronic properties of the sample, but also on the tip LDOS and on the sample tip distance. Therefore, assuming that the feedback loop is operating under the constant mode (which will be described more precisely in section 2.2.1.2) and that the tip electronic properties remain unchanged during the scan, the tip-surface distance is modified both for topological reasons (surface steps, holes, atomic corrugation) and also by electronic properties variations. The contrast in STM images of homogeneous sample, meaning sample with homogeneous electronic properties, is only due to the topology of the sample (Figure 2.5a).

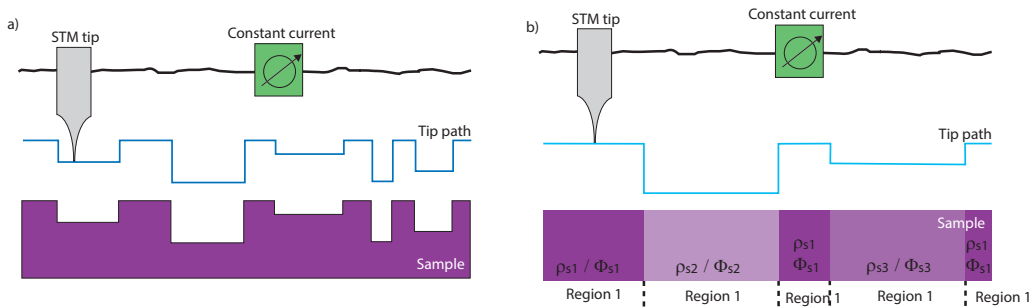


Figure 2.5: *Illustration of a constant current STM scan over (a) a homogeneous sample (b) an heterogeneous sample with different electronic properties. The resulting image in the second case not only corresponds to the topology of the sample but also to the electronic properties variations.*

In the case of inhomogeneous sample, the STM image contrast is not only due to the topology of the sample but also to the variations of the electronic properties of the

2. EXPERIMENTAL SET UP AND TECHNIQUES

sample (Figure 2.5b). Therefore, the basic interpretation of the STM images being a direct measure of the topological height of the surface is most of the time not entirely right. Chemisorbed oxygen on metallic surface is a good counter-intuitive illustration of that phenomenon. Indeed, even if the molecular oxygen atoms are chemisorbed on top of the surface, they appear like depressions (meaning under the surface) on the STM images. A major part of this work consisted in imaging molecules on surfaces. The previous model only considered the tunneling of electrons between two metallic electrodes. This model can be extended to molecules (insulators) adsorbed on surfaces, taking into account the energy levels of the adsorbed species (Figure 2.6). Depending on the sign of the bias voltage applied, empty (LUMO, LUMO+1, etc...) (Figure 2.6b) or occupied (HOMO, HOMO-1, etc..) (Figure 2.6a) states are involved in the tunneling process and therefore are observed on the STM images. However, due to the close proximity between the molecules and the surface, the molecules electronic states are often modified by the electronic coupling (Γ) with the surface atoms resulting in a broadening and/or a shift of the molecular levels with respect to free standing molecules. Consequently, a decoupling layer (*e.g.* sodium chloride layer) between the molecules and the metallic surface is usually required to observe the molecular orbitals of organic molecules. Thin layers (few monolayers) of insulating organic molecules can be successively imaged when adsorbed on top of metallic surfaces due to electronic coupling with the surface. The STM contrast of such molecules usually depends on the bias applied because of the molecular electronic states (often modified by the electronic coupling with the surface) involved in the tunneling process. To conclude, the contrast in STM images not only originates from topological height of the surface but also depends on the bias, the electronic properties of the sample and of the tip.

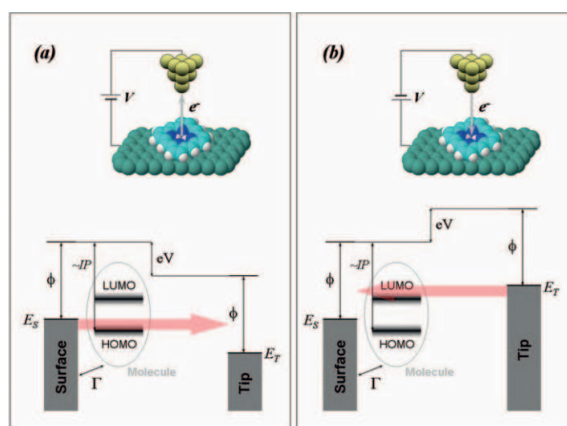


Figure 2.6: *Energy diagram for an STM junction when applying a negative (a) or positive (b) sample bias. A molecule is electronically coupled (Γ) to the substrate, leading to a shift and a broadening of the molecular orbitals. [119]*

2.2 Experimental set-up at CEA Saclay

All the experiments performed at CEA Saclay during this project were carried out in a UHV system made of two chambers. I will describe these chambers and the related instruments and pumping elements in this section.

2.2.1 STM head

An Omicron VT-STM coupled with a Nanonis electronic system for acquisition were used during this project. In this section, I will describe the main components of the STM head.

2.2.1.1 Piezo-electric scanners

A piezoelectric scanner is used to move the STM tip attached to the piezoelectric tube in all directions of the space (x, y, z) . This motion is produced by using a piezoelectric material which can be expanded or contracted when applying a voltage on it ($\approx 10 \text{ \AA}$ for 1V). Therefore, it is possible to adjust the position of the tip with a very high precision, which is mandatory especially for the z direction. Indeed, we have seen in the previous section that the tunnel regime is achieved when the tip is only few Angström away from the surface. Thus, a very precise control of the z position of the tip is necessary to prevent the tip from crashing into the surface. Piezoelectric motors are generally made of ceramic materials. They do not have to be magnetically shielded and can be made more compact and efficient than electric motor with a high degree of accuracy without significant vibrations or heat.

2.2.1.2 Current feedback loop and data acquisition

Two imaging modes are often used in STM:

The constant height mode: In this mode, the z position of the tip is fixed and the (x, y) piezo scanners sweep the area of interest line after line while the tunneling current is registered. This method suffers from a serious drawback. Indeed, if the height of the tip remaining constant, the tip can crash into the surface because of surface topology change (several steps) or pollution on the surface.

The constant current mode: This mode is very often used for Scanning Tunneling Microscopy measurements. The user applies a bias between the tip and the sample and set a desired tunneling current. Z-piezoscanner will move the tip upwards or backwards until the desired tunneling current is achieved. The z -variation necessary to reach the

2. EXPERIMENTAL SET UP AND TECHNIQUES

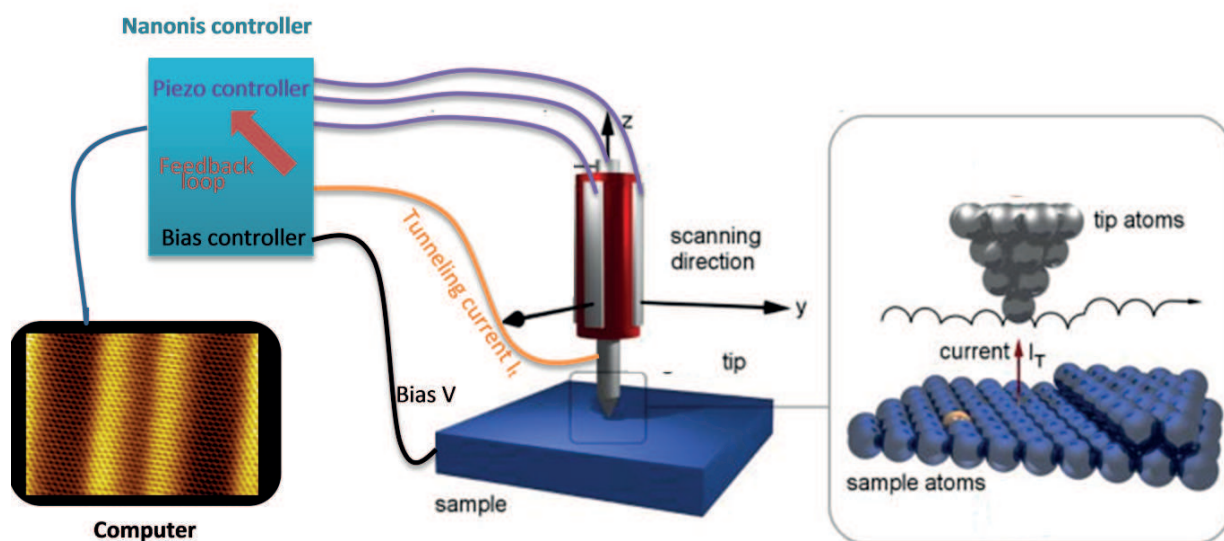


Figure 2.7: *Illustration of the working principle of an STM in the constant current mode. A bias is applied between a sharp tip and the sample separated by a distance of few Angström. The current tunneling between the sample and the tip is measured and the position of the tip is adapted using piezoscanners to maintain a set current value using a feedback loop. Adapted from ref [120].*

desired current is registered and the tip is moved to the neighboring measurement position through (x, y) displacement. The tunneling current is measured at the new position and similarly, the height of the tip is changed until the set current is reached. It goes on and on until the whole area has been scanned. Current feedback loop is driven by a proportional-integral-derivative (PID) controller on the Nanonis electronics. One has to precisely tune the feedback parameters in order for the tip to be stable and thus to get accurate measurements. One can also vary the scanning speed of the tip on the surface.

2.2.1.3 Vibration damping systems

Another essential part of an STM is the vibration isolation system, which minimizes the mechanical noise. The minimization of the mechanical noise is crucial to obtain well-resolved STM images and also to protect the tip from crashing into the surface. The vibration isolation of our STM apparatus consists of two systems. First, the whole STM head is suspended by vertical springs to isolate the STM head from vertical vibrations. In addition, copper plates are attached all around the STM head and permanent magnets fixed to the UHV chamber are positioned in between these copper plates. This system suppresses lateral displacements due to Eddy current damping generated when copper

plates are moving with respect to the permanent magnets. To conclude, vibration damping systems are used to suppress both vertical and lateral vibrations of the STM head that can dramatically affect our measurements. However, careful attention has to be taken when acquiring STM data since perturbation from the outside (sound, slamming doors, etc...) can badly affect our measurements despite these vibration damping systems.

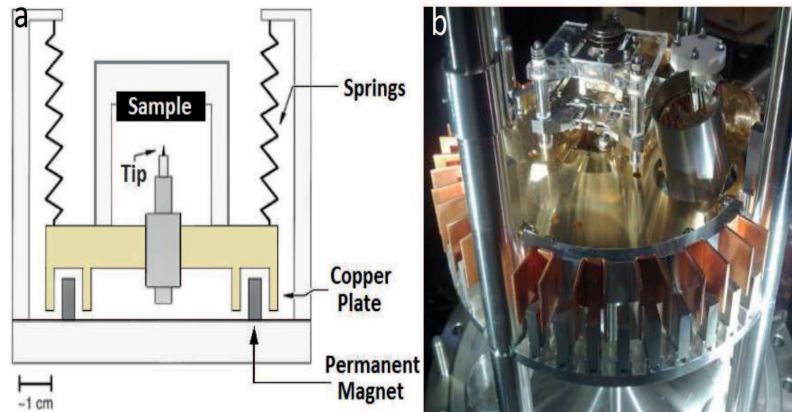


Figure 2.8: (a) Scheme of the STM head used during my PhD showing the two vibration damping systems (vertical springs and eddy current system). (b) Picture of the STM head of the VT Omicron STM used during my PhD [121].

2.2.2 Ultra high vacuum chambers

We used a commercial Omicron VT STM for our measurements. It consists of two main chambers operating in UHV separated by a valve. The STM head and a wobble stick to manipulate the sample are located in the first chamber also called STM chamber (Figure 2.9B). The second chamber is dedicated to the sample preparation (Figure 2.9A) (bombardment, annealing, evaporation) and a small load-lock chamber (Figure 2.9C) is connected to the preparation chamber to introduce or remove the samples and the tips without putting all the system at ambient pressure.

2.2.2.1 Pumping elements

As explained in the previous sections, our system operates under Ultra High Vacuum with typical pressure of $\approx 10^{-10}$ mbar. Our samples are kept “clean” in UHV environment, or at least mostly free of pollutants or contaminants for a respectable amount of time which is of prime importance when characterizing raw surfaces or system with monolayer coverages with atomic resolution. This UHV conditions are achieved after baking-out all the system at a temperature of around 100-150°C for typically 48 hours. The whole system

2. EXPERIMENTAL SET UP AND TECHNIQUES

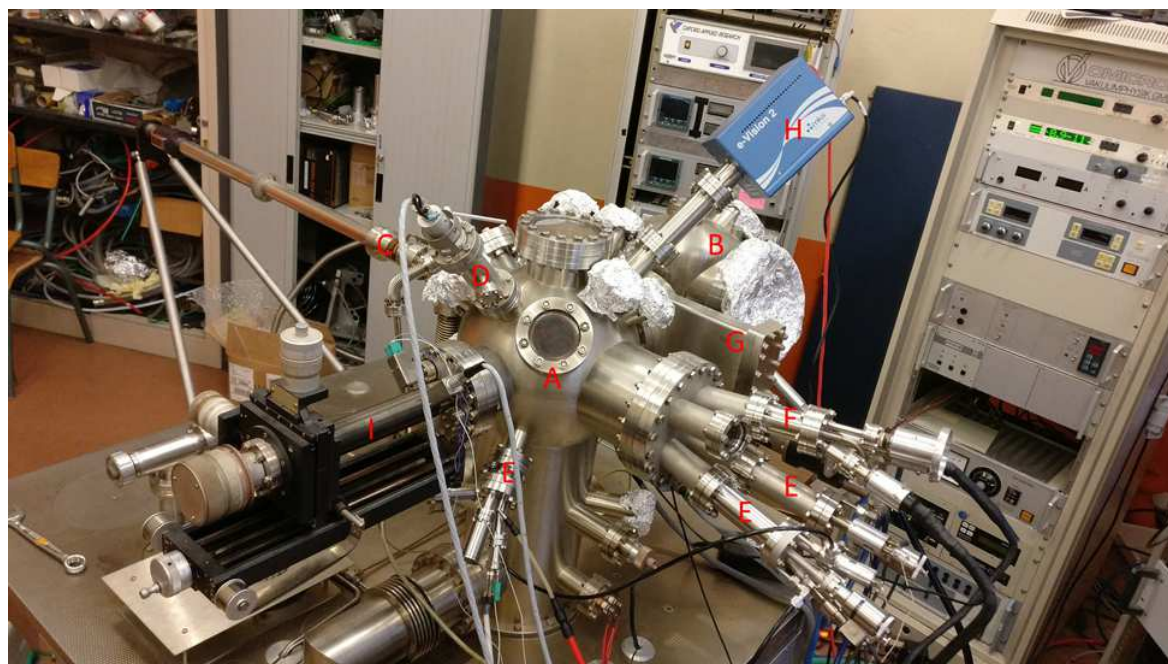


Figure 2.9: *Picture of the UHV system used at CEA Saclay made of two chambers: (A) Preparation chamber and (B) STM chamber separated by a valve (G). A load-lock (C) is attached to the preparation chamber for tip and sample transfer to/from UHV environment. An ion bombardment gun (D) is used for sample cleaning and preparation. Three k-cell organic evaporators (E) are attached to the preparation chamber as well as an electron-beam evaporator (F) for metal deposition. A quadrupole mass spectrometer (H) is also attached to the preparation chamber. A sample holder with heating capabilities is located at the end of a translation arm (I) allowing the transfer of the sample and the tip between the two chambers.*

is pumped by a primary pump which is an oil rotary pump (Figure 2.10a), pumping down from ambient pressure to approximately 10^{-3} mbar. An additional turbomolecular pump consisting in a quickly rotating rotor blade and stationary stator blade pair (Figure 2.10b) is used. The blades transfer their mechanical energy to the gas molecules through collisions. The angle of the blades slightly changes along the turbomolecular pump axis so that gas molecules have a greater probability to be pushed towards the outlet of the pump than being reflected towards the inlet according to the Knudsen cosine law. This pump cannot operate from ambient pressure. That is why a primary pump is associated with a turbomolecular pump. The whole system (primary + turbomolecular pump) can pump the system down to pressures of around $\approx 10^{-10}$ mbar. The main issue with turbomolecular pumps is that they are operating at high frequency (typically 10 kHz) thus generating mechanical noise in the STM head. For that reason, these pumps must be shut down be-

fore STM measurements. Another kind of pump called ionic pumps (one per chamber) are installed in our chambers. In these pumps, a HV field (few kV) is imposed between two electrodes leading to electrons emission. A magnetic field is also generated thus leading to helical trajectories for the electrons. These helical trajectories maximize the collisions between the electrons and the atoms or molecules of the residual gas. The gas molecules are ionized after the collision and are thus attracted to the electrodes. These electrodes are usually made of titanium. Gas molecules are thus glued on the electrode surface upon collision, thus leading to a pressure reduction. A Titanium Sublimation Pump (TSP) is also installed in the preparation chamber. A very high current (typically 40 A) flows into a titanium filament thus leading to the evaporation of titanium atoms. These atoms will collide with the residual gas molecules on the chamber and then stick them on the chamber walls. This kind of pump does not operate in continuous mode but only from time to time.

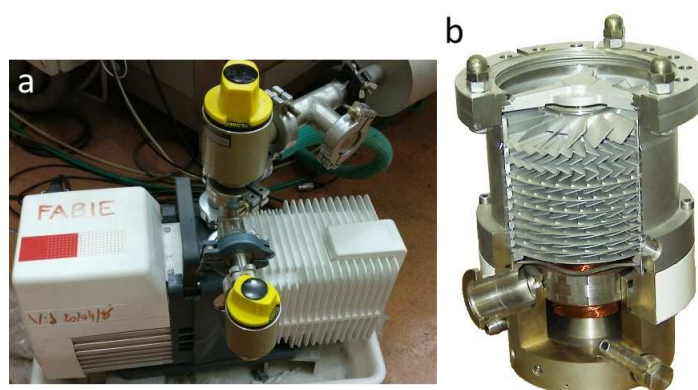


Figure 2.10: (a) *Picture of the Pfeiffer Adixen primary pump used at CEA Saclay* (b) *Picture of the typical interior view of a turbomolecular pump showing blades [122].*

To summarize, UHV conditions are used in order to synthesize and characterize sample with very low external pollution (and no solvent-molecule interaction as it can occur for STM at liquid/solid interface). In order to achieve UHV conditions, primary pumps coupled to a turbomolecular pump as well as ionic and TSP pumps are used.

2. EXPERIMENTAL SET UP AND TECHNIQUES

2.2.2.2 Surface preparation elements

The first step of a metal surface preparation is usually the ion sputtering. We used a so-called ion bombardment gun (Figure 2.9D) in order to bombard the surface with ionized Argon (Ar^+) atoms having a typical energy of 1 keV for typically 10 minutes. First atomic layers of the surface are usually ripped out, thus getting rid of the impurities or the pollution that was previously on the surface.

After this step, the metallic surface is usually not flat and a tungsten filament is heated at temperatures of around 500°C for typically one hour to anneal the sample and also outgas the residual Ar and the eventual remaining impurities.

2.2.2.3 Evaporation sources

Two different kinds of evaporators were used during my PhD:

Knudsen effusion cell or k-cell



Figure 2.11: *Picture of a Knudsen-cell evaporator similar to the one used during my PhD.*

The molecules (powder) are placed into a quartz crucible. This crucible is surrounded by a filament. A controlled current is set through this filament leading to the progressive heating of the powder. After reaching a given temperature, molecules start to sublime (from the solid phase to the gas phase) leading to an increase of the chamber pressure (Figure 2.9E and Figure 2.11).

Using the gas kinetic theory, the mean free path between two molecular collisions in the gas phase can be written as:

$$\bar{l} = \frac{k_B T}{\sqrt{2} \pi d_m^2 p} \quad (2.24)$$

where p is the pressure, T the temperature and d_m the molecule diameter.

2.2 Experimental set-up at CEA Saclay

Considering typical values corresponding to our working conditions, $T = 300K$, $p = 10^{-10}$ mbar and $d_m = 2$ nm, we get $\bar{l} \approx 2.3 \times 10^4$ m that is of course much greater than the typical dimensions of our chamber. Consequently, we consider that we are in the ballistic transport regime. In other words, the molecules are traveling without any collision from the evaporator to the sample and form a so-called “molecular beam”.

A thermocouple is also included in the evaporator allowing a fine monitoring of the temperature. A shutter is placed at the end of the k-cell tube preventing molecules from reaching the chamber. This shutter is only opened for the molecule deposition operation and thus provides an efficient way to control the deposition time. This allows to control the amount of molecules deposited on the surface which is crucial for deposition at submonolayer coverages. Three k-cell evaporators are installed on the preparation chamber.

Electron-Beam evaporator (e-beam evaporator)

We used a EGC04 e-beam evaporator from Oxford Applied Research for metal deposition (Figure 2.9F and Figure 2.12). This evaporator has four identical pockets consisting of one filament and one metallic rod. A significant current (typically 4A) is set in the filament thus leading the thermal emission of electrons. A high voltage (typically 2kV) is set between the filament and the metallic rod. Consequently, highly energetic thermal electrons are accelerated toward the metallic rod and are bombarding its apex, leading to a local heating. By increasing the current flowing in the filament, the number of thermal electrons emitted is increased. Consequently the number of electrons bombarding the metallic rod grows, increasing its temperature. An electrode is measuring the flux of metallic ions generated by the electrode bombardment. This flux value gives a good indication of the metal evaporation rate. Similarly to k-cells, the e-beam evaporator is water-cooled and a shutter controls the output. Up to four different materials can be co-deposited (at the same time) depending on the shutter position.

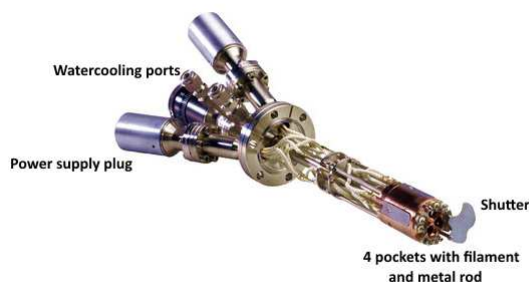


Figure 2.12: *Picture of an EGC04 e-beam evaporator used during my Ph.D.*

2.3 Au(111) substrate

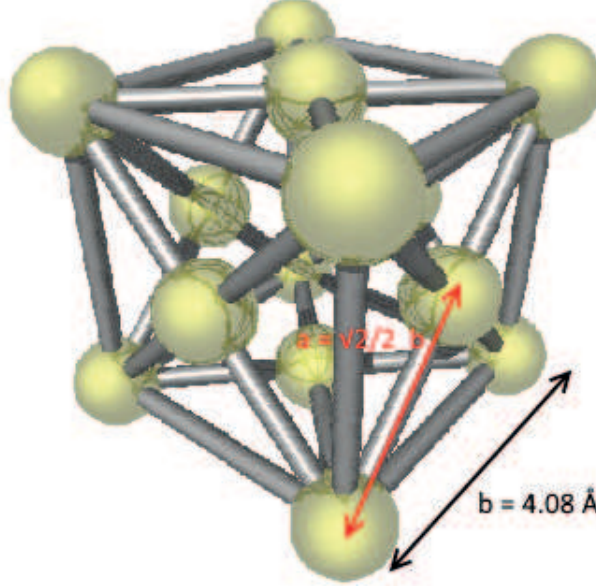


Figure 2.13: *Gold face centered cubic crystal.*

All the nanoarchitectures presented in the following chapters were engineered on an Au(111) surface. Au(111) surface reconstruction will be briefly described in this section.

Gold (atomic number 79) crystallizes in a faced centered cubic (fcc) structure with a lattice parameter b of 4.08 Å, represented in Figure 2.13. The distance between the two nearest gold neighboring atoms is $a = \frac{\sqrt{2}}{2} b$.

The Au(111) surface atoms are not arranged in the same way than the underlying atoms. A rearrangement (called surface reconstruction) of the atomic packing occurs at the surface in order to minimize the surface energy. An atomic overdensity is thus observed at the topmost surface layer involving a contraction in the $[1\bar{1}0]$ direction of the hexagonal lattice. In the $[1\bar{1}0]$ direction, the distance between 24 atoms of the topmost layer is equal to the distance between 23 bulk atoms (corresponding to a distance of $22a$). This contraction in the $[1\bar{1}0]$ direction induces a shift in the perpendicular $[11\bar{2}]$ direction and the appearance of hcp domains alternating with fcc domains. A periodic structure with a rectangular unit cell of $22 \times \sqrt{3} a$ is observed. The superstructure formed by the atomic rearrangement at the surface consists of alternating fcc and hcp packing domains with in a transition area in between (Figure 2.14). A corrugation is observed on the surface due to the height difference of surface atoms in the superstructure. The highest gold atom of the reconstruction unit-cell is observed in a bridge site at the hcp-fcc interface and the lowest is observed in the hcp domain (Figure 2.14b).

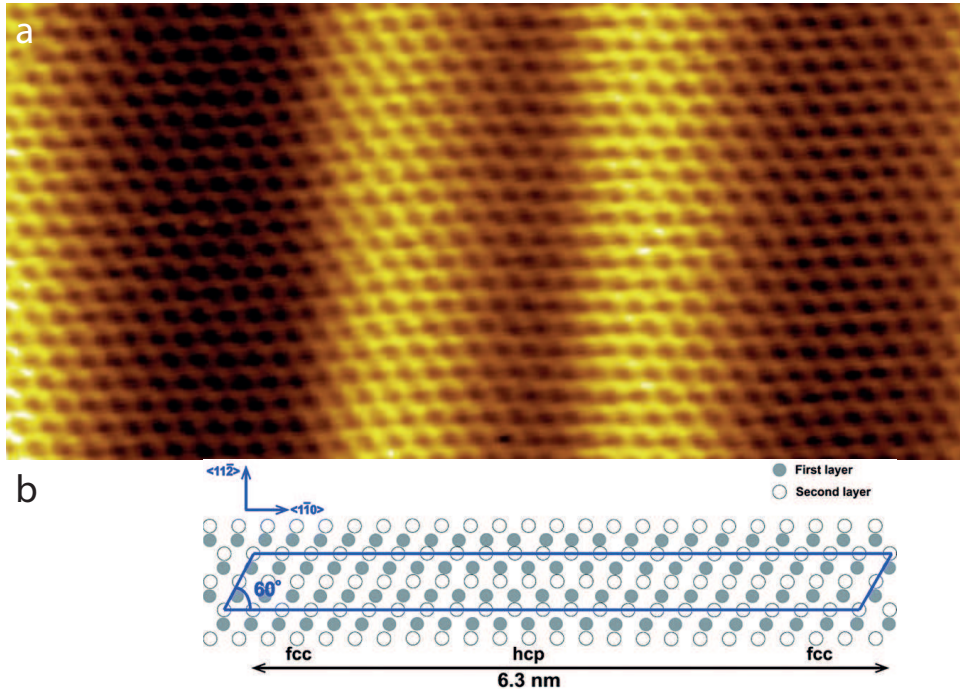


Figure 2.14: (a) Atomic resolution STM image of the fcc-hcp transition at the Au(111) reconstructed surface. $10 \times 5 \text{ nm}^2$; $V_s = 0.50 \text{ V}$, $I_t = 0.07 \text{ nA}$. (b) Position of the surface and bulk atoms (adapted from [123]) on the reconstructed surface.

The corrugation amplitude of the superstructure is typically of $0.20 \pm 0.05 \text{ \AA}$. These bridge atoms form periodic double-line domains. The Au(111) reconstructed surface thus exhibits a periodic pattern of pairwise parallel corrugation lines oriented in the $[11\bar{2}]$ direction (Figure 2.15). The large area between two corrugation lines corresponds to fcc domains and the small area between two neighboring corrugation lines corresponds to hcp domains. The distance between two pairs of corrugation lines corresponds to the periodicity of the superstructure ($22a = 63 \text{ \AA}$). It can be used as a reference to calibrate STM images.

2. EXPERIMENTAL SET UP AND TECHNIQUES

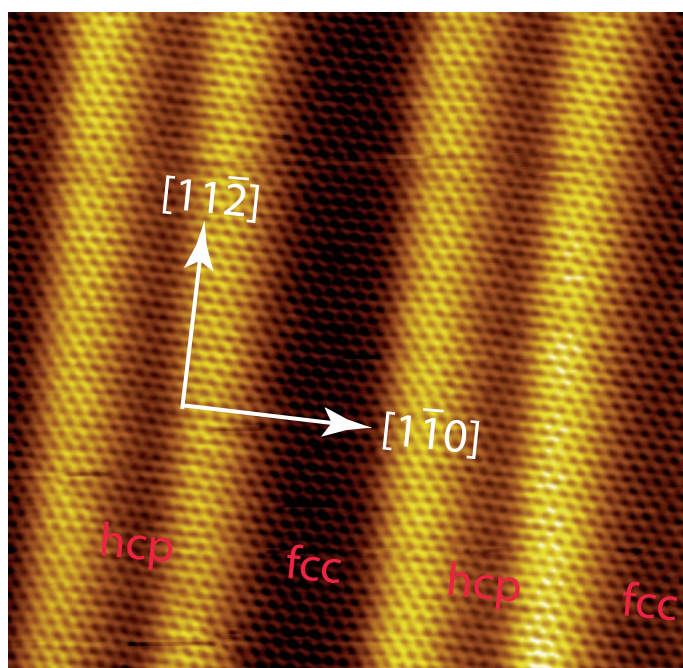


Figure 2.15: *STM image of the corrugation lines of the Au(111) reconstructed surface. $12 \times 12 \text{ nm}^2$; $V_s = 0.50 \text{ V}$, $I_t = 0.07 \text{ nA}$.*

An additional long-range periodicity can be observed in the reconstructed topmost layer. This periodicity is due to the rotation ($\pm 120^\circ$) of the corrugation lines direction according to the equivalent directions of gold crystal at the “elbows” of the reconstruction (Figure 2.16).

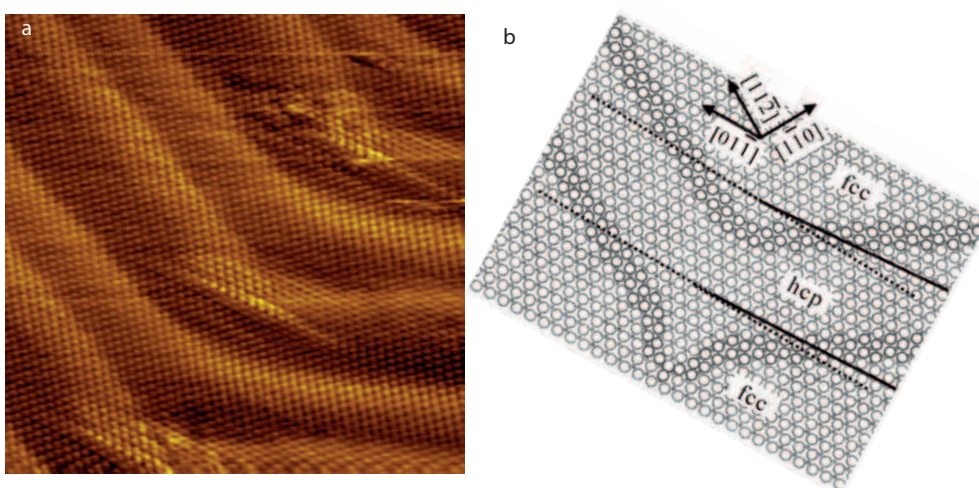


Figure 2.16: *Atomic resolution STM image of elbows of the Au(111) reconstructed surface. $12 \times 12 \text{ nm}^2$; $V_s = 0.70 \text{ V}$, $I_t = 0.17 \text{ nA}$. (b) $[124]$ Atomic representation of Au(111) elbows.*

A zig-zag pattern (often called “herringbone”) is thus observed with a typical distance of 250 \AA between two rotations (Figure 2.17). The rotation of the superstructure orientation thus allows the constraint relaxation along all the three equivalent $[\bar{1}\bar{1}0]$ directions of the Au(111) surface.

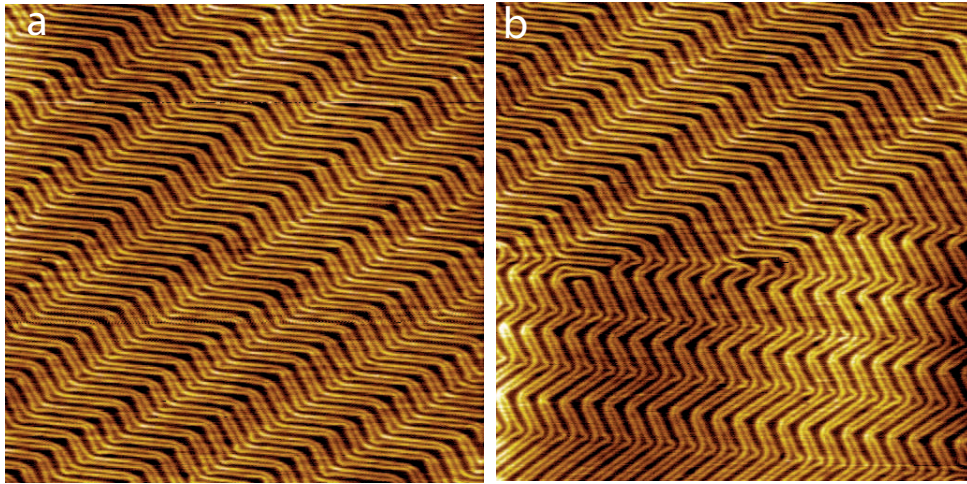


Figure 2.17: *Large scale STM images of the $22 \times \sqrt{3}$ herringbone surface reconstruction of the Au(111) surface. (a) $145 \times 145 \text{ nm}^2$; $V_s = 1.50 \text{ V}$, $I_t = 0.04 \text{ nA}$. (b) $145 \times 145 \text{ nm}^2$; $V_s = 1.50 \text{ V}$, $I_t = 0.04 \text{ nA}$.*

Chapter conclusion

In this chapter, the Scanning Tunneling Microscopy (STM) technique and the associated tunnel effect were described. STM appears as a powerful characterization technique in the scope of this project. STM allows the access to the properties of surfaces or thin films with an atomic resolution capability. To avoid external pollution, the nanoarchitectures presented in this manuscript were synthesized in an Ultra High Vacuum (UHV) environment on reconstructed Au(111) surfaces. The UHV experimental set-up including chambers, pumps, organic and inorganic evaporators were also described in this chapter. Finally, Au(111) substrate was presented.

2. EXPERIMENTAL SET UP AND TECHNIQUES

Chapter 3

PTCDI on Au(111): Influence of local arrangement on self-assembly electronic properties

The objective of this chapter is to demonstrate the influence of the local structural arrangement on the electronic properties of a 2D organic film on a metal surface. The example discussed in this chapter consists in thin films (< 1 monolayer) of perylene derivative (PTCDI) molecules evaporated on Au(111) substrate.

Perylene diimide derivatives are fascinating molecular building blocks for engineering organic devices due to their outstanding chemical and thermal stability as well as their long-lasting photostability [125]. These molecules usually possess the ability to self-assemble into well-defined structures on surfaces [126, 127, 128, 129, 130, 131]. Intense research effort is currently focused on optimizing molecular self-assembly to engineer organic layer [132, 133, 134, 135] with new or optimized structural, electronic and optical properties [136, 137, 138]. The transport model developed by Barraud *et al.* [139] reveals actually that interfacial metal/molecule hybridization is a key parameter driving the properties of organic devices. Engineering metal/organic interfaces at the molecular-level is expected to provide new opportunities to generate new electrical functionalities in supported organic nanoarchitectures. Sedona *et al.* were for example able to switch the catalytic activity of iron-phthalocyanine molecules deposited on Ag(110) [140] by driving supramolecular long-range arrangement and molecular local adsorption geometry. Molecular and nano-object electronic properties are also influenced by conformational changes [141, 142] as well as binding geometry and nature [143, 144, 145].

Intermolecular coupling resulting from molecular packing is for example strongly affecting the charge transport through an organic film. [146, 147, 148]. It is however usually

3. PTCDI ON Au(111): INFLUENCE OF LOCAL ARRANGEMENT ON SELF-ASSEMBLY ELECTRONIC PROPERTIES

unclear how molecular lateral packing affects molecular electronic properties at the atomic level in a 2D nanoarchitecture or if new localized electronic states can be generated in the organic single-layer.

3.1 Canted nanostructure

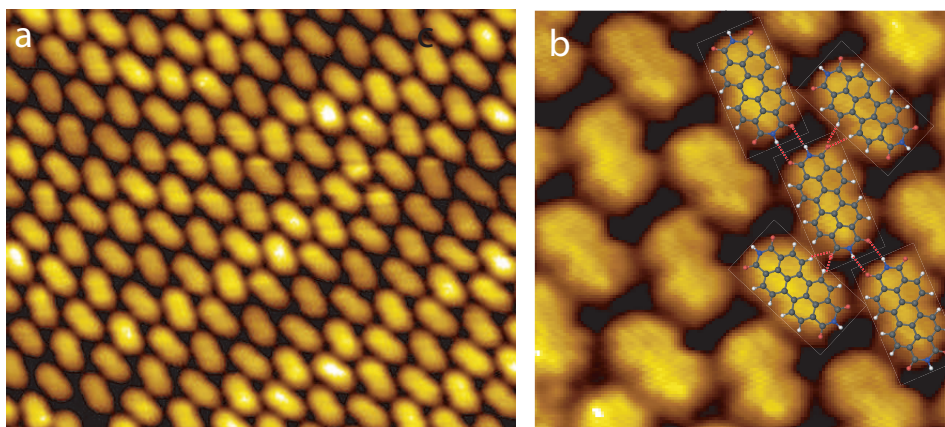


Figure 3.1: *STM images of PTCDI canted nanoarchitecture, (a) $14 \times 12 \text{ nm}^2$; $V_s = 0.60 \text{ V}$, $I_t = 0.2 \text{ nA}$, (b) $5 \times 5 \text{ nm}^2$; $V_s = 0.01 \text{ V}$, $I_t = 0.6 \text{ nA}$. Molecule model are superimposed to the STM image in (b).*

The STM image presented in Figure 3.1 shows that PTCDI self-assembles into a canted structure on Au(111)- $22 \times \sqrt{3}$ at room temperature¹. This structure has been previously described in detail by Mura *et al.* [131]. In contrast with the side-by-side arrangement (Figure 3.2a), no bright spot is observed in the vicinity of neighboring molecules, *i.e.* the gap between molecules appears dark in the STM image. In addition, no distinct intermolecular feature can be observed in this structure. The network unit cell of this hydrogen-bonded “canted” structure is a parallelogram with 1.6 nm and 1.5 nm unit cell constants and an angle of 95° between the axes. Calculations showed that oxygen atoms of PTCDI molecule are all forming $\text{O} \cdots \text{N-H}$ single or $\text{O} \cdots \text{H-C}$ double hydrogen bonds with neighboring molecules [131]. These bonds are represented by red dotted lines in the STM image (Figure 3.1b).

¹Experiments were performed in a ultrahigh vacuum (UHV) chamber at a pressure of 10^{-8} Pa. The Au(111) surface was sputtered with Ar^+ ions and then annealed in UHV at 600°C for 1 hour. PTCDI molecules, Figure 3.2e, were evaporated at 250°C and deposited on the gold surface kept at room temperature. Cut Pt/Ir tips were used to obtain constant current STM images at room temperature with a bias voltage applied to the sample. STM images were processed and analyzed using the home made FabViewer application [149].

3.2 Side-by-side arrangement

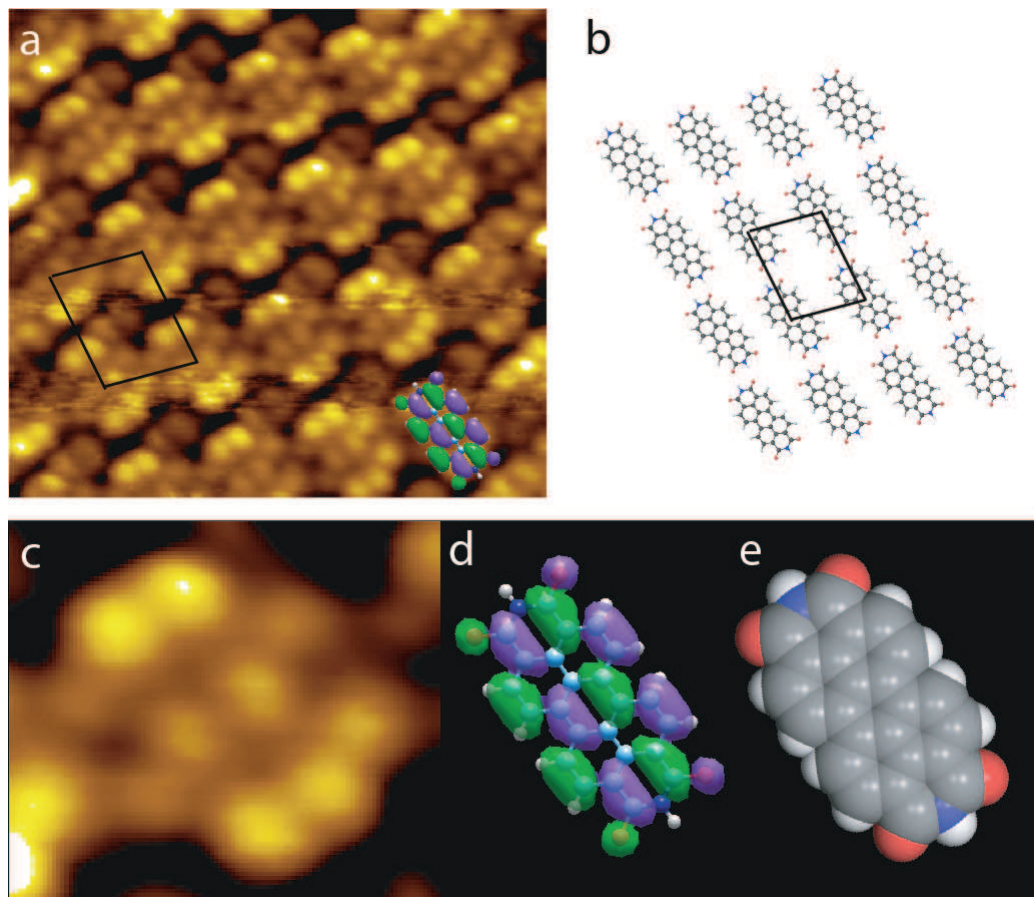


Figure 3.2: (a) High resolution STM image of the PTCDI parallel nanoarchitecture, $5 \times 5 \text{ nm}^2$; $V_s = 0.40 \text{ V}$, $I_t = 0.6 \text{ nA}$. (b) $1 \times 1 \text{ nm}^2$; (b) Scheme of the unit cell. The unit cell is represented by dotted purple lines. (d) Charge density contours of the PTCDI LUMO. (e) Scheme of the PTCDI molecule. Carbon atoms are gray, oxygen atoms are red, nitrogen atoms are blue and hydrogen atoms are white.

The STM image presented in Figure 3.2a shows that PTCDI also self-assembles into a compact nanoarchitecture on Au(111)- $22 \times \sqrt{3}$ at room temperature. The network unit cell is a parallelogram with 1.0 nm and 0.8 nm unit cell constants and an angle of 80° between the axes. Molecules are arranged side-by-side and are forming rows in this structure. Molecules of neighboring rows are bonded through double-hydrogen bonds ($\text{O} \cdots \text{H-N}$) between imide groups. Intermolecular features are surprisingly visible in the STM images at room temperature (Figure 3.2a). Figure 3.2c is a high resolution STM image of a single molecule in the nanoarchitecture. The molecule is composed of ten large bright spots in the STM images at positive bias (empty states). The size and spatial

3. PTCDI ON AU(111): INFLUENCE OF LOCAL ARRANGEMENT ON SELF-ASSEMBLY ELECTRONIC PROPERTIES

distribution of these spots are in a very good agreement with the calculated charge density contour of PTCDI lowest unoccupied molecular orbital (LUMO). The LUMO contour (Figure 3.2d) was calculated using complete neglect of differential overlap (CNDO) semi-empirical method. The charge densities related to the LUMO are mainly distributed over the perylene core and have a π character. Additional features are observed in the STM images in the gap between molecules of neighboring rows (in the center of the unit cell drawn in Figure 3.2a). These features are comparable to double-bright spots. It should be noticed that the intensity of these bright spots is lower than the intensity of molecular feature in the STM images.

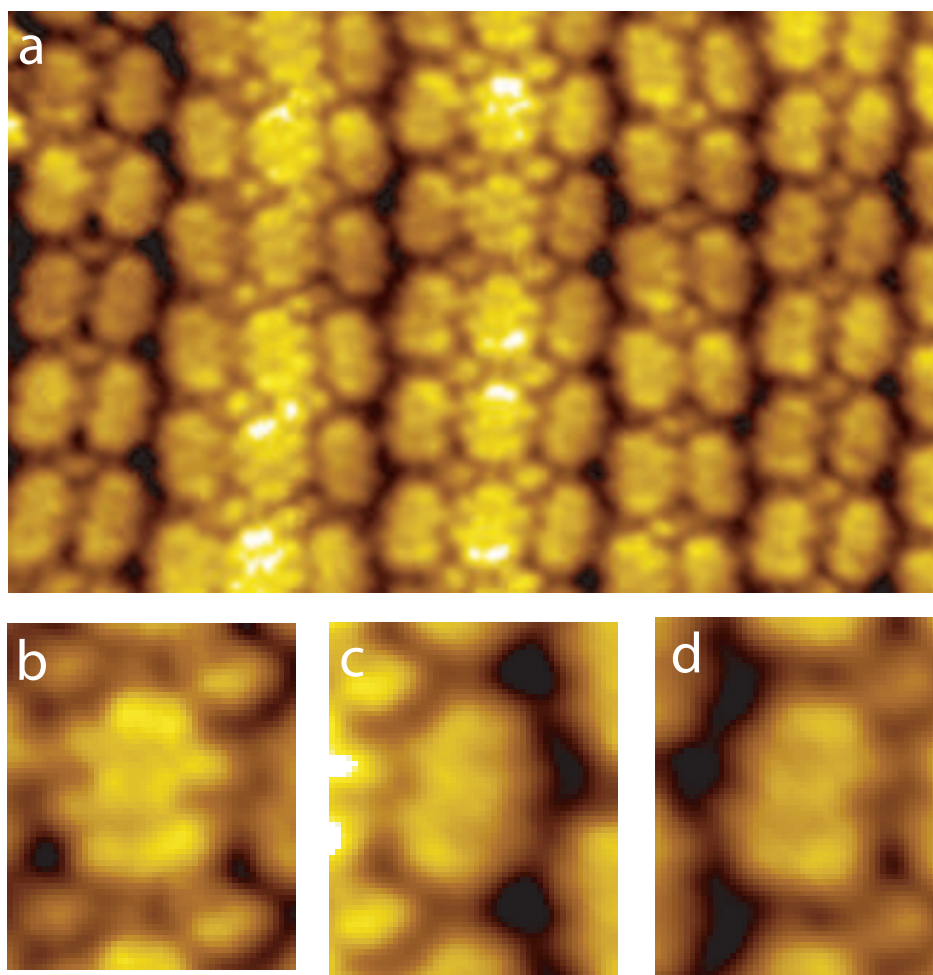


Figure 3.3: (a) STM image of the double and triple side-by-side PTCDI nanolines, $5 \times 5 \text{ nm}^2$; $V_s = 0.60 \text{ V}$, $I_t = 0.5 \text{ nA}$. Molecules of the central line (b) and the side line (c,d) of the triple-nanoline structure, $1 \times 0.8 \text{ nm}^2$.

The domain boundary between double and triple side-by-side PTCDI nanolines is shown in Figure 3.3. STM reveals again intermolecular features in these structures. The

features of central chain molecules in the triple-nanoline structure (Figure 3.3b) correspond to the spatial charge densities related to the LUMO, as it was observed for molecules in the side-by-side structure (Figure 3.2). In contrast the intramolecular features are highly reduced in the side-lines of the triple-nanoline structure (Figure 3.3c,d) as well as in the double-nanoline structure (Figure 3.3a). Bright spots are observed in the gap between molecules in the double-line as well as in the triple-line structures, when molecules are arranged side-by-side. In comparison the row boundary between nanoline-domains appears dark in the STM image. At the row boundary, molecules are not arranged side-by-side but adopt locally the packing of the canted structure.

3.3 Tip-induced structural reorganization

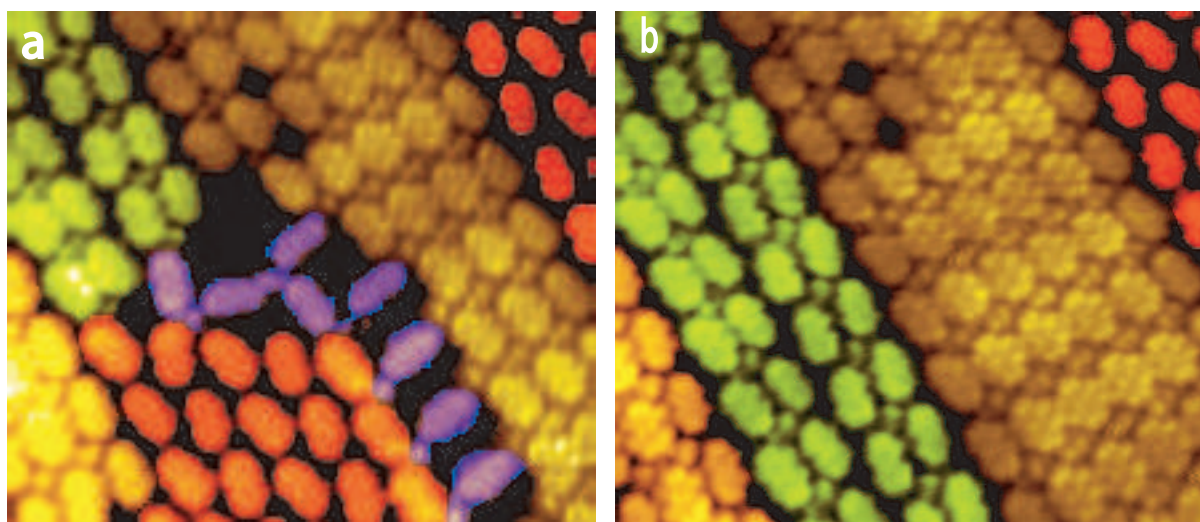


Figure 3.4: *Two successive STM images of PTCDI nanoarchitectures, $10 \times 10 \text{ nm}^2$; (a) $V_s = 0.70 \text{ V}$, $I_t = 0.4 \text{ nA}$, (b) $V_s = 0.50 \text{ V}$, $I_t = 0.2 \text{ nA}$.*

The Figure 3.4a shows an STM image of the domain boundary between several PTCDI nanoarchitectures. The double and triple-line structures are colored in green and yellow respectively, whereas the canted structure is colored in red and the side-by-side arrangement appears in brown color. The molecules colored in blue are single molecules perpendicularly bonded to the different PTCDI nanoarchitectures. This STM image reveals that bright spots are located between molecules in the side-by-side arrangement, and in the double and triple row structures. Bright spots are also observed at the junction between the canted structure and single blue molecules and at the junction between the canted structure and single blue molecules.

3. PTCDI ON AU(111): INFLUENCE OF LOCAL ARRANGEMENT ON SELF-ASSEMBLY ELECTRONIC PROPERTIES

Repeated STM scans at $V_t = 0.5$ V were used to modify molecular arrangement. After few STM scans, the binding of the blue molecule is broken. This leads to the rearrangement not only of the blue molecules but also of the neighboring red molecules in the canted structure. The resulting organic structure can be observed in Figure 3.4b. It results in the growth of the double-line (green) and the side-by-side structures (brown). The bright spots between molecules are visible in these newly-generated structures.

However two local defects (dark spots) are visible in the side-by-side structure in the top of Figure 3.4. A high resolution image of this area is presented in Figure 3.5a. The STM image shows that the molecules located between the two dark spots do not have exactly the same orientation as the neighboring molecules in the domain, *i.e.* they are rotated by few degrees. In addition, they do not have the same aspect as the other molecules in the side-by-side arrangement. After repeated STM scans on this area, these molecules adopt the same orientation as their neighbors. This leads to the disappearance of the two dark spots, which are replaced by bright double-spots (Figure 3.5b,c).

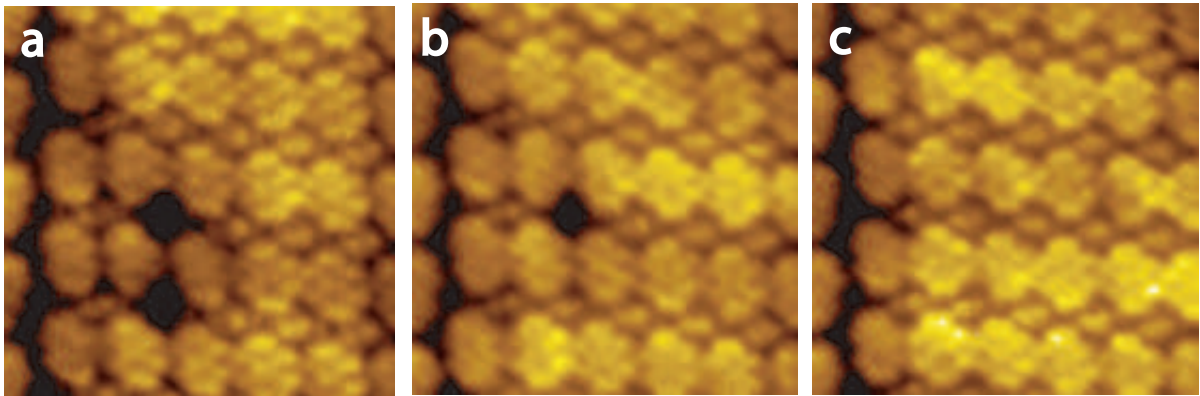


Figure 3.5: (a,b,c) Three successive STM images of PTCDI row nanoarchitecture, 10×6 nm²; $V_s = 0.50$ V, $I_t = 0.2$ nA.

3.4 Localized electronic coupling

The STM images show that bright spots appear at the extremity of molecules in specific 2D PTCDI nanoarchitectures. These spots are observed in the molecular side-by-side arrangement but not in the canted PTCDI structure, where molecular chains are shifted. The fact that the appearance on bright spots depends of molecular arrangement (Figure 3.4, 3.5), reveals that the bright spots result from lateral intermolecular electronic coupling. STM image analysis especially shows that this coupling is localized in the gap between neighboring molecules, where molecular oxygen atoms are not involved in

hydrogen bonds. In the case of the canted structure, Mura *et al.* showed previously that all PTCDI oxygen atoms are involved in hydrogen-bonds, due to the opposite molecular orientation ($\pm 12^\circ$) along neighboring chains. No bright spot is observed in this structure. When molecules are arranged side-by-side, two of their oxygen atoms are not forming hydrogen-bonds with neighboring molecules. These atoms are marked by yellow dotted circles in Figure 3.6a. This area corresponds to the location of double-bright spots in the STM image. These bright spots are also observed at the domain boundary between the canted structure and perpendicular molecules (Figure 3.6b). In that case as well oxygen atoms are not involved in hydrogen-bonding with neighboring molecules (yellow dotted circles in Figure 3.6b). This molecular arrangement also leads to the appearance of bright spots in the vicinity of the “non-connected” oxygen atoms. This electronic coupling is also observed at the domain edge (Figure 3.6c). It should be noticed that there is no bright spot at the molecular edge. Therefore, when a neighboring molecule is missing at the domain edge, no electronic coupling is observed around a non-connected oxygen atom (green dotted square in Figure 3.6c). The generation of this extremely localized electronic coupling therefore requires at least two neighboring molecules (along the main molecular axis (Figure 3.6c)) and one oxygen atom not involved in hydrogen bonding.

The STM images reveal moreover that the appearance of molecular lateral electronic coupling modifies the aspect of the PTCDI molecules. The LUMO state of the molecule can be surprisingly imaged with STM at room temperature. The molecular states are usually broaden at the interface with a metal surface. For this reason, these states are especially difficult to probe with STM at room temperature. This is why PTCDI molecules adopt the “usual” peanut-shape in the STM images at room temperature, as observed in the canted structure (Figure 3.1). The fact that the LUMO state is clearly resolved with STM in the side-by-side arrangement at room temperature demonstrates that lateral inter-molecular electronic coupling reduces molecule-substrate coupling (*i.e.* electronic states become sharper). The electronic states of the molecule in the side-by-side arrangement correspond then to those of an isolated molecule (*i.e.* a non-supported molecule).

Our observations show that it is therefore possible to generate and organize localized electronic states into various 2D nanoarchitectures by tailoring PTCDI assembly, *i.e.* side-by-side arrangement, double and triple-line structures. The STM tip can be used to create these structures, as shown in Figure 3.4. In addition, the STM tip can also be used to activate locally these states for example in the side-by-side arrangement, as demonstrated in the Figure 3.5c-d without modifying molecular arrangement.

3. PTCDI ON AU(111): INFLUENCE OF LOCAL ARRANGEMENT ON SELF-ASSEMBLY ELECTRONIC PROPERTIES

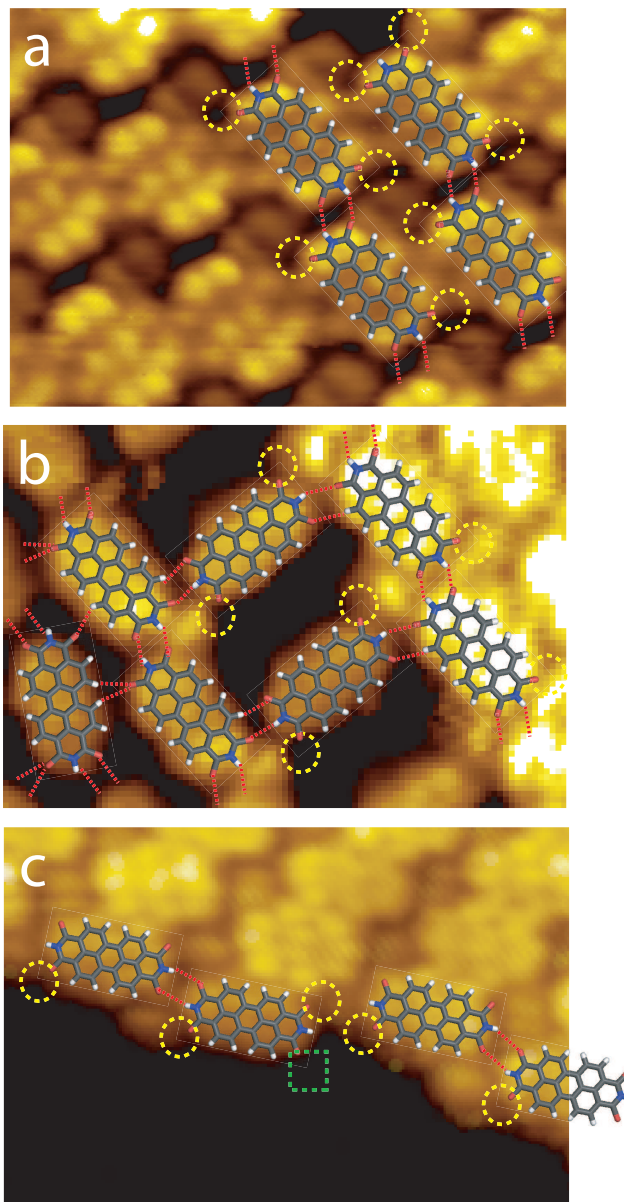


Figure 3.6: (a) $4 \times 3 \text{ nm}^2$; $V_s = 0.40 \text{ V}$, $I_t = 0.6 \text{ nA}$; (b) $4 \times 3 \text{ nm}^2$, $V_s = 0.70 \text{ V}$, $I_t = 0.4 \text{ nA}$; (c) $5 \times 4 \text{ nm}^2$, $V_s = 0.50 \text{ V}$, $I_t = 0.3 \text{ nA}$.

Chapter conclusion

In summary, we investigated lateral inter-molecular electronic coupling in PTCDI two-dimensional nanoarchitectures on Au(111) at room temperature. STM reveals that new localized electronic states appear between molecules in a side-by-side arrangement. We show that the STM tip can be used to modify PTCDI self-assembled nanoarchitecture and to activate these local electronic states. These results show that two-dimensional nanoarchitectures of localized electronic states can be engineered on Au(111) at room temperature taking advantage of PTCDI molecular self-assembly. These observations open new opportunities to engineer novel organic materials for the high density data storage at room temperature or to tune organic layer electronic property. Another way to modify or engineer new self-assembled nanoarchitectures with different structures and properties is to take advantage of other intermolecular interactions than H-bonds. In the following chapter, we will investigate the interaction between the PTCDI molecules studied in this chapter and sodium chloride on Au(111) surface.

3. PTCDI ON AU(111): INFLUENCE OF LOCAL ARRANGEMENT ON SELF-ASSEMBLY ELECTRONIC PROPERTIES

Chapter 4

Engineering of new PTCDI-NaCl hybrid ionic-organic nanostructures

The objective of this chapter is to take advantage of ionic-organic interactions to engineer organized 2D organic self-assembly. The system studied here consists in a combination of PTCDI molecules (studied in chapter 3) and sodium chloride (NaCl) on Au(111) surface. Pristine sodium chloride layers evaporated on Au(111) surface will be described. The influence of the annealing temperature on the formation of hybrid PTCDI-NaCl nanoarchitecture is also investigated in this chapter.

4.1 Sodium Chloride on Au(111)

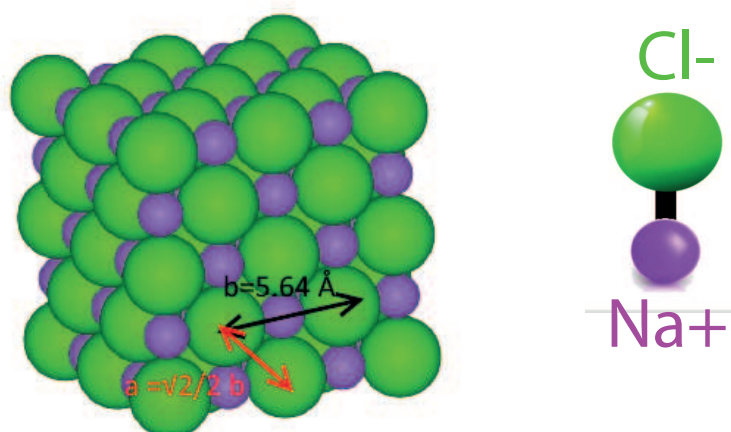


Figure 4.1: (a) Ball and stick model of sodium chloride crystal with face centered cubic lattice. Sodium (Na^+) ions are purple and chlorine (Cl^-) ions are green. The lattice constant is $b = 5.64 \text{ \AA}$.

4. ENGINEERING OF NEW PTCDI-NACL HYBRID IONIC-ORGANIC NANOSTRUCTURES

Sodium Chloride is an ionic compound of chemical formula NaCl, representing a 1 to 1 ratio of positively charged sodium and negatively charged chloride ions. In the bulk phase, NaCl crystallizes in a face-centered cubic (fcc) lattice with a lattice constant of 5.64 Å (Figure 4.1). Within the fcc lattice, the first ion is located at each lattice point whereas the counter ion is located halfway between lattice points along the fcc unit cell edge. Each ion is thus surrounded by six oppositely charged ions. The equivalent (100), (010) and (001) planes of the NaCl crystal are electronically neutral because they possess the same number of Na⁺ and Cl⁻ ions. Bulk sodium chloride is an electric insulator with a bandgap of 8.97 eV. However, NaCl can be imaged with Scanning Tunneling Microscopy when deposited at low thickness on metallic surface.

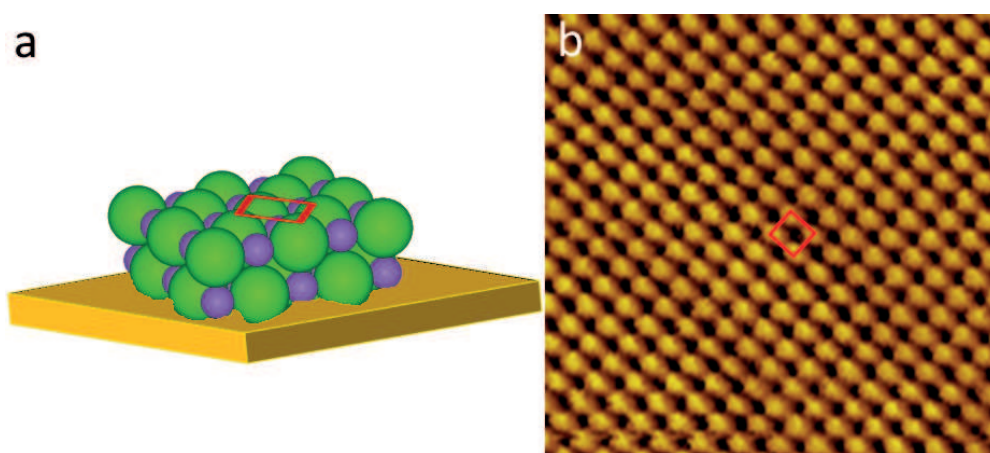


Figure 4.2: (a) Scheme and (b) atomic resolution STM image of a sodium chloride bilayer on Au(111) surface. The red square connects four closest chlorine ions. $5 \times 5 \text{ nm}^2$; $V_s = 0.40 \text{ V}$, $I_t = 0.21 \text{ nA}$.

When sodium chloride is evaporated at low coverage on a bare Au(111) surface, it forms square domains that grow preferentially at the step edges of the Au(111) surface. These islands can be observed with STM at reasonably low bias (lower or equal to $2V \ll \text{NaCl band gap}$). This is due to the electronic coupling between the sodium chloride and the surface. This coupling is strong enough to image the NaCl islands with thickness usually up to 3 monolayers. It should be noted that the NaCl islands can grow on both part of the step edges (top and bottom) without being disturbed (Figure 4.3).

Au(111)- $22 \times \sqrt{3}$ herringbone surface reconstruction is still observed meaning that the interaction between the sodium chloride and the atoms of the gold surface are rather small (Figure 4.4). NaCl islands are exhibiting (100) neutral facets as shown on the high resolution STM images (Figure 4.2). It was previously shown by DFT calculations that bright protrusions correspond to chlorine ions whereas dark depressions correspond to

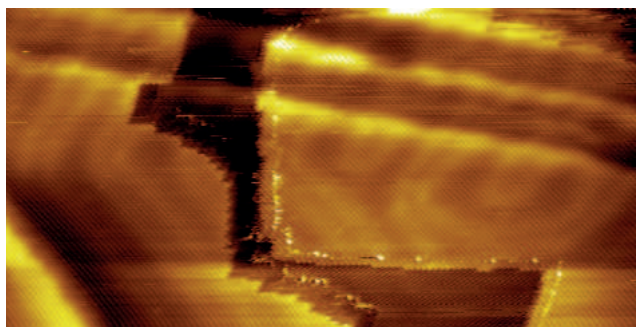


Figure 4.3: *STM image of a sodium chloride bilayer islands on Au(111) crossing the substrate step edges of the substrate. $56 \times 29 \text{ nm}^2$; $V_s = 1.21 \text{ V}$, $I_t = 0.11 \text{ nA}$.*

sodium ions [150, 151]. The lattice constant is measured to be $5.7 \pm 0.1 \text{ \AA}$ and the closest neighbor distance (spacing between two closest Na^+ or Cl^- ions) to be $4.05 \pm 0.1 \text{ \AA}$ on our STM images, very close to the bulk phase value and to other measurements on NaCl on Au(111) surface [152].

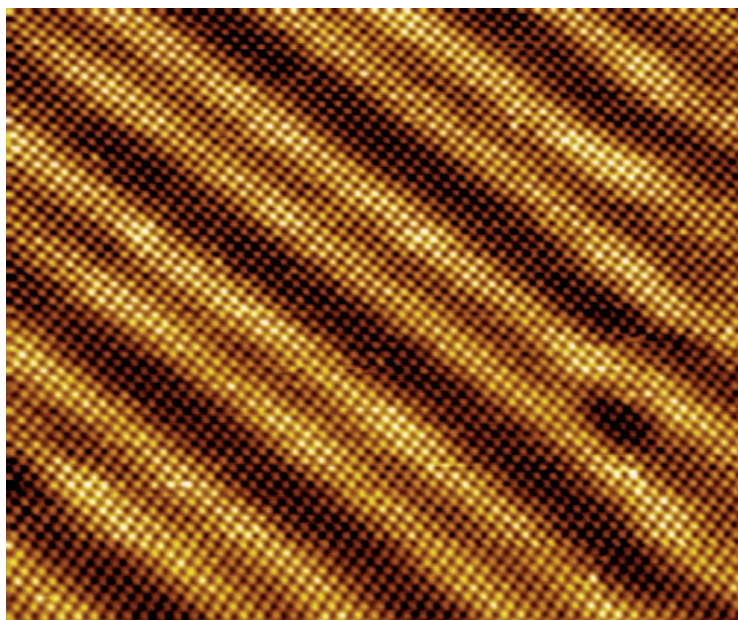


Figure 4.4: *Atomic resolution STM image of a sodium chloride bilayer on Au(111) surface showing the corrugation lines of the underlying substrate. $24 \times 19 \text{ nm}^2$; $V_s = 1.21 \text{ V}$, $I_t = 0.33 \text{ nA}$.*

4.2 Temperature dependent PTCDI-NaCl nanostructures on Au(111)

The idea discussed in the next section is to take advantage of organic-ionic interactions that occur between molecules and ionic salts. As introduced in section 1.1.2.5, ionic-organic interactions are not completely understood and yet not much explored. We have seen in Chapter 3 that PTCDI molecules spontaneously form H-bonded self-assembled organic films on Au(111) surface. Depending on the preparation conditions, adding metal adatoms on the surface will lead to totally different nanoarchitectures stabilized by metal-organic arrangement [153, 154]. As a comparison, the strength of the ionic bond can be ten times higher than H-bond interactions [155]. Among ionic materials, sodium chloride (Figure 4.1) is an attractive system because it can grow as a multilayer film on numerous metal surfaces when sublimated in vacuum [152, 156, 157, 158]. Sodium chloride is often used as a decoupling layer for molecules on metal surfaces. Indeed, the electronic properties of NaCl-supported molecules strongly differ from the properties of molecules directly on metal surface [159, 160]. NaCl can however violently react with polar molecules. H₂O is the archetypal polar molecule, it has a permanent dipole. When H₂O is mixed with NaCl, the positively-charged hydrogen atoms interact with the negatively-charged chloride ions and the negatively-charged oxygen atoms are aligned towards the positively-charged Na ions. This ion-dipole interaction leads to the dissolution of NaCl. Despite the strong NaCl-H₂O interaction, Chen *et al.* showed that a new type of 2D ice structure can grow on NaCl(100) film at low temperature in vacuum [161]. Recent observations in addition revealed that molecule-alkali metal ion interaction can modify 2D supramolecular assembly [43, 44, 45]. The objective of the experiments presented in this chapter is to take advantage on the eventual interactions between PTCDI molecules and sodium chloride to create another organized nanoarchitectures with different structures and electronic properties. We will use the annealing temperature as a parameter to tune the nanoarchitectures structure.

4.2.1 Room temperature deposition: Flower structure

4.2 Temperature dependent PTCDI-NaCl nanostructures on Au(111)

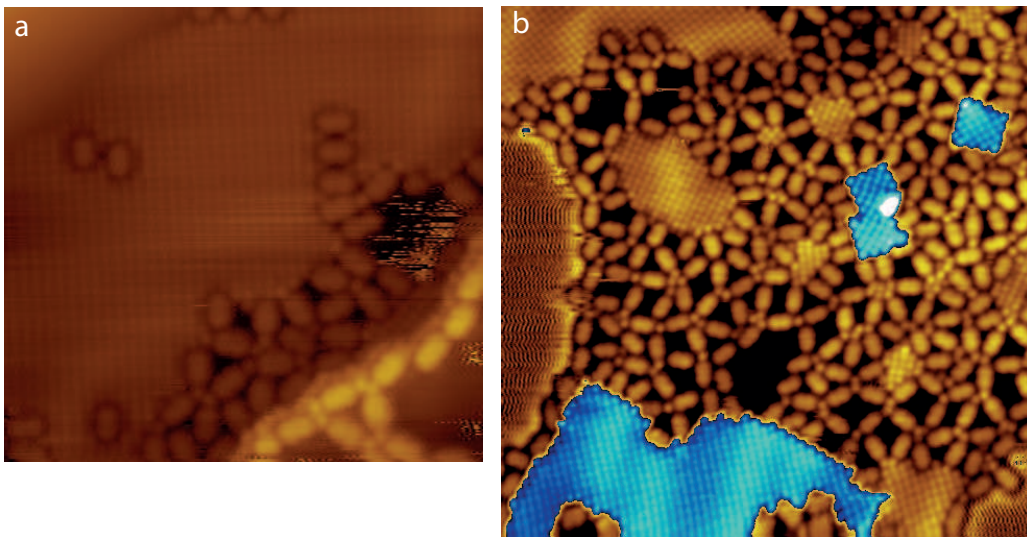


Figure 4.5: *STM images of the PTCDI-NaCl nanoarchitecture after deposition on Au(111)- $22 \times \sqrt{3}$ reconstructed surface at room temperature, $V_s = 1.3$ V, $I_t = 0.18$ nA; (a) PTCDI molecules trapped in NaCl monolayer domains 15×14 nm², (b) PTCDI molecules arranged in flower-like structure (petals: PTCDI, flower center: small NaCl clusters) 24×24 nm².*

4. ENGINEERING OF NEW PTCDI-NACL HYBRID IONIC-ORGANIC NANOSTRUCTURES

The flower pattern is presented in the high resolution STM image in Figure 4.6a. The center of the flower pattern is composed of a small NaCl island. The PTCDI molecules are attached almost perpendicularly to the NaCl island through their short side. This leads to the formation of a molecular flower with a NaCl center and PTCDI molecules as petals (Figure 4.6b).

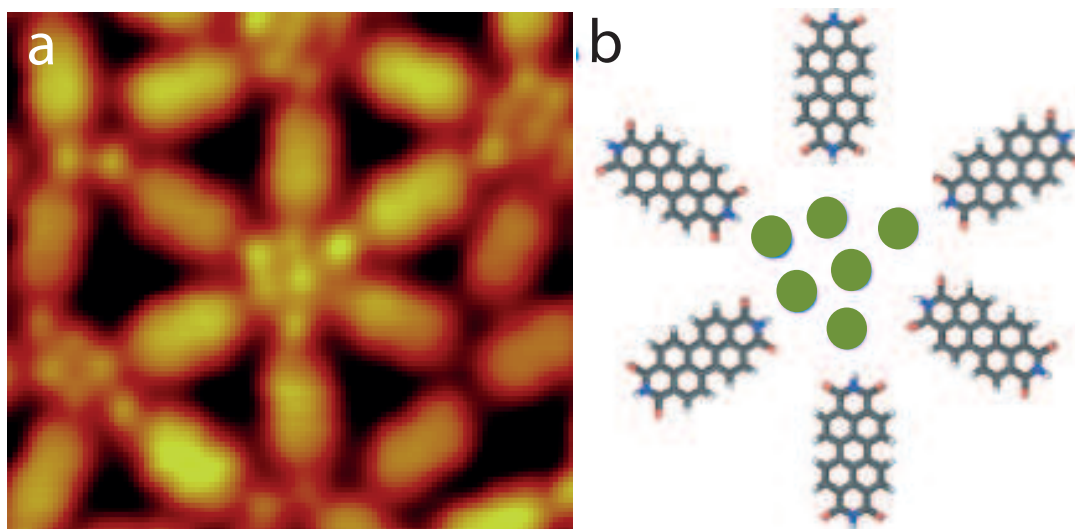


Figure 4.6: (a) High resolution STM image of PTCDI-NaCl flower $V_s = 1.2$ V, $I_t = 0.6$ nA, 5×5 nm² (b) Model of NaCl-PTCDI flower. NaCl dipoles are represented by green circles.

4.2.2 Porous mesh hybrid nanostructure after 100°C annealing

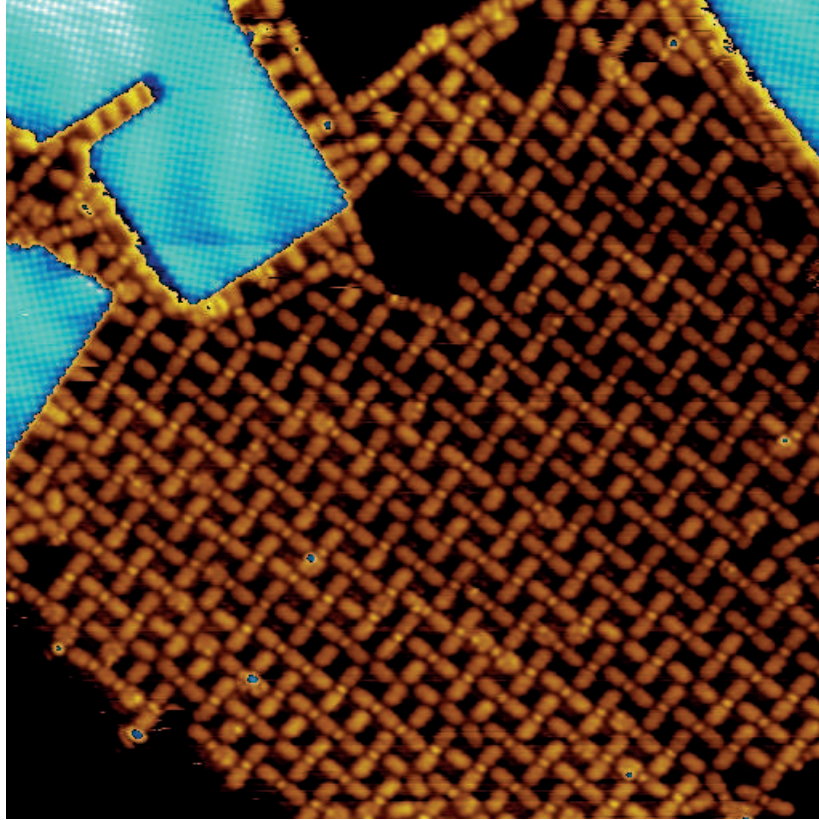


Figure 4.7: *STM image of the PTCDI-NaCl nanoarchitecture after deposition on Au(111)- $(22 \times \sqrt{3})$ at room temperature and post annealing at 100°C. $36 \times 36 \text{ nm}^2$, $V_s = 1.29 \text{ V}$, $I_t = 0.11 \text{ nA}$.*

Temperature is a key parameter that can influence molecular self-assembly [162]. The STM image in Figure 4.7 reveals that PTCDI molecules and NaCl form a new porous “mesh”-nanoarchitecture after annealing the surface at 100 °C for 40 minutes. The small NaCl islands are not visible anymore. NaCl now appears as a single round spot (Figure 4.8a), suggesting it corresponds to a single NaCl dimer. The network unit cell of this porous structure is a rectangle with 2.3 nm and 2.5 nm unit cell constants and an angle of $\sim 90^\circ$ between the axes. The model of this porous structure is presented in the Figure 4.8b.

The building block of this nanoarchitecture is a PTCDI \cdots NaCl \cdots PTCDI stick (Figure 4.9c). The two PTCDI molecules are aligned along their main axis and the NaCl dimer is connected the molecular imide group. This building block is highlighted by dotted ellipses in the model presented in Figure 4.8b. Neighboring PTCDI \cdots NaCl \cdots PTCDI sticks are almost perpendicular to each other in the “mesh”-nanoarchitecture (Figure 4.8).

4. ENGINEERING OF NEW PTCDI-NACL HYBRID IONIC-ORGANIC NANOSTRUCTURES

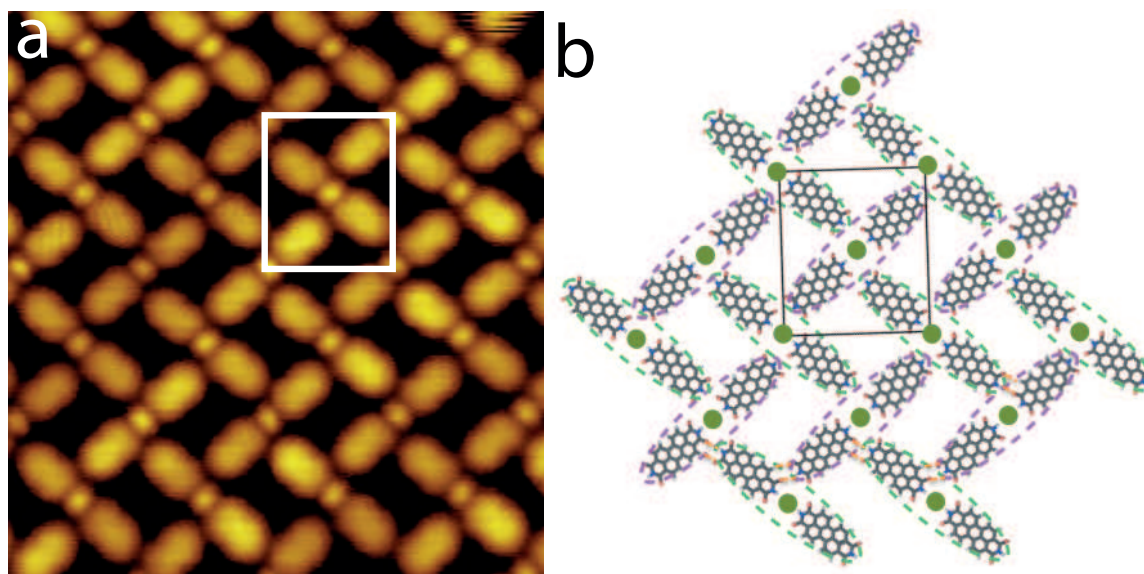


Figure 4.8: (a) STM image of the PTCDI-NaCl nanoarchitecture after deposition on $Au(111)-22 \times \sqrt{3}$ at room temperature and post annealing at 100°C $9 \times 11 \text{ nm}^2$; $V_s = 0.60 \text{ V}$, $I_t = 0.18 \text{ nA}$. (b) Model of the Mesh-nanoarchitecture. (NaCl dipoles are represented by green circles).

The angle between neighboring sticks is in fact $\sim 80^\circ$. Neighboring PTCDI-NaCl sticks appear to be preferentially connected through $\text{N-H} \cdots \text{O}$ and $\text{H} \cdots \text{O}$ bonds between PTCDI molecules (Figure 4.9).

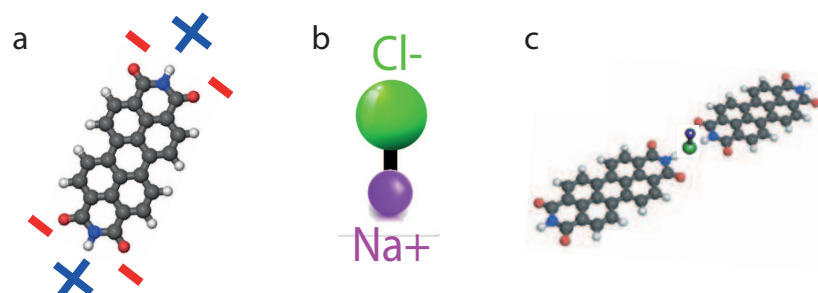


Figure 4.9: (a) Charge distribution and scheme of PTCDI. Gray balls are carbon atoms, red balls are oxygen atoms, white balls are hydrogen atoms, and blue balls are nitrogen atoms. (b) Sodium chloride dimer (c) Scheme of $\text{PTCDI} \cdots \text{NaCl} \cdots \text{PTCDI}$ stick (perspective).

4.2.3 Hybrid ladder and chain structures after 150°C annealing

After annealing the surface at 150 °C for 40 minutes, the STM image shows that PTCDI and NaCl self-assemble into a new epitaxial “ladder”-nanoarchitecture (Figure 4.11a). This structure is composed of parallel PTCDI···NaCl-dimer straight chains (NaCl-dimers appear as round spots in the STM image). In this structure, the neighboring PTCDI-NaCl chains are separated by single PTCDI molecules oriented almost perpendicularly to the chain direction. This “ladder” structure is very similar to the structure that is observed only very locally with pristine PTCDI molecules (Figure 3.6b and Figure 3.4a).

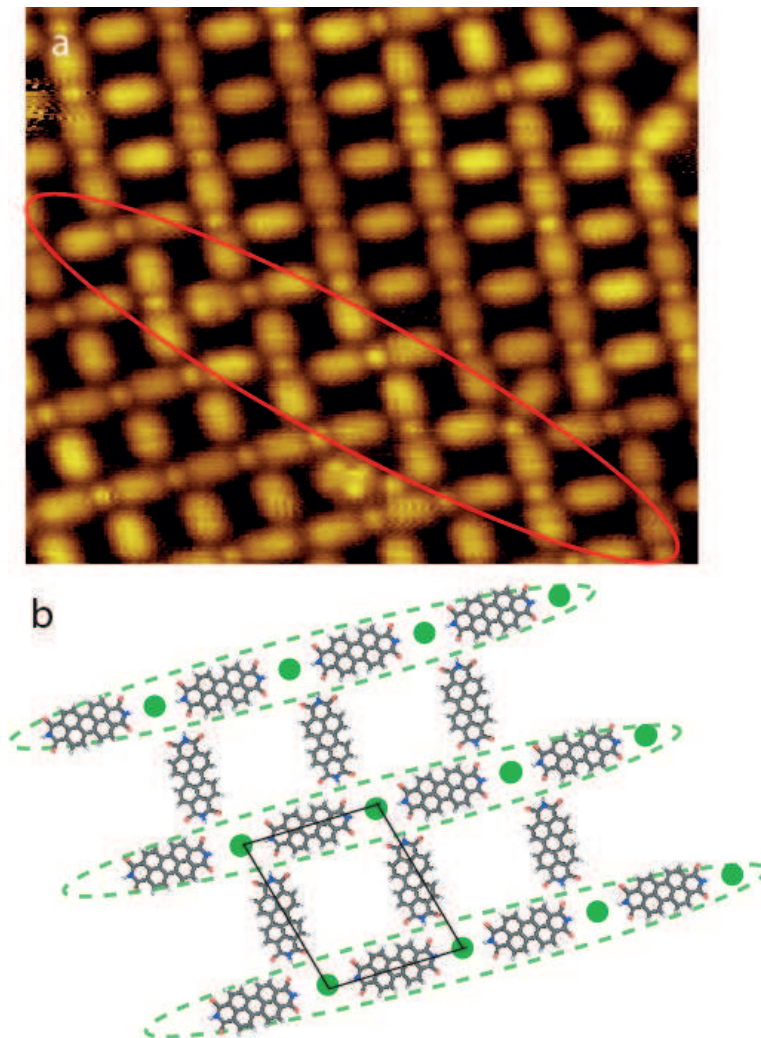


Figure 4.10: (a) STM image of the PTCDI-NaCl “ladder” nanoarchitecture. Local mesh nanoarchitecture is observed at the domain boundary, $12 \times 10 \text{ nm}^2$; $V_s = 1.3 \text{ V}$, $I_t = 0.08 \text{ nA}$. (b) Model of the ladder-nanoarchitecture. NaCl dipoles are represented by green circles.

4. ENGINEERING OF NEW PTCDI-NACL HYBRID IONIC-ORGANIC NANOSTRUCTURES

The “rung” PTCDI molecules are oriented almost perpendicularly to the PTCDI chain molecules to promote double H-bonds. The network unit cell of this porous structure is a parallelogram with 1.5 nm and 2.0 nm unit cell constants and an angle of $\sim 105^\circ$ between the axes. The model of this nanoarchitecture is presented in Figure 4.11b. The parallel PTCDI \cdots NaCl-dimer chains are highlighted by dotted ellipses. Ladder structure with different orientation are observed. Local “mesh” structure is observed at the boundary between two domains. This local mesh structure is highlighted by a red ellipse on the STM image (Figure 4.10a). Due to the geometry constraints of the mesh structure (sticks are almost perpendicular to each other), the ladder structure orientation appears to rotate of $\sim 90^\circ$ at the domain boundary.

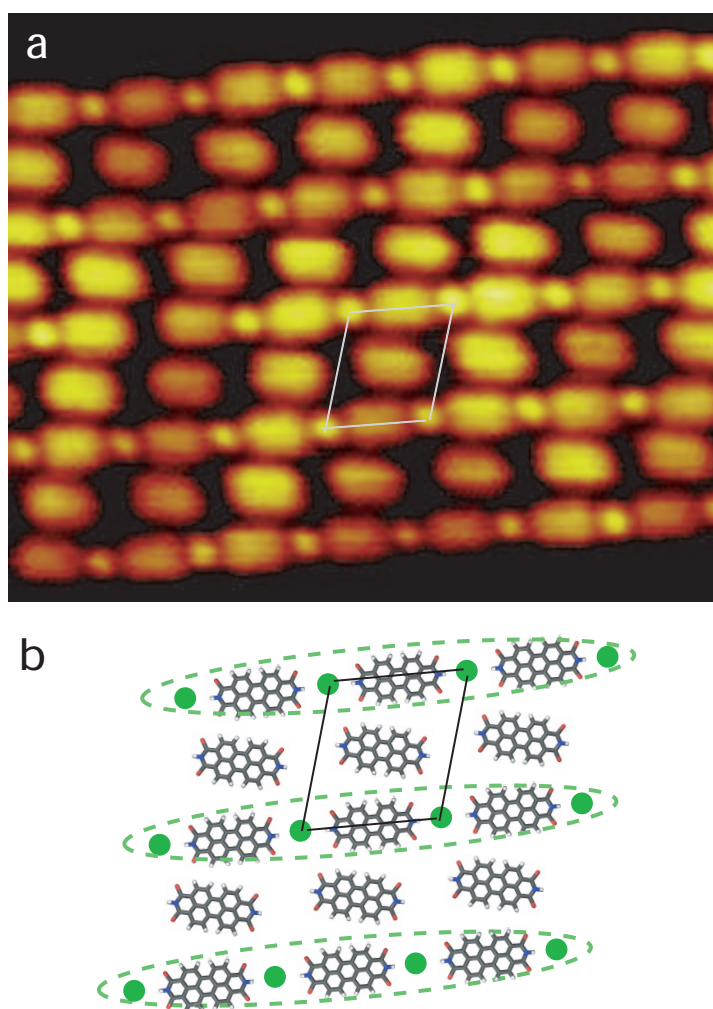


Figure 4.11: (a) STM image of the PTCDI-NaCl nanoarchitecture after deposition on $Au(111)-(22 \times \sqrt{3})$ reconstructed surface at room temperature and post annealing at 150°C , $10 \times 8 \text{ nm}^2$; $V_s = 1.9 \text{ V}$, $I_t = 0.2 \text{ nA}$. (b) Model of the chain-nanoarchitecture. NaCl dipoles are represented by green circles.

4.2 Temperature dependent PTCDI-NaCl nanostructures on Au(111)

Another kind of nanoarchitecture is observed after annealing the surface at 150 °C. The STM image shows that PTCDI and NaCl self-assemble into a “chain”-nanoarchitecture (Figure 4.11a). This structure is composed of parallel PTCDI \cdots NaCl-dimer straight chains. Neighboring PTCDI-NaCl chains are separated by a single PTCDI chain. The molecules are rotated within the PTCDI chains (12°) to promote hydrogen bonding (O \cdots H-C) with the PTCDI molecules of the neighboring PTCDI \cdots NaCl chains. The network unit cell of this porous structure is a parallelogram with 1.5 nm and 1.7 nm unit cell constants and an angle of $\sim 74^\circ$ between the axes. The model of this nanoarchitecture is presented in Figure 4.11b. The parallel PTCDI \cdots NaCl-dimer chains are highlighted by dotted ellipses.

In the previous chapter, it was shown that the ladder structure was less stable than the H-bonded chain structure. Consequently, the “ladder” nanoarchitecture can be interpreted as an intermediate structure in the phase transition between the mesh nanoarchitecture and the “chain” structure. The ladder structure combines the PTCDI perpendicular orientation of the mesh nanoarchitecture with the PTCDI-NaCl chains of the hybrid parallel “chain” structure. NaCl-PTCDI nanoarchitectures are coexisting with PTCDI films (NaCl islands) when PTCDI (NaCl) is in excess, respectively.

4.2.4 Investigation on the PTCDI-NaCl interactions

STM reveals that the subsequent deposition of NaCl on the Au(111) surface covered with a PTCDI layer leads to the formation of two-dimensional hybrid nanoarchitectures. NaCl essentially forms small islands in the organic layer when deposited on the surface at room temperature. NaCl also appears locally as single and paired round spots in the STM images (Figure 4.5b). There is no evidence of segregation of Na and Cl ions into Na or Cl-rich overlayer in the STM images at room temperature or after annealing. The bright spots localized in the gap between PTCDI molecules (Figures 4.7, 4.11, 4.10a) and in the NaCl islands (Figure 4.6) have similar contrast in the STM images. These are the reasons why NaCl single bright spots are attributed to single NaCl dimers, with Cl ions adsorbed on the surface. The NaCl dimers appear to break the known PTCDI 2D H-bonded self-assembled structures [131]. The dimers form small 2D clusters in the organic layer at room temperature.

The PTCDI molecules are arranged perpendicularly to NaCl islands, *i.e.* molecular imide group is connected to the edges of NaCl clusters. Indeed, the STM images (Figure 4.12) show that PTCDI molecules are aligned with the bright spots (position of Cl ions) of the NaCl single-layer island ((Figure 4.12a). In contrast PTCDI molecules are aligned with the junction between two bright spots (position of Na ions) of NaCl

4. ENGINEERING OF NEW PTCDI-NACL HYBRID IONIC-ORGANIC NANOSTRUCTURES

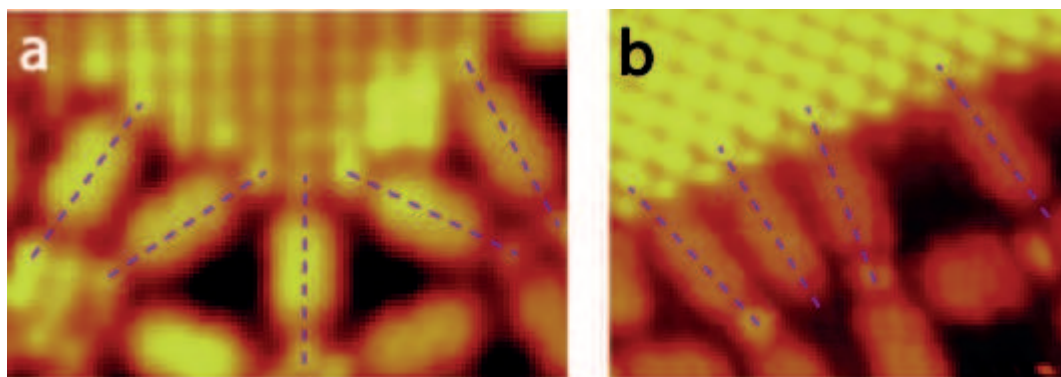


Figure 4.12: *STM images of PTCDI-NaCl island boundary. (a) NaCl single layer island $5 \times 3 \text{ nm}^2$; $V_s = 1.2 \text{ V}$, $I_t = 0.6 \text{ nA}$. (b) NaCl double-layer island, $5 \times 4 \text{ nm}^2$; $V_s = 1.3 \text{ V}$, $I_t = 0.18 \text{ nA}$. The molecular axis (dotted purple line) is superimposed to the STM image as a guide for the eyes.*

double-layer islands (Figure 4.12b). Surface post-annealing at 100°C leads to the dissociation of NaCl islands into NaCl dimers. At high temperature NaCl dimers are trapped between two imide groups of PTCDI. This results into the formation of straight PTCDI \cdots NaCl \cdots PTCDI sticks (Figure 4.9c). These sticks self-assemble almost perpendicularly into a porous mesh-structure at 100°C . Stick \cdots stick binding appears to be stabilized by double H-bonds (O \cdots H-C) between neighboring PTCDI molecules (Figure 4.8). At higher temperature the PTCDI-NaCl mesh-nanoarchitecture collapses to form new arrangements. PTCDI and NaCl dimers are then arranged sequentially along straight chains. These PTCDI-NaCl chains are separated by single PTCDI chains (Figure 4.11) or perpendicular molecules (Figure 4.10). The ladder structure appears as a phase transition structure between the mesh and the chain structure. In the chain structure, the PTCDI molecules are not perpendicular anymore. The chain-nanoarchitecture has a higher density ($1 \text{ mol./}128 \text{ \AA}^2$) than the mesh-structure ($1 \text{ mol./}144 \text{ \AA}^2$).

PTCDI molecules and NaCl strongly interact together to form 2D hybrid nanoarchitectures. The PTCDI skeleton has a non-uniform internal charge distribution. The oxygen atoms of the imide groups carry a negative partial charge whereas the N-H groups carry a positive partial charge (Figure 4.9a). The complementary charge distribution of NaCl-dimer and PTCDI appears to be at the origin of the long range self-assembly of these two building blocks (Figure 4.9c). The STM images show that NaCl-dimers and PTCDI molecules are aligned along the main molecular axis, *i.e.* NaCl-dimers are connected to molecular imide groups. Such interaction was not observed when mixing NaCl with PTCDA (3,4,9,10-perylene-tetracarboxylic-dianhydride) [163]. PTCDA shares the same skeleton as PTCDI except that each PTCDI N-H group is replaced by a single oxygen

4.2 Temperature dependent PTCDI-NaCl nanostructures on Au(111)

atom in PTCDA. This means that PTCDI N-H group is at the origin of PTCDI \cdots NaCl binding. STM images show that the PTCDI \cdots NaCl interaction is highly directional and selective. Previous calculations suggested that NaCl chlorine atoms appears brighter than Na atoms in the STM images [150, 151]. The STM images presented in Figure 4.6, Figure 4.8, Figure 4.11, Figure 4.10, therefore reveal that the NaCl-PTCDI nanoarchitectures are stabilized by electrostatic interactions between the positively charged PTCDI N-H group and the negatively charged Cl $^-$ ion of NaCl dimer. The Cl $^-$ ion appears to accept the binding of one to two N-H groups. This leads to arrangement of PTCDI and NaCl dimers into straight sticks or chains. The mesh, ladder and chain NaCl-PTCDI nanoarchitectures are both resulting from the assembly of a 2-fold coordination motif (PTCDI \cdots NaCl-dimer \cdots PTCDI (Figure 4.9)). These nanoarchitectures appear also to be stabilized by H-bonds between neighboring PTCDI molecules. The STM observations show that the NaCl \cdots PTCDI interactions are strong enough to stabilize the formation of porous nanoarchitectures at room temperature.

Chapter conclusion

In summary, we used scanning tunneling microscopy to investigate the interaction between PTCDI molecules and NaCl in vacuum. STM reveals that PTCDI and NaCl self-assemble on Au(111) and form different hybrid two-dimensional nanoarchitectures depending on the annealing temperature. Non-periodic flower structures consisting in NaCl center and PTCDI petals were formed after deposition at room temperature. A mesh structure consisting in an alternation of PTCDI \cdots NaCl-dimer \cdots PTCDI dimers in two directions is formed after annealing at 100 °C. After annealing at 150 °C, a “ladder” and a “chain” structure, both based on PTCDI-NaCl sticks were formed. Atomic resolution STM images reveal the ion location in these hybrid nanoarchitectures. We found that the organic-ionic interactions between PTCDI and NaCl originate from the electrostatic interaction between negatively charged chlorine ions and positively charged PTCDI N-H groups. These structures are also stabilized by H-bonds. This system is a promising alternative to metal-organic and multicomponent organic structures to engineer novel nanoarchitectures on surfaces.

4. ENGINEERING OF NEW PTCDI-NACL HYBRID IONIC-ORGANIC NANOSTRUCTURES

Chapter 5

On-surface synthesis of 2D covalent organic structures versus halogen-bonded self-assembly: competing formation of organic nanoarchitectures

In chapter 3 and 4, examples of nanostructure engineering based on molecular self-assembly stabilized by H-bonds or ionic-organic interactions were reported. Engineering nanostructures with higher stability can also be required. Given the energy range of intermolecular interactions involved in the self-assembly process, covalent bonds formation appear as an alternative to engineer 2D nanostructures with higher binding energy. In section 1.1.2.6, we have seen that several on-surface reactions can be used to build C-C covalent bonds. In this chapter, we will investigate the Ullmann on-surface reaction of an iodinated star-shaped molecule.

The objective of this chapter is to demonstrate the influence of the precursor diffusion on the competition between X-bonded self-assembly and on-surface Ullmann reaction. The system studied here consists in star-shape molecular precursors with terminal iodine atoms evaporated on Au(111) surface. Systems with increasing precursor coverage (up to more than one monolayer) will be investigated using STM.

It was shown in section 1.3 that molecules with peripheral halogen atoms are promising organic building blocks to engineer different types of two-dimensional porous carbon-nanoarchitectures. The molecular halogen atoms (X) can stabilize highly ordered organic nanoarchitectures through the formation of intermolecular halogen bonds [26, 27, 28,

5. ON-SURFACE SYNTHESIS OF 2D COVALENT ORGANIC STRUCTURES VERSUS HALOGEN-BONDED SELF-ASSEMBLY: COMPETING FORMATION OF ORGANIC NANOARCHITECTURES

29, 30] (section 1.1.2.3). Halogen-bonded self-assembled nanoarchitectures have been successfully created using molecules with bromine [31, 32, 33, 34] and iodine substituents [35].

In addition, these building blocks can also be used to engineer covalent nanoarchitectures taking advantage of on-surface polymerization. 2D covalent-nanoarchitectures have been fabricated using molecules with bromine atoms [28, 50, 54, 76, 97, 164, 165] as well as molecules with iodine atoms [28, 89, 166, 167]. However, the competing formation of halogen-bonded nanoarchitectures and covalent structures on catalytically active metal surfaces has still to be elucidated to optimize the formation of one specific type of organic structure. This is essential for example to trigger the formation of porous graphene-nanoarchitectures over the formation of self-assembled halogen-bonded films at room temperature.

The chemical structure of the 1,3,5-Tris(4-iodophenyl)benzene (TIPB) molecule is presented in Figure 5.1a. This 3-fold symmetry molecule is a star-shaped molecule. The molecular skeleton consists of a central benzene ring connected to three peripheral 4'-iodophenyl groups. Two molecules are expected to form a covalent dimer (Figure 5.1b) on metal surface through surface-assisted Ullmann coupling.

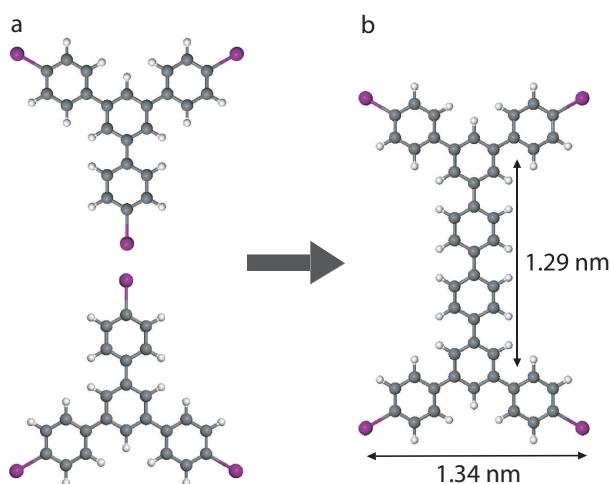


Figure 5.1: Scheme of 1,3,5-Tris(4-iodophenyl)benzene ($C_{21}H_{15}I_3$) dimer building block. Carbon atoms are gray, iodine atoms purple, hydrogen atoms white.

5.1 Low coverage ($<0.2\text{ML}$) deposition at room temperature: porous covalent nanostructure

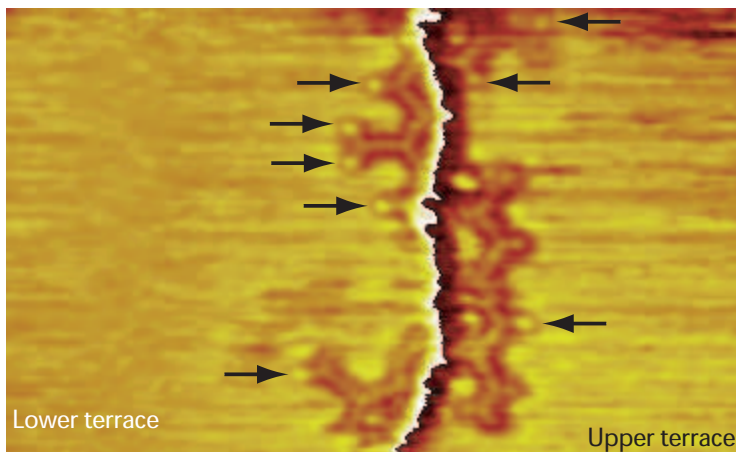


Figure 5.2: *STM image of the initial growth of the organic layer after low concentration deposition (less than 0.02 monolayer (ML)) on Au(111)- $22 \times \sqrt{3}$; $22 \times 12 \text{ nm}^2$, $V_s = 0.9 \text{ V}$, $I_t = 20 \text{ pA}$.*

The Figure 5.2 shows the Au(111) surface after low coverage deposition (less than 0.02 monolayer (ML)) of 1,3,5-Tris(4-iodophenyl)benzene (TIPB) molecules¹. The STM image reveals that molecules preferentially adsorb at the gold step edges. The molecules form small zig-zag chains on each side of the step edge. The center-to-center distance of adjacent molecules is $1.3 \pm 0.1 \text{ nm}$. This indicates intermolecular covalent bonding (Figure 5.1b). Bright spots can be observed at the apex of molecular arms (highlighted by black arrows in Figure 5.2). It has been previously experimentally observed with STM that halogen atoms, such as bromine and iodine, appear brighter than molecular carbon atoms [35, 168]. These bright spots therefore reveal that molecular iodine atoms are not systematically dissociated from molecular skeleton when molecules are adsorbed on the Au(111) surface at room temperature, in contradiction with previous reports [98, 165, 167].

¹Experiments were performed in a ultrahigh vacuum (UHV) chamber at a pressure of 10^{-8} Pa . The Au(111) surface was sputtered with Ar^+ ions and then annealed in UHV at 600°C for 1 hour. 1,3,5-Tris(4-iodophenyl)benzene molecules (90%, Aldrich) (Figure 5.1a), were evaporated at 180°C and deposited on the gold surface. Cut Pt/Ir tips were used to obtain constant current STM images at room temperature with a bias voltage applied to the sample. STM images were processed and analyzed using the home made FabViewer application [149].

5. ON-SURFACE SYNTHESIS OF 2D COVALENT ORGANIC STRUCTURES VERSUS HALOGEN-BONDED SELF-ASSEMBLY: COMPETING FORMATION OF ORGANIC NANOARCHITECTURES

STM images of the surface step edges after 0.10 ML deposition are presented in Figure 5.3a,b. The STM images show that small porous structures are growing from the Au(111) step edges to the surface terraces. The STM images also reveal that bright spots are now adsorbed on the step edges. This is particularly obvious in the high resolution STM image in Figure 5.3b. Free iodine adatoms generated during the polymerization of molecular building blocks appear to preferentially adsorb on the Au(111) step edges.

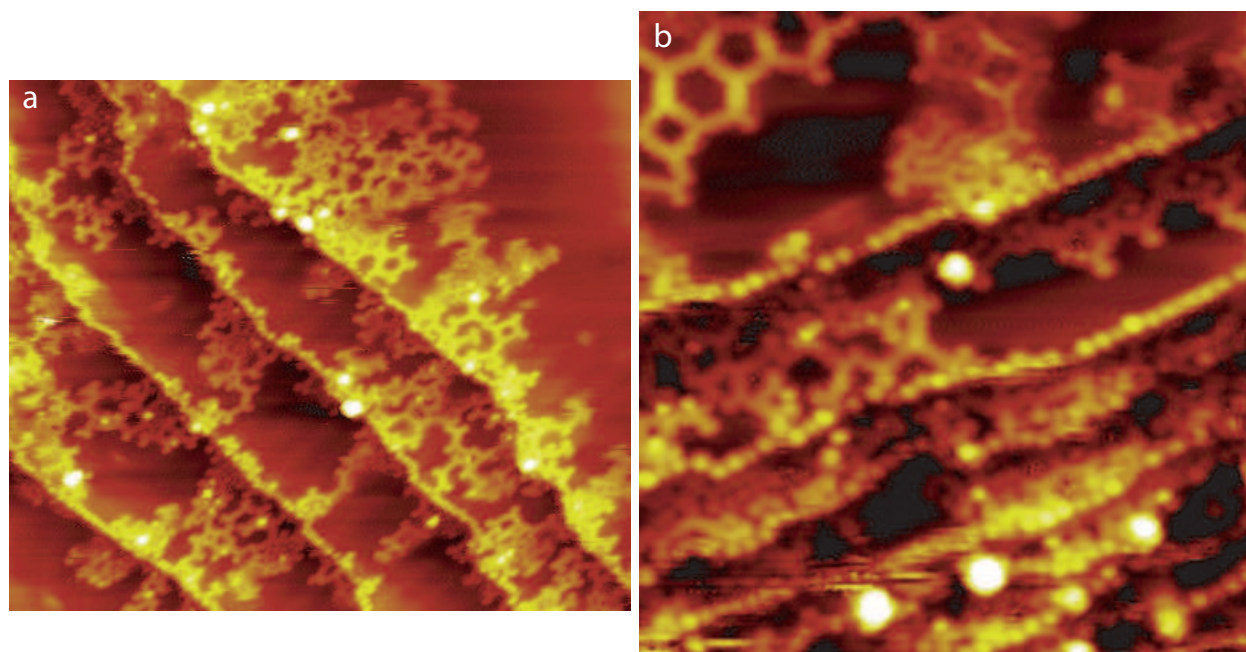


Figure 5.3: *STM images of the initial growth of the organic layer after low concentration deposition (0.1 monolayer (ML)) on Au(111)- $22 \times \sqrt{3}$. (a) $45 \times 38 \text{ nm}^2$, $V_s = 1.3 \text{ V}$, $I_t = 205 \text{ pA}$, (b) $20 \times 20 \text{ nm}^2$, $V_s = 1.3 \text{ V}$, $I_t = 245 \text{ pA}$.*

Figure 5.4 shows that small covalent porous structures are locally observed at the elbows of the gold herringbone reconstruction for 0.10 ML deposition. The formation of covalent structures appears however to be quite limited. Only one or two covalent cycles are usually observed in the elbows of the Au(111) herringbone surface reconstruction.

Above 0.1 monolayer deposition, a 2D porous nanoarchitecture is observed on the surface. This structure is composed of organic pores (Figure 5.5 and Figure 5.6a-f) and zig-zag chains (Figure 5.6g). The pores adopt a polygonal geometry. Tetragonal, pentagonal, heptagonal and octagonal cavities are mainly composing the organic structure, (Figure 5.6b-f). The measured center-to-center distance of the star-shape molecular building block is $1.3 \pm 0.1 \text{ nm}$. This reveals that the molecules are covalently linked through the dehalogenation of the molecular peripheral iodine atoms. The images in Figure 5.5b and

5.1 Low coverage ($<0.2\text{ML}$) deposition at room temperature: porous covalent nanostructure

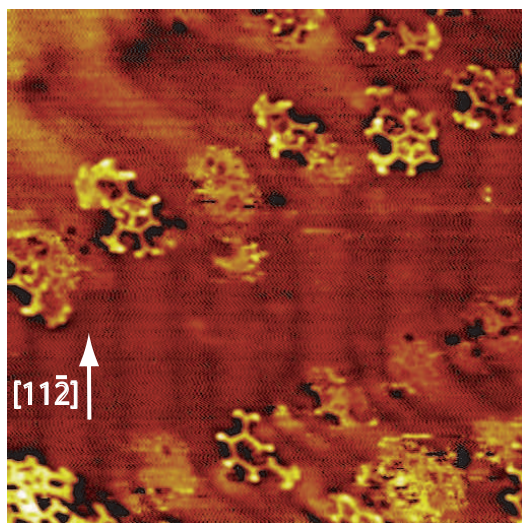


Figure 5.4: *STM image of the initial growth of the organic layer after low concentration deposition (0.1 monolayer (ML)) on the elbows of the Au(111)- $22 \times \sqrt{3}$. $36 \times 36 \text{ nm}^2$, $V_s = 1.3 \text{ V}$, $I_t = 205 \text{ pA}$.*

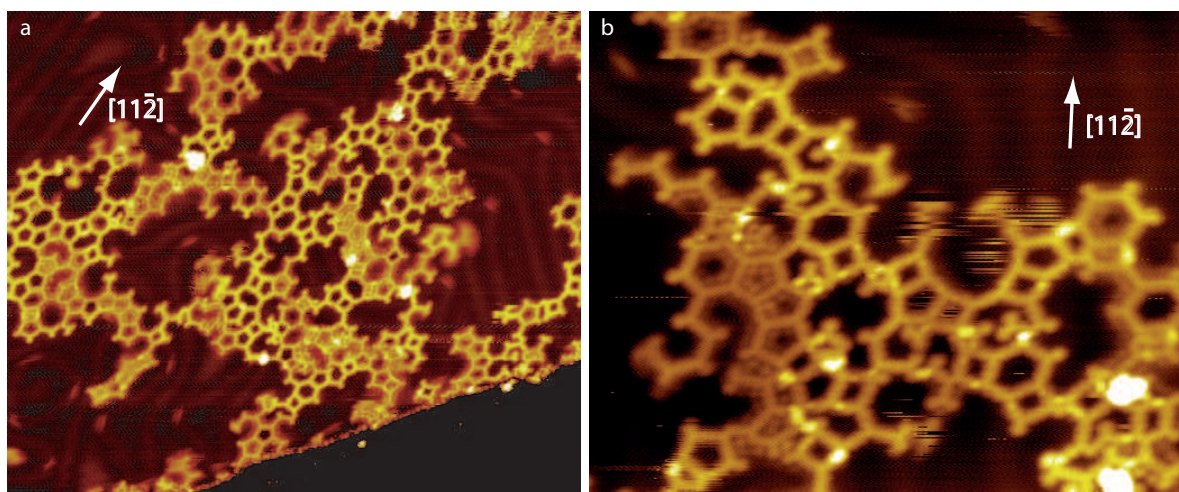


Figure 5.5: *STM images of the 1,3,5-Tris(4-iodophenyl)benzene self-assembled covalent porous nanoarchitecture on Au(111), (a) Large scale $50 \times 29 \text{ nm}^2$, $V_s = 0.9 \text{ V}$, $I_t = 20 \text{ pA}$ and (b) detailed structure $24 \times 19 \text{ nm}^2$, $V_s = 1.36 \text{ V}$, $I_t = 20 \text{ pA}$.*

Figure 5.6a are in addition showing that iodine adatoms are sometimes trapped inside the polygonal cavities of the covalent nanoarchitecture.

5. ON-SURFACE SYNTHESIS OF 2D COVALENT ORGANIC STRUCTURES VERSUS HALOGEN-BONDED SELF-ASSEMBLY: COMPETING FORMATION OF ORGANIC NANOARCHITECTURES

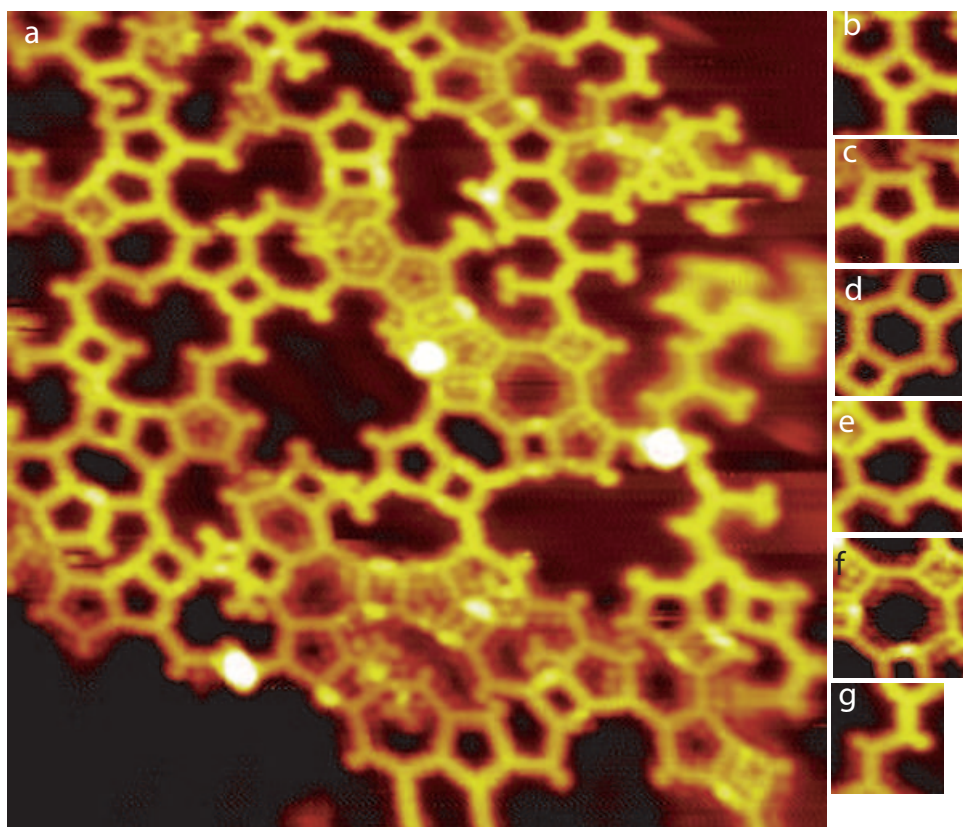


Figure 5.6: (a) STM image ($75 \times 60 \text{ nm}^2$, $V_s = 1.0 \text{ V}$, $I_t = 25 \text{ pA}$) of the 1,3,5-Tris(4-iodophenyl)benzene covalent porous nanoarchitecture on Au(111) with different pore geometry. (b) $3 \times 3 \text{ nm}^2$, (c) $3 \times 3 \text{ nm}^2$, (d) $3 \times 3 \text{ nm}^2$, (e) $3 \times 3 \text{ nm}^2$, (f) $3 \times 3 \text{ nm}^2$, (g) $3 \times 3 \text{ nm}^2$.

5.2 Submonolayer coverage ($0.2\text{ML} < C < 1\text{ML}$): unexpected halogen-bonded network growth

The STM images in Figure 5.7 and Figure 5.8 show TIPB molecular self-assembly on the Au(111) $-22 \times \sqrt{3}$ surface terraces above 0.2 monolayer deposition. Molecules now form small well-organized domains trapped between the gold reconstruction lines (Figure 5.7a,b). Ordered bright features can be observed inside the molecular domains. The size of the domain is increasing with molecular concentration. Molecular covalent structures can be observed at the edge of these molecular domains (Figure 5.7c). For one monolayer deposition (1 ML), the whole Au(111) surface is covered as shown in Figure 5.8. Different organic networks are coexisting, *i.e.* different bright patterns can be observed in the organic layer (Figure 5.7c and Figure 5.8). The bright patterns can adopt a well-

5.2 Submonolayer coverage ($0.2\text{ML} < C < 1\text{ML}$): unexpected halogen-bonded network growth

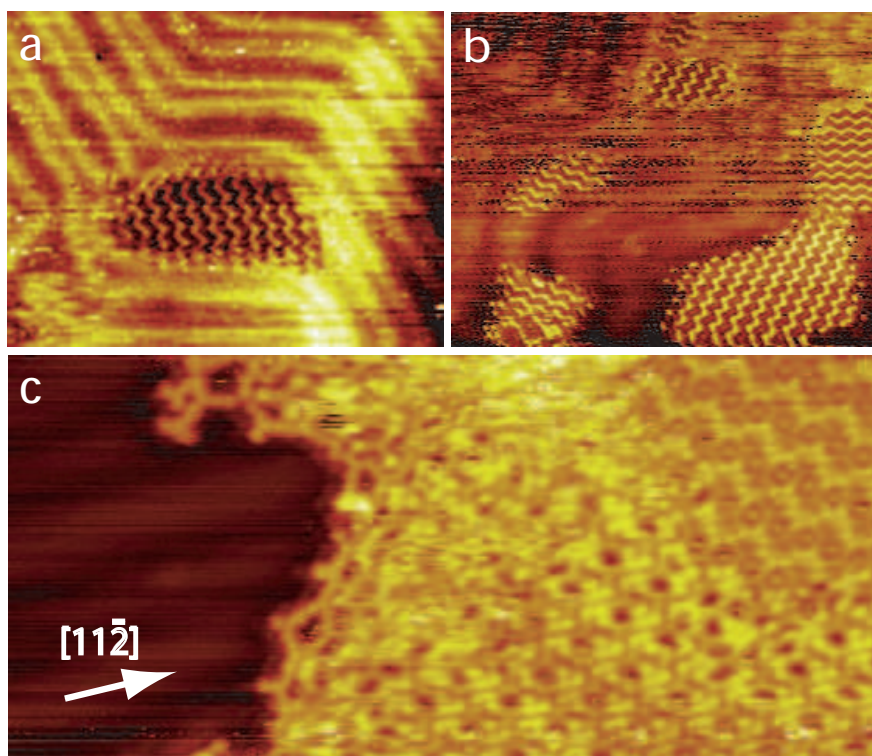


Figure 5.7: *STM images of the Au(111) terraces at increasing molecular coverage (a) $40 \times 31 \text{ nm}^2$, $V_s = 2.2 \text{ V}$, $I_t = 55 \text{ pA}$, (b) $50 \times 35 \text{ nm}^2$, $V_s = 2.2 \text{ V}$, $I_t = 55 \text{ pA}$, (c) $26 \times 12 \text{ nm}^2$, $V_s = 0.9 \text{ V}$, $I_t = 245 \text{ pA}$.*

ordered sine-wave (Figure 5.9) or a bow-tie structure (Figure 5.11). The boundaries of the molecular network appear in comparison quite defective.

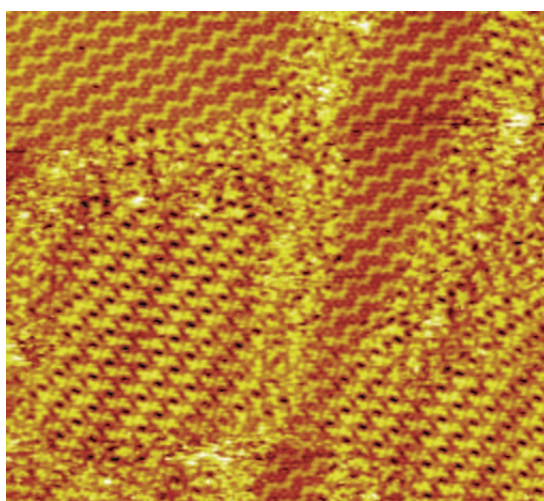


Figure 5.8: *STM image of the Au(111) surface for a TIPB coverage of around one monolayer, $36 \times 36 \text{ nm}^2$, $V_s = 0.6 \text{ V}$, $I_t = 245 \text{ pA}$.*

5. ON-SURFACE SYNTHESIS OF 2D COVALENT ORGANIC STRUCTURES VERSUS HALOGEN-BONDED SELF-ASSEMBLY: COMPETING FORMATION OF ORGANIC NANOARCHITECTURES

5.2.1 Sine-wave X-bonded structure

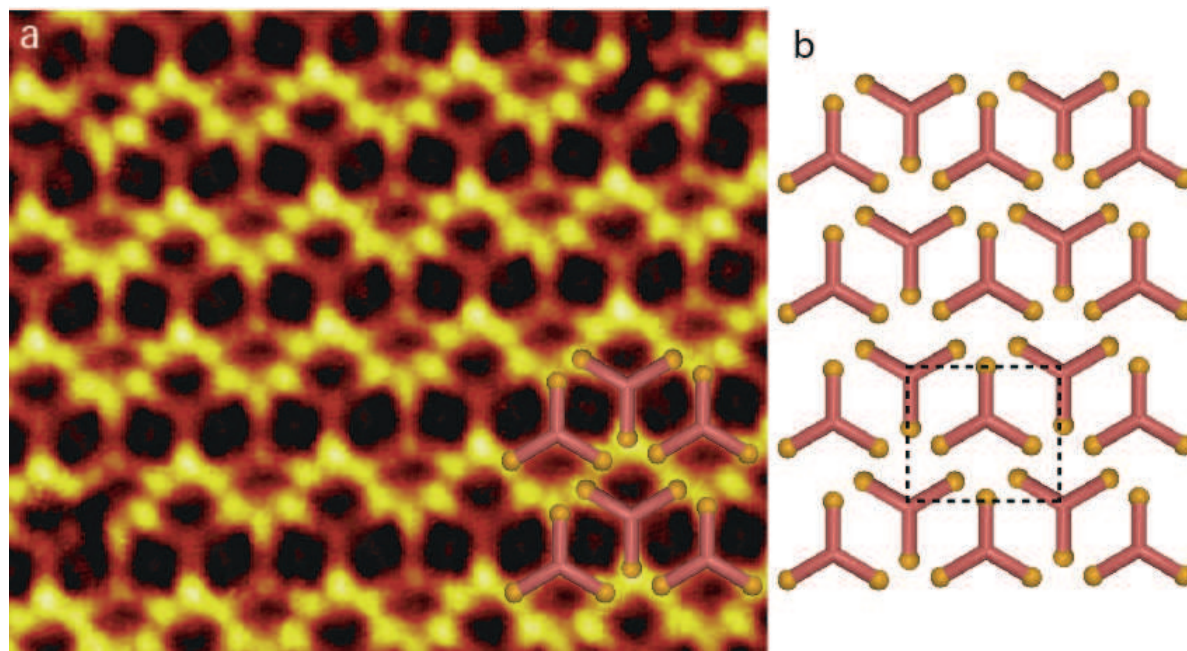


Figure 5.9: (a) High resolution STM image of the 1,3,5-Tris(4-iodophenyl)benzene sine-wave nanoarchitecture, $10 \times 8 \text{ nm}^2$, $V_s = 1.0 \text{ V}$, $I_t = 23 \text{ pA}$. (b) Model of the organic nanoarchitecture. Molecular skeleton is represented by an orange star and the iodine atoms are represented by yellow balls. The network unit cell is represented by a dotted black rectangle.

Figure 5.9a shows a high resolution STM image of the sine-wave organic nanoarchitecture observed in Figures 5.7. The STM image reveals that the molecules are self-assembled into an ordered porous structure on the surface. Neighboring side-by-side molecules are rotated by an angle of 180° , as it is highlighted by the molecular schemes superimposed to the STM image in Figure 5.9a. The molecular iodine atoms appear brighter than molecular carbon skeleton in the STM image. The bright sine-wave pattern results from the local arrangement of molecular iodine atoms. Each bright wave corresponds to an infinite iodine synthon X_∞ . The STM images presented in Figures 5.10 are showing that some molecular arms are locally dehalogenated. This does not affect the structure of the organic nanoarchitecture. The missing iodine atoms are highlighted by a white dotted circle superimposed to the STM images. The unit cell of the sine-wave nanoarchitecture is represented by a black dashed line in Figure 5.9b. The network unit cell of this porous structure is a rectangle with $2.1 \pm 0.2 \text{ nm}$ and $1.9 \pm 0.2 \text{ nm}$ unit cell constants. The unit cell is composed of two molecules. The molecular architecture appears to be stabilized by

5.2 Submonolayer coverage ($0.2\text{ML} < C < 1\text{ML}$): unexpected halogen-bonded network growth

halogen···halogen bonds between neighboring molecules. The angle between I-C groups of neighboring molecules is 180° and 120° .

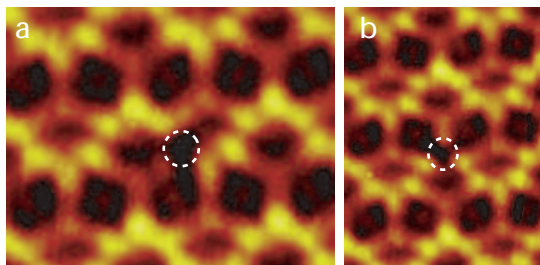


Figure 5.10: *High resolution STM images of sine-wave nanoarchitecture defects due to partially dehalogenated molecule. (a) $5 \times 3 \text{ nm}^2$, $V_s = 1.0 \text{ V}$, $I_t = 23 \text{ pA}$. (b) $3 \times 5 \text{ nm}^2$, $V_s = 1.0 \text{ V}$, $I_t = 23 \text{ pA}$.*

5.2.2 Bow-tie X-bonded structure

A second well-ordered organic nanoarchitecture is also usually observed on the Au(111) surface. High resolution STM images of this structure are presented in Figure 5.11. This organic nanoarchitecture is also porous. Six molecular schemes have been superimposed to the STM image in Figure 5.11b to visualize molecular assembly. Neighboring molecules are rotated by an angle of 180° . The molecules are however not adopting a strict side-by-side arrangement, as previously observed in the sine-wave structure. The molecular iodine atoms are forming 6-synthons (X_6) adopting a bow-tie shape. The network unit cell of this structure is a parallelogram with $2.2 \pm 0.2 \text{ nm}$ and $1.7 \pm 0.2 \text{ nm}$ unit cell constants and an angle of $75 \pm 3^\circ$ between the axes. The unit cell is composed of two molecules. The molecular architecture appears to be stabilized by halogen···halogen bonds between neighboring molecules. The angle between I-C groups of neighboring molecules is 60° and 120° .

5. ON-SURFACE SYNTHESIS OF 2D COVALENT ORGANIC STRUCTURES VERSUS HALOGEN-BONDED SELF-ASSEMBLY: COMPETING FORMATION OF ORGANIC NANOARCHITECTURES

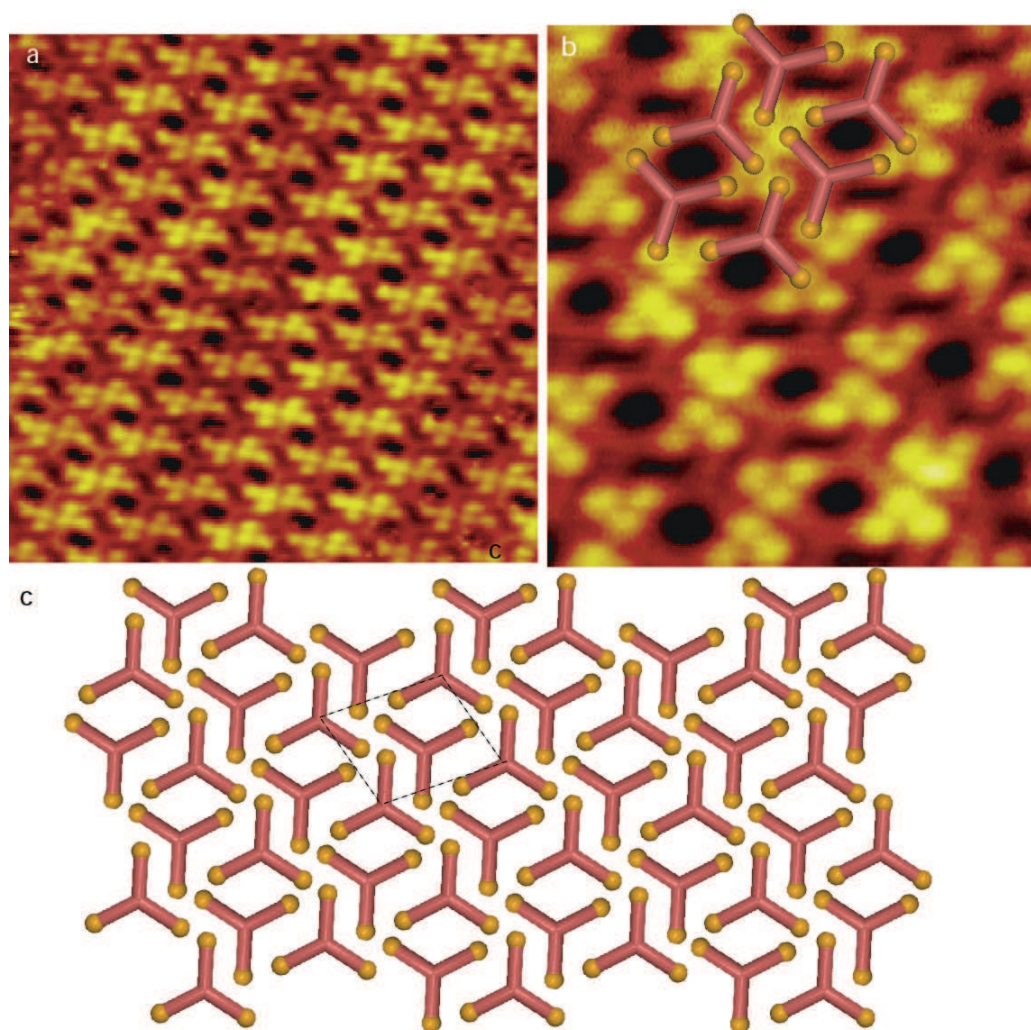


Figure 5.11: *High resolution STM images of the 1,3,5-Tris(4-iodophenyl)benzene bow-tie nanoarchitecture, (a) $14 \times 14 \text{ nm}^2$, $V_s = 1.3 \text{ V}$, $I_t = 20 \text{ pA}$, (b) $5 \times 6 \text{ nm}^2$, $V_s = 1.3 \text{ V}$, $I_t = 20 \text{ pA}$, (c) Model of the organic nanoarchitecture. The network unit cell is represented by a dotted black parallelogram.*

5.2.3 Covalent-dimer X-bonded structure

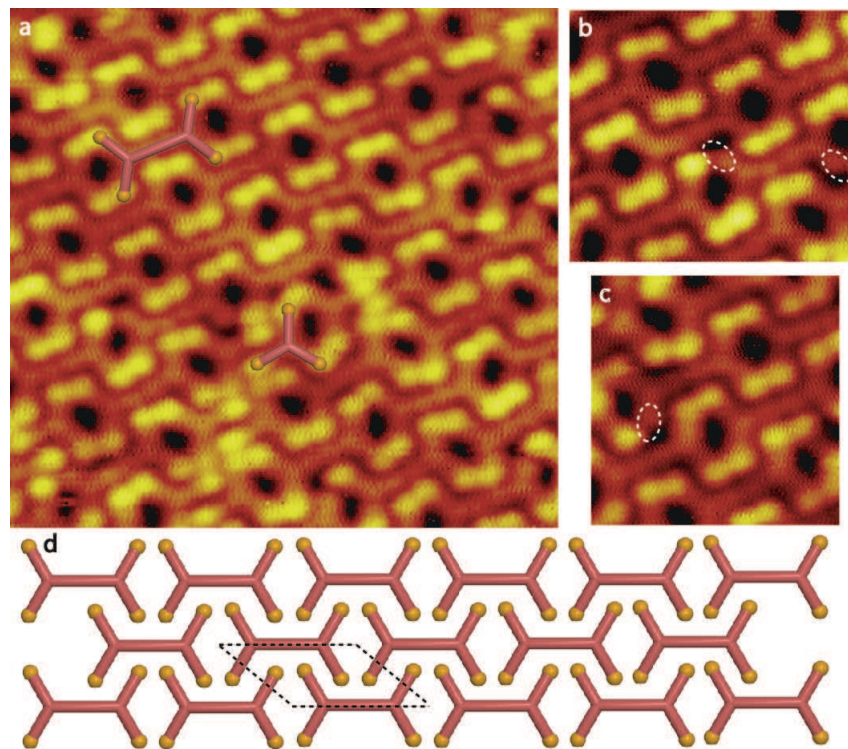


Figure 5.12: *STM images of the mixed covalent / X-bonded 1,3,5-Tris(4-iodophenyl)benzene nanoarchitecture on Au(111), (a) $10 \times 10 \text{ nm}^2$, $V_s = 1.3 \text{ V}$, $I_t = 205 \text{ pA}$, (b) $7 \times 7 \text{ nm}^2$, $V_s = 1.3 \text{ V}$, $I_t = 205 \text{ pA}$, (c) $7 \times 7 \text{ nm}^2$, $V_s = 1.3 \text{ V}$, $I_t = 205 \text{ pA}$, (d) Model of the molecular arrangement. The network unit cell is represented by a dotted black parallelogram.*

Another organic nanoarchitecture is locally observed on the Au(111) surface. An STM image of this structure is presented in Figure 5.12. Molecular iodine atoms are paired and are aligned on the surface in this structure. The high resolution STM image reveals that the building block of this structure is the 1,3,5-Tris(4-iodophenyl)benzene covalent-dimer, previously presented in Figure 5.1b. The molecular dimers are aligned along their axis on the surface and they are forming parallel chains. Neighboring dimers are bonded along their axis through double $X \cdots X$ bonds. The angle between I-C groups is 60° . The model of this arrangement is represented in Figure 5.12d. The network unit cell of this structure is a parallelogram rectangle with $2.7 \pm 0.2 \text{ nm}$ and $1.7 \pm 0.2 \text{ nm}$ unit cell constants and an angle of $43 \pm 3^\circ$ between the axes. The unit cell is composed of one dimer (2 covalently-linked molecules). Local defects can be observed in the organic layer, *i.e.* dehalogenated dimers (Figure 5.12b,c) and local bow-tie nanoarchitecture (see

5. ON-SURFACE SYNTHESIS OF 2D COVALENT ORGANIC STRUCTURES VERSUS HALOGEN-BONDED SELF-ASSEMBLY: COMPETING FORMATION OF ORGANIC NANOARCHITECTURES

superimposed star molecule scheme in Figure 5.12a). This structure is a mixed nanoarchitecture, combining covalent and $X \cdots X$ halogen bonds. The angle between I-C groups of neighboring molecules is 120° .

5.2.4 Covalent-chain assembly

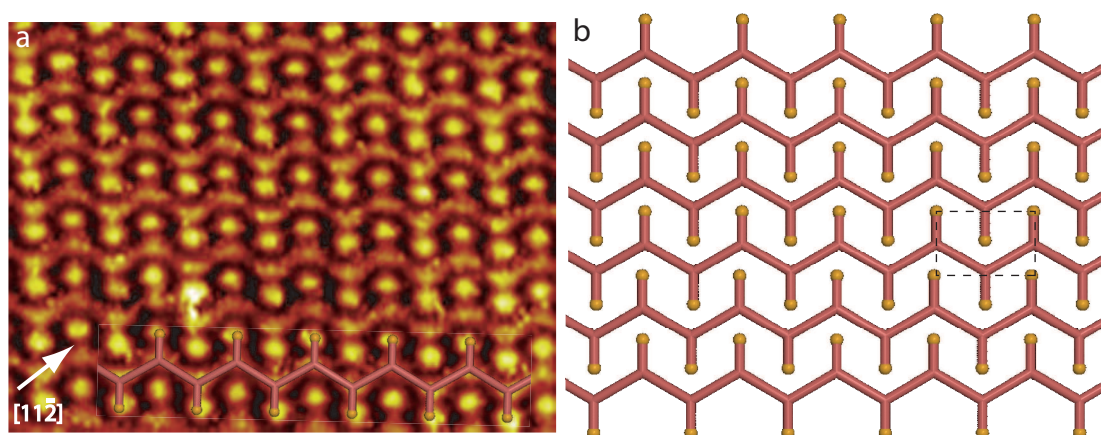


Figure 5.13: (a) STM image of the covalent chain-nanoarchitecture on Au(111), $14 \times 12 \text{ nm}^2$, $V_s = 1.9 \text{ V}$, $I_t = 55 \text{ pA}$. (b) Model of the zig-zag chain-nanoarchitecture. The network unit cell is represented by a dotted black square.

The STM image presented in Figure 5.13a reveals the existence of a fourth organic organized nanoarchitecture on the Au(111) surface. This structure is composed of covalent molecular zig-zag chains arranged side-by-side. The zig-zag chains result from the sequential covalent binding of molecules alternatively rotated by an angle of 180° . The model of the zig-zag chain arrangement is presented in Figure 5.13b. The network unit cell of this structure is a rectangle with $2.2 \pm 0.2 \text{ nm}$ and $1.6 \pm 0.1 \text{ nm}$ unit cell constants. The unit cell is composed of two covalently linked molecules. This structure is however only locally observed on the Au(111) surface.

5.3 Supramonolayer deposition ($>1\text{ML}$): on-top covalent nanoarchitectures

Figure 5.14 shows the Au(111) surface after 1.2 ML molecular deposition. The Au(111) surface is now fully covered by an organic layer. The STM images show that the first organic layer on the Au(111) surface is essentially composed of the sine-wave and bow-tie

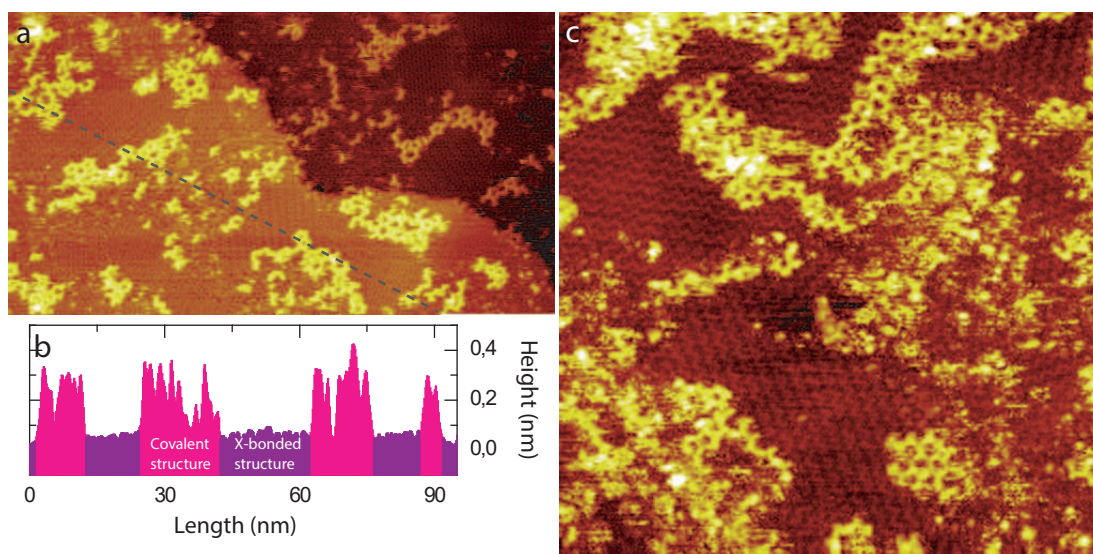


Figure 5.14: *STM images of the Au(111) surface after 1.2 ML molecular deposition, (a) 110×60 nm², $V_s = 2.1$ V, $I_t = 445$ pA. (b) Line profile taken along the blue dotted line in (a). (c) 60×60 nm², $V_s = 1.9$ V, $I_t = 445$ pA.*

nanoarchitectures, whereas the dimer and chain-structures are only locally observed (Figure 5.14c). The second organic layer appears to be exclusively composed of the covalent polygonal-nanoarchitecture that grows at low coverage (Figure 5.5 and Figure 5.6). The line profile in Figure 5.14b shows the height difference between the halogen-bonded first layer and the supported covalent nanoarchitectures.

5.4 Influence of the surface temperature

Temperature is known to strongly influence the on-surface Ullmann coupling process. In particular, temperature is reported to activate the dehalogenation of the precursors which is the first step of the Ullmann coupling reaction [95, 98]. We investigated the influence of the temperature in the case of TIPB molecules on Au(111) using two approaches. First, post-annealing was carried out after deposition of TIPB molecules on Au(111) surface kept at room temperature. Figure 5.15a is an STM image of the Au(111) surface after deposition of TIPB molecules at room temperature followed by post-annealing at 170°C. Intact (non-dehalogenated) TIPB molecules are observed on the surface forming X-bonded surface. The ratio of covalent over halogen-bonded structure was not affected significantly by the post-annealing. Post-annealing at higher temperature was carried out resulting in the same organization. Post-annealing thus appears not to trigger TIPB dehalogenation for monolayer coverage, even at high temperature.

5. ON-SURFACE SYNTHESIS OF 2D COVALENT ORGANIC STRUCTURES VERSUS HALOGEN-BONDED SELF-ASSEMBLY: COMPETING FORMATION OF ORGANIC NANOARCHITECTURES

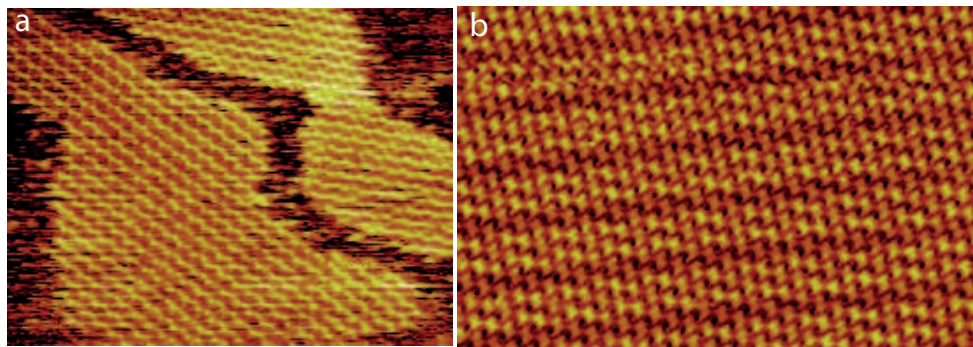


Figure 5.15: (a) STM image of X-bonded sine nanoarchitecture after deposition of TIPB molecule at room temperature on Au(111) followed by post-annealing at 170 °C. $43 \times 34 \text{ nm}^2$, $V_s = 2.0 \text{ V}$, $I_t = 20 \text{ pA}$. (b) STM image of X-bonded bow-tie nanoarchitecture after deposition of TIPB molecule on Au(111) surface kept at 430 °C. $43 \times 29 \text{ nm}^2$, $V_s = 2.0 \text{ V}$, $I_t = 20 \text{ pA}$.

Another approach consisting in evaporating TIPB molecules on an Au(111) surface heated at high temperature was investigated. Figure 5.15b is an STM image acquired after deposition of TIPB molecules on an Au(111) surface at 430 °C. Similarly to the post-annealing approach, TIPB molecules are still intact and forming X-bonded structures, even at 430 °C. Other trials were realized at higher temperature (up to 500 °C) and X-bonded nanoarchitectures are observed until the desorption temperature of the building blocks is reached.

5.5 Investigation on the diffusion limited TIPB dehalogenation

The self-assembly of 1,3,5-Tris(4-iodophenyl)benzene molecules on Au(111) surface in vacuum has been investigated using STM. STM images reveal that at low coverage, the molecules preferentially adsorb on the Au(111) step edges. The molecules form there covalent structures through deiodination. Small covalent structures are also observed at the herringbone elbows of the Au(111) reconstruction. Coverage increase essentially leads to the growth of halogen-bonded nanoarchitectures on the surface. The formation of covalent nanoarchitecture is in comparison less favored. In contrast with previous reports [165, 167, 169], our measurements show that the iodine dehalogenation process is a limited process on Au(111) at room temperature, *i.e.* iodine atoms can be undoubtedly identified with STM on the molecular skeleton in numerous cases on Au(111) (Figure 5.2). Our STM images are in fact showing that Au(111) step edges are preferential reaction sites

5.5 Investigation on the diffusion limited TIPB dehalogenation

for Ullmann coupling reaction. This effect was previously proposed by Saywell *et al.* for bromine-molecules [76]. They also observed that Au(111) step edges and kinks act as “active sites” and catalytically induce the cleavage of the molecular halogen atoms. This explains why covalent structures preferentially start growing from Au(111) step edges (Figure 5.2 and Figure 5.3).

The free iodine atoms produced during the Ullmann coupling are preferentially adsorbing on the Au(111) step edges. These atoms then form chains along the step edges, as it can be observed in Figure 5.3. The saturation of Au(111) step edges with iodine atoms reduces the catalytic activity of the Au(111) surface. At high coverage deposition, the formation of covalent nanoarchitectures is highly diminished. The molecules preferentially form halogen-bonded nanoarchitectures on the Au(111) surface. Molecules with missing iodine atoms are only locally observed in these structures, not only at room temperature but also at high temperature (Figure 5.15).

Increasing further the coverage leads to the competitive growth of the covalent structure and halogen-bonded nanoarchitectures. STM is showing that the halogen-bonded structures are preferentially covering the surface and are pushing away the covalent nanoarchitectures. The covalent nanoarchitectures are then decorating the edges of X-bonded structures. The covalent structures are finally squeezed at the domain boundary of X-bonded structures for 1 ML deposition (Figure 5.7c). This results in the formation of very defective domain boundaries (Figure 5.8). Two X-bonded nanoarchitectures are coexisting. They are presented in the high resolution STM images in Figure 5.9 and Figure 5.11. It should however be noticed that hybrid X-bonded-covalent nanoarchitectures (Figure 5.12) and covalent chain-nanoarchitectures (Figure 5.13) are only locally observed, their domain area is never larger than 200 nm². We have seen in section 1.1.2.3 that Bui *et al.* [23] previously classified the different types of C-X···X-C bonds depending on the angle between X-C groups. The angle between the molecular X-C group axis is 90-120°. The sine-wave structure appears therefore to be stabilized by type-I and type-II halogen bonds, whereas the bow-tie and dimer structures appear to be stabilized by type-II halogen bonds only.

Above one monolayer deposition, the Au(111) surface is fully covered by an organic layer, essentially composed of the X-bonded nanoarchitectures. A second layer is observed on top of the first X-bonded layer (Figure 5.14). STM images reveal that the second layer is surprisingly composed of polygonal-covalent nanoarchitectures. As the Au(111) surface is now covered by an organic layer and the step edges are already saturated with iodine adatoms, Ullmann reaction cannot occur anymore for new molecules reaching the gold

5. ON-SURFACE SYNTHESIS OF 2D COVALENT ORGANIC STRUCTURES VERSUS HALOGEN-BONDED SELF-ASSEMBLY: COMPETING FORMATION OF ORGANIC NANOARCHITECTURES

surface. It appears therefore that the preferential adsorption of the X-bonded nanoarchitectures on the Au(111) surface is propelling the initially-formed covalent structures on top of the X-bonded nanoarchitectures above 1 ML deposition. Figure 5.5 and Figure 5.6 obviously show that the packing density of the covalent nanoarchitecture is largely lower than the one of the X-bonded nanoarchitectures (Figure 5.7). The growth of the most compact structures is usually favored on surfaces because these structures not only favor intermolecular interactions but they also lower the surface free-energy of the sample [170].

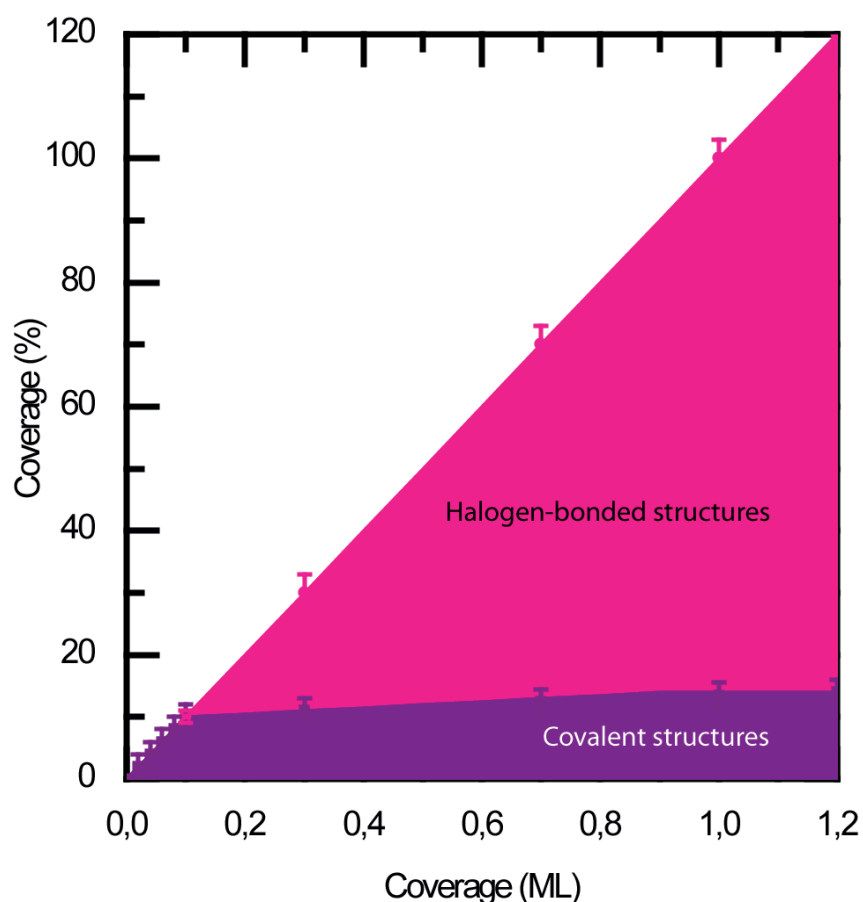


Figure 5.16: Evolution of halogen-bonded versus covalent nanostructures coverage with the TIPB deposition amount on Au(111) surface (from 0 to 1.2 ML).

The structure density is 1 mol. / 1.99 nm² for the sine-wave network, 1 mol. / 1.81 nm² for the bow-tie network, 1 mol. / 1.56 nm² for the hybrid dimer-network and 1 mol. / 1.76 nm² for the hybrid zig-zag network. In comparison, the density of the covalent hexagonal network is the smallest with 1 mol. / 2.16 nm², see Table 5.1. As the covalent nanoarchitecture is the less dense, it is pushed away from the Au(111) surface by the growth of the denser nanoarchitectures. In contradiction with Eder *et al.* statement, we prove that

5.5 Investigation on the diffusion limited TIPB dehalogenation

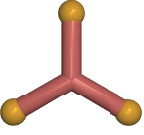
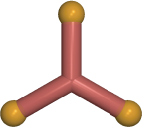
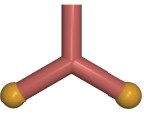
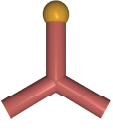
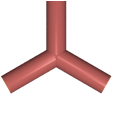
Arrangement	Building Block	Molecules per Unit Cell	Intermolecular Bonds	Packing Density
Sine-wave Figure 5.9		2	X-Bonds	1 mol. / 1.99 nm ²
Bow-tie Figure 5.11		2	X-Bonds	1 mol. / 1.81 nm ²
Hybrid dimer Figure 5.12		2	X-Bonds Covalent	1 mol. / 1.56 nm ²
Hybrid zig-zag Figure 5.13		2	X-Bonds Covalent	1 mol. / 1.76 nm ²
Covalent hexagonal Figure 5.5		2	Covalent	1 mol. / 2.16 nm ²

Table 5.1: Structure, bonding and packing density of the 1,3,5-Tris(4-iodophenyl)benzene nanoarchitectures. The carbon skeleton of the molecular building block is represented by an orange star and the iodine atoms are represented by yellow balls.

the presence of the covalent aggregates in a second layer is not unique to the solution approach and can also be obtained in vacuum [166].

The effect of surface temperature on Ullmann coupling reaction efficiency has been investigated in section 5.4. Molecules have been deposited on a hot surface and molecules have also been deposited on a surface at room temperature, followed by a post-annealing. The investigated temperature range goes from room temperature to 500 °C. STM images however reveal that temperature increase has not effect on the formation of covalent nanoarchitectures (Figure 5.15) for monolayer coverage films. X-bonded structures are still observed at high temperature and the competitive growth of the different structures is not modified. It therefore appears that the formation of covalent architectures is intrinsically connected to surface coverage. Low surface coverage allows TIPB molecules

5. ON-SURFACE SYNTHESIS OF 2D COVALENT ORGANIC STRUCTURES VERSUS HALOGEN-BONDED SELF-ASSEMBLY: COMPETING FORMATION OF ORGANIC NANOARCHITECTURES

to diffuse to the reactive sites (step edges and Au elbow). High coverage, on contrary, prevents molecules to diffuse to the reactive sites, that are increasingly poisoned by iodine atoms.

Chapter conclusion

To summarize, the on-surface synthesis of covalent nanoarchitectures and the self-assembly of star-shaped 1,3,5-Tris(4-iodophenyl)benzene molecules was investigated using scanning tunneling microscopy. STM shows that at low coverage covalent polygonal nanostructures appear at the Au(111) step edges and at the elbows of the Au(111) surface reconstruction. The iodine atoms generated by molecule dehalogenation diffuse on the surface and are then adsorbed at the surface step edges. Step edges that are known to be catalytically active sites of the gold surface are consequently progressively poisoned. Consequently, at high coverage, molecules arriving on the surface are no longer dehalogenated and two-dimensional halogen-bonded nanoarchitectures made of intact molecules are preferentially growing on the gold surface instead. These structures are pushing away the covalent nanoarchitectures at their domain boundaries. Above one monolayer deposition the whole Au(111) surface is covered with an organic layer and the covalent structures are propelled on top of the halogen-bonded organic layer (Figure 5.16). These observations open up new opportunities for decoupling covalent nanoarchitectures from catalytically active and metal surfaces in vacuum. The electronic decoupling induced by the halogen-bonded structures localized between the covalent structures and the surface could be for example investigated using low temperature scanning tunneling spectroscopy.

Chapter 6

Temperature-dependent hierarchical on-surface synthesis of porous halogen-bonded, hybrid and covalent two-dimensional nanoarchitectures

The objective of this chapter is to engineer porous covalent nanoarchitectures through hierarchical on-surface Ullmann reaction. In chapter 5, we studied the case of an iodine star-shaped precursor. To better understand the influence of the nature of precursor halogen substituent and its geometry, we will investigate the Ullmann coupling reaction of a different halogenated precursor in this chapter. The system studied here consists in star-shaped molecular precursors with two terminal bromine atoms per arm, evaporated on Au(111) surface. A temperature-dependent scanning tunneling microscopy and X-ray photoemission spectroscopy characterization of this system will be carried out.

The 2D covalent structures created by on-surface Ullmann coupling usually have limited dimensions and a high number of defects in comparison with self-assembled nanoarchitectures. The radical covalent-bonding usually proceeds in a random and uncontrollable manner. It is a non-reversible process preventing self-healing. In addition, different byproducts are inevitably created during the Ullmann coupling when the molecules possess more than one halogen atom. Therefore, the probability to generate defects is high when multi-axial directions for radical covalent bonding are possible. Temperature control has been used to adjust the kinetic reaction parameters to reduce the defect density during the formation of the covalent networks [165] but with limited success. In contrast, temperature control has been effective in triggering the sequential formation of hydrogen-bonded and metal-coordinated nanostructures [81]. Temperature control has

6. TEMPERATURE-DEPENDENT HIERARCHICAL ON-SURFACE SYNTHESIS OF POROUS HALOGEN-BONDED, HYBRID AND COVALENT TWO-DIMENSIONAL NANOARCHITECTURES

not yet proven to be an efficient stimulus to trigger the sequential formation of different 2D covalent networks.

The chemical structure of the 1,3,5-Tris(3,5-dibromophenyl)benzene (T2BPB) molecule is presented in Figure 6.1, top. This 3-fold symmetry molecule is a star-shaped molecule. The molecular skeleton consists of a central benzene ring connected to three peripheral 3,5-dibromophenyl groups. The bromine atoms of neighboring molecular arms are separated by 7.1 Å. Two molecules are expected to form on metal surfaces two kinds of covalent dimers through surface-assisted Ullmann coupling. The type-A dimer is stabilized by the formation of two covalent bonds, whereas the type-B dimer is stabilized by the formation of a single covalent bond (Figure 6.1, bottom).

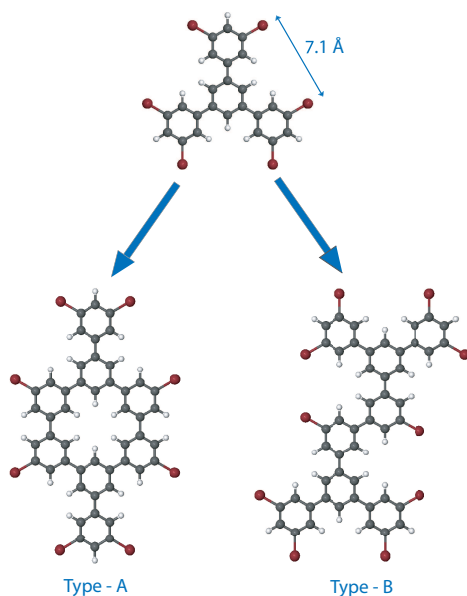


Figure 6.1: (a) Scheme of 1,3,5-Tris(3,5-dibromophenyl)benzene ($C_{24}H_{12}Br_6$) building block. Carbon atoms are gray, bromine atoms are red and hydrogen atoms are white. (b) Covalent dimer-A. (c) Covalent dimer-B.

6.1 Halogen-bonded nanoarchitecture at room temperature

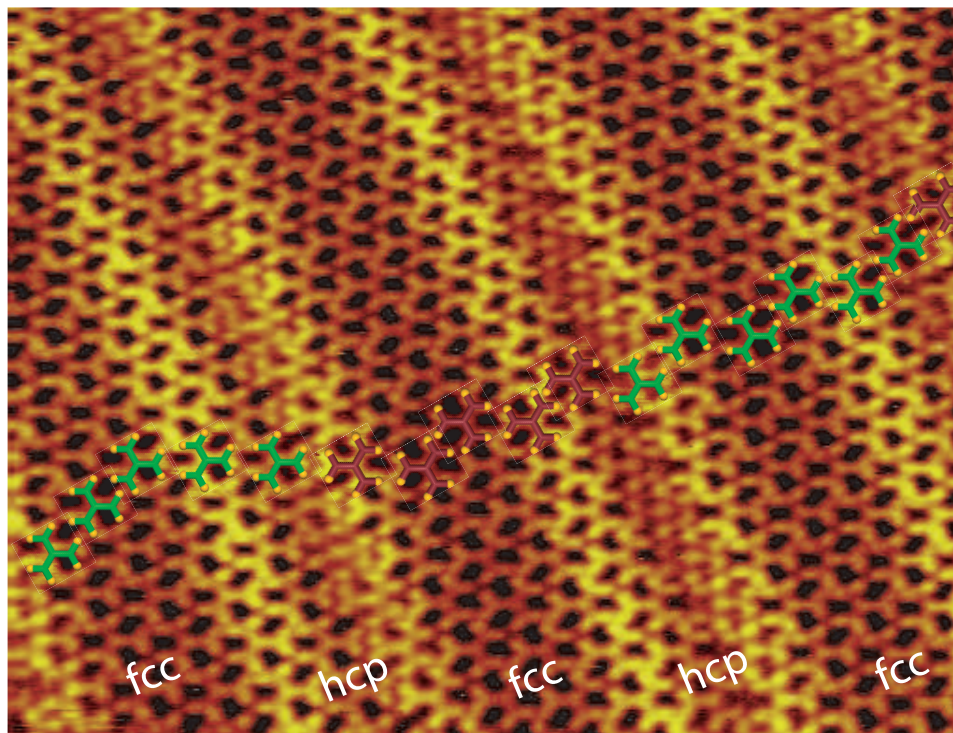


Figure 6.2: *STM image of the molecular self-assembly on Au(111)- $22 \times \sqrt{3}$ at room temperature; $19 \times 15 \text{ nm}^2$, $V_s = 1.0 \text{ V}$, $I_t = 32 \text{ pA}$. Green and red molecular schemes have been superimposed to the STM image to highlight the two molecular orientations.*

Figure 6.2 shows the Au(111)- $22 \times \sqrt{3}$ reconstructed surface after deposition of 1,3,5-Tris(3,5-dibromophenyl)benzene molecules at room temperature¹. The molecules self-assemble into a porous nanoarchitecture on the surface. Two molecular orientations can be observed in the organic layer (Figure 6.2 and Figure 6.3b). The molecules adopt the same orientation inside a domain but molecules of neighboring domains are rotated by 180° . Differently-oriented molecular schemes (red and green) have been superimposed to the STM images in Figure 6.2 and in Figure 6.3b as a guide for the eyes. The large scale STM image in Figure 6.2 reveals that molecular domain boundaries are located in the

¹Experiments were performed in a ultrahigh vacuum (UHV) chamber at a pressure of 10^{-8} Pa. The Au(111) surface was sputtered with Ar^+ ions and then annealed in UHV at 600°C for 1 hour. 1,3,5-Tris(3,5-dibromophenyl)benzene molecules (TCI Europe) (Figure 6.1a), were evaporated at 180°C and deposited on the gold surface. Cut Pt/Ir tips were used to obtain constant current STM images at room temperature with a bias voltage applied to the sample. STM images were processed and analyzed using the home made FabViewer application [149]

6. TEMPERATURE-DEPENDENT HIERARCHICAL ON-SURFACE SYNTHESIS OF POROUS HALOGEN-BONDED, HYBRID AND COVALENT TWO-DIMENSIONAL NANOARCHITECTURES

hcp areas of the Au(111)- $22 \times \sqrt{3}$ reconstruction. It has been previously observed that the gold reconstruction can drive the formation of domain boundary in a self-assembled organic layer [71].

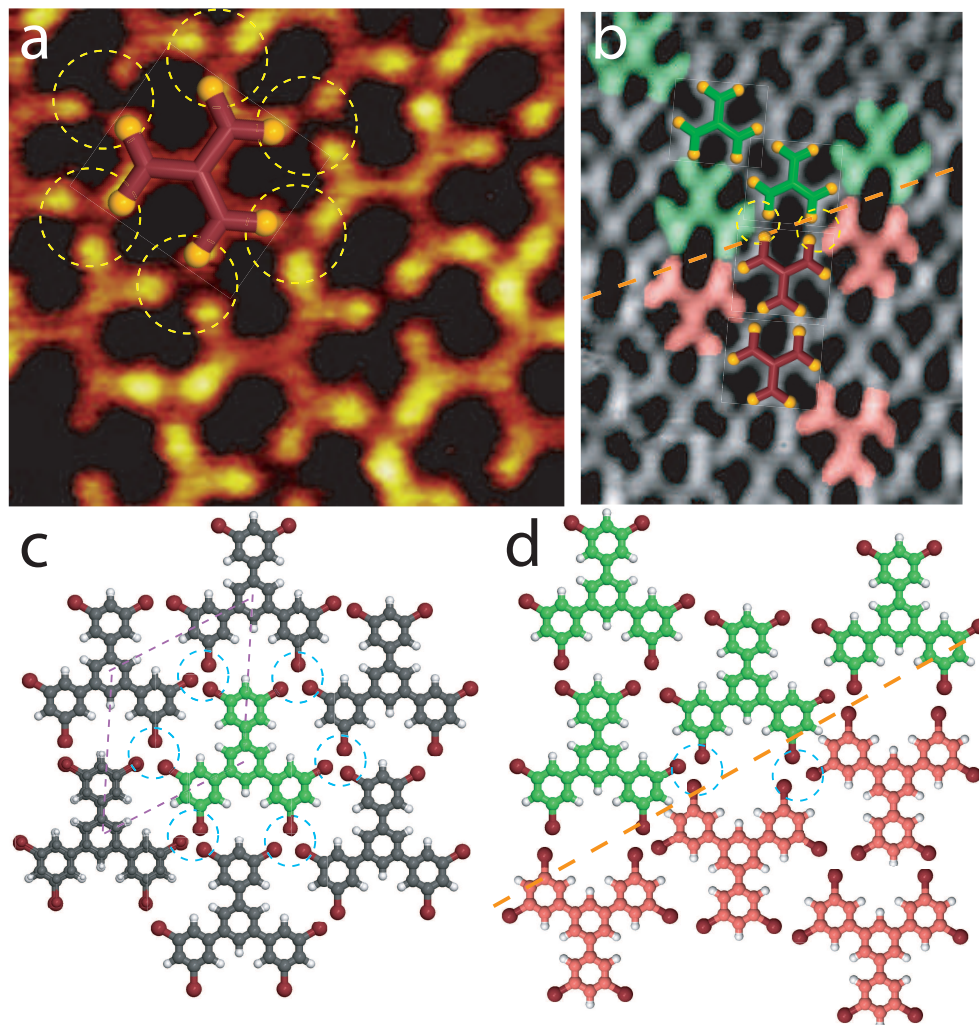


Figure 6.3: *STM images of the molecular self-assembly on Au(111)- $22 \times \sqrt{3}$ at room temperature. (a) X-bonded structure $3 \times 3 \text{ nm}^2$, $V_s = 1.4 \text{ V}$, $I_t = 26 \text{ pA}$ with corresponding molecular model (c) (b) Domain boundary $6 \times 7 \text{ nm}^2$, $V_s = 1.6 \text{ V}$, $I_t = 40 \text{ pA}$ with corresponding molecular model (d). Green and red molecular schemes have been superimposed to the STM image to highlight the two molecular orientations in (b). Few molecules have also been colored in green and red in the STM image (d). The superimposed dotted circles highlight the formation of halogen X_3 synthons.*

A high resolution STM image of the molecular arrangement inside a domain is presented in Figure 6.3a. Two bright spots can be observed at the apex of each molecular arm. It has been previously experimentally observed that halogen atoms, such as bromine

6.1 Halogen-bonded nanoarchitecture at room temperature

and iodine, appear brighter than molecular carbon atoms in STM images [35, 168]. The molecular arrangement appears to be stabilized by intermolecular halogen bonding. The molecular bromine atoms are forming 3-synthons (X_3) with neighboring molecules. These synthons are highlighted by dotted circles in Figure 6.3a,c. The angle between Br-C groups of neighboring molecules is 120° . The network unit cell of this structure is a lozenge with 1.22 ± 0.1 nm unit cell constant and an angle of $58 \pm 2^\circ$ between the axes. The unit cell is composed of one molecule. The model of this arrangement is presented in Figure 6.3c.

Figure 6.3b shows a high resolution STM image of molecular domain boundary. Neighboring molecules are rotated by an angle of 180° at the domain boundary. Despite the variation of orientation, no gap is observed in the organic layer. The organic structure is also stabilized by intermolecular X_3 -synthons at the domains boundaries (dotted circle in Figure 6.3b,d). The model of molecular arrangement at the domain boundary is presented in Figure 6.3d.

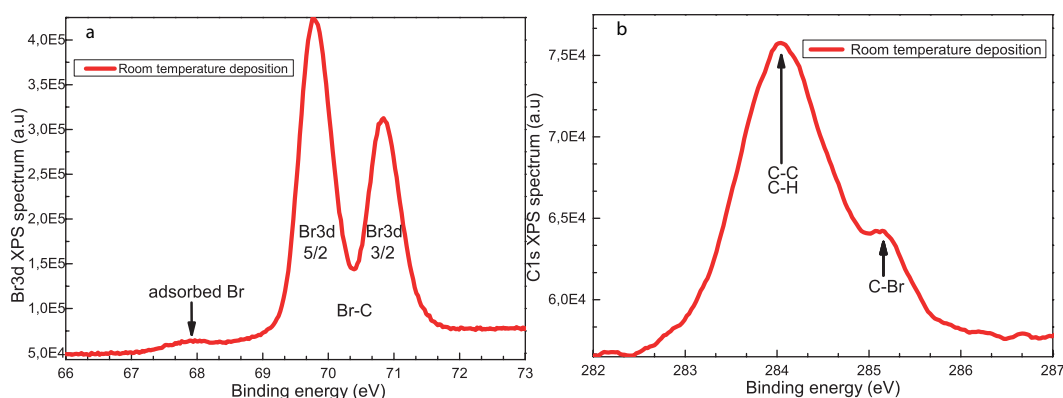


Figure 6.4: X-ray photoemission spectra acquired on TEMPO beamline at Soleil synchrotron after deposition of T2BPB molecules at room temperature on Au(111) surface. (a) Br_{3d} XPS spectrum acquired with a 185 eV photon energy. (b) C_{1s} XPS spectrum acquired with a 485 eV photon energy.

Figure 6.4a and b are respectively Br_{3d} and C_{1s} XPS spectra measured after room temperature deposition of T2BPB molecules on Au(111). C_{1s} was chosen to characterize the chemical environment of the carbon atoms. Br_{3d} core-level was chosen to characterize the bromine environment. Due to spin-orbit coupling, Br_{3d} spectrum has two separate components Br_{3d,5/2} and Br_{3d,3/2}. The intensity ratio of the two components (integrated area) corresponds to the ratio of the degeneracy of core-levels, here 3/2. A large doublet is observed on the Br_{3d} spectrum in Figure 6.4a. This spectrum was acquired with a photon energy of 185 eV and converted into binding energy. The Br_{3d,5/2} component is

6. TEMPERATURE-DEPENDENT HIERARCHICAL ON-SURFACE SYNTHESIS OF POROUS HALOGEN-BONDED, HYBRID AND COVALENT TWO-DIMENSIONAL NANOARCHITECTURES

centered at 69.8 eV whereas the $\text{Br}_{3d,3/2}$ peak is centered at 70.9 eV, corresponding to an energy shift of ≈ 1.1 eV, in accordance with the values of the literature [171]. This main component is attributed to bromine atoms still attached to the molecular skeleton, as it is observed on the STM images. A smaller component at lower binding energy is also observed near 68 eV. This component is attributed to bromine atoms detached from the molecules and adsorbed on the surface [171, 172]. Yet, all the T2BPB molecules were found to be intact after deposition at room temperature on Au(111) according to the STM observations. This component is in fact attributed to photoinduced debromination of the molecules after prolonged irradiation by the X-ray synchrotron beam. This phenomenon was already reported previously [173] and does not appear to significantly affect the measured spectrum. The C_{1s} spectrum is presented in Figure 6.4b. This spectrum was acquired with a photon energy of 485 eV and converted into binding energy. Two main components are observed on this spectrum. A large broad component is centered around 284.08 eV. It is attributed to C-H and C-C atoms of the T2BPB molecules. A shoulder is observed at higher binding energy centered around 285.16 eV. This shoulder is attributed to carbon atoms bonded to bromine atoms, similarly to other results of the literature [172, 173].

6.2 Formation of a 2D mixed halogen-bonded and single-covalent-bond hexagonal superstructure after annealing at 145°C

Figure 6.5 shows the Au(111) surface after deposition of 1,3,5-Tris(3,5-dibromophenyl) benzene molecules and post-annealing at 145 °C. The STM images presented in Figure 6.5 a,b reveal that a 2D hexagonal pattern appears in the organic domains. It should be noticed that the molecular contrast is inverted in the STM image presented in Figure 6.5b. This hexagonal nanoarchitecture corresponds to the triangular tiling or triangular tessellation structure. The organic layer is composed of close-packed triangular domains. Neighboring domains are rotated by 180°. There are six triangular domains connected to a vertex. The STM images show that triangular domains are separated by thick rows. The angle between the different rows is 60°.

A high resolution STM image of the hexagonal superstructure is presented in Figure 6.5c. This image reveals that the superstructure rows are composed of type-B covalent-dimers (green and orange) arranged side-by-side. In comparison, the triangular domains are composed of molecules (gray) adopting the halogen-bonded arrangement observed

6.2 Formation of a 2D mixed halogen-bonded and single-covalent-bond hexagonal superstructure after annealing at 145°C

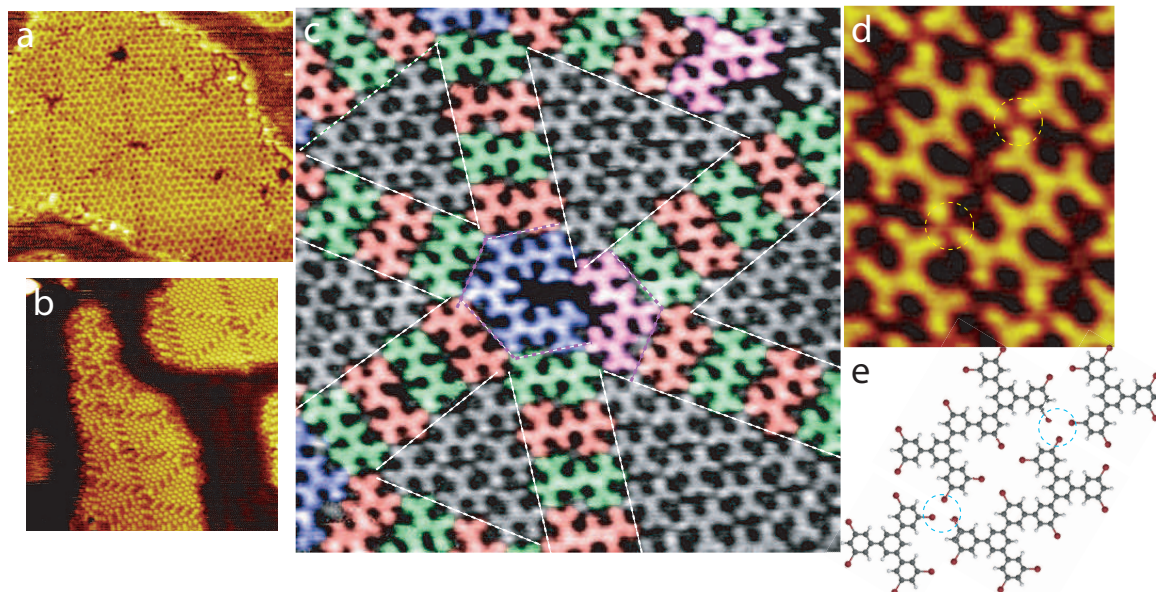


Figure 6.5: *STM images of the organic 2D nanoarchitecture on Au(111)- $22 \times \sqrt{3}$ after 145°C annealing. (a) $29 \times 26 \text{ nm}^2$, $V_s = 1.4 \text{ V}$, $I_t = 145 \text{ pA}$. (b) $36 \times 36 \text{ nm}^2$, $V_s = 1.0 \text{ V}$, $I_t = 15 \text{ pA}$. (c) $14 \times 14 \text{ nm}^2$, (d) $4 \times 6 \text{ nm}^2$, $V_s = 1.4 \text{ V}$, $I_t = 145 \text{ pA}$. In (d), molecular dimers have been colored in red, green and blue, yellow. Molecular trimers have been colored in dark green, and pentamers in pink, respectively. Dotted white lines highlight the border of halogen-bonded domains, whereas dotted white lines highlight the side of the two polymers in the center of the image. (e) Model of the dimer arrangement observed in (d). The superimposed dotted circles in (d,e) highlight the formation of halogen X_3 synthons.*

at room temperature (Figure 6.2). There is only one molecular orientation inside each domain. Molecules of neighboring domains are however rotated by an angle of 180° .

The dimers are forming X_3 -synthons with neighboring dimers and molecules (Figure 6.5d,e). The hexagonal-superstructure vertices, located at the intersection of the dimer-rows, appear to be defective covalent-hexagons. The molecular vertex in the center of the Figure 6.5c is for example composed of two covalent arches (in blue and pink colors). These two arches are composed of five and three covalently-linked molecules respectively. Two arches appear to be bonded through halogen bonds. A perfect covalent-hexagon would be made of six molecules covalently linked through type-B bond (see model in Figure 6.10e right).

Figure 6.6 shows a model of the hexagonal-superstructure observed in the STM images in Figure 6.5. In this model, a perfect covalent molecular vertex is considered (in blue). This vertex is composed of six covalently-linked molecules (type-B) leading to the formation of an hexagonal molecular vertex. Covalent dimers (red and green colors)

6. TEMPERATURE-DEPENDENT HIERARCHICAL ON-SURFACE SYNTHESIS OF POROUS HALOGEN-BONDED, HYBRID AND COVALENT TWO-DIMENSIONAL NANOARCHITECTURES

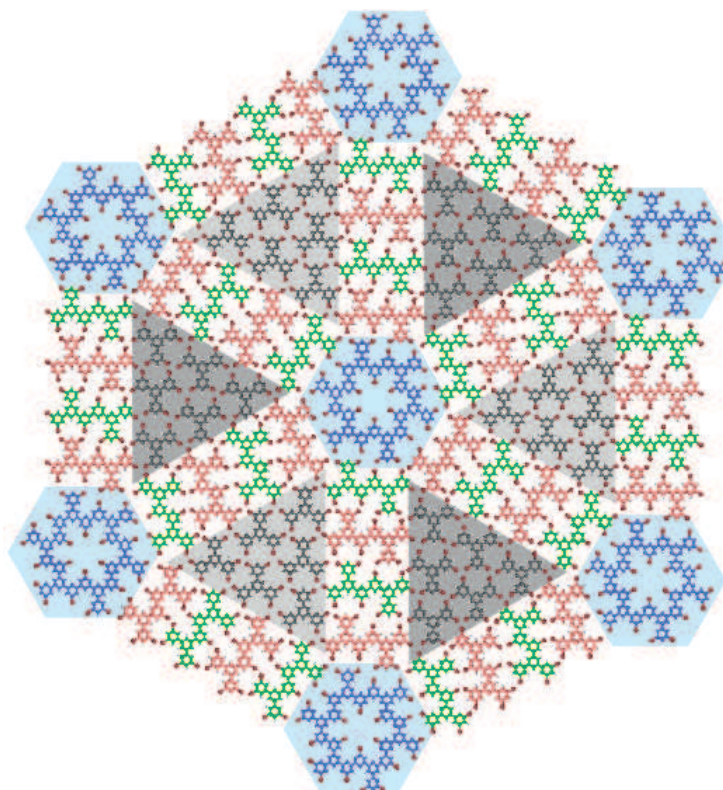


Figure 6.6: *Model of the wheel arrangement. Superimposed dotted circles highlight the formation of halogen X_3 synthons.*

are arranged side-by-side and are forming thick rows. These rows are connected to the side of the different vertices of the organic layer. The molecules forming the halogen-bonded structures observed in Figure 6.2 are represented in gray. As a guide for the eyes, a light-blue hexagon has been superimposed on top of the molecular vertices, and gray and light-gray triangles have been superimposed on top of the differently-oriented halogen-bonded domains, respectively.

Details of the wheel-arrangement model are presented in Figure 6.7. The hexagonal superstructure appears to be stabilized by the formation of halogen X_3 synthons only. These synthons are formed between the vertex (blue) and the neighboring dimers (orange and green), between two neighboring dimers and a molecule (gray) along the superstructure row and between three neighboring molecules in the triangular domains. The X_3 -synthons are highlighted by blue dotted lines in Figure 6.7.

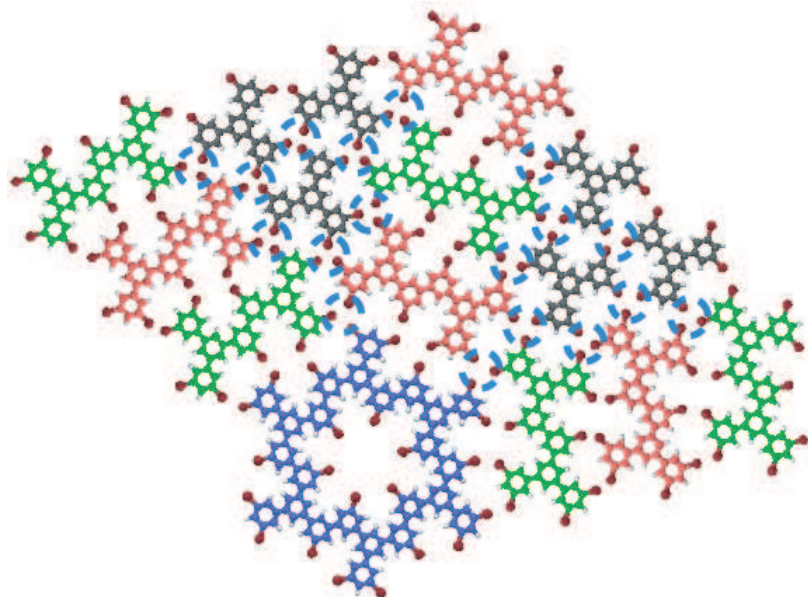


Figure 6.7: *Model of the wheel-arrangement. Superimposed dotted circles highlight the formation of halogen X_3 -synthons.*

6.3 Disappearance of 2D halogen-bonded nanoarchitecture after annealing at 165°C

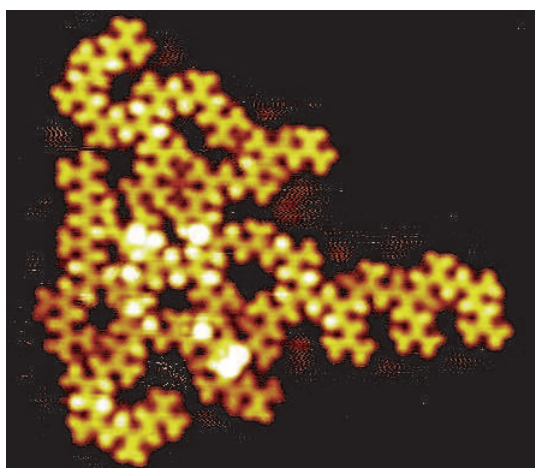


Figure 6.8: *STM image of the molecular self-assembly on $Au(111)-22 \times \sqrt{3}$ after 165°C annealing, (a) $14 \times 12 \text{ nm}^2$, $V_s = 1.3 \text{ V}$, $I_t = 55 \text{ pA}$.*

Figure 6.8 shows an STM image of a molecular domain on the Au(111) surface after post-annealing at 165°C. The STM image shows that these domains are composed of incomplete covalent hexagons. The hexagonal structures are stabilized by circular type-B

6. TEMPERATURE-DEPENDENT HIERARCHICAL ON-SURFACE SYNTHESIS OF POROUS HALOGEN-BONDED, HYBRID AND COVALENT TWO-DIMENSIONAL NANOARCHITECTURES

covalent bonding. These incomplete hexagons are mainly composed of five molecules (a perfect hexagon would be composed of six molecules (Figure 6.10e)). The halogen-bonded molecular arrangement (Figure 6.2) observed at room temperature and after annealing at 145 °C is not existing anymore on the Au(111) after the 165 °C annealing.

6.4 Single-covalent-bond chain-nanoarchitecture after annealing at 170 °C

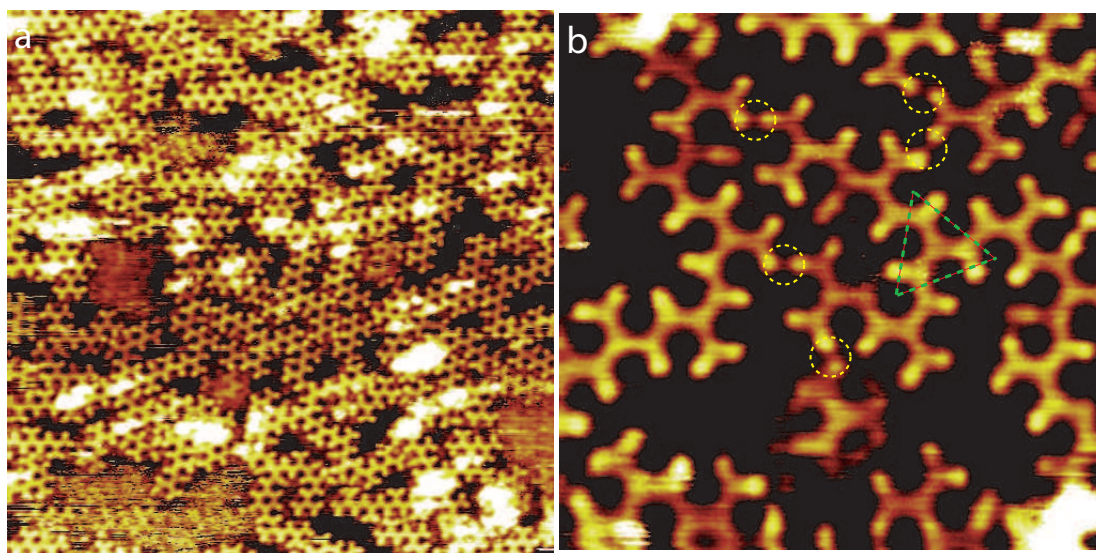


Figure 6.9: *STM images of the organic 2D nanoarchitecture on Au(111)- $22 \times \sqrt{3}$ after deposition on a 170 °C Au(111) surface. (a) $25 \times 25 \text{ nm}^2$, $V_s = 1.0 \text{ V}$, $I_t = 80 \text{ pA}$. (b) $7 \times 6 \text{ nm}^2$, $V_s = 1.0 \text{ V}$, $I_t = 80 \text{ pA}$.*

Figure 6.9 shows the Au(111) surface after deposition of 1,3,5-Tris(3,5-dibromophenyl) benzene molecules on a 170 °C Au(111) surface. The STM images show that the molecules form covalent chains on the surface. The chains are stabilized by type-B covalent coupling. Molecules are usually covalently linked to two other molecules along the chains (Figure 6.9b). This means that two out of their three arms are covalently bonded to other molecules. Molecules covalently linked to three molecules are however locally observed (dotted green triangle in Figure 6.9b). The STM image in Figure 6.9b shows that the arrangement of the covalent chains is mainly stabilized by X₂-synthons (dotted circles in Figure 6.9b) between neighboring chains.

6.5 Simultaneous formation of single and double covalently-bonded nanoarchitectures after annealing at 175°C

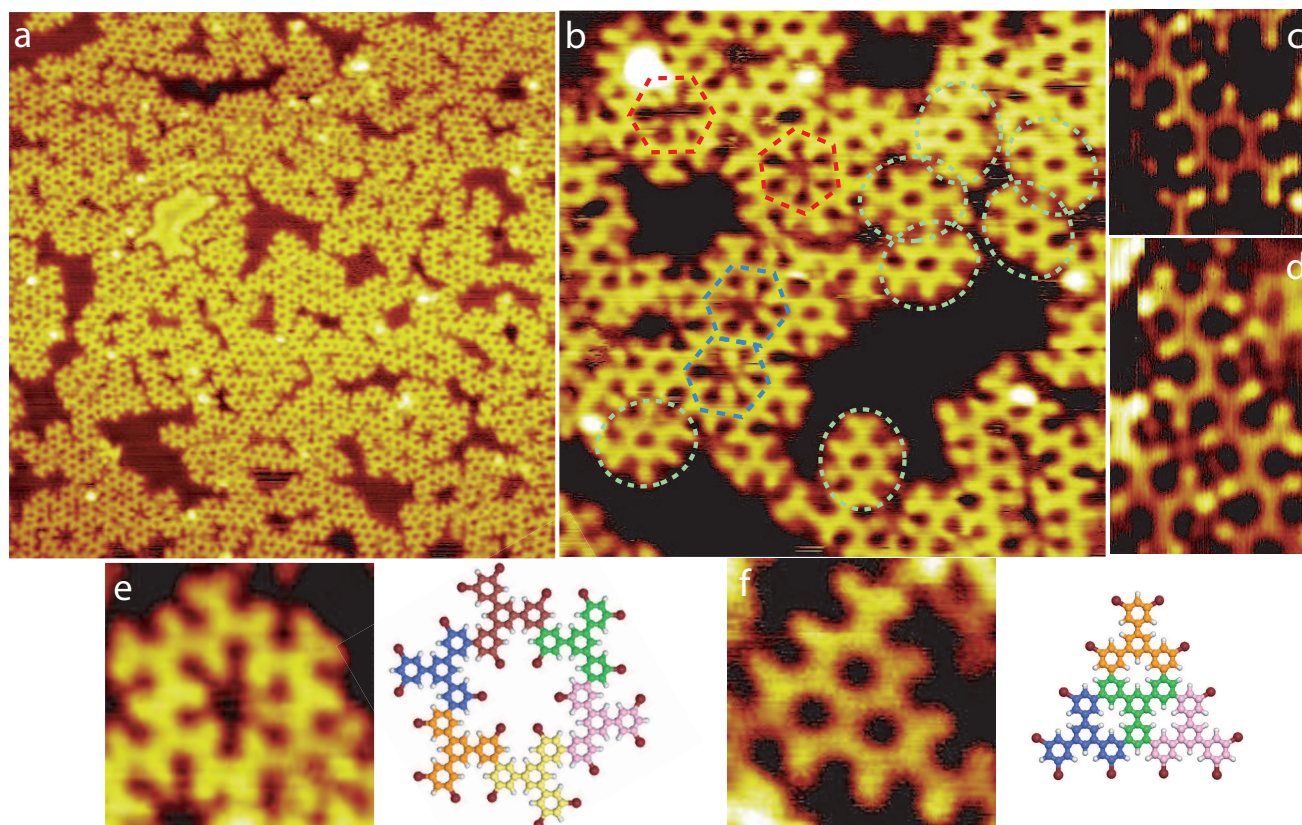


Figure 6.10: *STM images of the organic 2D nanoarchitecture on Au(111)- $22 \times \sqrt{3}$ after 175°C annealing. (a) $36 \times 36 \text{ nm}^2$, $V_s = 0.6 \text{ V}$, $I_t = 80 \text{ pA}$. (b) $12 \times 12 \text{ nm}^2$, $V_s = 0.5 \text{ V}$, $I_t = 80 \text{ pA}$. (c) $3 \times 3 \text{ nm}^2$, $V_s = 1.4 \text{ V}$, $I_t = 80 \text{ pA}$. (d) $4 \times 3 \text{ nm}^2$, $V_s = 1.4 \text{ V}$, $I_t = 80 \text{ pA}$. (e) $4 \times 4 \text{ nm}^2$, $V_s = 1.0 \text{ V}$, $I_t = 80 \text{ pA}$. (f) $3 \times 3 \text{ nm}^2$, $V_s = 1.2 \text{ V}$, $I_t = 80 \text{ pA}$. Molecular covalent hexagons and covalent dimer-A are highlighted by dotted gray hexagons and green ellipses in (b). STM images of a covalent hexagon and a covalent triangle with their respective model are presented in (e,f). As a guide for the eyes, molecules have been colored in blue, brown, green, pink, yellow and orange in the models.*

Figure 6.10a shows a large scale STM image of the Au(111) surface after deposition of 1,3,5-Tris(3,5-dibromophenyl)benzene molecules followed by a post-annealing at 175 °C. The STM image presented in Figure 6.10b reveals that different covalent nanoblocks are coexisting on the surface. The STM image shows that fully-completed covalent hexagons are now formed on the surface. This structure is chiral. The two hexagonal enantiomers

6. TEMPERATURE-DEPENDENT HIERARCHICAL ON-SURFACE SYNTHESIS OF POROUS HALOGEN-BONDED, HYBRID AND COVALENT TWO-DIMENSIONAL NANOARCHITECTURES

are respectively highlighted by blue and red dotted hexagons in Figure 6.10b. A high resolution STM image of one hexagon and its model are presented in Figure 6.10e. The covalent hexagon is composed of six molecules circularly covalently linked by type-B covalent bonds only.

Double-covalent bonds (type-A) are also appearing on the Au(111) surface after the 175 °C annealing (green dotted ellipses in Figure 6.10b). The high resolution STM image in Figure 6.10c shows a nanoblock made of three molecules bonded through one type-A and one type-B covalent bonds. Tiny structures only stabilized by double covalent bonds (type-A) are also locally observed. Figure 6.10f shows a high resolution STM image of type-A nanoblock made of five molecules (left) and its model (right). It should be noticed that linear single-covalent-bond chain structure are still observed on the surface (Figure 6.10d). Mixed type-A and B bonding is also observed (Figure 6.10b). The high resolution STM images in Figure 6.10c,d show that the molecules are not fully dehalogenated. The bright bromine atoms can still be observed on the molecular skeleton.

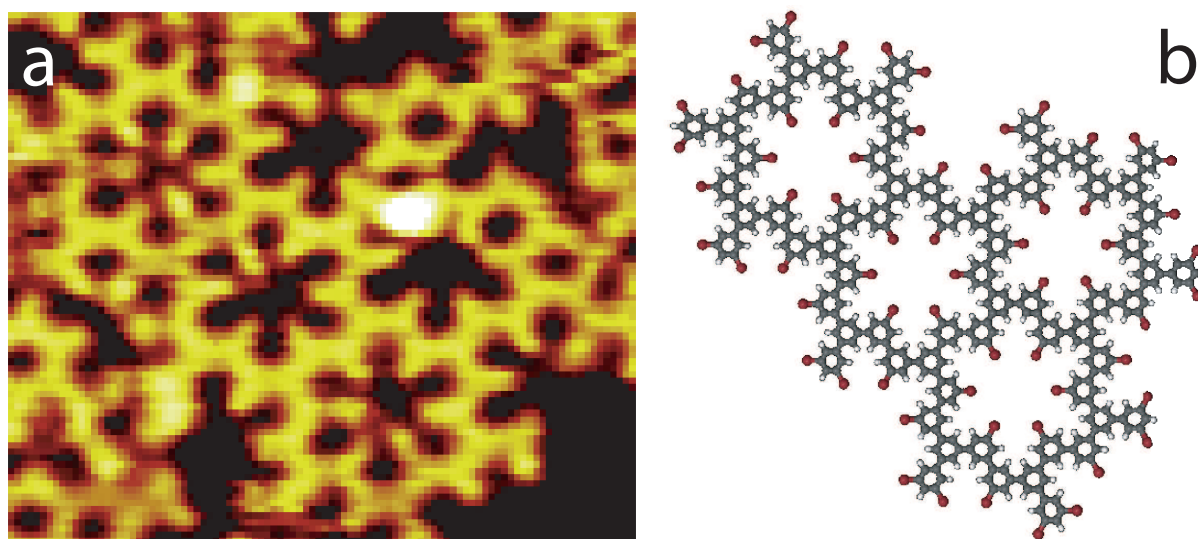


Figure 6.11: (a) STM image of periodic covalent nanoarchitecture after 175 °C annealing. $7 \times 6 \text{ nm}^2$, $V_s = 0.6 \text{ V}$, $I_t = 80 \text{ pA}$. (b) Molecular model.

In contrast with the organic covalent arrangements observed after post-annealing at 165 °C (Figure 6.8), the STM image in Figure 6.11 shows that 2D nanoarchitectures based on covalent hexagonal building blocks (Figure 6.10e) are locally formed on the surface after annealing at 175 °C. The porous domain observed in Figure 6.11 is for example composed of four single-covalent-bond hexagons. The molecules inside this structure are covalently linked to three neighbors through single-covalent bonds (type-B). The cavities

6.5 Simultaneous formation of single and double covalently-bonded nanoarchitectures after annealing at 175°C

resulting from this molecular arrangement adopt the shape of a six-branch star. The cavity separation is 19 Å in this 2D covalent structure.

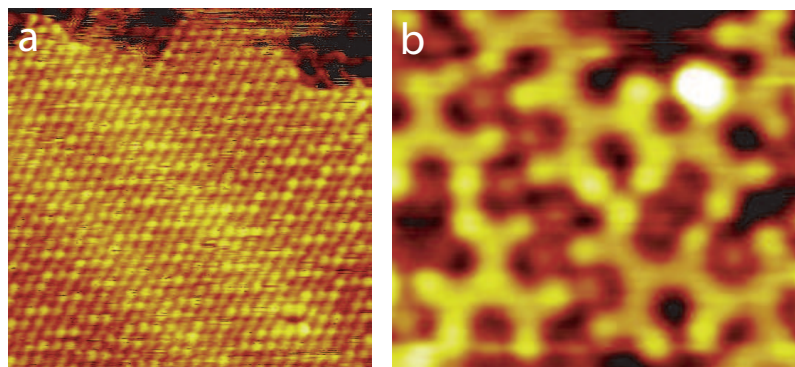


Figure 6.12: STM images of the bromine adatoms on Au(111)- $22 \times \sqrt{3}$ after 175°C annealing. (a) $17 \times 17 \text{ nm}^2$, $V_s = 0.9 \text{ V}$, $I_t = 90 \text{ pA}$. (b) $5 \times 3 \text{ nm}^2$, $V_s = 0.5 \text{ V}$, $I_t = 80 \text{ pA}$.

The STM images in Figure 6.10 show that the bromine adatoms produced during the dehalogenation process can form hexagonal domain (Figure 6.10a) on Au(111) or can be trapped in between the covalent structures (Figure 6.10b). Trapped bromine adatoms appear darker than the molecules in the STM images. It should be noticed that the Au(111)- $22 \times \sqrt{3}$ reconstruction can be observed underneath the bromine network in Figure 6.10a. This suggests that bromine adatoms are physisorbed on the Au(111) surface.

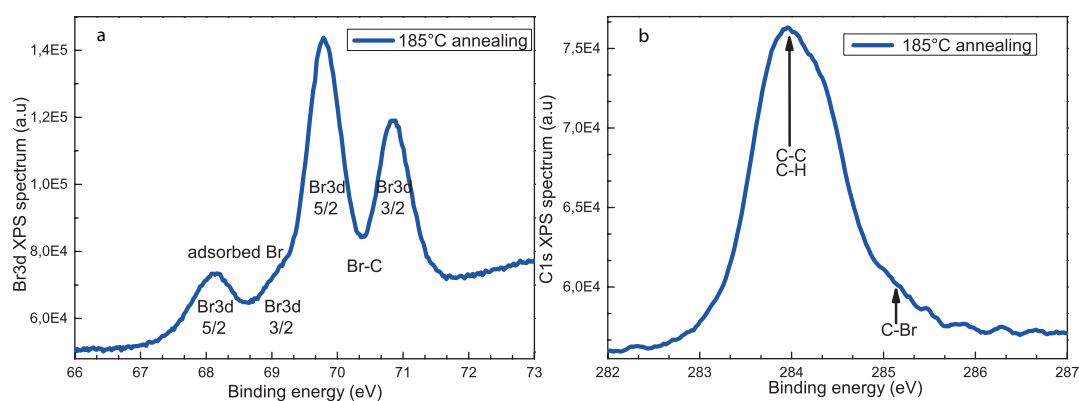


Figure 6.13: X-ray photoemission spectra acquired on TEMPO beamline at Soleil synchrotron after deposition of T2BPB molecules at room temperature on Au(111) surface followed by subsequent annealing at 185°C. (a) Br_{3d} XPS spectrum acquired with a 185 eV photon energy. (b) C_{1s} XPS spectrum acquired with a 485 eV photon energy.

Figure 6.13a and b are respectively Br_{3d} and C_{1s} XPS spectra measured after room temperature deposition of T2BPB molecules on Au(111) and subsequent annealing at

6. TEMPERATURE-DEPENDENT HIERARCHICAL ON-SURFACE SYNTHESIS OF POROUS HALOGEN-BONDED, HYBRID AND COVALENT TWO-DIMENSIONAL NANOARCHITECTURES

185 °C. The Br_{3d} and C_{1s} spectra were acquired with a photon energy of 185 eV and 485 eV respectively. Similarly to the room temperature deposition measurement, the Br_{3d} spectrum presents one main doublet (corresponding to Br-C). The other component at lower binding energy corresponding to Br adsorbed on surface appears as a doublet on this spectrum. The binding energy of the main doublet remains the same as for the room temperature deposition. The amplitude of the main doublet is however significantly lower than the room temperature deposition measurement. This is consistent with our STM observations that show that a large amount of T2BPB molecules are at least partially debrominated after 175 °C annealing. The intensity of the doublet corresponding to adsorbed Br atoms is significantly enhanced, in accordance with STM observations.

The C_{1s} spectrum is presented in Figure 6.13a. Two main components are still observed in this spectrum. The large broad component is centered around 283.6 eV, shifted from around 0.12 eV with respect to room temperature deposition. The shift of main carbon C_{1s} component was also reported in the literature for on-surface Ullmann coupling reaction [171, 174]. A shoulder (corresponding to C-Br) is still observed at higher binding energy but its intensity is strongly diminished compared to room temperature deposition measurement. Again, this is totally in agreement both with the high dehalogenation rate observed by STM at 175 °C and with the strong diminution of the main component of the Br_{3d} spectrum corresponding to bromine bonded to carbon atoms.

6.6 Exclusive formation of double covalently-bonded nanoarchitectures after deposition onto a 275 °C Au(111) surface

Figure 6.14a shows a large scale STM image of the Au(111) surface after deposition of 1,3,5-Tris(3,5-dibromophenyl)benzene molecules onto a 275 °C Au(111) surface. The high resolution STM images in Figure 6.14b,c reveal that the surface is now exclusively covered with porous double-covalent-bond (type-A) nanoarchitectures. An STM image of one of these structures and its model are presented in Figure 6.14c and d, respectively. The molecules inside these structures are covalently linked to three neighbors through double-covalent bonds (type-A). The cavities inside this structure adopt an hexagonal arrangement and a round aspect in the STM image. The cavity separation is 7 Å.

Figure 6.15a and b are respectively Br_{3d} and C_{1s} XPS spectra measured after room temperature deposition of T2BPB molecules on Au(111) and subsequent annealing at 260 °C. Br_{3d} spectrum was acquired with a photon energy of 185 eV and converted into

6.6 Exclusive formation of double covalently-bonded nanoarchitectures after deposition onto a 275°C Au(111) surface

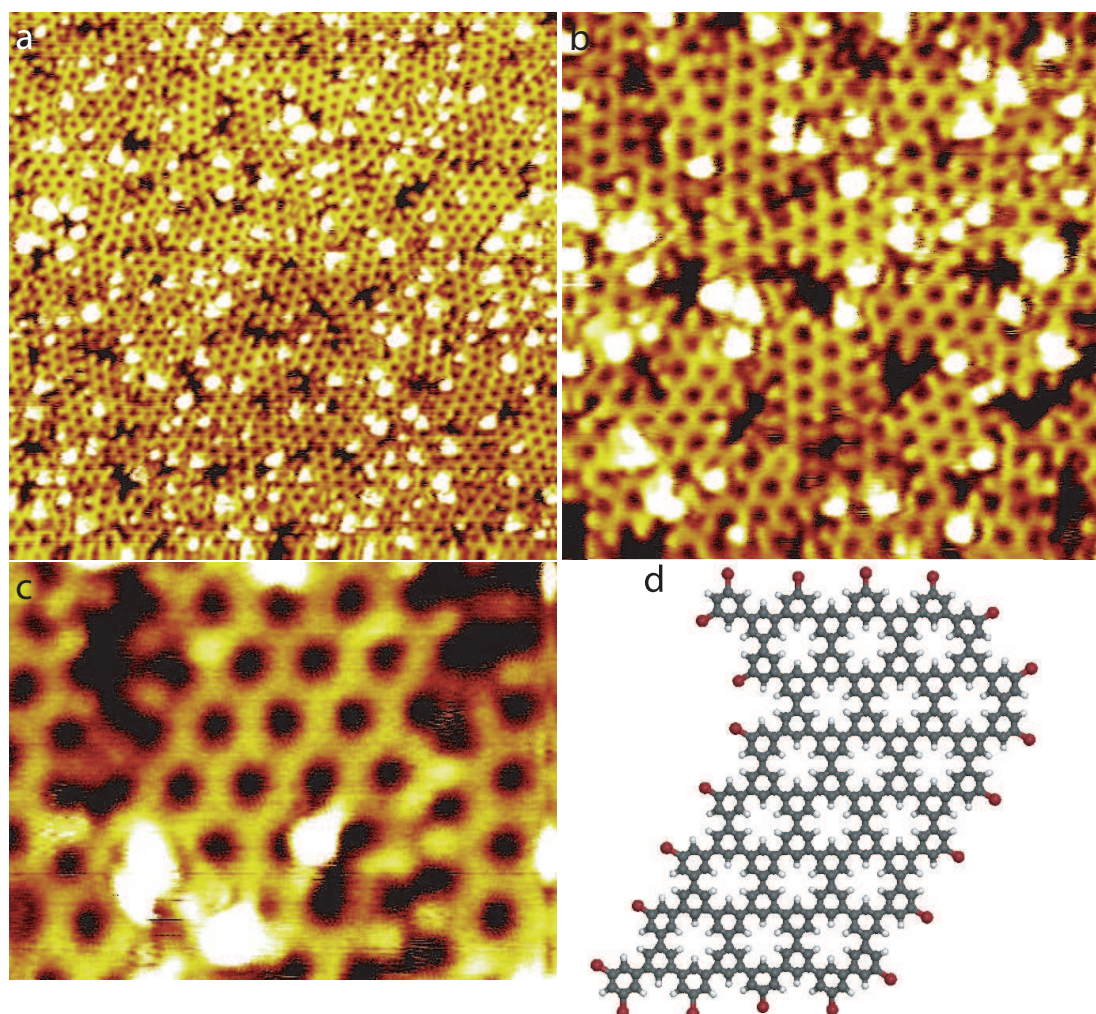


Figure 6.14: *STM images of the molecular arrangement after molecular deposition onto a 275°C Au(111)- $22 \times \sqrt{3}$ surface. (a) $24 \times 24 \text{ nm}^2$, $V_s = 0.4 \text{ V}$, $I_t = 45 \text{ pA}$. (b) $12 \times 12 \text{ nm}^2$, $V_s = 0.5 \text{ V}$, $I_t = 45 \text{ pA}$. (c) $5 \times 3 \text{ nm}^2$, $V_s = 0.4 \text{ V}$, $I_t = 80 \text{ pA}$. (d) Model of the covalent nanoarchitecture observed in the center of (c).*

binding energy. No bromine signal is observed. This is in agreement with STM observations that show that all the T2BPB molecules were fully debrominated after deposition on Au(111) at 275°C. The C_{1s} spectrum is presented in Figure 6.15b. This time, only one large component is observed in this spectrum. This large broad component is centered around 283.6 eV at the same position than for the 185°C annealing measurement. The shoulder component (corresponding to C-Br) at higher binding energy is not observed

6. TEMPERATURE-DEPENDENT HIERARCHICAL ON-SURFACE SYNTHESIS OF POROUS HALOGEN-BONDED, HYBRID AND COVALENT TWO-DIMENSIONAL NANOARCHITECTURES

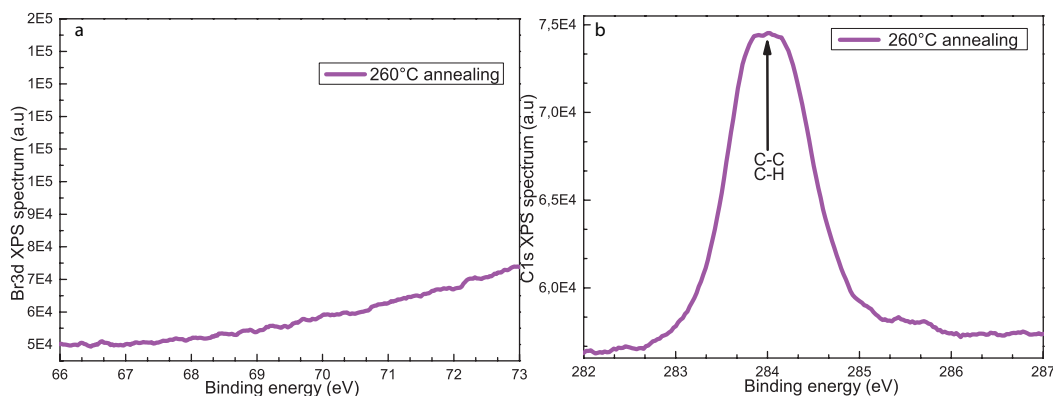


Figure 6.15: X-ray photoemission spectra acquired on TEMPO beamline at Soleil synchrotron after deposition of T2BPB molecules at room temperature on Au(111) surface followed by subsequent annealing at 260°C. (a) Br_{3d} XPS spectrum acquired with a 185 eV photon energy. (b) C_{1s} XPS spectrum acquired with a 485 eV photon energy.

anymore. This is in total agreement both with the disappearing of the main Br_{3d} component (corresponding to bromine bonded to carbon atoms) and the STM observations at 275 °C showing that all the T2BPB molecules were debrominated.

6.7 Summary of the temperature-dependent covalent nanostructures formation

The temperature-dependent self-assembly and on-surface reaction of 1,3,5-Tris(3,5-dibromophenyl)benzene (T2BPB) molecules on Au(111) surface in vacuum has been investigated using STM. STM images show that molecules self-assemble into halogen-bonded nanoarchitectures on the Au(111) surface at room temperature. The molecules are oriented in the same direction in a domain. The 2D arrangement is stabilized by X₃ halogen synthons (Figure 6.3a,c). STM images are here revealing that molecular domain boundaries are systematically observed in the gold surface hcp stacking region (see Figure 6.2). The molecules of neighboring domains are rotated by 180°. There is however no gap appearing in the organic layer, *i.e.* the molecules are also forming X₃ halogen synthons at the domain boundary (Figure 6.3b,d).

Local molecule dehalogenation and the on-surface synthesis of covalent structures through Ullmann coupling is observed after surface annealing at 145 °C. Not all the molecules are reacting on the surface but the concerned molecules are preferentially forming single-covalently bonded dimers (type-B covalent bond). Larger covalent blocks (involving three to four molecules) are in comparison locally observed. STM reveals that

6.7 Summary of the temperature-dependent covalent nanostructures formation

these organic building blocks are self-assembling into a mixed covalent and halogen-bonded 2D superstructure. This superstructure is composed of triangular halogen-bonded domains, stabilized by X_3 -synthons, separated by covalent-dimer rows. The three to four-molecule polymers are observed at the intersection of the dimers rows. The polymers conformation and arrangement lead to the formation of uncompleted (or defective) covalent hexagons (Figure 6.10e) that would appear in the non-defective 2D superstructure, presented in Figure 6.6. The 2D self-assembled hybrid superstructure is still stabilized by X_3 -synthons between the different organic building blocks (Figure 6.7).

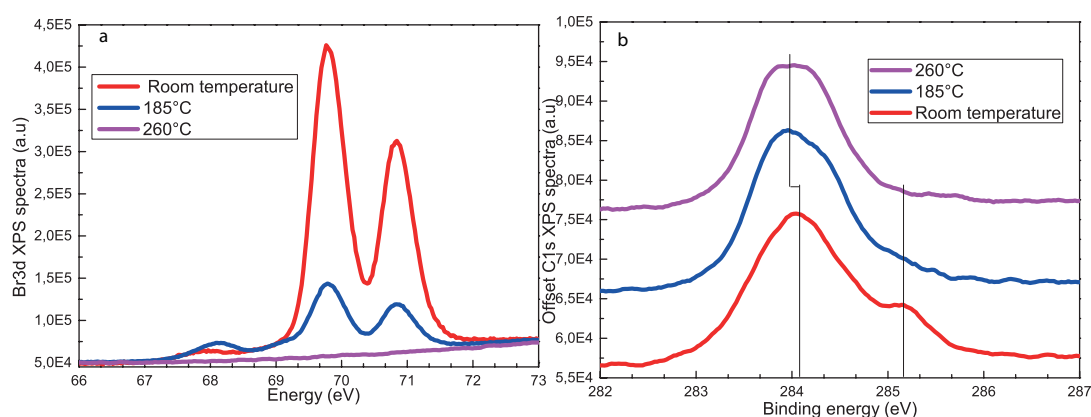


Figure 6.16: Evolution of the X-ray photoemission spectra acquired on TEMPO beamline at Soleil synchrotron after deposition of T2BPB molecules at room temperature on Au(111) surface depending on the surface temperature. (a) Br_{3d} XPS spectra acquired with a 185 eV photon energy. (b) Stacked C_{1s} XPS spectra acquired with a 385 eV photon energy.

The formation of X-bonded domains of single molecules is not observed above 165 °C surface annealing. At this temperature molecules are forming covalent chains, composed of more than four molecules bonded through single-covalent bonds (type-B). The molecules are usually covalently-linked to two neighbors. Molecules with three covalently-linked neighbors are only locally observed (Figure 6.9b). Halogen X_2 -synthons are now observed between neighboring chains. Single molecules are now only very locally observed (Figure 6.9b).

New covalent structures are appearing on the surface after annealing at 175 °C. Covalent hexagons made of six molecules can now be observed on the surface (Figures 6.10b,e, Figure 6.11). The number of molecules with three single-covalent bond neighbors is increasing. This leads to the local formation of the chiral covalent hexagon network (Figure 6.11). Small structures stabilized by double-covalent bond between molecules are in addition observed on the surface (Figures 6.10b,c,f). These structures are usually

6. TEMPERATURE-DEPENDENT HIERARCHICAL ON-SURFACE SYNTHESIS OF POROUS HALOGEN-BONDED, HYBRID AND COVALENT TWO-DIMENSIONAL NANOARCHITECTURES

composed of two molecules covalently linked through double-covalent bonds. Structures composed of three molecules are only locally observed (Figures 6.10f).

After surface annealing at 275 °C, large organic nanoarchitectures stabilized by intermolecular double-covalent bonds are observed on the surface (Figure 6.14). These structures are porous, with cavity size and separation smaller than those observed in the nanoarchitectures formed at 175 °C.

Figure 6.16 summarizes the evolution of the Br_{3d} (Figure 6.16a) and C_{1s} (Figure 6.16b) XPS spectra with the surface temperature. The shift of the main C_{1s} component after 185 °C annealing is highlighted by a vertical line. The disappearing of the C-Br shoulder with progressive debromination of the T2BPB molecules is also highlighted by a vertical line. The progressive debromination of T2BPB molecules is also observed in the Br_{3d} spectra. The intensity of the main doublet corresponding to Br-C strongly decreases after 185 °C and disappears at 260 °C. The intensity of the doublet corresponding to bromine atoms adsorbed on the surface increases after 185 °C annealing.

Chapter conclusion

The on-surface synthesis of covalent nanoarchitectures and the self-assembly of star-shaped 1,3,5-Tris(3,5-dibromophenyl)benzene (T2BPB) molecules was investigated using scanning tunneling microscopy. STM shows that molecules self-assemble into a porous halogen-bonded nanoarchitecture at room temperature. Increase of surface temperature leads to the formation of covalent nanostructures bonded by type-B covalent bonds through Ullmann coupling. The size of the covalent blocks as well as the number of covalent bonds between molecules increase with temperature. The number of single-covalent-bond linked molecule is increasing with temperature, until molecules have three covalently-linked neighbors. Then, double-covalently linked structures appear on the surface. The number of double-covalent-bond linked molecules is also increasing with temperature, until it reaches three after 275 °C annealing. Different types of mixed halogen-bonded/covalent as well as covalent porous nanoarchitectures can thus be engineered by precisely selecting Au(111) surface temperature. These observations open up new opportunities for tailoring 2D organic porous covalent films with tuneable cavity size and separation on metal surfaces.

Chapter 7

General Conclusion and Outlook

The objective of my PhD project was to engineer novel two-dimensional organic nanostructures and investigate their properties. Bottom-up approach was chosen to engineer such nanostructures. Both organic and inorganic building blocks were evaporated in an Ultra High Vacuum (UHV) environment on clean and flat metal surfaces (Chapter 2). Building blocks deposition was controlled with a high precision and repeatability using Knudsen-cell and electron-beam evaporators. The UHV environment permitted the engineering of high quality 2D nanostructures without being affected by the ambient environment. Scanning Tunneling Microscopy (STM) was used to characterize the nanostructures with atomic resolution. Local arrangement of the building blocks and the geometry as well as specific electronic properties of the 2D nanoarchitectures synthesized were measured. X-ray Photoemission Spectroscopy was also used in Chapter 6.

Two major approaches were investigated in this work.

The first approach relies on the self-assembly properties of specific building blocks. It consisted in taking advantage of intermolecular interactions between building blocks to spontaneously form ordered 2D nanostructures also called “self-assembled nanostructures”. It was shown in Chapter 1 that the self-assembly process results from the complex balance between building block-substrate and the building block-building block interactions. Several parameters can be used to engineer novel self-assembly such as tuning the building block geometry or the molecular functions.

In the Chapter 3, self-assembled organic thin films were engineered on Au(111) surface using a perylene derivative (PTCDI) molecule as building block. PTCDI building block has C=O and N-H chemical groups at its both ends allowing the formation of hydrogen bonds (H-bonds). PTCDI was shown to self-assemble into two different structures, canted and side-by-side, both stabilized by H-bonds between the building blocks. The electronic properties of the organic film were shown to strongly depend on the local structure. A

7. GENERAL CONCLUSION AND OUTLOOK

specific lateral intermolecular electronic coupling was evidenced for PTCDI molecules in side-by-side arrangement. Contrary to the molecules in the canted arrangement, side-by-side molecules appeared less coupled to the gold substrate (observation of the LUMO orbital) and localized electronic states were observed in between. Local modifications of the PTCDI self-assembled nanoarchitecture were performed using the STM tip, resulting in the activation of these localized electronic states. These observations open new perspectives to engineer novel organic materials and tune their electronic properties.

Another way to engineer organic self-assembly with new structures and properties is to take advantage of different inter-building blocks interaction. In the Chapter 4, ionic-organic interactions were investigated. These interactions were not completely understood and not much explored. Similarly to Chapter 3, PTCDI was used as organic building block. Sodium chloride (NaCl) was chosen as additional ionic inorganic building block. Pure NaCl was evaporated on Au(111) surface and found to form (100) faceted crystalline domains. PTCDI and NaCl were co-deposited on Au(111) surface and PTCDI molecules appeared to form nanostructures that differ from the canted or side-by-side arrangement observed for pure PTCDI in Chapter 3. Instead, PTCDI formed “flower” structure for which the molecules, forming petals, were all oriented towards the center of NaCl clusters. Temperature was then used to tune the nanoarchitecture and three other hybrid two-dimensional nanostructures were engineered depending on the annealing temperature of the surface. Atomic resolution STM images revealed the ion location in these hybrid nanoarchitectures. The organic-ionic interactions between PTCDI and NaCl were found to originate from the electrostatic interaction between negatively charged chlorine ions and positively charged PTCDI N-H groups. This ionic-organic interaction resulted in the formation of PTCDI \cdots NaCl \cdots PTCDI sticks or longer hybrid chains that appeared to be the repeating unit in these new hybrid nanoarchitectures. These structures were also stabilized by H-bonds. Adding NaCl to PTCDI building block allowed the engineering of temperature tunable hybrid nanoarchitectures with new structures and properties. Therefore, ionic-organic hybrid nanoarchitectures appear as a promising alternative to metal-organic and multicomponent organic structures to engineer novel nanoarchitectures on surfaces.

The second approach relies on the formation of covalent bonds between the building blocks. Due to the high binding energy of the covalent bonds compared to other intermolecular interactions used in molecular self-assembly, the covalent bonds are considered to be irreversible. To create supported two-dimensional covalent nanostructures, on-surface formation of covalent bonds between the precursors is required. Among the

different on-surface reactions leading to C-C covalent coupling, Ullmann coupling reaction was studied.

In the Chapter 5, star-shaped precursor with terminal iodine atoms (TIPB) was investigated on Au(111) surface. The influence of the precursor diffusion on the C-C bond formation was studied. Coverages lower than 0.2 ML lead to deiodinated TIPB molecules forming covalent nanostructures. These covalent structures evolved with the TIPB coverage from 1D chain structure to 2D porous covalent nanoarchitectures. Pores of different sizes and shapes were observed resulting in non-regular 2D structures. These covalent nanostructures were found to grow from the step edges of the Au(111) substrate. Free iodine atoms generated after TIPB dehalogenation were found sometimes trapped into the porous covalent structures and more often trapped along Au(111) step edges. Above 0.2 ML, unusual stop of the Ullmann reaction was observed. Evaporated TIPB molecules above 0.2 ML appeared to not be dehalogenated. Instead, TIPB molecules formed organized porous structures stabilized by halogen-halogen bonding. X-bonded area appeared to grow with increasing TIPB coverage, thus squeezing covalent nanostructures at their boundaries. Above 1 ML coverage, squeezed covalent nanostructures were propelled on top of the X-bonded network. Annealing or deposition at higher temperature did not affect the X-bonded structures much for monolayer coverage. This unusual behavior was explained by the diffusion limited dehalogenation process and the progressive poisoning of the surface step edges by iodine atoms. These step edges are known to be important catalytic sites. Low surface coverage allows TIPB molecules to diffuse to the reactive sites (step edges and Au elbow) and to form covalent nanostructures. High coverage on contrary prevents molecules to diffuse to the reactive sites, that are increasingly poisoned by iodine atoms. Consequently, TIPB molecules stayed intact on the surface and form X-bonded self-assembly. Covalent structures were reported to be propelled on top of the halogen-bonded organic layer above 1 ML coverage. These observations potentially open up new opportunities for decoupling covalent nanoarchitectures from catalytically active and metal surfaces in vacuum.

In the Chapter 6, another star-shaped precursor was studied for on-surface Ullmann coupling application. In contrast with TIPB having terminal iodine atoms studied in Chapter 5, the building building block studied in this chapter had terminal bromine atoms. Two equivalent bromine atoms are attached to each arm of the T2BPB molecules. Two T2BPB molecules can form two kinds of covalent dimers with one or two covalent bonds between the two precursors. Therefore, T2BPB potentially allowed the engineering of covalent nanoarchitectures with structures which differ from single substituted star-shaped precursors. In this chapter, the influence of the temperature on the growth of

7. GENERAL CONCLUSION AND OUTLOOK

covalent organic nanoarchitecture by on-surface Ullmann coupling reaction was studied. All the T2BPB molecules were found to be intact when evaporated on Au(111) surface at room temperature. T2BPB molecules formed X-bonded self-assembled nanostructure with two possible orientations for T2BPB molecules. The orientation was shown to be affected by the underlying Au(111) reconstruction and to flip at the hcp areas of the gold surface. After annealing at 145 °C, T2BPB molecules appeared to form triangular tessellation structure. This structure was composed of intact X-bonded domains separated by lines of covalently bonded dimers. The vertices of such structure were (defective) hexagonal structures made of covalently bonded T2BPB. After annealing at temperature higher than 165 °C, only covalent nanoarchitectures were observed and consequently no more X-bonded structure. After deposition at higher temperature (275 °C), only one kind of covalent bond was observed (double bonds). Consequently, large periodic porous 2D covalent hexagonal carbon nanostructures were successfully engineered.

The results presented in this manuscript open new perspectives. Self-assembly was shown to be a versatile process to generate high quality two-dimensional nanostructures. A single organic building block like PTCDI was shown to have totally different electronic properties depending on the local arrangement, opening new perspectives in the molecular electronics domain. Moreover, the same building block was shown to form new organized hybrid ionic-organic nanostructures associated to sodium chloride. Ionic-organic interaction was shown to be a promising alternative to metal-organic interactions thus broadening the 2D self-assembly possibilities. The other prospects concern the on-surface formation of two-dimensional covalent nanostructures. Graphene and associated two-dimensional covalent carbon nanostructures appear as promising materials for the future electronic devices. On-surface Ullmann coupling was shown to be a promising approach to engineer such carbon nanostructures on surface and the diffusion of precursor was shown to be crucial for the activation of the reaction. Large periodic porous carbon nanostructures have been synthesized through temperature-controlled hierarchical coupling reaction. Other alternatives can be envisioned to improve the size and the quality of such nanostructures. Highly energetic photons such as UV light could be used to trigger the activation of the carbon-halogen dissociation reaction. Different catalytically active materials could also be deposited on the surface to tune the dehalogenation reaction activation for example.

Appendix A

Interfacing and automating of laboratory equipments

The objective of this chapter is to present the programming work done during this project. As explained in the previous chapters, a high precision and reproducibility were required to engineer two-dimensional nanostructures on surface. Controlling and measuring the heating stage temperature with precision was mandatory for temperature-dependent nanoarchitecture engineering. For example, it was shown in Chapter 4 that four different hybrid PTCDI-NaCl nanoarchitectures could be engineered depending on the surface temperature. In Chapter 6, it was shown that a difference of few degrees could drive the formation of different covalent nanostructures by on-surface Ullmann coupling reaction. The objective of this programming work was also to improve the time efficiency of repetitive tasks such as surface preparation. Another objective was to monitor and save the different parameters of the experiment. For example, it is very helpful to keep a log file of the pressure to have the history of every event and potentially understand the origin of failures, outgasings, leaks etc. . . All the programs presented in this chapter have been created using the Labview software. For the sake of simplicity, I will not describe precisely the code of the programs. This chapter will be focused on the various options, securities and capabilities of such programs.

A.1 Pressure monitor

A.1.1 AML PGC2 gauge controller

The objectives were to collect, display and save all the useful parameters measured by the pressure gauge controller with the highest precision available. I used an old PGC2 pressure gauge controller manufactured by AML. PGC2 can communicate with a RS232 port. Actually, this device is only capable of sending information and not receiving it. It communicates at a speed of 2400 baud using frame with one start bit, two stop bits, no parity and no handshaking. Each frame contains 106 bytes and the device sends one frame every second. The task was to discriminate each part of the string and to extract the corresponding information. The pressure readings correspond to IG1-IG4 because the controller actually measures the pressure four times in a second. These IG are strings of pressure written in scientific notation with two-digit precision (e.g “1.0+03”). These strings were converted into numbers or “double precision float” in the Labview language. We will refer to these numbers as “double” in the following.

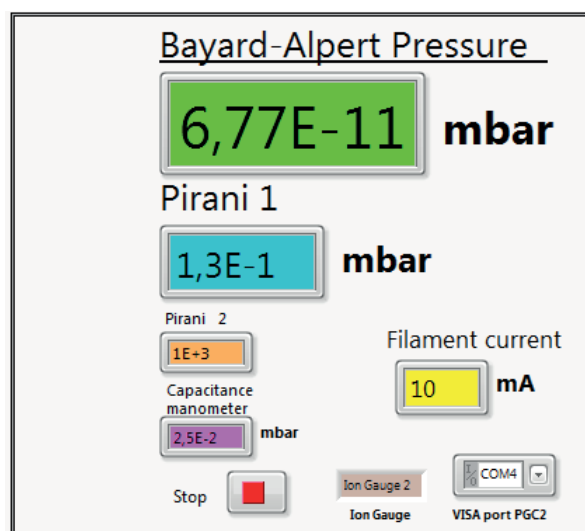


Figure A.1: User interface of the PGC2 pressure controller program.

The four pressures were then averaged and displayed in a dynamic graph (Figure A.2). The program can consequently display a pressure value once a second, with a higher precision than the display located at the facade of the controller that only has two digits. The program can also display several other parameters such as the emission current, the ion gauge in use, the unit of pressure measurement and the capacitance manometer value that are also collected and processed. The pressure measured by the Pirani gauge placed

A.1 Pressure monitor

just before the turbomolecular pump is also displayed. This program can thus display both the Bayard-Alpert and the Pirani gauge pressure at the same time, which is not possible on the controller itself.

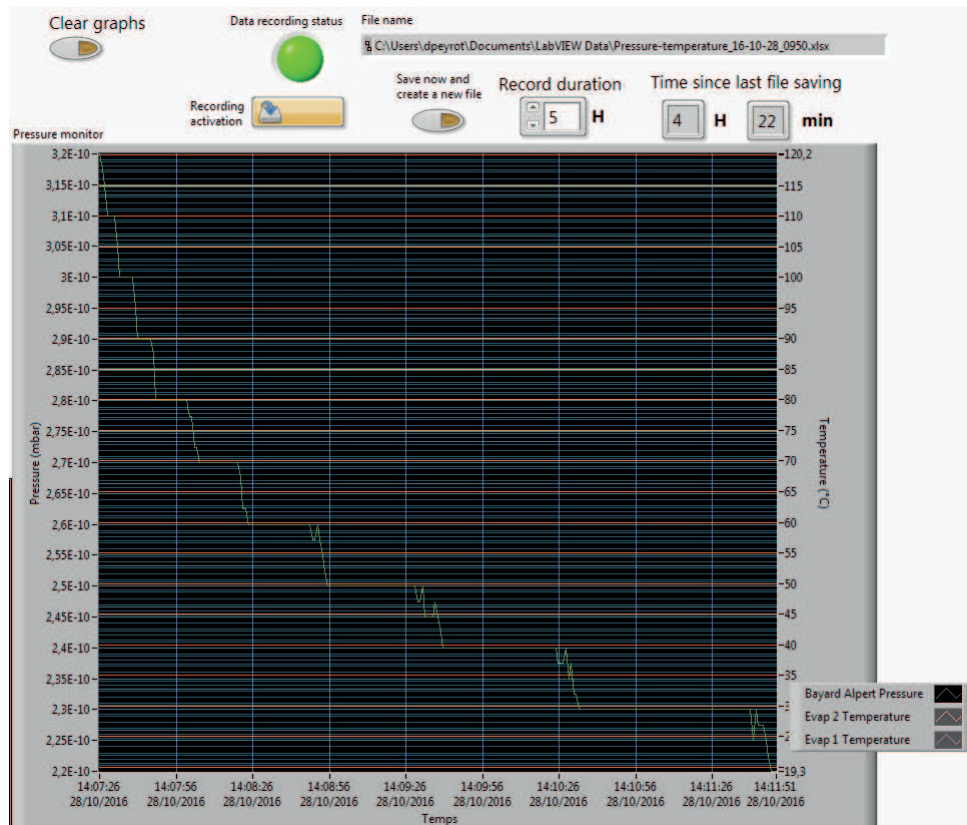


Figure A.2: User interface of the PGC2 pressure controller program showing the pressure evolution on a dynamic time-stamped graph.

A.2 Power supply controller

A.2.1 Delta Elktronika ES230-10

A.2.1.1 RS232 Model

Power supplies were used for essentially two applications in the lab: heating the sample and/or controlling evaporators. In this section, I will describe the program designed for sample heating application. The objectives of this program were to gain time efficiency, reproducibility and precision for sample heating procedure. A typical heating process consists in progressively increasing the current flowing in the tungsten filament until the targeted temperature is achieved. The current value is kept constant to keep a stable sample temperature and is then progressively decreased to cool down the sample. I used a Delta Elktronika ES230-10 power supply with RS232 interface. A type-K thermocouple is located near the sample on the heating stage for temperature measurements. When I started my PhD, the heating process was entirely manual. The operator had to gradually increase the current in the filament by turning the knob on the power supply front panel and control the temperature wiring the thermocouple signal to a multimeter. The objective of my program was then to drive automatically a complete heating process and monitor the filament current and power as well as the sample temperature.

The temperature is monitored by a NI-TC01 thermocouple module that is connected to the computer *via* USB. Delta Elktronika ES230-10 communicates at a baud rate of 9600. It comes with a driver allowing the configuration of the serial connection, as well as read/write access on current, voltage, max current and voltages limits as well as various alarms and indicators. This driver was used almost without modification in my program for the so-called “manual mode”. In the manual mode (Figure A.3), output voltage and current values are displayed and knobs are used to modify their values from the computer interface. However, since we wanted to automatize the heating process, I added a second mode called “auto mode”. The switch between auto and manual mode is made by sliding a button.

The auto-mode is entirely “current controlled” (Figure A.4), meaning that the voltage is set to the maximum value and only the output current value is changed. This mode consists in creating a sequence made of three phases. First, the current increases linearly from a set value (I_{min}) to another set value (I_{max}) within a given time ($t_{ramp-up}$). Then, the output current value remains constant at I_{max} for a time t_{stat} . Finally, the current decreases linearly from I_{max} to I_{min} within a given time $t_{ramp-down}$.

A.2 Power supply controller

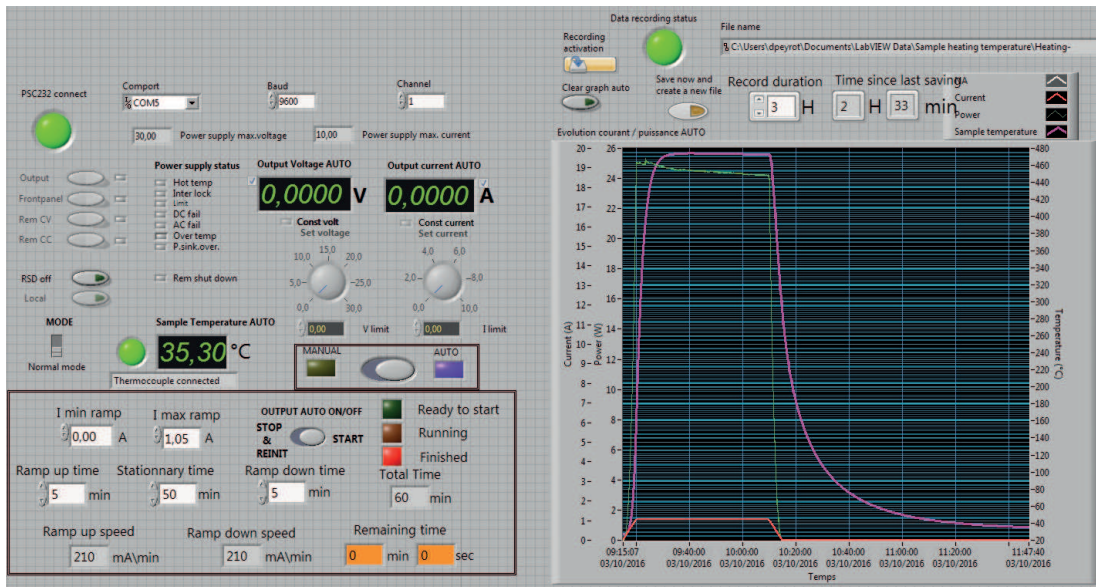


Figure A.3: User interface of the Delta-Elektronika power supply controller program (RS232) in the manual mode.

The program automatically computes the corresponding ramping-up and down speeds expressed in mA/min from the parameters entered by the user. Once all the parameters are set, the “ready to start” green signal is lighted and the user only has to slide the “output on-off” button to the start position. After that, the predefined sequence will start, the green signal will be off and the orange “running” signal lighted. The remaining time expressed in minutes and seconds is displayed on the program. When the sequence ends, the “finished” red signal is on and the output current value remains at I_{min} . To stop and reinitialize the sequence, the user only has to slide the button “output auto on/off” back to the “Stop and Reinit” position.

Our program is thus able to drive a complete sample-heating cycle with high precision and reproducibility. The ramp-up/down and stationary time are set with an error range lower than a second. The output parameters are measured at least two times per second. The precision on the targeted and measured current values is not limited by the program and is therefore limited by the power supply intrinsic properties (around 1mA). The set of data including output voltage, current and thermocouple temperature is displayed on a dynamic graph. Timestamped graph data are automatically stored in an .xls file with a frequency that is defined by the user (typically every three hours). After that, all the data are cleared from the buffer and a new graph is displayed. The user also has the option to save the data and start a new log file, but also to clear the graph, at every moment,

A. INTERFACING AND AUTOMATING OF LABORATORY EQUIPMENTS

pushing the button “save now and create a new file” and “clear graph auto”, respectively.

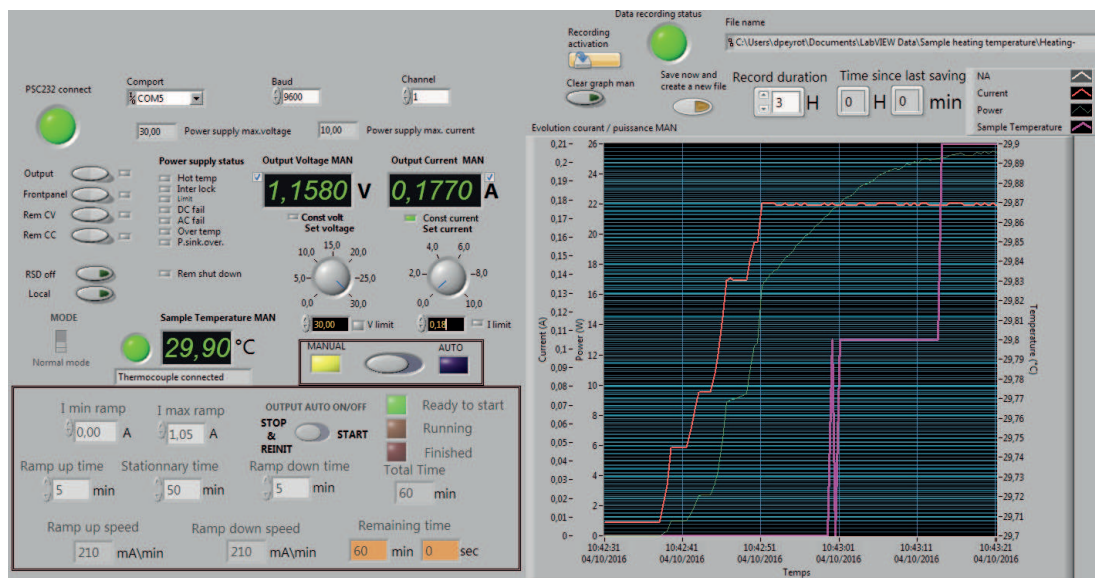


Figure A.4: User interface of the Delta-Elektronika power supply (RS232) controller program in the auto-mode.

A.2.1.2 Ethernet Model

A similar power supply with ethernet port option was also interfaced. The user interface and the functions available on the ethernet power supply program are almost exactly the same as the RS232 model. However, due to intrinsic differences in the communication protocols, the communication structure of this program strongly differs from the RS232 program. The power supply is identified on the network by its IP address that the user has to enter in the program to communicate with it. To control (write and/or read) parameters of the power supply, the user has to send predefined commands such as “sour:curr\s 1.5” and “sour:volt\s 10” to respectively set the output current at 1.5A and the voltage at 10V. To get the measured output values, the user has to send “meas:curr?\n” and “meas:volt?\n”. UDP protocol was unsuccessfully used to communicate with the power supply. TCP protocol was used instead. The rest of the program architecture is similar to the RS232 version.

A.2.2 Elektro automatic PS 2000

Another power supply model PS2000 manufactured by Elektro Automatik was also interfaced. It communicates with the computer using USB. It was delivered with protected driver programs that were used in my program. A sub-program (or sub-VI in the Labview language) developed by the manufacturer is used to identify the device by its serial number. Once the connection is made, sub-VIs, which are adapted from the program developed by the manufacturer, are used to set and measure the output voltage/current. The rest of the structure is similar to the program developed for the Delta Elektronika power supplies. The performances of this program are still limited to the power supply properties.

A.3 K-cell evaporators controller

The objective of this section was to build a program that can precisely control and monitor the temperature of different k-cell evaporators. An auto-mode had to be implemented to progressively increase and/or decrease the current in the k-cell filament. This option can be used to heat the crucible at pre-heat temperature (usually 30-20 °C under the typical evaporation temperature) or to cool down the evaporator after the molecule deposition. An additional alarm preventing crucible overheat had also to be implemented.

A.3.1 Createc K-cell evaporators

The controllers of the k-cell evaporators manufactured by Createc were interfaced. In these controllers, the crucible temperature and the filament current are controlled by a Eurotherm 3504 controller that has a RS232 output. Eurotherm provides a Labview driver for their controllers that I partially used in my program. Eurotherm controller communicates at a baud rate of 19200 with no parity bit. The built-in drivers include a VI to initialize the serial connection with the device, a VI to read the manual setpoint value and another one to read the temperature. However, no driver was included to control and change this manual setpoint. The memory address of the controller where this setpoint is stored was found. I built a program that simply replaces the previous setpoint value by a new value in the controller memory. The output current delivered through the k-cell filament is simply given by the active setpoint times a power limitation. This limitation is set by turning a knob on the front panel of the Createc controller. Therefore, depending on the knob position, a completely different current can be delivered for a given

A. INTERFACING AND AUTOMATING OF LABORATORY EQUIPMENTS

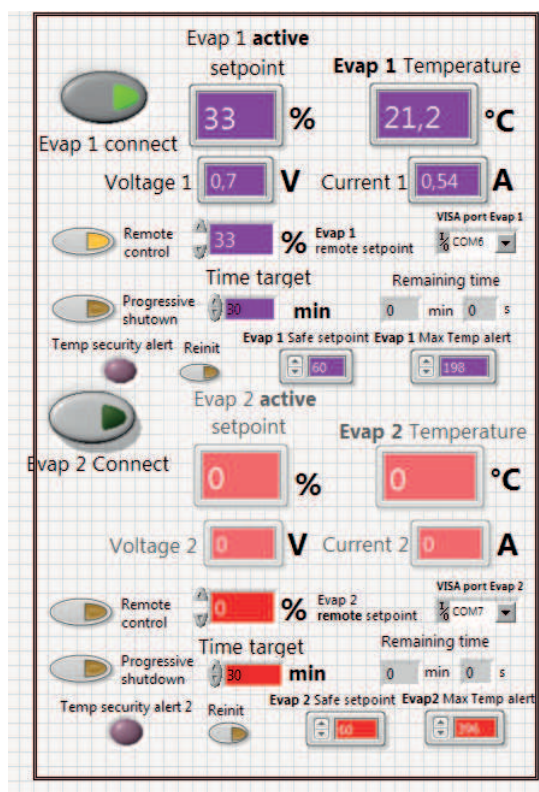


Figure A.5: *User interface of the Createc evaporator controller program.*

Eurotherm setpoint. Consequently, the only information of Eurotherm setpoint was not sufficient and we needed also to monitor the filament voltage and current. Unfortunately, this information was not available in our controllers. The Eurotherm controller was then opened and the voltages applied to the LCD screen displaying the current and the voltage applied to the filament on the front panel of the controller, were measured. These voltages were found to be actually proportional to the values displayed on the LCD displays, and therefore to the real voltage and current value. Two pairs (one for the voltage, one for the current) of two wires were welded from the displays connectors to the back of the controller where they were welded to the pins of an unused serial port. A special connector was connected to this port out of the controller with four wires. The voltages between both pairs are measured by a NI-USB-6000 USB device and sent to the computer. Tests were performed to calibrate the proportional factors between the voltages read at the output of the LCD displays and the value actually displayed on these monitors. These operations were done for the two Eurotherm controllers of the lab.

In my program, once the button “evap connected” is pressed, the active setpoint of the Eurotherm controller, the k-cell temperature, and the filament voltage and current are displayed and monitored. I also added a remote control button that sets the value

of the active setpoint from the computer. When this button is pressed, the initial value of the remote setpoint is automatically set to the active setpoint value measured at the last iteration of the program so as to avoid brutal changes of the filament current. Let us consider that the active setpoint was for example fixed at 42% before the remote control button was pushed and that the remote control value was for example set at 0%. Once the remote control button is pushed, the remote setpoint is automatically changed from 0 to 42% so that the active setpoint value does not change. This is only true for the first iteration after the user pressed the button. After this iteration, the remote setpoint value set by the user will be transferred to the controller as active setpoint. An additional security was added to prevent accidents related to excessive heating of the crucible and consequently unwanted evaporation of large amount of molecules in the chamber. Depending on the molecules placed in the crucible, the user defines a temperature alert (typically 5-10 °C higher than the usual evaporation temperature of the molecules) and a security setpoint (typically half or two third of the active setpoint used to reach the molecule evaporation conditions). If the temperature monitored by the controller becomes higher than this alert temperature, the program will automatically set the active setpoint value to the security setpoint defined by the user. This is true even if the remote setpoint control mode is not activated. The controller will stay at the security setpoint value until the “reinit” button is pressed by the user. After the user has pressed the “reinit” button and only if the temperature has dropped under the maximum temperature limit, the user will be free to set another active setpoint of his choice. Another progressive shutdown option was also implemented in the program. This option requires the remote control mode to be activated. The user sets a time target for the evaporator shutdown. After the button progressive shutdown is pressed, the remote setpoint value is automatically and linearly decreased by the program itself until it reaches zero after the time target.

To summarize, this program allows the monitoring and the control of the temperature (read), active setpoint (read/write) and current/voltage (read) of the evaporators. There are at least two or three iterations per second. The precision of the temperature displayed is imposed by the Eurotherm controller (0.1 °C). The active setpoint precision is 0.1%. The accuracy of I/V measurements is around 0.01 A/V respectively. In the standard mode, the active setpoint is only read but not modified by the program. The user is thus free to modify the active setpoint on the controller front panel. If the user pushes the remote control button, the remote setpoint value is automatically set to the previous setpoint value so as to avoid any brutal variations of the filament current value. After that, the user is free to modify the setpoint value on the computer interface and it is

A. INTERFACING AND AUTOMATING OF LABORATORY EQUIPMENTS

no longer possible to modify the active setpoint on the controller front panel. If the evaporator temperature reaches a given limit, the evaporator setpoint is set to a security limit until the user acknowledges the alarm and reinitializes it. This is true whether the remote control mode is activated or not. An option is also available to progressively shut down the evaporator active setpoint with selected duration.

A.3.2 Custom evaporators

Power supply control programs were adapted to use the power supplies for controlling k-cell evaporators that do not come with a dedicated controller. These programs have the same architecture and were developed to control the ES2030-10 (RS232 and ETH model) and the PS2000 power supply. The evaporator temperature is read using a TC01 USB module, similarly to the heating stage controller. If the thermocouple is not connected to the TC01 module, a red light, a message “thermocouple disconnected” and a 0 temperature will be displayed. An additional feature was added to make these programs compatible with most of the evaporators. Indeed, the TC01 driver is only supporting type-K thermocouple and is not capable of measuring temperature using type-C thermocouple that are sometimes used in k-cell evaporators (the Createc models for example). I added a feature for type-C thermocouple that uses a 6th order polynomial fit to convert the type-C thermocouple voltage to temperature.

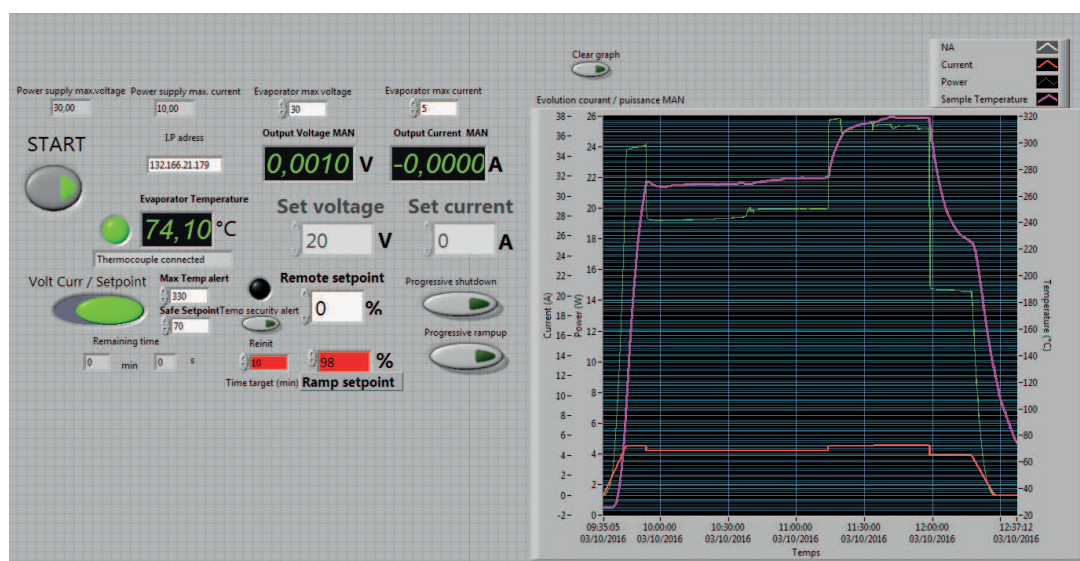


Figure A.6: User interface of the Delta-Elektronika power supply (ETH) evaporator controller program.

Two modes are available in the evaporator programs.

- **The Volt/Curr mode** which is similar to the manual mode of the power supply programs.
- **The Setpoint mode** which is similar to Createc controller program. The user sets a maximum value for evaporator current and voltage (equivalent to turning the power limit knob on the Createc controller). After that, the user sets a remote setpoint that corresponds to a percentage of the maximum current value for the evaporator. For example, if the max current set for the evaporator is 5 A and if the user sets a 50% setpoint, the output current will be 2.5 A. Temperature alert security and progressive shutdown option work exactly as in the Createc controller program. An additional progressive ramp-up option was introduced. The user sets a ramp setpoint and a time target. The program will raise linearly the setpoint from the initial value (when the progressive ramp-up button is pressed) to the ramp setpoint within the desired time. The performances of this program are similar to the performances of the power-supply program.

A. INTERFACING AND AUTOMATING OF LABORATORY EQUIPMENTS

Appendix B

X-ray photoemission spectroscopy and synchrotron radiation

The objective of this chapter is to present the X-ray Photoemission Spectroscopy measurement technique used in Chapter 6. The experimental set-up at Soleil Synchrotron TEMPO beamline, where the measurements were carried out, will also be presented.

B.1 X-ray photoemission spectroscopy (XPS)

B.1.1 General presentation and associated physical processes

The photoemission spectroscopy (XPS) (also called “Electron Spectroscopy for Chemical Analysis” (ESCA)) is a spectroscopic technique relying on the irradiation of a sample with photons of known energy and the consecutive electron photoemission. This phenomenon corresponds to a photoelectric process which has been discovered in 1887 by Franck and explained in 1905 by Einstein. Depending on the energy of the incoming photons, different levels of the sample can be probed. For example, X-ray photons can be used to probe the core-level electrons of the sample whereas UV photons can only be used to probe the valence shell electrons. The photoemission spectroscopy measurements are based on the analysis of the kinetic energy of the extracted photoelectron (Figure B.2). From the energy conservation during the photoemission process, the initial binding energy of the photoelectron extracted from the sample follows the relation B.1:

$$h\nu = E_B + E_K + W_a \tag{B.1}$$

B. X-RAY PHOTOEMISSION SPECTROSCOPY AND SYNCHROTRON RADIATION

where E_B is the photoelectron initial binding energy, E_K its kinetic energy, W_a the work function of the analyzer, h the Planck constant and ν the frequency of the excitation photon at the origin of the photoemission process.

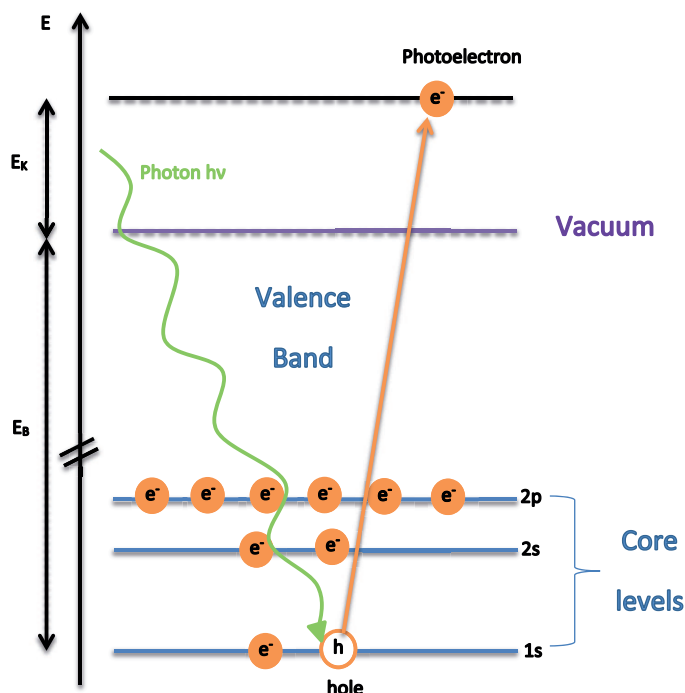


Figure B.1: *Illustration of the XPS measurements principle. X-ray photons are absorbed by the sample leading to the ionization of core-levels and to the emission of photoelectrons having a kinetic energy E_K .*

The photoemission spectroscopy measurements can be easily explained by a simple three-step model:

First step: Photoemission of an electron. Through photoelectric effect, a photon of energy $E = h\nu$ can eject an electron, from the core-levels for example, whose binding energy is less or equal to the photon energy. The photoemission process leads to the subsequent formation of an electron hole in the respective core-level (ionization).

Second step: The photoemitted electron travels toward the surface:

Third step: Depending on the number of inelastic collisions that the photoemitted electrons encounter in their way to the surface, they can reach the surface with different kinetic energies:

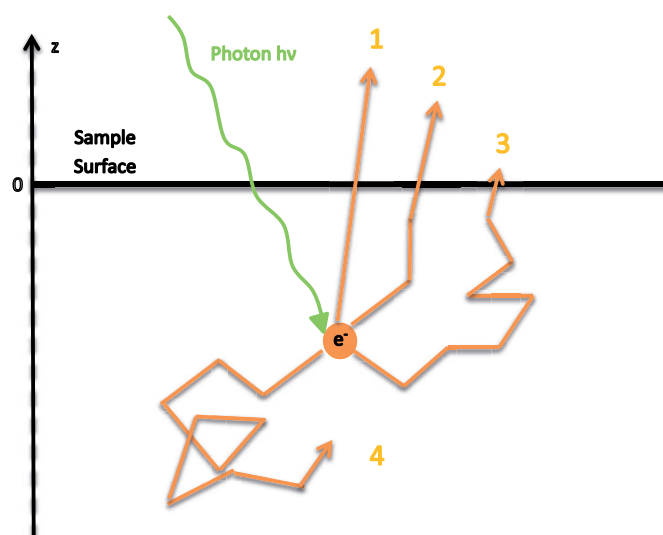


Figure B.2: *Illustration of the inelastic scattering process of the photoemitted electrons.*

- **Case 1:** The electron suffers from no inelastic collision (i.e undergoes no kinetic energy loss) within the sample on its way to the surface. This gives rise to the main photoemission peak observed in the photoemission spectrum (1 in Figure B.2).
- **Case 2:** The photoemitted electron undergoes a moderate kinetic energy loss due to a few number of inelastic collisions before reaching the surface. This leads to the appearance of satellite peaks at higher binding energy in the photoemission spectrum (2 in Figure B.2).
- **Case 3:** The photoemitted electron undergoes a huge kinetic energy loss due to a large number of inelastic collisions. This leads to the appearance of secondary electron peaks at very high binding energy in the photoemission spectrum (3 in Figure B.2).
- **Case 4:** The photoemitted electron cannot reach the surface because of too many inelastic collisions (4 in Figure B.2).

Therefore, electron inelastic collisions within the sample are of prime importance for XPS measurements. It can be shown that photoemitted electron beam follows a Beer-

B. X-RAY PHOTOEMISSION SPECTROSCOPY AND SYNCHROTRON RADIATION

Lambert law attenuation in the substrate:

$$I(z) = I_0 \exp\left(\frac{-z}{\lambda}\right) \quad (\text{B.2})$$

where $I(z)$ is the electron intensity at distance z from the initial emission site, I_0 the electron intensity at the initial emission site. λ is the electron inelastic mean free path, in other words, the typical distance an electron can travel within the sample before an inelastic collision occurs.

From the equation B.2, one notes that the photoelectrons emitted in the XPS measurements are only coming from the part of the sample atoms that are close to the surface. Typical sampling depth is usually taken at 3λ corresponding to the depth at which 95% of the photoelectrons were scattered.

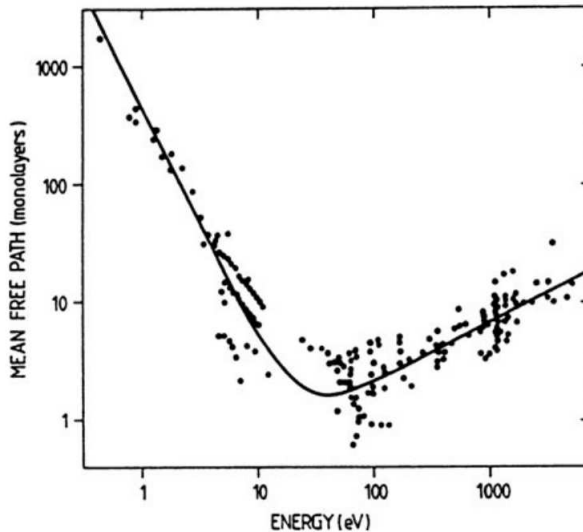


Figure B.3: *Inelastic mean free path (IMFP) of electrons in solids as a function of their energy [175].*

The electron inelastic mean free path also depends on the electron kinetic energy. Surface-sensitive ability is of prime importance to measure the electronic properties of surfaces or nanostructures at mono or sub-monolayer range. Figure B.3 shows the typical dependence of the electron inelastic mean free path with the electron kinetic energy. One can notice that the minimum inelastic electron mean free path corresponds to a kinetic energy of approximately 50-100 eV. Therefore, the use of a tuneable photon source such as a synchrotron radiation could be a great advantage to make extremely surface-sensitive measurements. To do so, one has to select the incoming photon energy to be approximately 50-100 eV greater than the electron binding energy of the element to probe.

B.1.2 Hemispherical electron analyzer

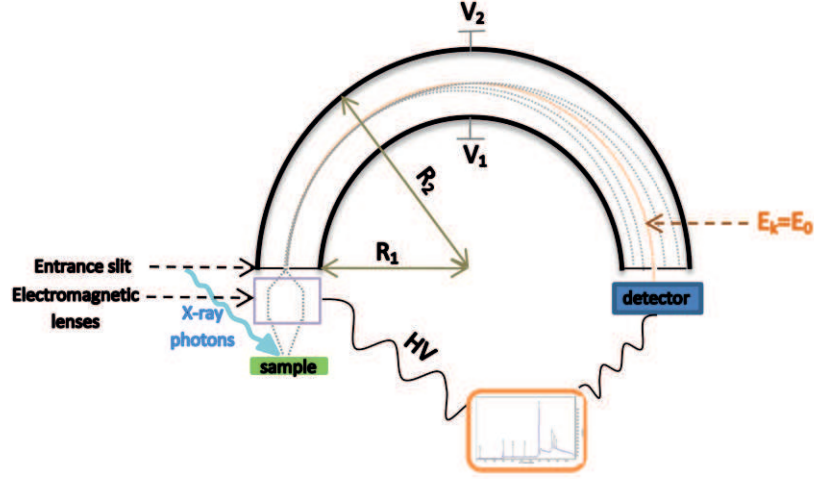


Figure B.4: Scheme of a typical hemispherical spectrometer that is used in photoemission spectroscopy measurements.

The determination of the photoelectron kinetic energy with a high precision is necessary to obtain reliable and detailed core-level electron spectroscopy information. For that purpose, a hemispherical photoelectron detector also called electron analyzer is used. The inner hemisphere (radius of curvature R_1) is put at a potential V_1 whereas the outer hemisphere is put at potential V_2 . Therefore, an electric field is generated and the incoming electrons are deflected. One can show that only the electrons having an energy E_0 imposed by equation B.3 finally reach the detector at the other end of the analyzer. One can tune the bias $V_2 - V_1$ to selectively detect electrons with specific kinetic energy on the detector. This energy E_0 is also called the “pass energy” of the analyzer.

$$E_0 = e \frac{(V_2 - V_1)}{\frac{R_2}{R_1} - \frac{R_1}{R_2}} \quad (\text{B.3})$$

Slits are positioned at the entrance and output to improve the resolution of the analyzer. This resolution also depends on the radius of curvature of the hemispheres as well as the incidence angle of the incoming electrons. It can be expressed as:

$$\Delta E = E_0 \left[\frac{w}{R_1 + R_2} + \frac{\alpha^2}{4} \right] \quad (\text{B.4})$$

where w is the average of entrance and output slits widths and α the incidence angle of the incoming electron beam. Therefore, a lower pass energy leads to a better resolution.

B. X-RAY PHOTOEMISSION SPECTROSCOPY AND SYNCHROTRON RADIATION

However, lowering the pass energy also leads to a reduction of signal to noise ratio (SNR) of the detected electrons.

Electromagnetic lenses are positioned just before the entrance of the electron analyzer. They have two main functions:

- They focus the electron beam inside the hemispherical analyzer.
- They precisely and controllably decelerate the electrons reducing their kinetic energy down to the pass energy E_0 of the analyzer.

In sweep mode, the pass energy of the analyzer is fixed. At the same time, the voltage applied to the electrostatic lenses is swept. Photoemission spectrum can be acquired plotting the number of photoelectrons detected (counts on the detector) against their kinetic energy.

B.1.3 Spectroscopic measurements and peak shape

One can also use the relation B.1 to plot the electron counts against the binding energy of the core-level electrons, thus gaining knowledge on the sample chemistry and composition. Indeed, the core-level electron binding energy depends on the material. For example, the typical electron binding energy for the 1s core-level is 285 eV for carbon, 400 eV for nitrogen and 530 eV for oxygen. One can also determinate the nature of the chemical environment of the sample by XPS, getting insight on the different kinds of chemical bonds on the sample. For example, C-O, C-N and C-C bonds can be discriminated. One can get information about for example the oxidation states of some elements analyzing the shifts of the photoemission components in the spectra. Moreover, one can also get quantitative information through XPS measurements. Indeed, the photoemission peak area is proportional to the number of atoms involved in the photoemission process. Consequently, the analysis of the photoemission peaks intensities can give quantitative information about the sample stoichiometry.

Photoemission spectra are composed of several spectral functions, which take into account all the possible excitation processes in the sample of interest. These spectral functions can be represented by a set of peaks, *e.g.* main lines and satellites, multiplets, doublets depending on the spin-orbit degeneracy. The peak shapes are typically determined by a Voigt function. The Voigt function is a convolution between a Lorentzian and a Gaussian distribution. The Lorentzian contribution originates from the limited lifetime of the core-hole state. The Gaussian broadening is mostly due to the incoming

B.2 X-ray spectroscopy facilities and equipment

X-ray radiation, thermal broadening and also to the resolution of the electron analyzer. Chemical and structural inhomogeneities in the surroundings of the emitting atoms often also contribute to the Gaussian broadening [176].

In conclusion, X-ray Photoemission Spectroscopy is based on the photoemission of core-level electrons. The kinetic energy of the photoemitted electrons is measured with an electron analyzer. The binding energies of the sample core-level electrons are derived from the measurements. The incoming photon energy can be adjusted using a tunable X-ray source such as synchrotron radiation to minimize the photoelectron mean free path. Measurements with high surface sensitivity can thus be achieved. From the analysis of the XPS spectra, peak shape, position, intensity and chemical environment (composition, stoichiometry, oxidation state) of the sample are probed.

B.2 X-ray spectroscopy facilities and equipment

B.2.1 Soleil Synchrotron



Figure B.5: *Aerial picture of the Soleil Synchrotron located in Saint Aubin, France [177].*

Synchrotron facilities provide a photon beam with a wide energy range that can be used *inter alia* for X-ray spectroscopic measurements such as XPS. SOLEIL (“Sun” in French) is a synchrotron facility in Saint-Aubin, near Paris. It performed its first electron acceleration on May 14, 2006. It is a circular accelerator of electrons providing a broad range photon excitation beam, from hard X-ray to infrared [178].

The synchrotron radiation is the light emitted by relativistic electrons (which velocity is close to the speed of light) of very high energy (2.75 GeV at Soleil) spinning in a storage ring (354 m in circumference at Soleil). This is done by tangentially curving the electron beam with a magnetic field (Lorentz force).

- To reach such energies, a small electron beam emitted by an electron cannon is first accelerated in a 16-meter long linear accelerator (Linac) reaching $E_K = 100$ MeV.

B. X-RAY PHOTOEMISSION SPECTROSCOPY AND SYNCHROTRON RADIATION

- After this initial acceleration, the electron beam is directed towards a circular accelerator called the booster until the electrons reach an energy of 2.75 GeV.
- The electrons are injected into the storage ring of 354 m circumference and spin for several hours.
- In the storage ring, magnetic devices control the trajectory of the electrons and make them controllably oscillate. The electrons then lose energy emitting photons (synchrotron radiation).
- The synchrotron radiation is then processed by optical systems toward experimental stations also called beamlines. There are 26 beamlines at Soleil, each one devoted to a special photon range, analysis technique and purpose.

XPS measurements presented in this manuscript were acquired using one of these 26 beamlines called TEMPO.

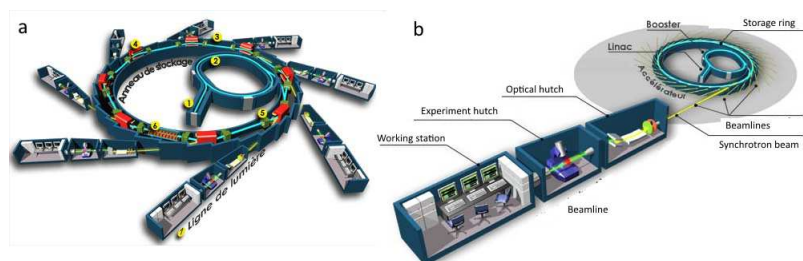


Figure B.6: *Scheme of the Soleil Synchrotron [178].*

B.2.2 TEMPO beamline

The TEMPO beamline has two undulators HU80 and HU44 with a output X-ray photon energy range varying between 50 and 1500 eV. It is equipped with two UHV chambers and one load-lock chamber. Organic molecules can be deposited on the sample in the preparation chamber on which standard surface preparation elements are installed (Ar^+ gun, electron bombardment heating system). The sample can be transferred in the measurement chamber where a cryostat can be used to cool the sample at $T \approx 50\text{K}$ using liquid He. X-ray photon beam irradiates the sample and the photoelectrons are collected in a SCIENTA SES 2002 analyzer. The sample stage is motorized so that one can easily change the position of the beam on the sample (to avoid beam damage, especially for organic molecules). To conclude, the TEMPO beamline is perfectly suited

B.2 X-ray spectroscopy facilities and equipment

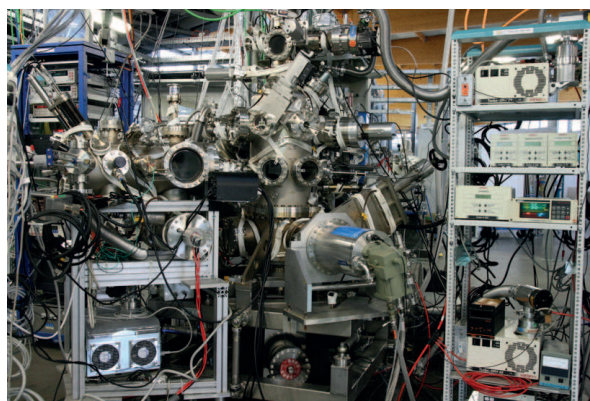


Figure B.7: *Picture of the TEMPO experimental station [178].*

for XPS measurements of core-levels but also valence band measurements, with a very high energy resolution and surface sensitivity. TEMPO capabilities perfectly fit with the characterization of low coverage 2D nanoarchitectures studied during my PhD. The XPS measurements reported in this manuscript were all obtained at the TEMPO beamline of the Soleil Synchrotron.

Résumé

Elaboration de nanoarchitectures organiques bidimensionnelles par auto-assemblage et réactions sur surface

Ces dernières années ont été marquées par de grandes évolutions technologiques à travers notamment une course à la miniaturisation. De gros efforts de recherche se concentrent en particulier sur le domaine de l'électronique organique mais aussi sur de nouveaux matériaux bidimensionnels comme le graphène. Ces matériaux 2D présentent des propriétés physiques exceptionnelles et sont des candidats prometteurs pour le développement de futurs dispositifs électroniques.

Au cours de cette thèse, l'approche ascendante, qui consiste à assembler ensemble des petites briques élémentaires, a été utilisée pour élaborer des nanostructures bidimensionnelles originales sur des surfaces. Les propriétés de ces nanostructures ont été étudiées par microscopie à effet tunnel et par spectrométrie photoélectronique X. Des nanostructures bidimensionnelles ont été élaborées par auto-assemblage de briques moléculaires, stabilisées par des interactions intermoléculaires. En particulier, des nanostructures stabilisées par liaison hydrogène, halogène et ionique-organique ont été étudiées. Des états électroniques localisés dus à un couplage électronique latéral particulier entre des molécules de PTCDI ont été observés. Ce couplage se manifeste par la modification locale des états électroniques des molécules étudiées mais également par l'apparition d'états électroniques localisés entre ces molécules. De nouvelles nanoarchitectures ont également été créées après déposition de molécules organiques (PTCDI) et de composés ioniques (chlorure de sodium) sur une surface d'Au(111) puis en faisant varier la température. Plus précisément, quatre types de nanoarchitectures hybrides ioniques-organiques différentes ont été réalisées et observées par microscopie à effet tunnel. Des nanostructures peu organisées en forme de fleurs apparaissent à température ambiante, laissant place à une structure poreuse organisée en forme de filet de pêche après recuit à 100 °C, puis à des structures en chaîne après recuit à plus haute température. En particulier, la position des composés ioniques dans ces nanostructures hybrides a pu être observée. Cela a permis d'expliquer et de comprendre la formation de ces nanostructures qui apparaissent comme

stabilisées par des interactions N-H / Cl- spécifiques. Des nanostructures organiques covalentes ont aussi été élaborées par une réaction de couplage d'Ullmann sur la surface. Dans un premier lieu, un précurseur organique en forme d'étoile avec des substituants iodés (TIPB) a été déposé sur une surface d'Au(111). A faible taux de couverture (en dessous de 0.2 monocouche), la formation de nanostructures covalentes poreuses a été observée après dépôt de TIPB sur la surface à température ambiante. Les nanostructures covalentes formées sont poreuses mais pas régulières et apparaissent comme croissant à partir des bords de marches de la surface d'or. Au-dessus de 0.2 monocouche, de nouvelles structures apparaissent et se développent sur la surface. Ces structures respectivement en forme de vague et de noeud-papillon sont en fait constituées de molécules de TIPB intactes stabilisées par liaison halogène. L'apparition de ces nouvelles structures constituées de molécules intactes est attribuée à l'empoisonnement des bords de marches de la surface d'or qui sont connus comme étant des sites catalytiques actifs de la surface, par des atomes d'iode. Au-dessus d'une monocouche, la croissance des nouvelles structures vague et noeud papillon va provoquer l'expulsion des structures covalentes en couche. Un deuxième précurseur organique en forme d'étoile, avec deux bromes au bout de chaque branche (T2BPB) a également été déposé sur une surface d'Au(111) en faisant varier sa température. A température ambiante, une structure poreuse constituée de molécules intactes stabilisées par liaison halogène-halogène est formée. En augmentant la température de la surface, des chaînes puis des structures covalentes sont successivement formées. En particulier, de grandes nanostructures carbonées hexagonales poreuses régulières (graphène nanoporeux) ont notamment été synthétisées à haute température. Ces travaux ouvrent de nouvelles perspectives pour la réalisation de matériaux organiques bidimensionnels aux propriétés contrôlées.

Mots-clefs: Auto-assemblage, Microscopie à Effet Tunnel, Surface, Ullmann, Ultra Vide.

Publications and oral presentations

Publications

- **D. Peyrot** and F. Silly
On-Surface Synthesis of Two-Dimensional Covalent Organic Structures versus Halogen-Bonded Self-Assembly: Competing Formation of Organic Nanoarchitectures
ACS Nano **10**, 5490-5498 (2016)
- J. Hieulle, **D. Peyrot**, Zhen Jiang and F. Silly
Engineering two-dimensional hybrid NaCl-organic coordinated nanoarchitectures on metal surfaces
Chem. Comm. **51**, 13162-13165 (2015)

Oral communications and poster presentation

Poster presentation

- **International conference on molecular electronics (ELECMOL2016)**,
Paris-France, August 2016
- **International Symposium on "On Surface Chemistry"**,
Paris-France, May 2016
- **Hierarchical Assembled Organic Materials for Electronics (HOME-RIC) fall school**,
Bordeaux-France, October 2014

- **WE-Heraeus International Seminar on "Functional Molecules at Surfaces"** ,
Bad Honnef-Germany, May 2014

Oral communications

- **International Conference on Molecular Electronics (ELECMOL2016)**,
Paris-France, August 2016
- **International Conference on Nanoscience and Nanotechnology (ICONN)**,
Canberra-Australia, February 2016
- **European Materials Research Society (EMRS) spring meeting**,
Lille-France, May 2015
- **Forum des microscopies á sondes locales** ,
Troyes-France, March 2015
- **International Conference On "Novel Nanomaterial: engineering and properties" (ICON²)**,
Paris-France, September 2015

B. X-RAY PHOTOEMISSION SPECTROSCOPY AND SYNCHROTRON RADIATION

References

- [1] Richard P. Feynman. There's plenty of room at the bottom. *Engineering and Science*, 23(5):22–36, 1960. [iii](#)
- [2] Intel Discloses Newest Microarchitecture and 14 Nanometer Manufacturing Process Technical Details. [iii](#)
- [3] Johannes V. Barth, Giovanni Costantini, and Klaus Kern. Engineering atomic and molecular nanostructures at surfaces. *Nature*, 437(7059):671–679, September 2005. [iv](#), [1](#), [3](#)
- [4] A. K. Geim and K. S. Novoselov. The rise of graphene. *Nat. Mater.*, 6(3):183–191, March 2007. [iv](#)
- [5] Thomas G. Pedersen, Christian Flindt, Jesper Pedersen, Niels Asger Mortensen, Antti-Pekka Jauho, and Kjeld Pedersen. Graphene antidot lattices: Designed defects and spin qubits. *Phys. Rev. Lett.*, 100(13):136804, April 2008. [v](#)
- [6] GM Whitesides, JP Mathias, and CT Seto. Molecular self-assembly and nanochemistry: a chemical strategy for the synthesis of nanostructures. *Science*, 254(5036):1312–1319, 1991. [1](#)
- [7] Michel Simard, Dan Su, and James D. Wuest. Use of hydrogen bonds to control molecular aggregation. self-assembly of three-dimensional networks with large chambers. *Journal of the American Chemical Society*, 113(12):4696–4698, 1991. [1](#)
- [8] Leonard J. Prins, David N. Reinhoudt, and Peter Timmerman. Noncovalent synthesis using hydrogen bonding. *Angewandte Chemie International Edition*, 40(13):2382–2426, 2001. [1](#)
- [9] Steven De Feyter and Frans C. De Schryver. Two-dimensional supramolecular self-assembly probed by scanning tunneling microscopy. *Chem. Soc. Rev.*, 32:139–150, 2003. [1](#)

REFERENCES

- [10] Carlos J. Villagmez, Takashi Sasaki, James M. Tour, and Leonhard Grill. Bottom-up assembly of molecular wagons on a surface. *Journal of the American Chemical Society*, 132(47):16848–16854, 2010. PMID: 21038918. [1](#)
- [11] Johannes V. Barth. Molecular architectonic on metal surfaces. *Annual Review of Physical Chemistry*, 58(1):375–407, 2007. PMID: 17430091. [2](#), [3](#), [4](#), [6](#)
- [12] J.V. Barth, J. Weckesser, N. Lin, A. Dmitriev, and K. Kern. Supramolecular architectures and nanostructures at metal surfaces. *Applied Physics A*, 76(5):645–652, 2003. [3](#)
- [13] J.V. Barth. Transport of adsorbates at metal surfaces: from thermal migration to hot precursors. *Surface Science Reports*, 40(35):75 – 149, 2000. [3](#)
- [14] Angelika Khnle. Self-assembly of organic molecules at metal surfaces. *Current Opinion in Colloid and Interface Science*, 14(2):157 – 168, 2009. [4](#), [5](#), [22](#)
- [15] Maya Schock, Roberto Otero, Sladjana Stojkovic, Frauke Hummelink, André Gourdon, Erik Laegsgaard, Ivan Stensgaard and Christian Joachim, , and Flemming Besenbacher. Chiral close-packing of achiral star-shaped molecules on solid surfaces. *The Journal of Physical Chemistry B*, 110(26):12835–12838, 2006. PMID: 16805577. [7](#)
- [16] Wende Xiao, Xinliang Feng, Pascal Ruffieux, Oliver Grning, Klaus Mllen, and Roman Fasel. Self-assembly of chiral molecular honeycomb networks on au(111). *Journal of the American Chemical Society*, 130(28):8910–8912, 2008. PMID: 18558672. [8](#)
- [17] Elangannan Arunan, Gautam R. Desiraju, Roger A. Klein, Joanna Sadlej, Steve Scheiner, Ibon Alkorta, David C. Clary, Robert H. Crabtree, Joseph J. Dannenberg, Pavel Hobza, Henrik G. Kjaergaard, Anthony C. Legon, Benedetta Mennucci, and David J. Nesbitt. Definition of the hydrogen bond (IUPAC Recommendations 2011). *Pure and Applied Chemistry*, 83(8):1637–1641, 2011. [8](#)
- [18] Maya Lukas, Ross E. A. Kelly, Lev N. Kantorovich, Roberto Otero, Wei Xu, Erik Laegsgaard, Ivan Stensgaard, and Flemming Besenbacher. Adenine monolayers on the au(111) surface: Structure identification by scanning tunneling microscopy experiment and ab initio calculations. *The Journal of Chemical Physics*, 130(2), 2009. [8](#), [9](#)

- [19] Sylvain Clair, Stéphane Pons, Ari P. Seitsonen, Harald Brune, Klaus Kern, and Johannes V. Barth. Stm study of terephthalic acid self-assembly on au(111): Hydrogen-bonded sheets on an inhomogeneous substrate. *The Journal of Physical Chemistry B*, 108(38):14585–14590, 2004. [8](#)
- [20] Sebastian Stepanow, Nian Lin, Franck Vidal, Aitor Landa, Mario Ruben, Johannes V. Barth, and Klaus Kern. Programming supramolecular assembly and chirality in two-dimensional dicarboxylate networks on a cu(100) surface. *Nano Letters*, 5(5):901–904, 2005. PMID: 15884891. [8](#)
- [21] Timothy Clark, Matthias Hennemann, Jane S. Murray, and Peter Politzer. Halogen bonding: the σ -hole. *Journal of Molecular Modeling*, 13(2):291–296, 2007. [10](#)
- [22] Pierangelo Metrangolo and Giuseppe Resnati. Halogen bonding: A paradigm in supramolecular chemistry. *Chemistry A European Journal*, 7(12):2511–2519, 2001. [10](#)
- [23] Thai Thanh Thu Bui, Slimane Dahaoui, Claude Lecomte, Gautam R. Desiraju, and Enrique Espinosa. The nature of halogen-halogen interactions: A model derived from experimental charge-density analysis. *Angewandte Chemie International Edition*, 48(21):3838–3841, 2009. [10](#), [101](#)
- [24] Peter Politzer, Jane S. Murray, and Timothy Clark. Halogen bonding: an electrostatically-driven highly directional noncovalent interaction. *Phys. Chem. Chem. Phys.*, 12:7748–7757, 2010. [10](#)
- [25] Eric Bosch and Charles L. Barnes. Triangular halogen-halogen-halogen interactions as a cohesive force in the structures of trihalomesitylenes. *Crystal Growth & Design*, 2(4):299–302, 2002. [10](#), [11](#)
- [26] Jianwei Xu, Xueming Liu, Joseph Kok-Peng Ng, Tingting Lin, and Chaobin He. Trimeric supramolecular liquid crystals induced by halogen bonds. *J. Mater. Chem.*, 16(35):3540–3545, September 2006. [11](#), [87](#)
- [27] Hai Yue Gao, Qian Jin Shen, Xiao Ran Zhao, Xiao Qing Yan, Xue Pang, and Wei Jun Jin. Phosphorescent co-crystal assembled by 1,4-diiodotetrafluorobenzene with carbazole based on $c-i \cdots \pi$ halogen bonding. *J. Mater. Chem.*, 22(12):5336–5343, February 2012. [11](#), [87](#)

REFERENCES

- [28] L. Lafferentz, V. Eberhardt, C. Dri, C. Africh, G. Comelli, F. Esch, S. Hecht, and L. Grill. Controlling on-surface polymerization by hierarchical and substrate-directed growth. *Nat. Chem.*, 4(3):215–220, 2012. [11](#), [33](#), [35](#), [87](#), [88](#)
- [29] Pierangelo Metrangolo, Giuseppe Resnati, Tullio Pilati, Rosalba Liantonio, and Franck Meyer. Engineering functional materials by halogen bonding. *J. Polym. Sci. Pol. Chem.*, 45(1):1–15, 2007. [11](#), [88](#)
- [30] Franck Meyer and Philippe Dubois. Halogen bonding at work: Recent applications in synthetic chemistry and materials science. *CrystEngComm*, 15(16):3058–3071, March 2013. [11](#), [88](#)
- [31] Bao Zha, Xinrui Miao, Pei Liu, Yumeng Wu, and Wenli Deng. Concentration dependent halogen-bond density in the 2d self-assembly of a thienophenanthrene derivative at the aliphatic acid/graphite interface. *Chem. Commun.*, 50(64):9003–9006, July 2014. [11](#), [88](#)
- [32] Andrew DiLullo, Shih-Hsin Chang, Nadjib Baadji, Kendal Clark, Jan-Peter Klöckner, Marc-Heinrich Prosenc, Stefano Sanvito, Roland Wiesendanger, Germar Hoffmann, and Saw-Wai Hla. Molecular kondo chain. *Nano Lett.*, 12(6):3174–3179, June 2012. [11](#), [88](#)
- [33] Bulent Baris, Vincent Luzet, Eric Duverger, Philippe Sonnet, Frank Palmino, and Frederic Chérioux. Robust and open tailored supramolecular networks controlled by the template effect of a silicon surface. *Angew. Chem., Int. Ed.*, 50(18):4094–4098, 2011. [11](#), [88](#)
- [34] Kyung-Hoon Chung, Howon Kim, Won Jun Jang, Jong Keon Yoon, Se-Jong Kahng, Jhinhwan Lee, and Seungwu Han. Molecular multistate systems formed in two-dimensional porous networks on ag(111). *J. Phys. Chem. C*, 117(1):302–306, January 2013. 00009. [11](#), [88](#)
- [35] Fabien Silly. Selecting two-dimensional halogen-halogen bonded self-assembled 1,3,5-tris(4-iodophenyl)benzene porous nanoarchitectures at the solid-liquid interface. *J. Phys. Chem. C*, 117(39):20244–20249, October 2013. [11](#), [88](#), [89](#), [109](#)
- [36] Sebastian Stepanow, Nian Lin, Dietmar Payer, Uta Schlickum, Florian Klappenberger, Giorgio Zoppellaro, Mario Ruben, Harald Brune, Johannes V. Barth, and Klaus Kern. Surface-assisted assembly of 2d metalorganic networks that exhibit unusual threefold coordination symmetry. *Angewandte Chemie International Edition*, 46(5):710–713, 2007. [12](#)

- [37] Bradley J. Holliday and Chad A. Mirkin. Strategies for the construction of supramolecular compounds through coordination chemistry. *Angewandte Chemie International Edition*, 40(11):2022–2043, 2001. [12](#)
- [38] Mario Ruben, Javier Rojo, Francisco J. Romero-Salguero, Lindsay H. Uppadine, and Jean-Marie Lehn. Grid-type metal ion architectures: Functional metallosupramolecular arrays. *Angewandte Chemie International Edition*, 43(28):3644–3662, 2004. [12](#)
- [39] Alexander Semenov, Joachim P. Spatz, Martin Mller, Jean-Marie Lehn, Bernd Sell, Dieter Schubert, Christian H. Weidl, and Ulrich S. Schubert. Controlled arrangement of supramolecular metal coordination arrays on surfaces. *Angewandte Chemie International Edition*, 38(17):2547–2550, 1999. [12](#)
- [40] Mario Ruben. Squaring the interface: surface-assisted coordination chemistry. *Angewandte Chemie International Edition*, 44(11):1594–1596, 2005. [12](#)
- [41] Nian Lin, Sebastian Stepanow, Franck Vidal, Klaus Kern, Mohammad S. Alam, Stefan Stromsdorfer, Viacheslav Dremov, Paul Muller, Aitor Landa, and Mario Ruben. Surface-assisted coordination chemistry and self-assembly. *Dalton Trans.*, pages 2794–2800, 2006. [12](#)
- [42] Ludwig Bartels. Tailoring molecular layers at metal surfaces. *Nat. Chem.*, 2(2):87–95, January 2010. [13](#)
- [43] Christian Wäckerlin, Cristian Iacovita, Dorota Chylarecka, Petra Fesser, Thomas A. Jung, and Nirmalya Ballav. Assembly of 2d ionic layers by reaction of alkali aalides with the organic electrophile 7,7,8,8-tetracyano-p-quinodimethane (tcnq). *Chem. Commun.*, 47(32):9146–9148, August 2011. [13](#), [14](#), [76](#)
- [44] Daniel Skomski, Sabine Abb, and Steven L. Tait. Robust surface nano-architecture by alkalicarboxylate ionic bonding. *Journal of the American Chemical Society*, 134(34):14165–14171, 2012. PMID: 22880959. [14](#), [15](#), [76](#)
- [45] Tomoko K. Shimizu, Jaehoon Jung, Hiroshi Imada, and Yousoo Kim. Supramolecular assembly through interactions between molecular dipoles and alkali metal ions. *Angew. Chem. Int. Ed.*, 53(50):13729–13733, December 2014. [14](#), [76](#)
- [46] Qinmin Guo, Min Huang, Shuangzan Lu, and Gengyu Cao. Ionic compound mediated rearrangement of 3, 4, 9, 10-perylene tetracarboxylic dianhydride molecules on ag(100) surface. *Nanotechnology*, 26(27):275603, 2015. [14](#), [15](#)

REFERENCES

- [47] Janine C. Swarbrick, J. Ben Taylor, and James N. O’Shea. Electrospray deposition in vacuum. *Applied Surface Science*, 252(15):5622 – 5626, 2006. Proceedings of the Eight International Conference on Atomically Controlled Surfaces, Interfaces and Nanostructures and the Thirteenth International Congress on Thin Films AC-SIN8/ICTF13. [16](#)
- [48] Robert Lindner and Angelika Khnle. On-surface reactions. *ChemPhysChem*, 16(8):1582–1592, 2015. [16](#)
- [49] Rico Gutzler, Luis Cardenas, Josh Lipton-Duffin, Mohamed El Garah, Laurentiu E. Dinca, Csaba E. Szakacs, Chaoying Fu, Mark Gallagher, Martin Vondracek, Maksym Rybachuk, Dmitrii F. Perepichka, and Federico Rosei. Ullmann-type coupling of brominated tetrathienoanthracene on copper and silver. *Nanoscale*, 6:2660–2668, 2014. [16](#)
- [50] Leonhard Grill, Matthew Dyer, Leif Lafferentz, Mats Persson, Maike V. Peters, and Stefan Hecht. Nano-architectures by covalent assembly of molecular building blocks. *Nature Nanotechnology*, 2(11):687–691, November 2007. [16](#), [32](#), [33](#), [34](#), [88](#)
- [51] Hong-Ying Gao, Hendrik Wagner, Dingyong Zhong, Jörn-Holger Franke, Armido Studer, and Harald Fuchs. Glaser coupling at metal surfaces. *Angewandte Chemie International Edition*, 52(14):4024–4028, 2013. [16](#)
- [52] Borja Cirera, Yi-Qi Zhang, Jonas Björk, Svetlana Klyatskaya, Zhi Chen, Mario Ruben, Johannes V. Barth, and Florian Klappenberger. Synthesis of extended graphdiyne wires by vicinal surface templating. *Nano Letters*, 14(4):1891–1897, 2014. PMID: 24564910. [16](#)
- [53] Dimas G. de Oteyza, Patrick Gorman, Yen-Chia Chen, Sebastian Wickenburg, Alexander Riss, Duncan J. Mowbray, Grisha Etkin, Zahra Pedramrazi, Hsin-Zon Tsai, Angel Rubio, Michael F. Crommie, and Felix R. Fischer. Direct imaging of covalent bond structure in single-molecule chemical reactions. *Science*, 340(6139):1434–1437, 2013. [16](#)
- [54] Jinming Cai, Pascal Ruffieux, Rached Jaafar, Marco Bieri, Thomas Braun, Stephan Blankenburg, Matthias Muoth, Ari P. Seitsonen, Moussa Saleh, Xinliang Feng, Klaus Müllen, and Roman Fasel. Atomically precise bottom-up fabrication of graphene nanoribbons. *Nature*, 466(7305):470–473, July 2010. [16](#), [88](#)

- [55] Jia Liu, Pascal Ruffieux, Xinliang Feng, Klaus Mullen, and Roman Fasel. Cyclotrimerization of arylalkynes on au(111). *Chem. Commun.*, 50:11200–11203, 2014. [16](#), [17](#)
- [56] Sylvain Clair, Mathieu Abel, and Louis Porte. Growth of boronic acid based two-dimensional covalent networks on a metal surface under ultrahigh vacuum. *Chem. Commun.*, 50:9627–9635, 2014. [16](#)
- [57] Takashi Yokoyama, Shiyoshi Yokoyama, Toshiya Kamikado, Yoshishige Okuno, and Shinro Mashiko. Selective assembly on a surface of supramolecular aggregates with controlled size and shape. *Nature*, 413(6856):619–621, October 2001. [18](#), [19](#), [20](#)
- [58] Violeta Iancu, Kai-Felix Braun, Koen Schouteden, and Chris Van Haesendonck. Probing the electronic properties of trimesic acid nanoporous networks on au(111). *Langmuir*, 29(37):11593–11599, 2013. PMID: 23944842. [19](#)
- [59] Roozbeh Shokri, Francois Vonau, Marion Cranney, Dominique Aubel, Ashok Narladkar, Benjamin Isare, Laurent Bouteiller, Laurent Simon, and Günter Reiter. Consequences of varying adsorption strength and adding steric hindrance on self-assembly of supramolecular polymers on carbon substrates. *The Journal of Physical Chemistry C*, 116(40):21594–21600, 2012. [19](#)
- [60] Nataliya Kalashnyk, Praveen Ganesh Nagaswaran, Simon Kervyn, Massimo Riello, Ben Moreton, Tim S Jones, Alessandro De Vita, Davide Bonifazi, and Giovanni Costantini. Self-Assembly of Decoupled Borazines on Metal Surfaces: The Role of the Peripheral Groups. *Chemistry (Weinheim an Der Bergstrasse, Germany)*, 20(37):11856–11862, September 2014. [19](#)
- [61] Yeliang Wang, Stefano Fabris, Thomas W. White, Federico Pagliuca, Paolo Moras, Marco Papagno, Dinesh Topwal, Polina Sheverdyaeva, Carlo Carbone, Magali Lingfelder, Thomas Classen, Klaus Kern, and Giovanni Costantini. Varying molecular interactions by coverage in supramolecular surface chemistry. *Chem. Commun.*, 48:534–536, 2012. [21](#)
- [62] Meike Sthr, Markus Wahl, Christian H. Galka, Till Riehm, Thomas A. Jung, and Lutz H. Gade. Controlling Molecular Assembly in Two Dimensions: The Concentration Dependence of Thermally Induced 2d Aggregation of Molecules on a Metal Surface. *Angewandte Chemie International Edition*, 44(45):7394–7398, November 2005. [20](#)

REFERENCES

- [63] Anna Lisa Pinardi, Gonzalo Otero-Irurueta, Irene Palacio, Jose Ignacio Martinez, Carlos Sanchez-Sanchez, Marta Tello, Celia Rogero, Albano Cossaro, Alexei Preobrajenski, Berta Gmez-Lor, Andrej Jancarik, Irena G. Star, Ivo Star, M. Francisca Lopez, Javier Mndez, and Jose Angel Martin-Gago. Tailored formation of n-doped nanoarchitectures by diffusion-controlled on-surface (cyclo)dehydrogenation of heteroaromatics. *ACS Nano*, 7(4):3676–3684, 2013. PMID: 23506342. [22](#)
- [64] Takayuki Suzuki, Theresa Lutz, Dietmar Payer, Nian Lin, Steven L. Tait, Giovanni Costantini, and Klaus Kern. Substrate effect on supramolecular self-assembly: from semiconductors to metals. *Phys. Chem. Chem. Phys.*, 11:6498–6504, 2009. [23](#)
- [65] Younes Makoudi, Frank Palmino, Madjid Arab, Eric Duverger, and Frédéric Chérioux. Complete supramolecular self-assembled adlayer on a silicon surface at room temperature. *Journal of the American Chemical Society*, 130(21):6670–6671, 2008. PMID: 18459775. [23](#)
- [66] Bulent Baris, Judicaël Jeannoutot, Vincent Luzet, Frank Palmino, Alain Rochefort, and Frédéric Chérioux. Noncovalent bicomponent self-assemblies on a silicon surface. *ACS Nano*, 6(8):6905–6911, 2012. PMID: 22746840. [23](#)
- [67] Conrad Becker and Klaus Wandelt. *Surfaces: Two-Dimensional Templates*. Springer Berlin Heidelberg, Berlin, Heidelberg, 2009. [24](#)
- [68] Steven L. Tait, Alexander Langner, Nian Lin, Sebastian Stepanow, Chandrasekar Rajadurai, Mario Ruben, and Klaus Kern. One-dimensional self-assembled molecular chains on cu(100): Interplay between surface-assisted coordination chemistry and substrate commensurability. *The Journal of Physical Chemistry C*, 111(29):10982–10987, 2007. [24](#)
- [69] Y. Zou, L. Kilian, A. Schll, Th. Schmidt, R. Fink, and E. Umbach. Chemical bonding of {PTCDA} on ag surfaces and the formation of interface states. *Surface Science*, 600(6):1240 – 1251, 2006. [25](#)
- [70] Tait Steven L., Langner Alexander, Lin Nian, Chandrasekar Rajadurai, Fuhr Olaf, Ruben Mario, and Kern Klaus. Assembling isostructural metal-organic coordination architectures on cu(100), ag(100) and ag(111) substrates. *ChemPhysChem*, 9(17):2495–2499, 2008. [25](#)

- [71] Fabien Silly, Adam Q. Shaw, G. A. D. Briggs, and Martin R. Castell. Epitaxial ordering of a perylenetetra-carboxylic diimide-melamine supramolecular network driven by the au(111)-(223) reconstruction. *Applied Physics Letters*, 92(2), 2008. [26](#), [30](#), [108](#)
- [72] Matthias Böhringer, Karina Morgenstern, Wolf-Dieter Schneider, Richard Berndt, Francesco Mauri, Alessandro De Vita, and Roberto Car. Two-dimensional self-assembly of supramolecular clusters and chains. *Phys. Rev. Lett.*, 83:324–327, Jul 1999. [26](#)
- [73] J. A Theobald, N. S Oxtoby, M. A Phillips, N. R Champness, and P. H Beton. Controlling molecular deposition and layer structure with supramolecular surface assemblies. *Nature*, 424(6952):10291031, 2003. [27](#)
- [74] N. Neel J. Kroger, H. Jensen and R. Berndt. Self-organization of cobalt-phthalocyanine on a vicinal gold surface revealed by scanning tunnelling microscopy. *Surface Science*, 601(18):4180 – 4184, 2007. ECOSS-24 Proceedings of the 24th European Conference on Surface Science. [27](#)
- [75] Qiang Sun, Liangliang Cai, Yuanqi Ding, Honghong Ma, Chunxue Yuan, and Wei Xu. Single-molecule insight into wurtz reactions on metal surfaces. *Phys. Chem. Chem. Phys.*, 18:2730–2735, 2016. [28](#), [30](#)
- [76] Alex Saywell, Jutta Schwarz, Stefan Hecht, and Leonhard Grill. Polymerization on stepped surfaces: Alignment of polymers and identification of catalytic sites. *Angew. Chem. Int. Ed.*, 51(21):5096–5100, May 2012. [28](#), [88](#), [101](#)
- [77] Li Wang, Huihui Kong, Xiu Chen, Xinli Du, Feng Chen, Xiaoqing Liu, and Hongming Wang. Conformation-induced self-assembly of rubrene on au(111) surface. *Applied Physics Letters*, 95(9), 2009. [29](#), [30](#)
- [78] A. Dmitriev, N. Lin, J. Weckesser, J. V. Barth, and K. Kern. Supramolecular assemblies of trimesic acid on a cu(100) surface. *The Journal of Physical Chemistry B*, 106(27):6907–6912, 2002. [30](#), [31](#)
- [79] Mario Ruben, Dietmar Payer, Aitor Landa, Alessio Comisso, Chiara Gattinoni, Nian Lin, Jean-Paul Collin, Jean-Pierre Sauvage, Alessandro De Vita, and Klaus Kern. 2d supramolecular assemblies of benzene-1,3,5-triyl-tribenzoic acid: Temperature-induced phase transformations and hierarchical organization with macrocyclic molecules. *J. Am. Chem. Soc.*, 128(49):15644–15651, 2006. [30](#)

REFERENCES

- [80] Sigrid Weigelt, Christian Bombis, Carsten Busse, Martin M. Knudsen, Kurt V. Gothelf, Erik Lgsgaard, Flemming Besenbacher, and Trolle R. Linderoth. Molecular self-assembly from building blocks synthesized on a surface in ultrahigh vacuum: Kinetic control and topo-chemical reactions. *ACS Nano*, 2(4):651–660, 2008. PMID: 19206595. [30](#)
- [81] Qitang Fan, Tao Wang, Liming Liu, Jin Zhao, Junfa Zhu, and J. Michael Gottfried. Tribromobenzene on cu(111): Temperature-dependent formation of halogen-bonded, organometallic, and covalent nanostructures. *The Journal of Chemical Physics*, 142(10), 2015. [30](#), [39](#), [105](#)
- [82] Qitang Fan, J. Michael Gottfried, and Junfa Zhu. Surface-catalyzed cc covalent coupling strategies toward the synthesis of low-dimensional carbon-based nanostructures. *Accounts of Chemical Research*, 48(8):2484–2494, 2015. PMID: 26194462. [32](#), [33](#)
- [83] Fritz Ullmann. Ueber symmetrische biphenylderivate. *Justus Liebigs Annalen der Chemie*, 332(1-2):38–81, 1904. [32](#)
- [84] Ke Ji Shi, Ding Wang Yuan, Cheng Xin Wang, Chen Hui Shu, Deng Yuan Li, Zi Liang Shi, Xin Yan Wu, and Pei Nian Liu. Ullmann reaction of aryl chlorides on various surfaces and the application in stepwise growth of 2d covalent organic frameworks. *Organic Letters*, 18(6):1282–1285, 2016. PMID: 26938859. [32](#), [34](#), [36](#)
- [85] Emily A. Lewis, Colin J. Murphy, Melissa L. Liriano, and E. Charles H. Sykes. Atomic-scale insight into the formation, mobility and reaction of ullmann coupling intermediates. *Chem. Commun.*, 50:1006–1008, 2014. [32](#)
- [86] E. A. Lewis, C. J. Murphy, A. Pronschinske, M. L. Liriano, and E. C. H. Sykes. Nanoscale insight into c-c coupling on cobalt nanoparticles. *Chem. Commun.*, 50:10035–10037, 2014. [32](#)
- [87] E. Charles H. Sykes, Patrick Han, S. Alex Kandel, Kevin F. Kelly, Gregory S. McCarty, and Paul S. Weiss. Substrate-mediated interactions and intermolecular forces between molecules adsorbed on surfaces. *Accounts of Chemical Research*, 36(12):945–953, 2003. PMID: 14674785. [33](#)
- [88] Weihua Wang, Xingqiang Shi, Shiyong Wang, Michel A. Van Hove, and Nian Lin. Single-molecule resolution of an organometallic intermediate in a surface-supported ullmann coupling reaction. *Journal of the American Chemical Society*, 133(34):13264–13267, 2011. PMID: 21761920. [33](#)

- [89] J. A. Lipton-Duffin, O. Ivasenko, D. F. Perepichka, and F. Rosei. Synthesis of polyphenylene molecular wires by surface-confined polymerization. *Small*, 5(5):592–597, March 2009. [33](#), [88](#)
- [90] J. A. Lipton-Duffin, J. A. Miwa, M. Kondratenko, F. Cicoira, B. G. Sumpter, V. Meunier, D. F. Perepichka, and F. Rosei. Step-by-step growth of epitaxially aligned polythiophene by surface-confined reaction. *Proceedings of the National Academy of Sciences*, 107(25):11200–11204, 2010. [33](#)
- [91] Saw-Wai Hla, Ludwig Bartels, Gerhard Meyer, and Karl-Heinz Rieder. Inducing all steps of a chemical reaction with the scanning tunneling microscope tip: Towards single molecule engineering. *Phys. Rev. Lett.*, 85:2777–2780, Sep 2000. [33](#)
- [92] Markus Kittelmann, Markus Nimmrich, Robert Lindner, Andr Gourdon, and Angelika Khnle. Sequential and site-specific on-surface synthesis on a bulk insulator. *ACS Nano*, 7(6):5614–5620, 2013. PMID: 23682961. [34](#)
- [93] Meaghan M. Blake, Sanjini U. Nanayakkara, Shelley A. Claridge, Luis C. Fernandez-Torres, E. Charles H. Sykes, and Paul S. Weiss. Identifying reactive intermediates in the ullmann coupling reaction by scanning tunneling microscopy and spectroscopy. *The Journal of Physical Chemistry A*, 113(47):13167–13172, 2009. PMID: 19658380. [34](#)
- [94] Stephen J. Blanksby and G. Barney Ellison. Bond dissociation energies of organic molecules. *Accounts of Chemical Research*, 36(4):255–263, 2003. PMID: 12693923. [35](#)
- [95] Jonas Bjrk, Felix Hanke, and Sven Stafstrm. Mechanisms of halogen-based covalent self-assembly on metal surfaces. *Journal of the American Chemical Society*, 135(15):5768–5775, 2013. PMID: 23506285. [35](#), [39](#), [99](#)
- [96] Hermann Walch, Rico Gutzler, Thomas Sirtl, Georg Eder, and Markus Lackinger. Material- and orientation-dependent reactivity for heterogeneously catalyzed carbon-bromine bond homolysis. *The Journal of Physical Chemistry C*, 114(29):12604–12609, 2010. [36](#)
- [97] Rico Gutzler, Hermann Walch, Georg Eder, Stephan Kloft, Wolfgang M. Heckl, and Markus Lackinger. Surface mediated synthesis of 2d covalent organic frameworks: 1,3,5-tris(4-bromophenyl)benzene on graphite(001), cu(111), and ag(110). *Chem. Commun.*, pages 4456–4458, 2009. [36](#), [88](#)

REFERENCES

- [98] Marco Bieri, Manh-Thuong Nguyen, Oliver Grning, Jinming Cai, Matthias Treier, Kamel At-Mansour, Pascal Ruffieux, Carlo A. Pignedoli, Daniele Passerone, Marcel Kastler, Klaus Mllen, and Roman Fasel. Two-dimensional polymer formation on surfaces: Insight into the roles of precursor mobility and reactivity. *Journal of the American Chemical Society*, 132(46):16669–16676, 2010. PMID: 21043454. [36](#), [37](#), [89](#), [99](#)
- [99] Christopher Bronner, Jonas Bjrk, and Petra Tegeder. Tracking and removing br during the on-surface synthesis of a graphene nanoribbon. *The Journal of Physical Chemistry C*, 119(1):486–493, 2015. [37](#), [40](#)
- [100] Jihun Park, Kye Yeop Kim, Kyung-Hoon Chung, Jong Keon Yoon, Howon Kim, Seungwu Han, and Se-Jong Kahng. Interchain interactions mediated by br adsorbates in arrays of metalorganic hybrid chains on ag(111). *The Journal of Physical Chemistry C*, 115(30):14834–14838, 2011. [38](#)
- [101] Tuan Anh-Pham, Fei Song, Manh-Thuong Nguyen, Zheshen Li, Florian Studener, and Meike Sthr. Comparing ullmann coupling on noble metal surfaces: On-surface polymerization of 1,3,6,8-tetrabromopyrene on cu(111) and au(111). *Chemistry A European Journal*, 22(17):5801–5801, 2016. [38](#), [39](#)
- [102] Arunabh Batra, Dean Cvetko, Gregor Kladnik, Olgun Adak, Claudia Cardoso, Andrea Ferretti, Deborah Prezzi, Elisa Molinari, Alberto Morgante, and Latha Venkataraman. Probing the mechanism for graphene nanoribbon formation on gold surfaces through x-ray spectroscopy. *Chem. Sci.*, 5:4419–4423, 2014. [39](#)
- [103] Jonas Bjrk, Sven Stafstrm, and Felix Hanke. Zipping up: Cooperativity drives the synthesis of graphene nanoribbons. *Journal of the American Chemical Society*, 133(38):14884–14887, 2011. PMID: 21859135. [39](#)
- [104] Tom Carpy. *A scanning tunnelling microscopy and spectroscopic study of bromine functionalised molecules on metal surfaces*. PhD thesis, Dublin City University, 2015. [39](#)
- [105] G. Binnig, H. Rohrer, Ch. Gerber, and E. Weibel. Surface studies by scanning tunneling microscopy. *Phys. Rev. Lett.*, 49:57–61, Jul 1982. [41](#)
- [106] G. Binnig, H. Rohrer, Ch. Gerber, and E. Weibel. 7x7 reconstruction on si(111) resolved in real space. *Phys. Rev. Lett.*, 50:120–123, Jan 1983. [41](#)

-
- [107] JOSEPH A. STROSCIO and D. M. EIGLER. Atomic and molecular manipulation with the scanning tunneling microscope. *Science*, 254(5036):1319–1326, 1991. [41](#)
- [108] M. F. Crommie, C. P. Lutz, and D. M. Eigler. Confinement of electrons to quantum corrals on a metal surface. *Science*, 262(5131):218–220, 1993. [41](#)
- [109] R. Wiesendanger. *Scanning Probe Microscopy and Spectroscopy: Methods and Applications*. Oxford University Press, 1994. [41](#)
- [110] G. Binnig, C. F. Quate, and Ch. Gerber. Atomic force microscope. *Phys. Rev. Lett.*, 56:930–933, Mar 1986. [41](#)
- [111] E. Betzig, J. K. Trautman, T. D. Harris, J. S. Weiner, and R. L. Kostelak. Breaking the diffraction barrier: Optical microscopy on a nanometric scale. *Science*, 251(5000):1468–1470, 1991. [41](#)
- [112] Christian Frétigny Lionel Aigouy, Yannick de Wilde. *Les nouvelles microscopies : A la découverte du nanomonde*. Belin, 2006. [42](#)
- [113] C. J. Davisson and L. H. Germer. Reflection of Electrons by a Crystal of Nickel. *Proceedings of the National Academy of Sciences of the United States of America*, 14(4):317–322, April 1928. [42](#)
- [114] C. J. Chen. *Introduction to Scanning Tunneling Microscopy*. Oxford University Press, 1993. [45](#)
- [115] J. Bardeen. Tunnelling from a many-particle point of view. *Phys. Rev. Lett.*, 6:57–59, Jan 1961. [46](#)
- [116] Joel A. Appelbaum and W. F. Brinkman. Theory of many-body effects in tunneling. *Phys. Rev.*, 186:464–470, Oct 1969. [46](#)
- [117] J. Tersoff and D. R. Hamann. Theory and application for the scanning tunneling microscope. *Phys. Rev. Lett.*, 50:1998–2001, Jun 1983. [48](#)
- [118] J. Tersoff and D. R. Hamann. Theory of the scanning tunneling microscope. *Phys. Rev. B*, 31:805–813, Jan 1985. [48](#)
- [119] Thomas Muller. Scanning tunneling microscopy : a tool for studying self-assembly and model systems for molecular devices, 2010. [Online; accessed 28-August-2016]. [50](#)

REFERENCES

- [120] S. Woedtke. PhD thesis, Inst. f. Exp. u. Ang. Phys. der CAU Kiel, 2002. [52](#)
- [121] Jeremy Hieulle. *Structures and Electronic Properties of Organic Self-Assembled Monolayers Characterized by STM and XPS*. PhD thesis, École Polytechnique, 2013. [53](#)
- [122] Wikipedia-Liquidat. Interior view of a turbomolecular pump, 2005. [Online; accessed 01-September-2016]. [55](#)
- [123] Hairong Wu, Kai Sotthewes, Peter M. Schon, G. Julius Vancso, and Harold J. W. Zandvliet. Ordering and dynamics of oligo(phenylene ethynylene) self-assembled monolayers on au(111). *RSC Adv.*, 5:42069–42074, 2015. [59](#)
- [124] Zhao-Xiong Xie, Zhi-Feng Huang, and Xin Xu. Influence of reconstruction on the structure of self-assembled normal-alkane monolayers on au(111) surfaces. *Phys. Chem. Chem. Phys.*, 4:1486–1489, 2002. [60](#)
- [125] Chen Li and Henrike Wonneberger. Perylene imides for organic photovoltaics: Yesterday, today, and tomorrow. *Adv. Mater.*, 24(5):613–636, 2012. [63](#)
- [126] Qing Hua Wang and Mark C. Hersam. Room-temperature molecular-resolution characterization of self-assembled organic monolayers on epitaxial graphene. *Nat. Chem.*, 1(3):206–211, May 2009. [63](#)
- [127] Han Huang, Shi Chen, Xingyu Gao, Wei Chen, and Andrew Thye Shen Wee. Structural and electronic properties of ptcda thin films on epitaxial graphene. *ACS Nano*, 3(11):3431–3436, November 2009. [63](#)
- [128] M. Mura, X. Sun, F. Silly, H. T. Jonkman, G. A. D. Briggs, M. R. Castell, and L. N. Kantorovich. Experimental and theoretical analysis of h-bonded supramolecular assemblies of ptcda molecules. *Phys. Rev. B*, 81(19):195412, May 2010. [63](#)
- [129] Christian Weiss, Christian Wagner, Ruslan Temirov, and F. Stefan Tautz. Direct imaging of intermolecular bonds in scanning tunneling microscopy. *J. Am. Chem. Soc.*, 132(34):11864–11865, 2010. [63](#)
- [130] J. Lobo-Checa, M. Matena, K. Muller, J. H. Dil, F. Meier, L. H. Gade, T. A. Jung, and M. Stohr. Band formation from coupled quantum dots formed by a nanoporous network on a copper surface. *Science*, 325(5938):300–303, July 2009. [63](#)

- [131] M. Mura, F. Silly, G. A. D. Briggs, M. R. Castell, and L. N. Kantorovich. H-bonding supramolecular assemblies of ptcdi molecules on the au(111) surface. *J. Phys. Chem. C*, 113(52):21840–21848, December 2009. [63](#), [64](#), [83](#)
- [132] Hiroyuki Tanaka, Tomohiro Ikeda, Masayuki Takeuchi, Kazuki Sada, Seiji Shinkai, and Tomoji Kawai. Molecular rotation in self-assembled multidecker porphyrin complexes. *ACS Nano*, 5(12):9575–9582, December 2011. [63](#)
- [133] Y. Makoudi, M. Beyer, J. Jeannoutot, F. Picaud, F. Palmino, and F. Chérioux. Supramolecular self-assembly of brominated molecules on a silicon surface. *Chem. Commun.*, 50(43):5714–5716, May 2014. [63](#)
- [134] S. Beniwal, S. Chen, D. A. Kunkel, J. Hooper, S. Simpson, E. Zurek, X. C. Zeng, and A. Enders. Kagome-like lattice of π - π stacked 3-hydroxyphenalenone on cu(111). *Chem. Commun.*, 50(63):8659–8662, July 2014. [63](#)
- [135] Johannes Seibel, Laura Zoppi, and Karl-Heinz Ernst. 2d conglomerate crystallization of heptahelicene. *Chem. Commun.*, 50(63):8751–8753, July 2014. [63](#)
- [136] Bappaditya Roy, Partha Bairi, and Arun K. Nandi. Supramolecular assembly of melamine and its derivatives: Nanostructures to functional materials. *RSC Advances*, 4(4):1708–1734, December 2013. [63](#)
- [137] Soichi Yokoyama, Takashi Hirose, and Kenji Matsuda. Phototriggered formation and disappearance of surface-confined self-assembly composed of photochromic 2-thienyl-type diarylethene: a cooperative model at the liquid/solid interface. *Chem. Commun.*, 50(45):5964–5966, May 2014. [63](#)
- [138] Yibao Li, Keqing Zhao, Yanlian Yang, Ke Deng, Qingdao Zeng, and Chen Wang. Functionalization of two-component molecular networks: recognition of Fe^{3+} . *Nanoscale*, 4(1):148–151, December 2011. [63](#)
- [139] Clément Barraud, Pierre Seneor, Richard Mattana, Stéphane Fusil, Karim Bouzehouane, Cyrille Deranlot, Patrizio Graziosi, Luis Hueso, Ilaria Bergenti, Valentin Dediu, Frédéric Petroff, and Albert Fert. Unravelling the role of the interface for spin injection into organic semiconductors. *Nat. Phys.*, 6(8):615–620, 2010. [63](#)
- [140] F. Sedona, M. Di Marino, D. Forrer, A. Vittadini, M. Casarin, A. Cossaro, L. Floreano, A. Verdini, and M. Sambì. Tuning the catalytic activity of ag(110)-supported fe phthalocyanine in the oxygen reduction reaction. *Nat. Mater.*, 11(11):970–977, 2012. [63](#)

REFERENCES

- [141] P. Liljeroth, J. Repp, and G. Meyer. Current-Induced hydrogen tautomerization and conductance switching of naphthalocyanine molecules. *Science*, 317(5842):1203–1206, August 2007. [63](#)
- [142] Z. J. Donhauser, B. A. Mantooth, K. F. Kelly, L. A. Bumm, J. D. Monnell, J. J. Stapleton, D. W. Price, A. M. Rawlett, D. L. Allara, J. M. Tour, and P. S. Weiss. Conductance switching in single molecules through conformational changes. *Science*, 292(5525):2303–2307, June 2001. [63](#)
- [143] Fabian Mohn, Jascha Repp, Leo Gross, Gerhard Meyer, Matthew S. Dyer, and Mats Persson. Reversible bond formation in a Gold-Atom Organic-Molecule complex as a molecular switch. *Phys. Rev. Lett.*, 105(26):266102, December 2010. [63](#)
- [144] Byoung-Young Choi, Se-Jong Kahng, Seungchul Kim, Hajin Kim, Hyo Kim, Young Song, Jisoon Ihm, and Young Kuk. Conformational molecular switch of the azobenzene molecule: A scanning tunneling microscopy study. *Phys. Rev. Lett.*, 96(15), April 2006. [63](#)
- [145] A. O. Gusev, A. Taleb, F. Silly, F. Charra, and M.-P. Pileni. Inhomogeneous photon emission properties of self-assembled metallic nanocrystals. *Adv. Mater.*, 12(21):1583–1587, 2000. [63](#)
- [146] Kolja Kolata, Tobias Breuer, Gregor Witte, and Sangam Chatterjee. Molecular packing determines singlet exciton fission in organic semiconductors. *ACS Nano*, June 2014. [63](#)
- [147] Dorota Niedzialek, Vincent Lemaure, Dmytro Dudenko, Jie Shu, Michael Ryan Hansen, Jens Wenzel Andreasen, Wojciech Pisula, Klaus Müllen, Jérôme Cornil, and David Beljonne. Probing the relation between charge transport and supramolecular organization down to ångström resolution in a benzothiadiazole-cyclopentadithiophene copolymer. *Adv. Mater.*, 25(13):1939–1947, April 2013. [63](#)
- [148] Yujie Dong, Bin Xu, Jibo Zhang, Xiao Tan, Lijuan Wang, Jinlong Chen, Hongguang Lv, Shanpeng Wen, Bao Li, Ling Ye, Bo Zou, and Wenjing Tian. Piezochromic luminescence based on the molecular aggregation of 9,10-bis((e)-2-(pyrid-2-yl)vinyl)anthracene. *Angew. Chem. Int. Ed.*, 51(43):10782–10785, October 2012. [63](#)

-
- [149] F. Silly. A robust method for processing scanning probe microscopy images and determining nanoobject position and dimensions. *J. Microsc-Oxford*, 236(3):211–218, 2009. [64](#), [89](#), [107](#)
- [150] W. Hebenstreit, J. Redinger, Z. Horozova, M. Schmid, R. Podlucky, and P. Varga. Atomic resolution by STM on ultra-thin films of alkali halides: experiment and local density calculations. *Surf. Sci.*, 424(23):L321–L328, April 1999. [75](#), [85](#)
- [151] K. Glöckler, M. Sokolowski, A. Soukopp, and E. Umbach. Initial growth of insulating overlayers of nacl on ge(100) observed by scanning tunneling microscopy with atomic resolution. *Phys. Rev. B*, 54(11):7705–7708, September 1996. [75](#), [85](#)
- [152] Xiaonan Sun, Marcella P. Felicissimo, Petra Rudolf, and Fabien Silly. Nacl multi-layer islands grown on au(111)-(22 × $\sqrt{3}$) probed by scanning tunneling microscopy. *Nanotech.*, 19(49):495307, December 2008. [75](#), [76](#)
- [153] S. Jensen and C. J. Baddeley. Formation of ptc-di-based metal organic structures on a au(111) surface modified by 2-d ni clusters. *J. Phys. Chem. C*, 112(39):15439–15448, October 2008. [76](#)
- [154] Miao Yu, Wei Xu, Nataliya Kalashnyk, Youness Benjalal, Samuthira Nagarajan, Federico Masini, Erik Laegsgaard, Mohamed Hliwa, Xavier Bouju, Andr Gourdon, Christian Joachim, Flemming Besenbacher, and Trolle R. Linderoth. From zero to two dimensions: supramolecular nanostructures formed from perylene-3,4,9,10-tetracarboxylic diimide (PTCDI) and ni on the au(111) surface through the interplay between hydrogen-bonding and electrostatic metal-organic interactions. *Nano Research*, 5(12):903–916, December 2012. [76](#)
- [155] Johannes V. Barth. Molecular architectonic on metal surfaces. *Annu. Rev. Phys. Chem.*, 58(1):375–407, May 2007. [76](#)
- [156] R. Bennowitz, A. S. Foster, L. N. Kantorovich, M. Bammerlin, C. Loppacher, S. Schär, M. Guggisberg, E. Meyer, and A. L. Shluger. Atomically resolved edges and kinks of nacl islands on cu(111): Experiment and theory. *Phys. Rev. B*, 62(3):2074–2084, 2000. [76](#)
- [157] Ch. Bombis, F. Ample, J. Mielke, M. Mannsberger, C. J. Villagómez, Ch. Roth, C. Joachim, and L. Grill. Mechanical behavior of nanocrystalline NaCl islands on cu(111). *Phys. Rev. Lett.*, 104(18):185502, May 2010. [76](#)

REFERENCES

- [158] Gregory Cabailh, Claude R Henry, and Clemens Barth. Thin nacl films on silver (001): island growth and work function. *N. J. Phys.*, 14(10):103037, October 2012. [76](#)
- [159] Jascha Repp, Gerhard Meyer, Sladjana M. Stojković, André Gourdon, and Christian Joachim. Molecules on insulating films: Scanning-tunneling microscopy imaging of individual molecular orbitals. *Phys. Rev. Lett.*, 94:026803, Jan 2005. [76](#)
- [160] Thomas Leoni, Olivier Guillermet, Hermann Walch, Véronique Langlais, Andrew Scheuermann, Jacques Bonvoisin, and Sébastien Gauthier. Controlling the charge state of a single redox molecular switch. *Phys. Rev. Lett.*, 106:216103, May 2011. [76](#)
- [161] Ji Chen, Jing Guo, Xiangzhi Meng, Jinbo Peng, Jiming Sheng, Limei Xu, Ying Jiang, Xin-Zheng Li, and En-Ge Wang. An unconventional bilayer ice structure on a nacl(001) film. *Nature Commun.*, 5, May 2014. [76](#)
- [162] Fabien Silly, Adam Q. Shaw, Kyriakos Porfyrakis, G. A. D. Briggs, and Martin R. Castell. Pairs and heptamers of c_{70} molecules ordered via ptc-di-melamine supramolecular networks. *Appl. Phys. Lett.*, 91(25):253109, 2007. [79](#)
- [163] Xiaonan Sun and Fabien Silly. Nacl islands decorated with 2d or 3d 3,4,9,10-perylene-tetracarboxylic-dianhydride nanostructures. *Appl. Surf. Sci.*, 256(7):2228–2231, January 2010. [84](#)
- [164] Leif Lafferentz, Francisco Ample, Hao Yu, Stefan Hecht, Christian Joachim, and Leonhard Grill. Conductance of a single conjugated polymer as a continuous function of its length. *Science*, 323(5918):1193–1197, February 2009. [88](#)
- [165] Johanna Eichhorn, Damian Nieckarz, Oliver Ochs, Debabrata Samanta, Michael Schmittel, Pawel Jerzy Szabalski, and Markus Lackinger. On-surface ullmann coupling: The influence of kinetic reaction parameters on the morphology and quality of covalent networks. *ACS Nano*, 8(8):7880–7889, August 2014. [88](#), [89](#), [100](#), [105](#)
- [166] Georg Eder, Emily F. Smith, Izabela Cebula, Wolfgang M. Heckl, Peter H. Beton, and Markus Lackinger. Solution preparation of two-dimensional covalently linked networks by polymerization of 1,3,5-tri(4-iodophenyl)benzene on au(111). *ACS Nano*, 7(4):3014–3021, April 2013. [88](#), [103](#)

- [167] Stefan Schlögl, Wolfgang M. Heckl, and Markus Lackinger. On-surface radical addition of triply iodinated monomers on au(111) - the influence of monomer size and thermal post-processing. *Surf. Sci.*, 606(1314):999–1004, July 2012. [88](#), [89](#), [100](#)
- [168] Jian Shang, Yongfeng Wang, Min Chen, Jingxin Dai, Xiong Zhou, Julian Kuttner, Gerhard Hilt, Xiang Shao, J. Michael Gottfried, and Kai Wu. Assembling molecular sierpiński triangle fractals. *Nat. Chem.*, 7(5):389–393, May 2015. [89](#), [109](#)
- [169] Denis Syomin and Bruce E. Koel. Adsorption of iodobenzene (c_6h_5i) on au(111) surfaces and production of biphenyl ($c_6h_5-c_6h_5$). *Surf. Sci.*, 490(3):265–273, 2001. [100](#)
- [170] J. Christopher Love, Lara A. Estroff, Jennah K. Kriebel, Ralph G. Nuzzo, and George M. Whitesides. Self-assembled monolayers of thiolates on metals as a form of nanotechnology. *Chem. Rev.*, 105(4):1103–1170, April 2005. [102](#)
- [171] Luis Cardenas, Rico Gutzler, Josh Lipton-Duffin, Chaoying Fu, Jaclyn L. Brusso, Laurentiu E. Dinca, Martin Vondracek, Yannick Fagot-Revurat, Daniel Malterre, Federico Rosei, and Dmitrii F. Perepichka. Synthesis and electronic structure of a two dimensional [small pi]-conjugated polythiophene. *Chem. Sci.*, 4:3263–3268, 2013. [110](#), [118](#)
- [172] Lars Smykalla, Pavel Shukryna, Marcus Korb, Heinrich Lang, and Michael Hietschold. Surface-confined 2d polymerization of a brominated copper-tetraphenylporphyrin on Au(111). *Nanoscale*, 7(9):4234–4241, February 2015. [110](#)
- [173] Marco Di Giovannantonio, Mohamed El Garah, Josh Lipton-Duffin, Vincent Meunier, Luis Cardenas, Yannick Fagot Revurat, Albano Cossaro, Alberto Verdini, Dmitrii F. Perepichka, Federico Rosei, and Giorgio Contini. Insight into Organometallic Intermediate and its evolution to covalent bonding in surface-confined ullmann polymerization. *ACS Nano*, 7(9):8190–8198, September 2013. [110](#)
- [174] Min Chen, Jie Xiao, Hans-Peter Steinrück, Shiyong Wang, Weihua Wang, Nian Lin, Wolfgang Hieringer, and J. Michael Gottfried. Combined photoemission and scanning tunneling microscopy study of the surface-assisted ullmann coupling reaction. *The Journal of Physical Chemistry C*, 118(13):6820–6830, April 2014. 00024. [118](#)
- [175] Hans Luth. *Solid Surfaces, Interfaces and Thin films, Fifth edition*. Springer, 2004. [142](#)

REFERENCES

- [176] R. Hesse, T. Chassé, and R. Szargan. Peak shape analysis of core level photoelectron spectra using unifit for windows. *Fresenius' Journal of Analytical Chemistry*, 365(1):48–54, 1999. [145](#)
- [177] Lightsources.org. Soleil synchrotron, 2016. [Online; accessed 31-August-2016]. [145](#)
- [178] Synchrotron SOLEIL. Soleil in 3 questions, 2016. [Online; accessed 31-August-2016]. [145](#), [146](#), [147](#)

Titre : Elaboration de nanoarchitectures organiques bidimensionnelles par auto-assemblage et réactions sur surface

Mots clés : Auto-assemblage, Microscopie à Effet Tunnel, Surface, Ullmann, Ultra Vide.

Résumé : Ces dernières années ont été marquées par de grandes évolutions technologiques à travers notamment une course à la miniaturisation. De gros efforts de recherche se concentrent en particulier sur le domaine de l'électronique organique mais aussi sur de nouveaux matériaux bidimensionnels comme le graphène. Ces matériaux 2D présentent des propriétés physiques exceptionnelles et sont des candidats prometteurs pour le développement de futurs dispositifs électroniques.

Au cours de cette thèse, l'approche ascendante, qui consiste à assembler ensemble des petites briques élémentaires, a été utilisée pour élaborer des nanostructures bidimensionnelles originales sur des surfaces.

Des états électroniques localisés dus à un couplage électronique latéral particulier entre les molécules ont été observés. Quatre nanoarchitectures hybrides ioniques-organiques différentes ont été réalisées en faisant varier la température de la surface. Des nanostructures organiques covalentes ont aussi été élaborées par une réaction de couplage d'Ullmann sur la surface. Deux précurseurs différents en forme d'étoile avec des substituants iodés et bromés respectivement, ont été étudiés. De grandes nanostructures carbonées hexagonales poreuses ont notamment été synthétisées en faisant varier la température du substrat. Ces travaux ouvrent de nouvelles perspectives pour la réalisation de matériaux organiques bidimensionnels aux propriétés contrôlées.

Title : Engineering two-dimensional organic nanoarchitectures using self-assembly and on-surface reactions

Keywords : Self-assembly, Scanning Tunneling Microscopy, Surface, Ullmann, Ultra High Vacuum

Abstract : Over the last few years, important technological developments were made following a trend towards miniaturization. In particular, lots of research efforts are put into the research on organic electronics and on 2D materials like graphene. Such 2D materials show great physical properties and are promising candidates for the development of future electronic devices.

In this project, bottom-up approach consisting in assembling elementary building blocks together, was used to engineer novel two-dimensional nanostructures on metal surfaces. The properties of these two-dimensional nanostructures were investigated using Scanning Tunneling Microscopy (STM) and X-ray Photoemission Spectroscopy (XPS). Two-dimensional nanostructures based on the self-assembly of organic building blocks stabilized by intermolecular interactions were

engineered. In particular, nanostructures stabilized by hydrogen bonds, halogen bonds and ionic-organic interactions were investigated. Localized electronic states due to specific molecular lateral electronic coupling were observed. Four different ionic-organic nanoarchitectures were engineered varying the substrate temperature. Covalent organic nanostructures were also engineered by on-surface Ullmann coupling reaction. Two different star-shaped precursors with iodine and bromine substituents respectively, were investigated. Large periodic porous 2D covalent hexagonal carbon nanostructures were successfully engineered by temperature driven hierarchical Ullmann coupling. These results open new perspectives for the development of 2D organic materials with controlled structures and properties.

